UNIVERSITÉ DE NEUCHÂTEL

Arene ruthenium assemblies to treat hypoxic tumors

A dissertation submitted to the University of Neuchâtel,
for the degree of Doctor ès Sciences,
by

Marie Gaschard

Graduated with a Master diploma
"*Chimie Moléculaire*"
from UPMC (Paris VI), France

Examination members:

- **Pr. Bruno Therrien**
  Thesis supervisor,
  University of Neuchâtel, Switzerland
- **Pr. Stephan von Reuss**
  Internal examiner,
  University of Neuchâtel, Switzerland
- **Pr. Guy Royal**
  External examiner,
  University of Grenoble, France

Thesis defended on
April 24, 2020

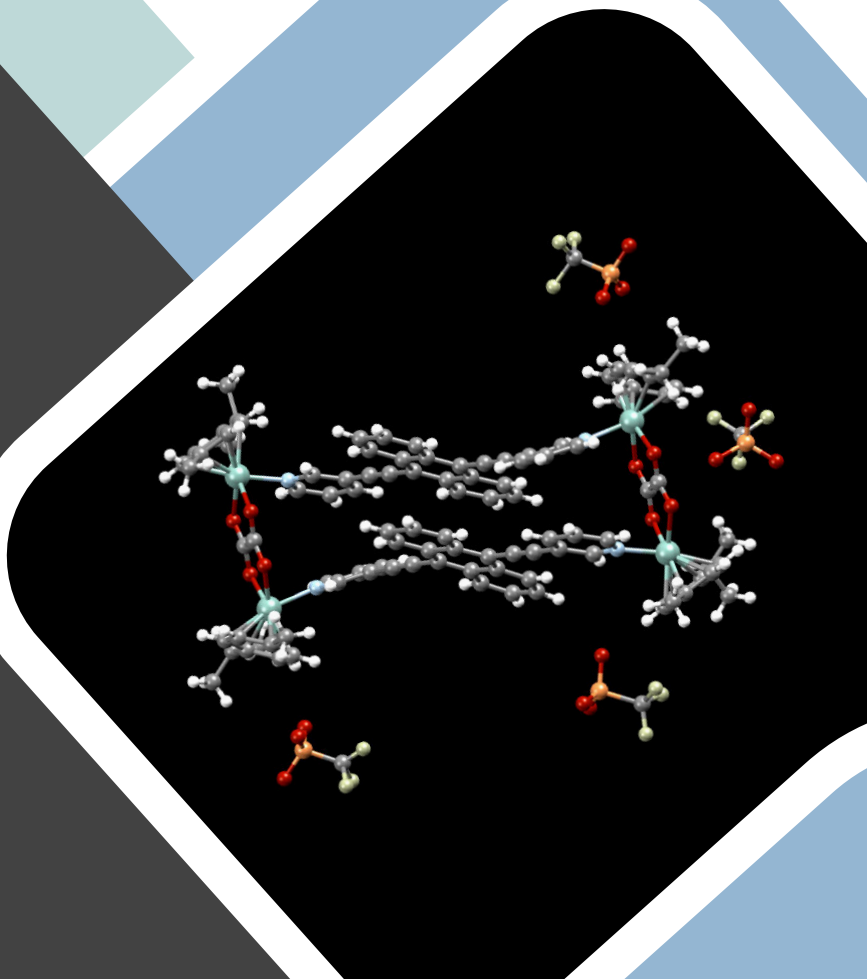

UNIVERSITÉ DE NEUCHÂTEL

Faculté des Sciences
Secrétariat-décanat de Faculté
Rue Emile-Argand 11
2000 Neuchâtel – Suisse
Tél : + 41 (0)32 718 21 00
E-mail : secretariat.sciences@unine.ch

IMPRIMATUR POUR THESE DE DOCTORAT

La Faculté des sciences de l'Université de Neuchâtel autorise l'impression de la présente thèse soutenue par

Madame Marie GASCHARD

Titre:

"Arene ruthenium assemblies to treat hypoxic tumors"

sur le rapport des membres du jury composé comme suit:

- Prof. titulaire Bruno Therrien, directeur de thèse, Université de Neuchâtel, Suisse
- Prof. ordinaire Stephan von Reuss, Université de Neuchâtel, Suisse
- Prof. Guy Royal, professeur des universités, Université de Grenoble, France

Neuchâtel, le 27 avril 2020

Le Doyen, Prof. P. Felber

P. Fel

Acknowledgements

First, I would like to deeply thank Pr. Bruno Therrien for giving me the opportunity to work in Neuchâtel. He entrusted me with the practical class by nominating me as responsible of it. It was an enriching experience and I was not conscious of my great interest for teaching to young scientists. In addition, he presented me a pioneering project for his group and let me autonomous about my research.

I also would like to express my gratefulness to Pr. Stephan von Reuss, from the University of Neuchâtel (Switzerland), and to Pr. Guy Royal, from the University of Grenoble (France), for accepting to be part of my defense committee and for taking time to read, to correct and to discuss this manuscript with me, especially during this hard period of quarantine (COVID-19).

I thank all the scientists I worked with as well. First, Pr. Guy Royal and especially his student, Dr. Margot Jacquet, who welcomed me for few days in November 2017. Then, Pr. Christoph Schalley, from the University of Berlin (Germany), and his PhD students Daniel Stares and Sarajit Naskar, for having worked and analyzed my molecules. My thanks are also going to the analytical teams involved in my work: the members of the NPAC from the University of Neuchâtel, the mass spectrometry service from the University of Fribourg and the elemental analysis service from the University of Zurich. A big thank for my colleague, Manuel Ángel Gallardo Villagrán, who did all the biological tests with my compounds when he was in Limoges, under the supervision of Pr. Bertrand Liagre. Special thanks to Pr. Reinhard Neier, with whom I discuss a lot during these four years.

I would like to point out the work of the caretaker of the building, Mohamed Billa, and the two people working in the CPAC, Habib Abdelkhalek and Matthieu Bueche, who were always nice and available for me.

During my PhD, I have met a lot of people in Neuchâtel and I would like address them my thanks and my gratefulness.

First, all my lab mates, especially Thomas and Johanna, who made my first times so pleasant in Neuchâtel; Manuel and João, "the new guys", who made my days in the lab so much nicer and funnier; Diogo and Bastian, my two Swiss apprentices, who gave me an exceptional technical and psychological support.

For six months, I had the great pleasure to work with my dear sweet Salma. She was always full of life, particularly with her way to say "Hello Marie" every morning. She gave me the opportunity to discover her country and the Iranian culture. I will always remember her.

It was also a pleasure to share enjoyable moments with the people from the University. Particularly, I would like to mention Giau for his presence and for making us laugh; Yassine, for his lovely extravagance and his wisdom; Cristina, to be more than a colleague but also a supportive friend; Magda and Sarah, for their kindness and for all the good moments shared outside of the lab; Mathilde, for her unconditional friendship and for our early breakfasts and long discussions. Special mention for Magda and Mathilde: they made their best to create a good atmosphere in the institute (thank you so much gurlzzzzz!). Sonia and James, Pamela and Tobias for being such lovely people; Lucienne, who accepted to sew my wedding dress, and Norbert, my favorite non-chemist partner.

I spent a lot time with the team of my husband and I would like to express my thanks to first, his boss, Pr. Brigitte Mauch-Mani, who is an amazing chief. I am glad for having met her and for knowing such a beautiful person; and Fares, for being an excellent friend, for accepting me in his office and for all the stories about Algeria.

I also want to say a big thank to the two women who gave me my first opportunity to work in a research lab: Dr. Anne Vessières-Jaouen and Dr. Michèle Salmain. They also gave me an unfailing moral support during these four years.

To finish, I would like to mention all the people dear to my heart.

First, my friends from Brest: Mathilde, Geoffrey, Clémence, Jérémy, Guillaume, Jonas, Erell, Adrien and Henri. Many thanks for all the moment of madness, joy and laughs. I have not enough space to describe how much I like you!

Some special words for my dearest friends “les babes” (Sonia, Matthieu), their daughters Heather and Hailey, Franz and his girlfriend Eliane: my world without you would be empty and imperfect.

My biggest thanks are going to the most important people in my life: my family and especially my brothers, Anthony and Cédric, and my parents. Without their support and their presence, I would not be able to reach that point. I can never say enough thank you for what you brought me.

And the last words, for my love, Francesco. *Sei la cosa pìu bella che mi sia successa a Neuchâtel. Sei diventato una parte inseparabile di me. Ti amo tanto.*

Abstract and Keywords

The actual therapies for fighting cancers are not always efficient and are commonly followed by side effects, since the solutions are not enough selective. Photodynamic therapy (PDT) is an appealing treatment to tackle the issue of selectivity. In fact, to work and to be efficient, PDT needs to combine in the same physico-temporal space three elements: a light, a drug (also called photosensitizer) and oxygen. Nevertheless, the lack of oxygen is one of the main characteristics in a majority of cancers. This phenomenon is called hypoxia. The efficiency of a treatment which needs oxygen will consequently be reduced. So, there is a real need to find a solution to bypass hypoxia.

One of the possible answers is the synthesis of new structures able to transport oxygen into tumorous cells. Our attention was focused on arene ruthenium complexes with subunits that can capture oxygen. These probes are derivatives of anthracene or dimethyldihydropyrene cores. Then, this work consisted, not only in the synthesis and in the characterization of these molecules, but also in their studies in solution and *in vitro*, to determine their ability to transfer oxygen to cells, and ultimately to cancer cells.

Keywords: Arene ruthenium, dimethyldihydropyrene, anthracene, photodynamic therapy, singlet oxygen, hypoxia.

Résumé et Mots-Clés

Les thérapies actuelles pour lutter contre les cancers ne sont pas toujours efficaces et sont généralement accompagnées d'effets secondaires, car les solutions apportées ne sont pas suffisamment sélectives et touchent également les cellules saines. La thérapie photodynamique (*photodynamic therapy*, PDT) est un nouveau traitement très prometteur pour surmonter ce problème de sélectivité. En effet, pour fonctionner et être efficace, la PDT a besoin d'avoir dans un même espace spatio-temporel trois éléments : la lumière, le médicament sensible à la lumière (appelé aussi photosensibilisateur) et l'oxygène. Or, le manque d'oxygène, ou hypoxie, est la caractéristique de la plupart des cancers. L'efficacité de ce nouveau traitement est donc réduite. Il est plus que nécessaire de trouver une solution pour contourner l'hypoxie.

Une des clés possibles est la synthèse de nouvelles structures pouvant transporter de l'oxygène jusqu'aux cellules cancéreuses. L'attention a été portée sur des dérivés d'arène ruthénium contenant des sous-unités jouant le rôle de capteurs d'oxygène. Ces derniers sont des dérivés d'anthracène ou de diméthyldihydropyrène. Ce travail de thèse a donc consisté non seulement à la synthèse et à la caractérisation de ses molécules, mais également à leur étude en solution et *in vitro*, afin de déterminer leur capacité à transporter l'oxygène.

Keywords: Arène ruthénium, diméthyldihydropyrène, anthracène, thérapie photodynamique, oxygène singulet, hypoxie.

Table of contents

Table of illustrations

Figures

Tables

Schemes

Abbreviations

A	
K	Ångström (1Å = 10^{-10} m)
A_{anthr}	Ruthenium assembly containing an anthracene core
A_{anthr}-EPO	Endoperoxide form of A_{anthr}
Acetyl-CoA	Acetyl coenzyme A
A_{DHP}	Ruthenium assembly containing a dimethyldihydropyrene core
AgOTf	Silver trifluoromethanesulfonate or silver triflate
AKT	Protein kinase B (also called PKB)
AMPK	AMP-activated protein kinase
Ang2	Angiopoietin 2
ARNT	Aryl hydrocarbon receptor nuclear translocator
ASCT2	Alanine-serine-cysteine transporter 2 (SLC1A5 gene)
ASR	Age-standardized rate
ATP	Adenosine triphosphate
B	
	$BF_3{\cdot}Et_2O$Boron trifluoride etherate
bFGF	Basic fibroblast growth factor
BNIP-3	BCL2 interacting protein 3 (gene)
BODIPY	Boron-dipyrromethene
BOLD-MRI	Blood oxygen level-dependent MRI
	t-BuOK Potassium *tert*-butoxide
C	
$(CD_3)_2CO$	Acetone-d6
C-C bond	Carbon-carbon bond
C_6H_6	Benzene
CAIX	Carbonic anhydrase IX
cAMP	Cyclic adenosine monophosphate
CDK	Cyclin-dependent kinase
CH_2Cl_2 / CD_2Cl_2	Dichloromethane / Dichloromethane-d2
$CHCl_3$ / $CDCl_3$	Chloroform / Chloroform-d3
CH_3CN / CD_3CN	Acetonitrile / Acetonitrile-d3
CH_3OH	Methanol
Cl^-	Chloride anion
CO_2	Carbon dioxide
COSY	Correlated Spectroscopy
CPD	Cyclophanediene
CPD-EPO	Endoperoxide form of CPD
CRT	Chemoradiotherapy
CXCR4	CXC chemokine receptor type 4
D	
DAMPS	Damage-associated molecular patterns
DAPI	4′,6-diamidino-2-phenylindole
DFT	Density functional theory
DHP	Dimethyldihydropyrene

DLI	Drug-light interval
DMF	Dimethylformamide
DMSO	Dimethylsulfoxide
DNA	Deoxyribonucleic acid
DNA$^{\bullet}$	Radical DNA
dobq	2,5-dioxido-1,4-benzoquinonato
donq	5,8-dioxido-1,4-naphtoquinonato
DOSY	Diffusion spectroscopy

E

E-cad	E-cadherin
E_0	Standard electrode potential
ECM	Extracellular matrix
EF5	18F-2-nitroimidazolpentafluoropropylacetamide
EMT	Epithelial-to-mesenchymal transition
EPOs	Endoperoxides
EPR	Enhanced permeability and retention
ERK1/2	Extracellular signal-regulated kinase
ESI-MS	Electrospray ionization mass spectrometry
Et_2O	Diethylether
Et_3N	Triethylamine
EtOH	Ethanol
EU	European Union
EtOAc	Ethyl acetate
ε	Molar attenuation coefficient (in $mol^{-1}.L^{1}.cm^{1}$)

F

18-F	Fluor 18 (isotope)
FAZA	18F-fluoro-azomycin-arabinoside
Fe^{2+}	Iron(II) cation
Fe^{3+}	Iron(III) cation
FMISO	18F-fluoromisonidazole
Fructose-1,6-bisP	Fructose-1,6-bisphosphate
Fructose-6-P	Fructose-6-phosphate

G

Glucose-6-P	Glucose-6-phosphate
GLUT1	Glucose transporter 1
GLUT3	Glucose transporter 3
Glyceraldehylde-3-P	Glyceraldehyde-3-phosphate
GPCRs	G protein-coupled receptors
GSK	Glycosine synthase kinase

H

4-HPR	4-hydroxy(phenyl)retinamide or fenretinide
H^+	Hydrogen cation, usally called proton
H_2O	Water
H_2O_2	Hydrogen Peroxide
HBr	Hydrogen bromide
HCl	Hydrochloric acid
HCO_3^-	Hydrogencarbonate ion
HDI	Human development index
HeLa	Immortal cell line (from Henrietta Lacks, died of cervical cancer)
HIF	Hypoxia-inducible factor
HIF-OH	Hydroxylated hypoxia-inducible factor
HMBC	Heteronuclear multiple bond correlation

HOMO	Highest occupied molecular orbital
HpD	Hematoporphyrin derivative
HPV	Human papillomavirus
HSPs	Heat shock proteins
HSQC	Heteronuclear single quantum correlation
HX4	18F-flortanidazole

I

I^-	Iodide ion
ILCT	Intra-ligand charge-transfer
IR	Infrared
ISC	Intersystem crossing

K

$kJ.mol^{-1}$	Kilo-joule per mole
KOH	Potassium hydroxide

L

L_{anthr}	Ligand containing an anthracene core
L_{anthr}-EPO	Endoperoxide form of L_{anthr}
L_{DHP}	Ligand containing a DHP core
L_{DHP}-EPO	Endoperoxide form of L_{DHP}
LEDs	Light-emitting diodes
LKB1	Liver kinase B1
LOX	Lysyl oxidase
LUMO	Lower unoccupied molecular orbital
λ	Wavelength, in nm

M

M	Molar (1 M = 1 mol. L^{-1})
$M^{-1}.cm^{-1}$	Liter per (mole*centimeter), unit of molar attenuation coefficients
m/z	mass/charge
MAPK	Mitogen-activated protein kinase
MCT	Monocarboxylate transporter
MeI	Iodomethane
MeOH	Methanol
$MgSO_4$	Magnesium sulfate
MLCT	Metal-to-ligand charge-transfer
mmHg	Millimeter of mercury (1mmHg = 133.3224 Pa)
MMPs	Matrix metallopeptidases
MRI	Magnetic resonance imaging
MSA	Methanesulfonic acid
mTOR	Mechanistic target of rapamycin
MTT	Bromure de 3-(4,5-dimethylthiazol-2-yl)-2,5-diphenyl tetrazolium
MYC	Family of oncogenes
µL	Microliter (1µm = 10^{-6} L)
µm	Micrometer (1µm = 10^{-6} m)
µs	Microsecond (1µs = 10^{-6} s)

N

n-BuLi	*n*-Butyllithium
Na_2CO_3	Sodium carbonate
$NaBH_4$	Sodium borohydride
NADP	Nicotinamide adenine dinucleotide phosphate
NADPH	Reduced form of NADP
NaOH	Sodium hydroxide

NBS	*N*-bromosuccinimide
NFκB	Nuclear factor-κB
NGO	Non-governmental organization
nm	Nanometre (1nm = 10^{-9} m)
$^{1}H/^{13}C$ NMR	Proton/carbon nuclear magnetic resonance
NO	Nitric oxide

O

$^{1}O_2$	Singlet oxygen
$^{3}O_2$	Molecular oxygen
O_2	Dioxygen, commonly called oxygen
$O_2(^{1}\Delta_g)$	Singlet oxygen with a spin pairing in the external orbital
$O_2(^{1}\Sigma_g)$	Singlet oxygen with a spin inversion in the external orbital
$O_2(^{3}\Sigma_g)$	Molecular oxygen
$O_2^{\bullet-}$	Superoxide anion (radical)
$OH^{\bullet}$	Hydroxide radical
OO∩OO ligands	Bridging ligands (dobq, donq or oxa)
OTf^{-}	Triflate anion
Oxa	Oxalato

P

^{1}PS	Photosensitizer at an excited singlet state
$^{1}PS_0$	Phostosensitizer at S_0 state
$^{1}PS_1$	Phostosensitizer at S_1 state
$^{3}PS^{*}$	Photosensitizer at an excited triplet state
$^{3}PS_1$	Phostosensitizer at T_1 state
6-P-gluconate	6-phosphate-gluconate
p38	Class of MAPK
p53	Tumor protein 53 (transcriptor factor)
Pa.s	Pascal*second
$Pd(OAc)_2$	Palladium(II) acetate
$Pd(PPh_3)_4$	Palladium(0)-tetrakis(triphenylphosphine)
PDGF	Platelet-derivated growth factor
PDT	Photodynamic therapy
PET	Positron emission tomography
PF_6^{-}	Hexafluorophosphate ion
PHDs	Prolyl-4-hydroxylases
pH_e	Extracellular pH
pH_i	Intracellular pH
PI	Phototoxic index
PI3K	Phosphoinositide-3-kinase
pO_2	Partial pressure of oxygen
PPh_3	Triphenylphosphine
ppm	Parts per billion
PS	Photosensitizer
PS^{*}	Excited photosensitizer
$PS^{\bullet-}$	Photosensitizer radical anion
$PS^{\bullet+}$	Photosensitizer radical cation
pta	1,3,5-triaza-7-phosphatricyclo-[3.3.1.1]decane
pVHL	Von Hippel Lindau protein

R

RNA	Ribonucleic acid
ROS	Reactive oxygen species
RT	Room temperature
RTK	Receptor tyrosine kinase

Ru(dobq)	Ruthenium clip with a dobq group as bridging unit
Ru(donq)	Ruthenium clip with a donq group as bridging unit
Ru(oxa)	Ruthenium clip with an oxa group as bridging unit

S

s	Seconde
S_0	Singlet ground state
S_1	Singlet excited state 1
SDF-1	Stroma cell-derived factor 1
SN2	Glutamine transporter system N 2
SOD	Superoxide dismutase

T

T_1	Triplet excited state 1
TCA	Tricarboxylic acid
TGF-β	Transforming growth factor β
THF	Tetrahydrofuran
TLC	Thin layer chromatography
TLR	Tool-like receptor
TME	Tumor microenvironment
TPP	Tetraphenylporphyrin
tpvb	1,2,3,4-tetrakis{2-(4-pyridyl)vinyl}benzene

U

UK	United Kingdom
US$	American Dollar
USA	United States of America
UV	Ultraviolet
UV-VIS	Ultraviolet-visible

V

VEGF	Vascular endothelial growth factor

W

WHO	World health organization

X

Xe-Hg	Xenon-mercury

Z

$ZnBr_2$	Zinc(II) bromide

List of structures

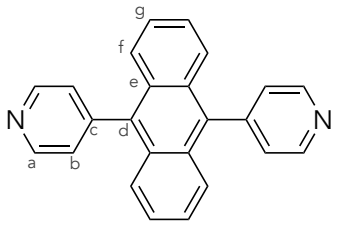

L_1

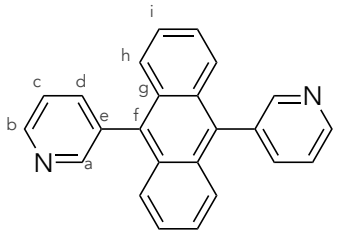

L_2

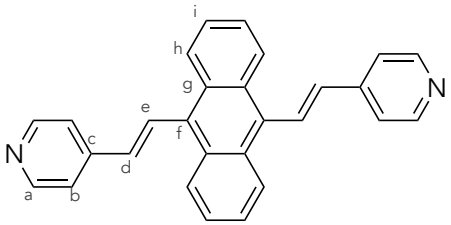

L_3

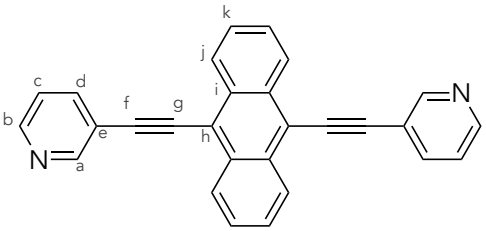

L_4

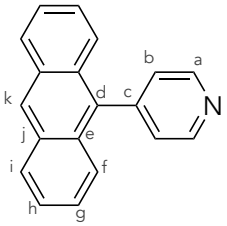

L_5

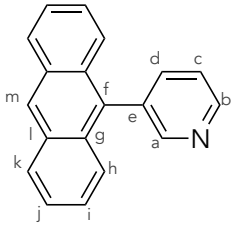

L_6

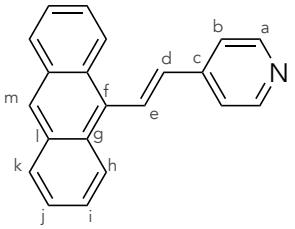

L_7

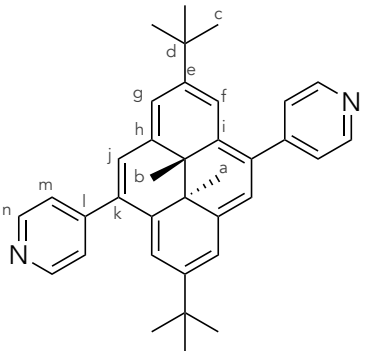

L8

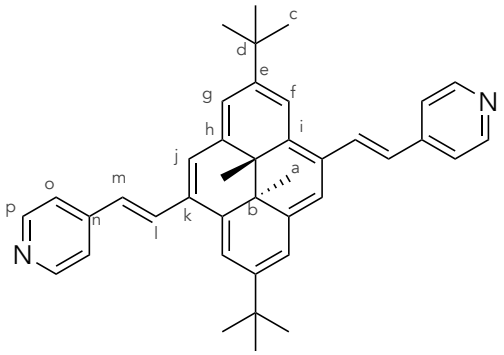

L9

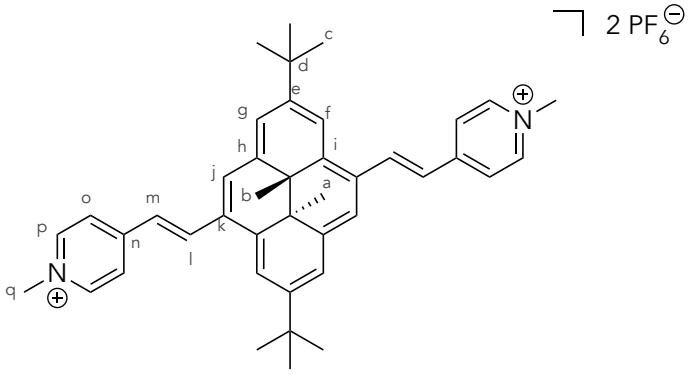

L10

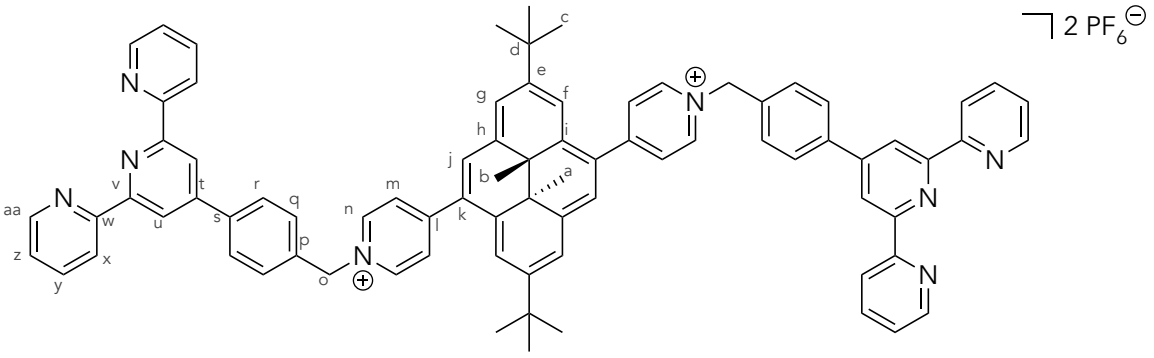

L11

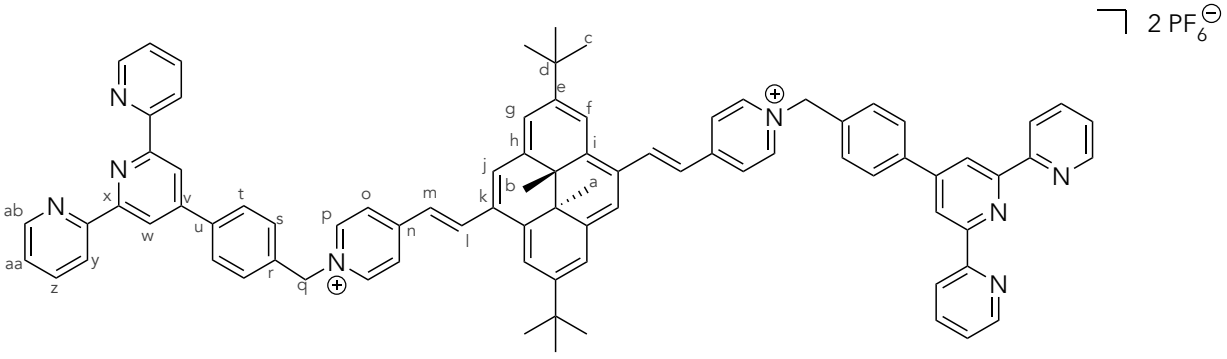

L12

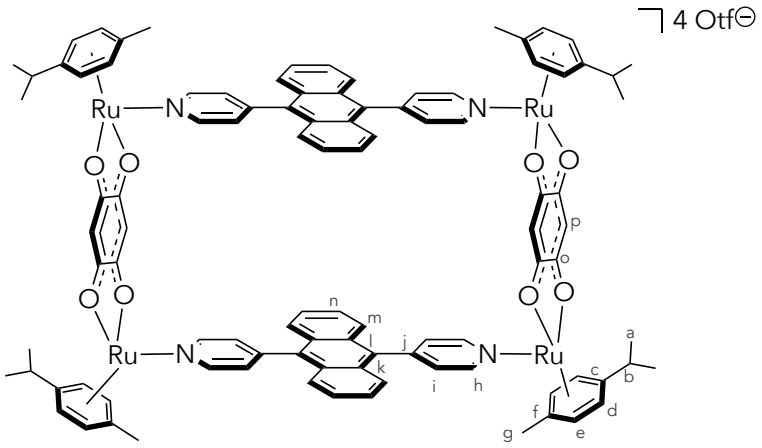
4 Otf⊖
Ru
N
O
p
o
n
m
l
j
k
i
h
a
b
c
d
e
f
g

A_1

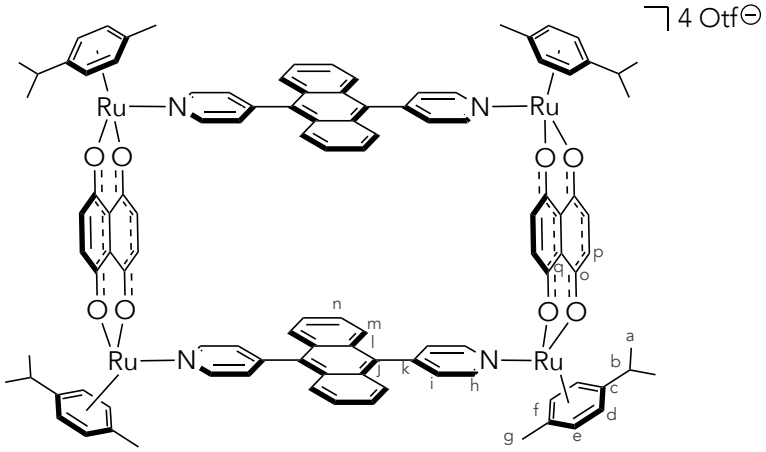
4 Otf⊖
Ru
N
O
q
p
o
n
m
l
j
k
i
h
a
b
c
d
e
f
g

A_2

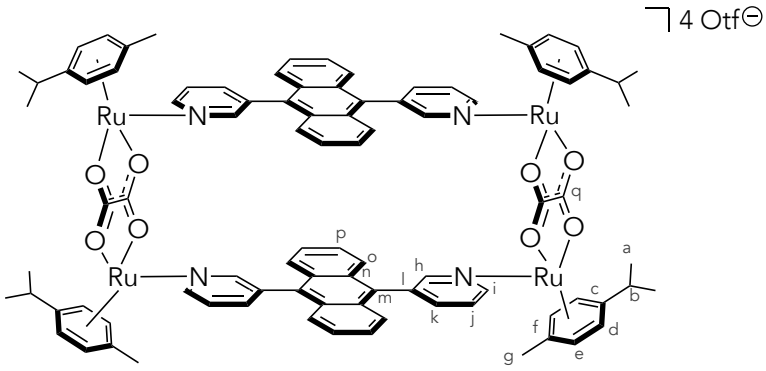
4 Otf⊖
Ru
N
O
q
p
o
n
m
l
h
i
j
k
a
b
c
d
e
f
g

A_3

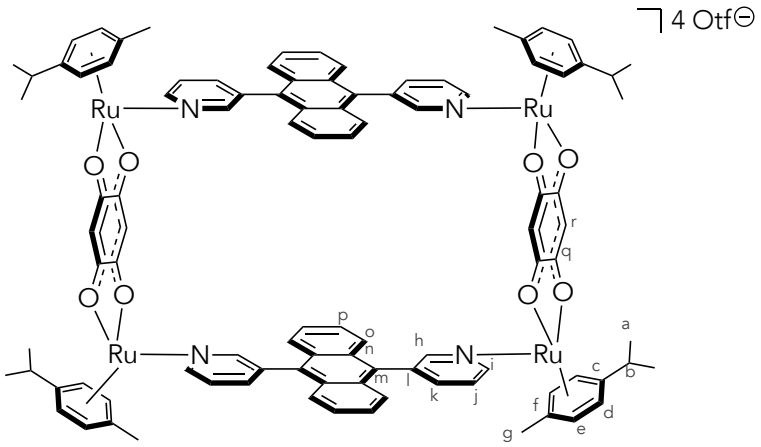
4 Otf⊖
Ru
N
O
p
o
n
h
i
m
l
k
j
r
q
a
b
c
d
e
f
g

A_4

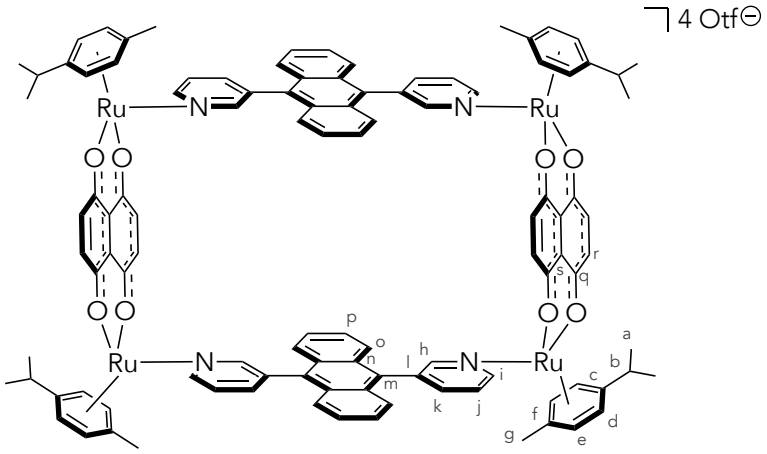
4 Otf⊖
Ru
N
O
p
o
n
h
l
i
m
k
j
r
s
q
a
b
c
d
e
f
g

A_5

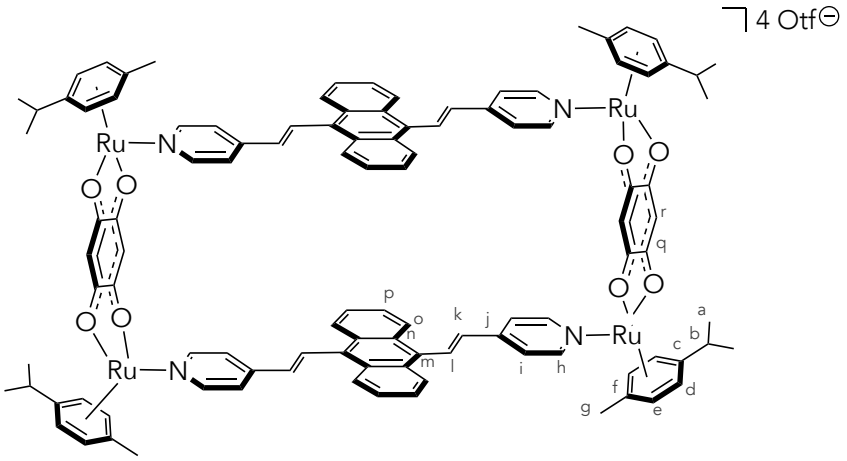
4 Otf⊖
Ru
N
O
p
o
n
k
j
l
m
i
h
r
q
a
b
c
d
e
f
g

A_6

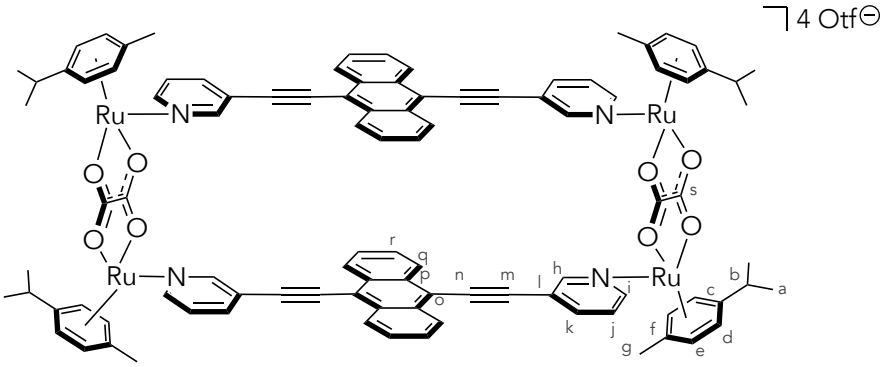
4 Otf⊖
Ru
N
O
r
q
p
n
m
l
h
i
o
k
j
s
b
a
c
f
d
g
e

A_7

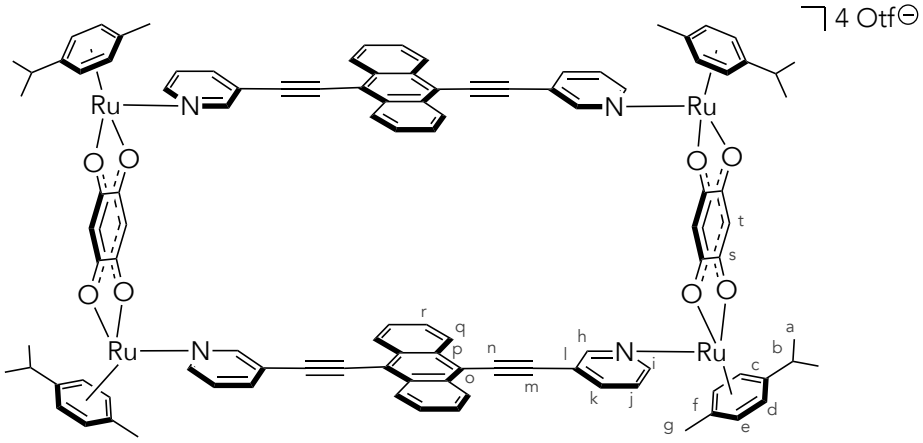
4 Otf⊖
Ru
N
O
r
q
p
n
m
l
h
i
o
k
j
t
s
a
b
c
f
d
g
e

A_8

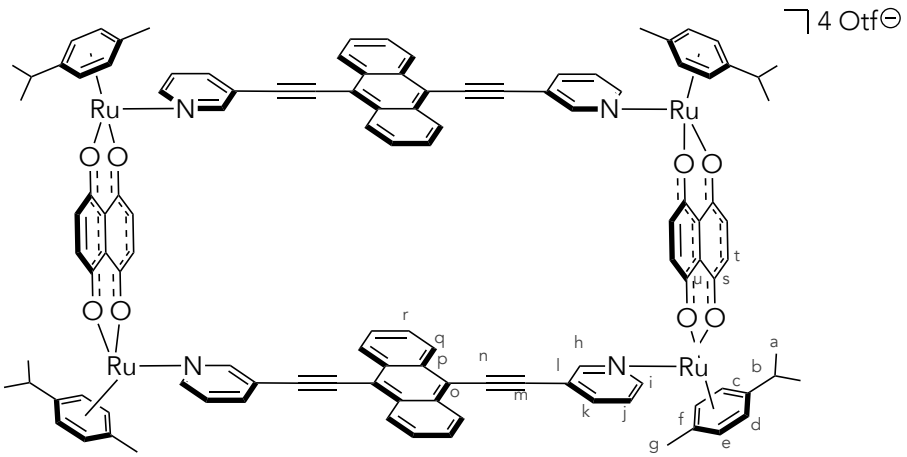
4 Otf⊖
Ru
N
O
r
q
p
n
m
l
h
i
o
k
j
t
s
a
b
c
f
d
g
e

A_9

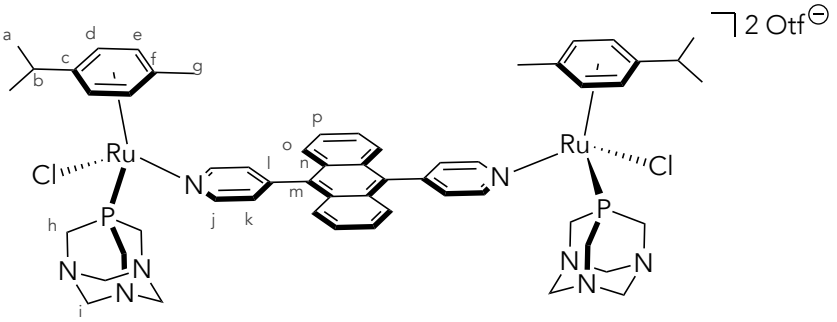

A10

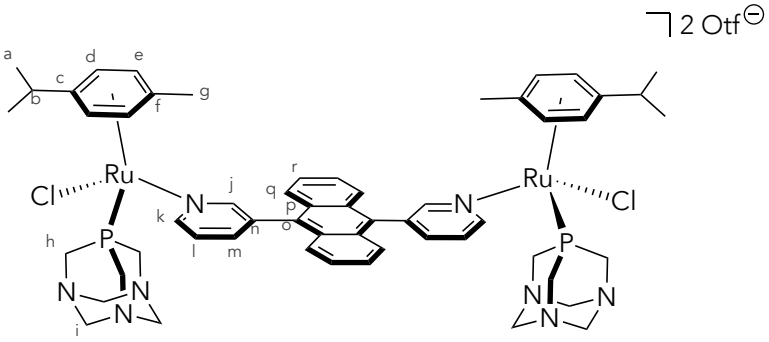

A11

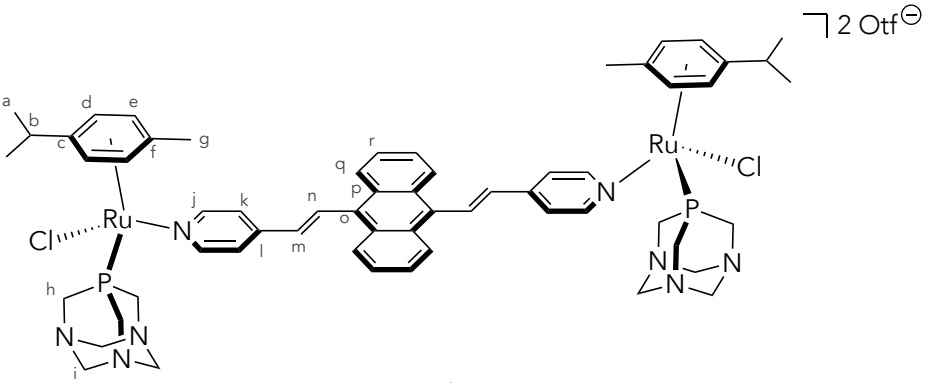

A12

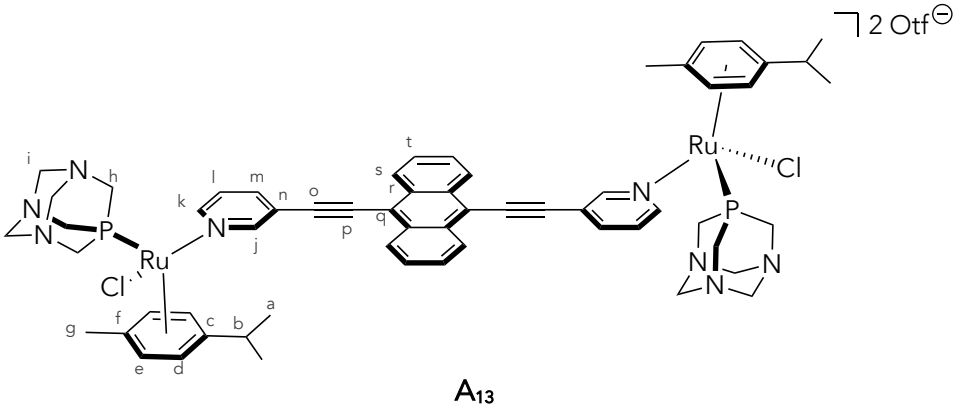

A13

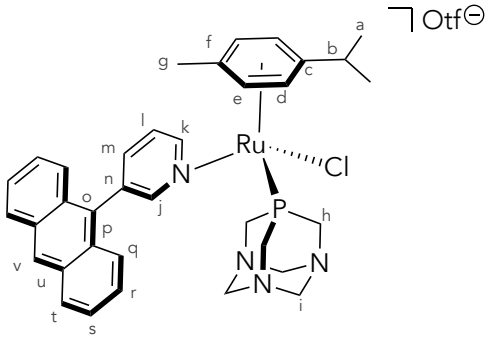

A14

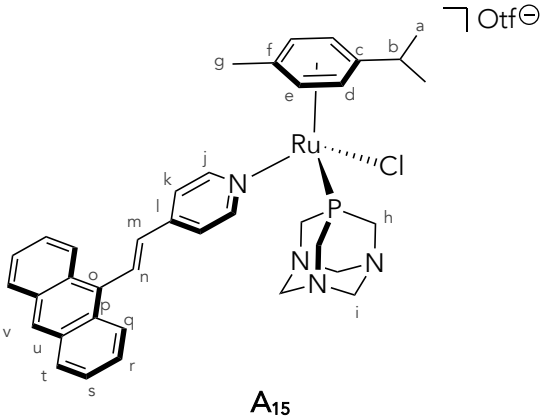

A15

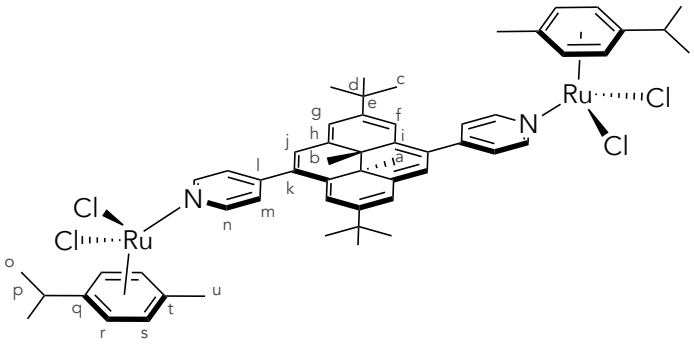

A16

1. General introduction

1.1. Cancer: a global burden

1.1.1. A disease that affects humankind

One of the major causes of morbidity and mortality in the world is cancers. The latter term is plural because there are hundred kinds of cancer but all share common features. Then, the term "cancer" is defined as an uncontrollable development of abnormal cells that can acquire mobility through the body, infiltrate other tissues, and can unfortunately lead to death.[1]

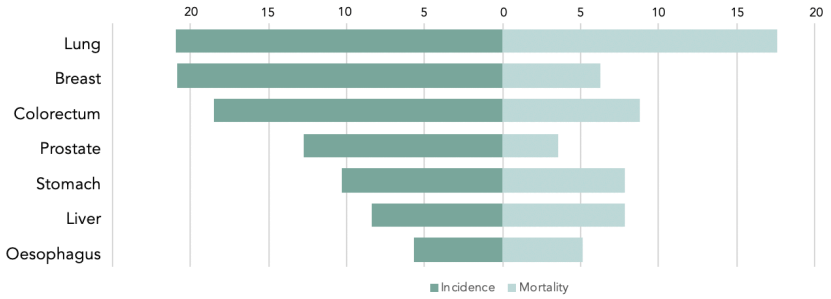

Figure 1: Age-standardized incidence and mortality rates for the most common cancers (2018, world, both sexes, all ages).[4]

Every year, the World Health Organization (WHO) publishes the global cancer statistics on its website.[2] WHO reported for 2018, for both sexes and all ages, around 18 million of new cases and almost 9.6 million of deaths, that is to say about 1 in 6 global deaths is due to cancer.[3] So far, the deadliest cancers are lung (18.4% of the global total deaths), followed by colorectal (9.2%), stomach and liver (8.2% each).[4] Figure 1 shows the repartition of the age-standardized rates for the incidence and the mortality for the most commonly recorded cancers.[4] Not all cancers automatically lead to death because people can be in remission or totally cured, thanks to an early-diagnosis or a better access to treatment. From a global

perspective, all the data concerning cancer are closely related to the value of the Human Development Index (HDI). In fact, high-income countries show higher age-standardized incidence and prevalence rates (figures 2 and 3) than countries with low HDIs.[5] These facts can be explained by the development and the access to better care services in developed countries, unlike to developing countries where there are poor clinical outcomes, coupled to a lower education regarding the health care and unstable politics (wars and revolutions) and economies.[6]

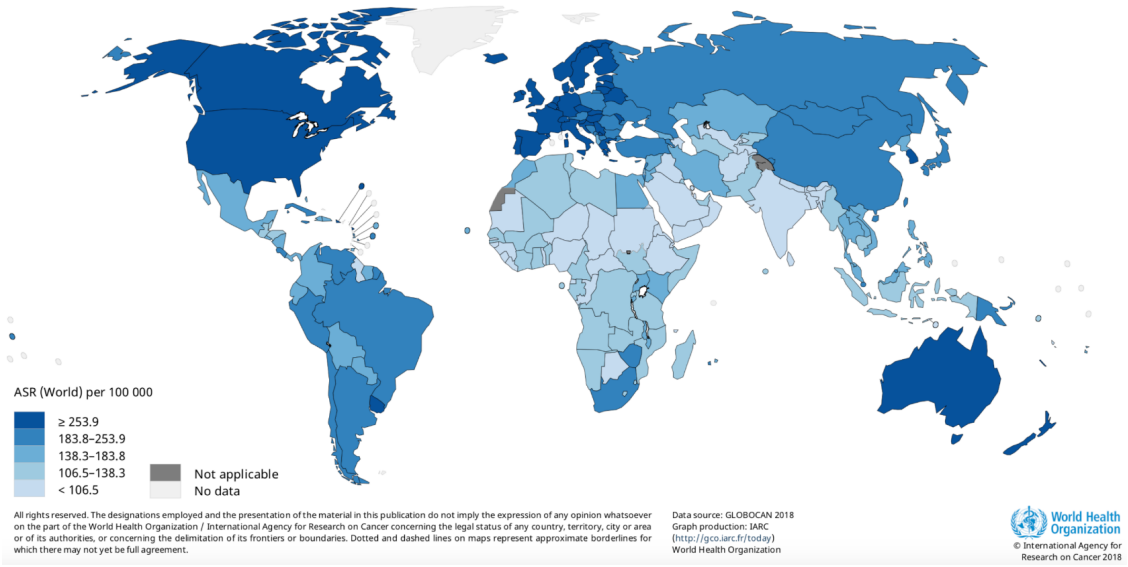

Figure 2: Age-standardized incidence rate (2018, world, both sexes, all ages).[5]

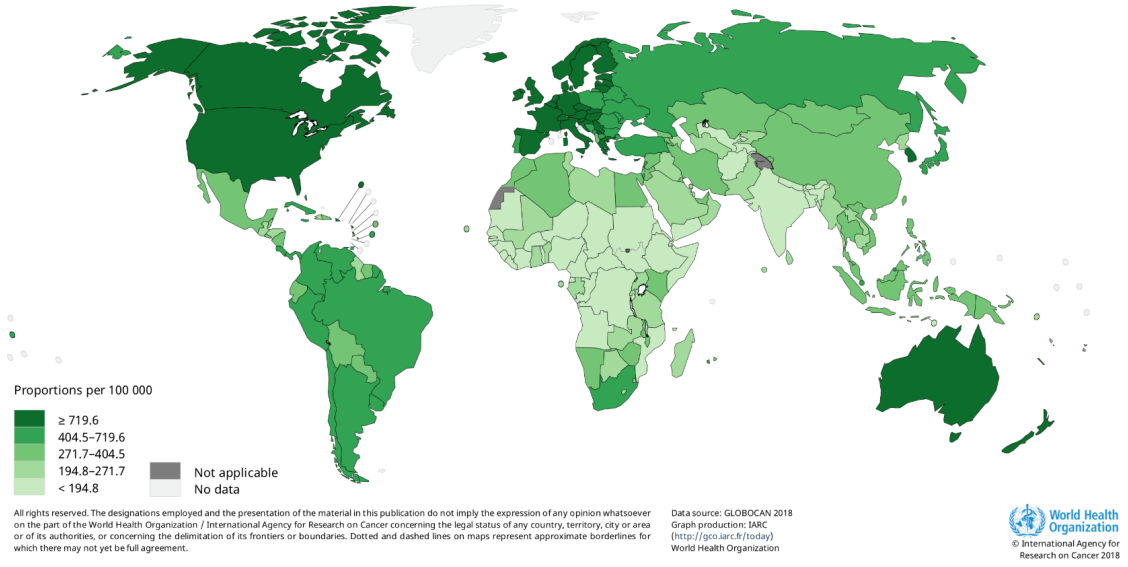

Figure 3: Age-standardized prevalence rate (2018, world, both sexes, all ages).[5]

Cancer is not only a burden on health but also on the global economy. In fact, its total annual cost in 2010 was estimated at about 1.16 trillion US$.[7] Therefore, for both economic and medical reasons, governments and Non-Governmental Organizations (NGO) try to educate people on health issues and to change people's behaviors. The main risk factors are multiple like tobacco use, being obese, lack of physical activity coupled with an unhealthy diet and alcohol use, infections (HPV or hepatitis B) or radiations (UV/ionizing). An estimation gives an interval between 30 and 50% of cases that could be avoided with intense prevention campaigns or avoidance of risks factors.[3]

1.1.2. Main characteristics of cancers

Cancer appears when there is a collapse of regulatory mechanisms in a normal cell. All the cell behaviors, such as proliferation, differentiation or death, are tightly controlled to ensure the integrity of the cell, and consequently, of the whole organism. Cancer cells succeed in escaping these controls: they grow quickly, they are uncontrollably divided and they spread out to surrounding tissues, and eventually throughout the body.[8] Their principal characteristics will be succinctly discussed in this section.

First, it is important to mention the existence of a wide variety of cancer. Many kinds of human cells can be the starting point of tumors, leading to around a hundred different types of cancers, all having specific and distinct characteristics.[9] Then, a specific vocabulary is employed. Tumor is the generic term to indicate the abnormal proliferation of cells, gathering benign and malignant tumors. A benign tumor is the static type of cancer, where cells remain confined in their original location. Usually, when it is possible, a benign tumor is removed during a surgery and the outcome is normally positive. A malignant tumor is more aggressive because it is more invasive by spreading throughout the tissues, *via* the blood and/or the lymphatic circulations. Then, the term of metastasis is used.[10] Other words exist and depend on the location where cancer cells arise. Three main types gather the majority of cancers: carcinomas (around 90% of human cancers), lymphomas (around 7%) and sarcomas (rare in humans). Carcinomas take for origin epithelial cells, whereas lymphomas appear from blood-forming or immune system cells and sarcomas derivate from connective tissues (like fibrous tissues, muscle, cartilage, bone).[9]

Cancers start after a combination of several mutations in genes. Mutations permanently occur in the body because each time the genome is replicated, there is a non-negligible probability to get them. However, most of the mutations are silent because they are either neutral for the entire genome, or not suitable and then suppressed. When it is not the case, the combined mutations provoke a perturbation in the cell cycle control and in the information sensing from the cell environment. Therefore, cancer cells can escape from all the regulatory mechanisms and become immortal. Mutations can be generated by many factors and the term of carcinogen is used for all substances that cause cancer. Carcinogens can be chemical (components of tobacco smoke), physical (ultraviolet or ionizing radiations) or biological (viruses, bacteria or parasites). They can damage the DNA with mutations or contribute to cancer development with the stimulation of proliferation processes.[3,9]

As mentioned before, cancer cells can escape to cellular regulatory controls. Normally, cells have the ability to sense their everchanging environment thanks to signals received *via* receptors, which initiate one or several biochemical reactions. This phenomenon is described as the signal transduction cascade. This succession of biochemical reactions regulates all the information about cells behavior, like its proliferation, migration, differentiation, death, motility or its metabolism. If the mechanisms are deregulated, cell homeostasis is impacted and a tumor can appear and survive. In cancer, two main classes of genes are altered: oncogenes and tumor suppressor genes. The first type facilitates the cell division, whereas the second one stops or postpones it. 125 genes (54 oncogenes and 71 tumor suppressor genes) have been identified in cancer propagation and describes as "must-driver genes".[11] In brief, gene mutations provoke either the activation of oncogenes or the suppression of tumor suppressor genes, or even both, and cells can be expanded into the body.[1,9] There are also several important distinctions between cancerous and normal cells. However, only the principal characteristic of tumors and its consequences will be described in the next section.

1.2. Hypoxia: a hallmark of cancer cells

1.2.1. General statements

1.2.1.1. Definition of oxygen levels

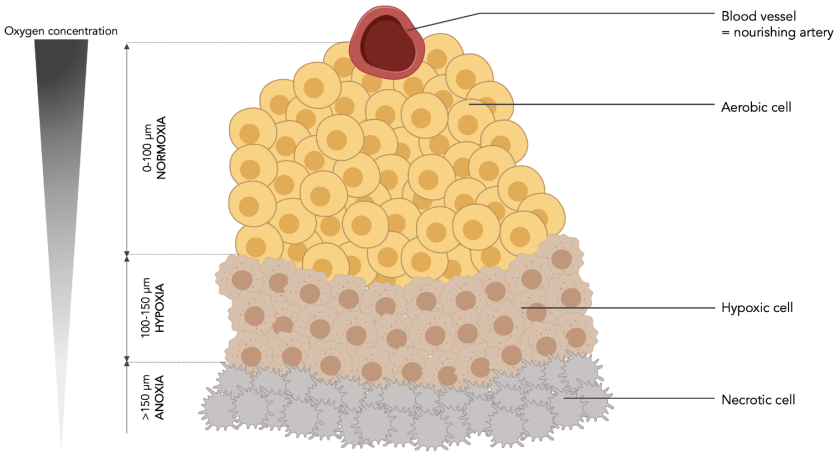

Figure 4: Three areas observed in a solid tumor, depending on the distance from the blood vessel.[12,15,16]

Hypoxia is a hallmark of human solid tumors.[12] This fundamental physiological feature corresponds to a low oxygen concentration in tissues.[13] Hypoxia happens when the oxygen demand is outgrowing the supply. In fact, cancerous cells grow in the surroundings of blood vessels, to ensure them a good nutrients and oxygen supply. However, the development of abnormal cells is so fast that the oxygen consumption is high and its diffusion is struggled.[14] In general, the available oxygen is consumed within 70-100 µm from the blood vessel. Therefore, this area is called normoxia and corresponds to well-oxygenated and very-proliferative cells. Then, the zone of hypoxia is situated at around 100-150 µm from the vasculature, where a population of cells survive despite a lower oxygen concentration. In such situation, normal cells generally enter in apoptosis, while cancerous cells adapt their behavior to survive in this hostile environment with a poor nutrition. Beyond this area, the oxygen concentration is dramatically low, even zero. The term of anoxia describes the zone where necrotic cells stand (figure 4).[15,16] When dealing with partial pressure of oxygen (pO2), physoxia is another employed term to indicate the physiological oxygen level in healthy tissues.[16] Table 1 summarizes the typical oxygen levels in various environment using a pO2 notation.[16]

Situations	mmHg	%O_2
Standard atmospheric	760	100.0
Oxygen in air (atmospheric pressure)	160	21.0
Inhaled oxygen in pulmonar alveoli	100	13.5
Oxygen in arterial blood	70	9.5
Oxygen at the end of venous circulation	50	6.5
Physoxia (depending the tissue, see table 2)	38	5.0
Physiological hypoxia (with normal hypoxic responses)	15	2.0
Pathological hypoxia (disruption to normal homeostasis)	8	1.0

Table 1: Approximative oxygen levels in different situations.[16]

1.2.1.2. Determination of oxygen levels

Hypoxia was first described in the 1950s by Thomlinson and Gray. Gray observed the importance of tissue oxygenation for a good efficiency of radiation treatments.[17] Then, with the collaboration of Thomlinson, he proved the existence of hypoxic and necrotic regions at a certain distance of an irregular vasculature.[18] After this discovery, information on hypoxia was mostly pulled from *in vivo* studies on rodent tumors.[19] The 1990s saw the development of a new method using an Eppendorf electrode, developed by Vaupel and his team.[20] Since then, different values of oxygen levels were precisely measured in healthy and cancerous tissues: they differ depending on their location (table 2). In general, physoxia is around 40 mmHg in healthy tissue and the value drops to an interval between 2 and 20 mmHg for hypoxia in cancer cells.[15]

Nowadays, several different methods exist to detect and quantify hypoxia in tumors. They are usually combined to obtain an accurate result. Some methods are direct but with the disadvantage to be invasive, such as the use of a polarographic oxygen electrode or a luminescence-based optical sensor.[27,28] Other techniques are employed in immunohistochemistry with hypoxic biomarkers. The most known markers derive from 2-nitroimidazole: pimonidazole and EF5.[29,30] They can also be useful for the Positron Emission Tomography (PET) imaging, a non-invasive method that can spatially map all the regions affected by hypoxia. For that imaging method, tracers labelled with 18-F are used and they are named FMISO, EF5, FAZA or HX4.[28,29,31,32,33] However, false results may be obtained because of remained unbound tracers.[29] Another non-invasive method, the Magnetic Resonance Imaging (MRI) is also routinely employed in hypoxia detection. Several types of

MRI have been developed but the most widespread is the BOLD-MRI.[28,29,34] Nevertheless, this technique allows an indirect measurement of hypoxia levels and strongly depends on the blood flow, leading sometimes to false estimations.[29]

	Normal tissues		*Cancerous tissues*	
Tumor type	pO_2 (mmHg)	$\%O_2$	pO_2 (mmHg)	$\%O_2$
Brain[21]	26.0	3.4	13.0	1.7
Breast[21]	52.0	6.8	10	1.3
Head and neck[22]	51.2	6.7	14.6	1.9
Lung[23]	42.8	5.6	16.6	2.2
Pancreas[24]	51.6	6.8	2.7	0.4
Prostate[25]	30.0	3.9	2.4	0.3
Rectal[26]	52.0	6.8	19.0	2.5

Table 2: Comparison of oxygen levels in some healthy and cancerous tissues.

Now, it is undoubtedly recognized that hypoxia leads to poor diagnostics because it usually permits the tumor to withstand cancer treatments.[35] Basically, when their environment becomes hypoxic, cancer cells modify their mechanism to survive and continue to grow. This is possible mainly because of (1) the development of a new vascularization, (2) the morphologic change after an epithelial-to-mesenchymal transition (EMT), (3) the formation of metastases thanks to a higher motility, an improved plasticity and a bad quality vascularization and finally (4) the resistance towards treatments.[14]

The mechanisms coming out of hypoxia are very complex but they will be explained succinctly, with their consequences, in the next section in order to understand why hypoxia is an important element to take into consideration when improving cancer treatments.

1.2.2. Implication of the HIF pathway and its main impacts on cancer cells

1.2.2.1. HIF pathway and its main characteristics

Our organism is extremely regulated by thousands of mechanisms: HIF pathway is one of them. HIF is an abbreviation for Hypoxia-Inducible Factor and represents the major transcriptional complex implied during cellular adaptation to oxygen levels. It was identified almost 30 years ago by Semenza.[36] The transcriptional complex HIF is composed by three

types: HIF-1, HIF-2 and HIF-3. So far, HIF-1 is the most studied and it is usually the one overexpressed in a majority of tumors.[37] HIF-1 is a heterodimer protein and it consists of two subunits, α and β. Instead of its innate partner 1β, HIF-1α is only detected when there is hypoxia since it is more stimulating for a low cellular pO_2 (figure 5).[38]

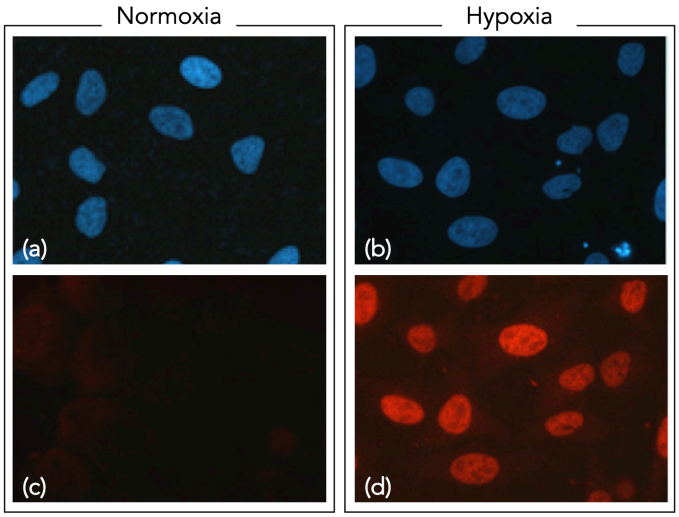

Figure 5: Immunofluorescence pictures of HeLa cell cultures in different oxygen levels, normoxia (a and c) and hypoxia (b and d). The fluorescent stains color the nuclei (a and b) and the HIF-1α (c and d). HIF-1α is only detected in the nucleus during hypoxia.[38]

Then, HIF-1α can be viewed as a cellular oxygen sensor, even it is regulated by both hypoxic and non-hypoxic factors (figure 6).[14,39] When there is a viable oxygen concentration (normoxia), two prolines of HIF-α are hydroxylated with O_2 by prolyl-4-hydroxylases (PHDs) to form HIF-OH. Then, HIF-OH is destabilized and recognized by Von Hippel Lindau protein (pVHL), to be ubiquitinated and finally degraded by a proteasome (figure 6). HIF-α is also regulated by other factors during normoxia, such as ROS (Reactive Oxygen Species), cytokines, lipopolysaccharides and/or growth factors via different receptors (figure 6). When hypoxia appears in cancer cells: the hydroxylation process stops and provokes the stabilization of HIF-α, that allows its accumulation within the cell. Then, HIF-α is translocated into the nucleus and undergoes a dimerization with the other subunit β, generally called ARNT (Aryl hydrocarbon Receptor Nuclear Translocator). The gene transcription starts and engages cells to adaptive pathways with biological consequences, like the development of new blood vessels and metastases, thus escaping from death or metabolic changes.[12,14,37]

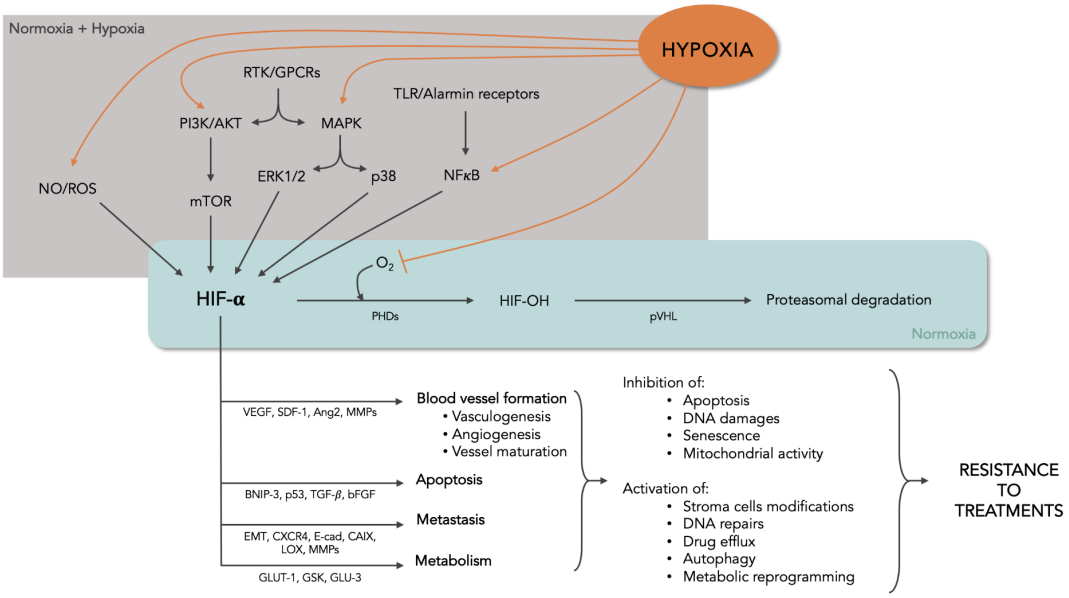

Figure 6: Simplified HIF-α mechanism during normoxia and hypoxia, with implicated signaling molecules.[14,39]

1.2.2.2. Development of a new vasculature

While the tumor grows, its nutrient and oxygen demands get bigger and bigger, to finally surpass the supplies. Therefore, the environment slowly become hypoxic. To cope with this issue and to recover the original nourishing function of the vasculature, one of the tumor cells strategies is to modulate with angiogenic growth factors (VEGF, SDF-1 and Ang2) to activate the creation of new vessels.[40] It combines three mechanisms: vasculogenesis, angiogenesis and vessel maturation. Vasculogenesis is the proper formation of vessel; angiogenesis is the formation of new vessels from the pre-existing vasculature; and maturation consists of the consolidation of the new vasculature. However, hypoxia triggers a disequilibrium in the production of the anti- and the pro-angiogenic factors. Therefore, the blood vessel formation is fast but extremely chaotic, poorly organized and leads to an abnormal, elongated, dilated, immature and leaky vasculature (figure 7).[14,40,41]

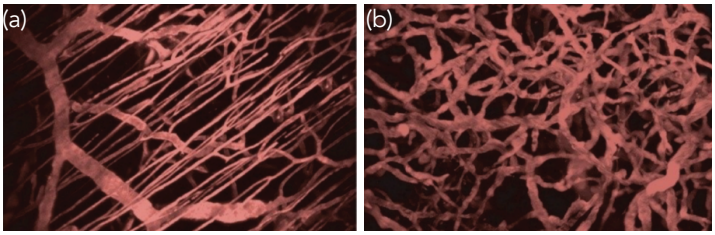

Figure 7: Vasculature in healthy (a) and in cancerous (b) mice.[41]

1.2.2.3. Metastasis and morphological changes

Partly because of these heterogeneous blood vessels, the formation of metastases is greatly facilitated. Figure 8 shows their formation.[42] The first step is the development of mutated cells. The altered cells have selective advantages and promote the tumor growth. A hyperplasia describes the development of abnormal cells, slowly forming a benign mass. Because the tumor develops and its nutrients and oxygen needs increase, new blood vessels grow in the surroundings. Then, the hyperplasia turns into a carcinoma and it becomes invasive with the initiation of cell migration inside the tissue. Cancerous cells easily circulate in the blood and the lymphatic system since the new vasculature is irregular and facilitates the intra- and extra-vasation. Finally, cancer cells are spread somewhere else in the body: metastases grow and succeed to escape their original hostile hypoxic environment.[1, 9, 42]

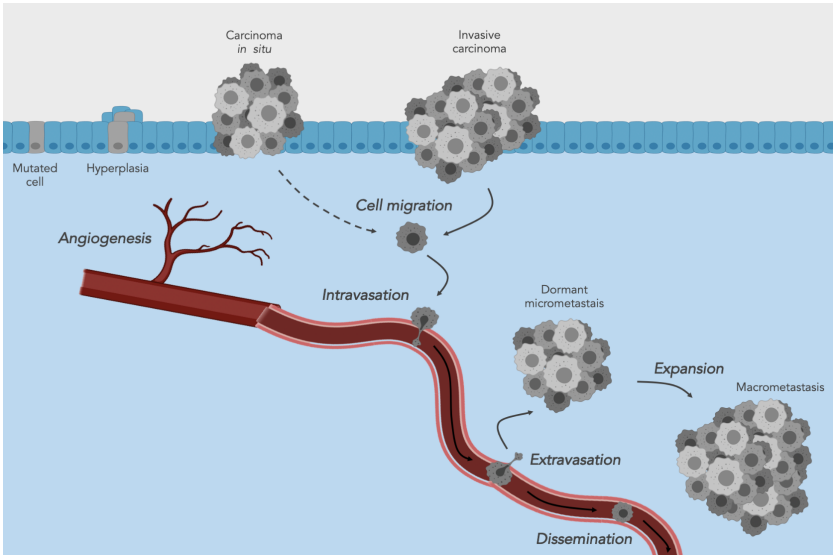

Figure 8: Carcinoma progression, from its formation to the appearance of metastasis.[42]

The development of metastases is also made possible by a morphological change allowed by an epithelial-to-mesenchymal transition (EMT). This biological phenomenon, firstly described by Hay in 1995, allows several biochemical modifications to generate mesenchymal cells from polarized epithelial cells (figure 9).[43,44] Epithelial cells are juxtaposed and tied to each other. The whole form a coherent tissue with a specific function, whereas mesenchymal tissue has a supporting role. During the EMT, cells lose their adhesion to each other in aid of extracellular matrix (ECM) components, such as fibronectin and vitronectin, due to the

downregulation of E-cadherins and integrins.[45,46,47] In that manner, cancer cells have a greater motility and get a certain invasiveness.[14,42,43,46,47]

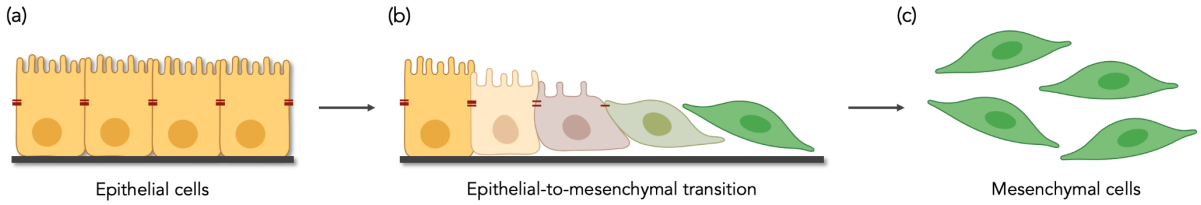

Figure 9: Epithelial and mesenchymal phenotypes before (a), during (b) and after (b) the EMT.[44]

1.2.2.4. A metabolic switch towards an aerobic glycolysis

Metastases are the result of an uncontrollable division and rapid proliferation of tumor cells. Another mechanism controlled by the HIF pathway is their metabolic adaption to follow this cadence.[14] It was observed that glucose consumption is higher in proliferative cells (for instance, stem and tumor cells) than normal differentiated cells.[48] A first hypothesis was made by Warburg in the 1920s: the different nature of the glucose catabolism between cancer and normal cells might be explained by the deregulation of mitochondria (powerhouse of the cell) and let the glucose ferment to obtain a large amount of lactate.[49,50,51] This adaptive behavior is now described as the "Warburg effect" or also called aerobic glycolysis, since this mechanism is working perfectly with or without oxygen.[52] However, Warburg was wrong about the non-functional mitochondria: instead of an irreversible injury in the respiratory mechanism, an adaptative metabolism is set up in order to get a better balance between energy (production of ATP, a biomolecule giving an efficient quantity of energy for all the cellular processes) and small molecules (such as amino acids, lipids or nucleotides) productions.[52] Normally, depending on cellular pO_2, cells have two possibilities for using molecules of glucose: oxidative phosphorylation or anaerobic glycolysis. When oxygen is present in enough quantity, the oxidative phosphorylation is the main pathway. It starts with the progressive and enzymatic degradation of glucose into pyruvate. Then, the pyruvate is carried into mitochondria and the cellular respiration initiates, with the Krebs cycle (also known as TCA cycle), giving ATP and CO_2. In contrast, when there is a low oxygen concentration, cells can overcome this lack by promoting the anaerobic glycolysis and then, produce a large quantity of lactate and in a smaller part, ATP.[52,53,54] The first mechanism provides 36 moles of

ATP per mole of glucose completely oxidized, whereas the second generates only 2 moles.[55] The Warburg effect appears as a compromise between the oxidative phosphorylation and anaerobic glycolysis: the aerobic glycolysis produces 4 moles of ATP for 1 mol of glucose.[56] Cancer cells can cope with this sacrifice because they can easily find energy sources, since they are able to circulate. Therefore, they do not have an urgent need to optimize and increase their ATP yield. They prefer converting a part of the degraded glucose into small biomolecules or NADPH in order to have enough material for building new cells and proliferate.[52,54] Figure 10 summarizes the metabolic pathways in proliferating cells.[52,57] As shown, there is the intervention of oncogenes (PI3K/AKT, tyrosine kinase, MYC) and tumor suppressor genes (LKB1/AMPK, p53) to regulate the mechanistic flow and stimulate, for example, the production of acetyl-CoA, glycolytic intermediates or ribose, respectively essential for the synthesis of fatty acids (lipids), non-essential amino acids or nucleotides. Glucose and glutamine bring a big part of free energy, nitrogen and carbon inside the cell. Then, instead of ATP, glucose and glutamine appear to be fundamental for the cancer cells: their transporters (GLUT for glucose or ASCT2/SN2 for glutamine) are also stimulated to bring enough quantity of cellular fuel or to evacuate the produced lactate and H^+ ions, considered as waste-products, outside the cell (*via* MCT).[52]

The increased production of H^+ by the aerobic glycolysis leads to an acidic tumor microenvironment (TME).[57] In fact, the activity of MCTs is increased and facilitates a H^+ efflux from the cellular cytoplasm to the extracellular environment. This phenomenon contributes to an inversion of pH between inside and outside of cancer cells.[57] In healthy cells, the intracellular pH (pH_i) is around 7.2 and the extracellular pH (pH_e) around 7.4; whereas in cancer cells, pH_i is higher than 7.4 and pH_e between 6.7 and 7.1.[57,58,59] The rise of pH_i encourages cell proliferation, reduces apoptosis, stimulates glycolysis but in the meantime inhibits the gluconeogenesis (that is to say, the synthesis of glucose from the lactate) and boosts the cytoskeletal restructuring. As for the acidification of pH_e, it promotes the degradation of ECM, restricts the role of HCO_3^- ions, acting as a buffer outside of cells, and stimulates the activity of acid-activated protease, for increasing tumor propagation.[57]

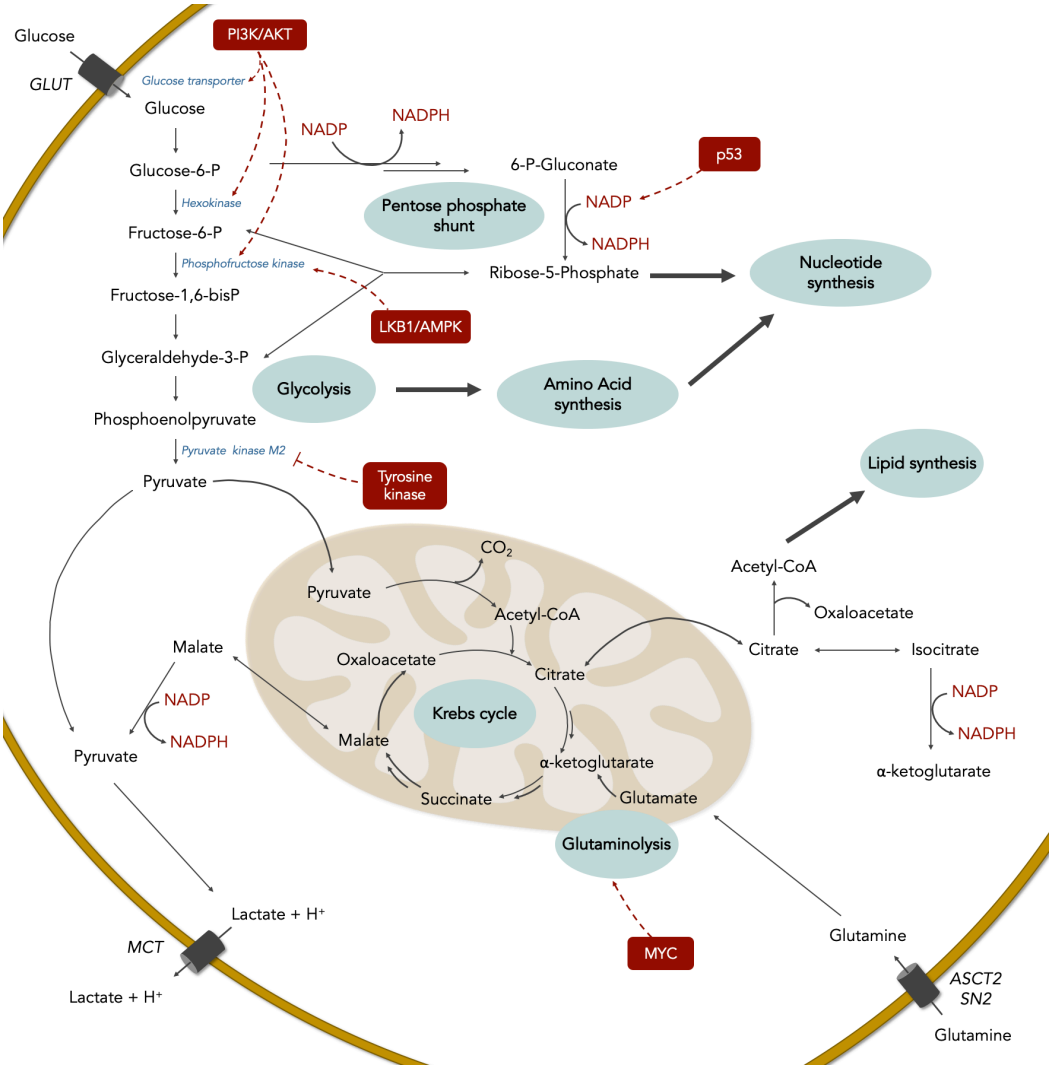

Figure 10: Metabolic pathways in proliferating cells. Box: tumor suppressor or oncogenes; Oval: main metabolic events; Light italic: enzymes for biochemical reaction; Dark italic: transporter names.[52,57]

1.2.2.5. Appearance of resistance towards anti-cancerous drugs

Because of the existence of complex mechanisms and all the consequences resulting from their modification, tumors are difficult to fight because they develop a certain resistance to treatments.[14,29] As already explained above, all these effects are mainly controlled by the activated HIF-1α pathway, consecutively to hypoxia (see figure 6).[14,39] Radio resistance is known for years to be less efficient when the oxygen concentration is low.[17] Usually, when radiations are carried out, there is a direct and an indirect impact on the DNA itself and the production of radicals DNA$^{\bullet}$. When there is enough oxygen, molecules of water are either converted by radiolysis to hydroxyl radicals or react with O_2 and electrons to form $O_2^{\bullet}$. All these radicals provoke DNA damages and conduct to cell death. However, when the

concentration is low (hypoxia), DNA is interacting with reducing species (such as SH-containing species) and becomes DNA-H, that not damage the integrity of the genomic support and lead to cell survival and by extension to radio resistance.[60,61,62] As for drug resistance, it is mainly due to the poor vasculature in cancer cells that induces a slowdown of the proliferation, a bad delivery and a limited diffusion. A pH modification also changes the drug distribution between intra- or extra-cellular compartments: the rise of the drug efflux concentrates the major part of the drug outside of the cell. This phenomenon can be explained by the combination of (1) protonation of drugs (usually weak bases) outside the cell, which prevent their passive permeation through the membrane and (2) basification of the cellular cytoplasm which permits the formation of charged compounds and lets the drug across cellular membranes.[39,57,62,63,64] Table 3 summarizes the different resistance phenotypes noticed on cancer cell lines, using different types of drug.[39]

Cancer cell model	Drug
• *Apoptosis inhibition*	
Breast cancer cells	Paclitaxel (Taxol®), Docetaxel (Taxotere®)
Colon cancer cells	Adriamycin (Doxorubicin®), Etoposide, Oxaliplatin
Fibrosarcoma cells	Cisplatin, Etoposide
Gastric cancer cells	5-Fluorouracil (5-FU®)
Glioblastoma cells	Adriamycin (Doxorubicin®)
Head and neck squamous cell carcinoma	Paclitaxel (Taxol®)
Neuroblastoma cells	Etoposide, Vincristine
Pancreatic cells	5-Fluorouracil (5-FU®), Adriamycin (Doxorubicin®), Gemcitabine
• *Autophagy induction*	
HeLa cells	4-HPR
• *DNA damage inhibition*	
Breast cancer cells	Etoposide
Mouse embryonic fibroblasts	Etoposide, Carboplatin
Prostate cancer cells	Etoposide
• *Drug efflux*	
Breast cancer cells	Methotrexate
Colon cancer cells	Adriamycin (Doxorubicin®)
Glioma cells	Etoposide, Adriamycin (Doxorubicin®)
Oral squamous cell carcinoma	5-Fluorouracil(5-FU®), Cisplatin
• *Senescence inhibition*	
Gastric cancer cells	5-Fluorouracil (5-FU®)

Table 3: List of some cancer cells lines, developing drug resistance (phenotype, in italic).[39]

1.3. Photodynamic therapy: a promising treatment

As described previously, cancer cells have many characteristics which differ from normal cells. Therapies have been drawn on them, trying to find weaknesses in the diabolical mechanism of tumors. Nowadays, the most effective way to fight cancer is the prevention coupled with an early detection, especially for people with inherited cancer susceptibilities, since early-stage cancers are easier to treat. Late-discovered cancers are fought with common treatments when it is possible (depending on the stage, localization, type of tumors and on the general health of patients): surgery, radiotherapy and chemotherapy. Usually, they are combined to lower the recurrence of cancer by maximizing the rate of cell death. However, these treatments are usually followed by unpleasant side effects: hair loss, mouth sores, appetite loss, nausea/vomiting, diarrhea/constipation, increased risk of infection and fatigue. As just explained before, common anti-cancer therapies lead to some resistance and the risk of relapse is high. In order to avoid that, researchers are focusing their attention on more specific therapeutics to target only cancer cells. For instance, there is a development of antiangiogenic drugs, immunotherapy, cancer vaccines or the improvement of a new promising method, photodynamic therapy (PDT).[9,65,66] Next sections will be dedicated to the description of PDT.

1.3.1. The therapeutic power of the combination "light-drug"

Since thousands of years, the great potential of the light is known. Egyptian, Chinese or even Indian civilizations already employed a combination of drugs and light to cure skin diseases, such as vitiligo, psoriasis or rickets.[67,68,69,70] However, the real capacity of the light was not well exploited until the beginning of the 20th century. This century saw the rise of a number of modern discoveries and inventions. It starts with Raab in 1900: he observed lethal effects of acridine orange on infusoria and the correlation between the strength of the response and the red-light dose.[71] The same year, Prime employed eosin dye as an oral drug for epilepsy and noticed the development of dermatitis on his patients, after being exposed to sun light.[72] In 1903, Finsen received the Nobel Prize in Medicine for his work on phototherapy (figure 11, a). He was able to develop a treatment for smallpox and tuberculosis,

using red light and UV light respectively.[73] Few years later, Von Tappeiner (figure 11, b) and his collaborator Jesionek saw improvements in curing skin cancer after using eosin and white light.[74] It leads Von Tappeiner to define in 1907 the photodynamic therapy as a new treatment combining drug and a certain dose of light.[75] In 1913, Meyer-Betz reported for the first time human photosensitization by hematoporphyrin: he exposed his own skin to the light after using hematoporphyrin and noted the swelling of the irradiated area and felt a certain pain.[76]

Figure 11: (a) Niels Ryberg Finsen [1860-1904]; (b) Hermann Von Tappeiner [1847-1927]. [77,78]

The next important step in the field was the detection of the tumor by employing fluorescent methods. In 1955, Rassmussan, Taxal and Figge measured a red fluorescence after the intravenous administration of hematoporphyrin hydrochloride. The fluorescence rate was proportional to the administrated dose of photosensitizer (PS).[79] In the 1960s, Lipson and Baldes observed the accumulation of HpD (hematoporphyrin derivative, isolated by Schwartz few years earlier) in tumors by measuring its fluorescence.[80,81] These discoveries are important for the development of cancer diagnosis. Then, HpDs were extensively studied. In 1972, Diamond noticed the reduction of the growth of a mice glioma after using HpD for several weeks, but only in the superficial area and not in the deeper zone.[82] In 1975, Dougherty and his collaborators published a study where 87% of mice showed a complete response after treating their skin cancer by a combination of red light and HpD.[83] Consecutively, in 1976, Kelly and Snell made the first human study with HpD within the scope of PDT for bladder cancer.[84] Finally, in 1993, Canada was the first country to authorize clinical trials with the first approved PDT drug, photofrin®.[85] Since then, many PS as PDT drugs have been synthesized and studied (more detailed in section 1.3.2.4).

1.3.2. PDT: a three-element mechanism

Photodynamic therapy is an innovative treatment which creates a certain phototoxicity by the combination of three elements: a light-absorbing drug, also called photosensitizer (PS), a light at a specific wavelength and molecular oxygen. PDT appears to be promising because of its high selectivity. In fact, its biggest advantage is to be harmful only when the three elements are gathered in a same physical and temporal space.[86,87]

1.3.2.1. PDT in practice

In clinics, the photosensitizer is generally administrated intravenously, but it can be also given topically. Then, it is taken up by both healthy and cancer cells (systemic distribution of the drug). Normally, the organism is able to evacuate the drug through a good lymphatic circulation. Nevertheless, as largely explained before, tumor vasculature is very bad and there is a poor lymphatic drainage. So, PS is mostly retained by cancer cells. This phenomenon is commonly known as the Enhanced Permeability and Retention (EPR) effect and was first detailed by Maeda in 1986.[88] After a certain time, varying between 5 minutes and 24 hours, the cancerous area is irradiated by a light, with a wavelength specific to the drug (figure 12).[87] Finally, the combination of the light and the PS, in presence of oxygen, triggers oxidative damages and leads to cell death. [86,87]

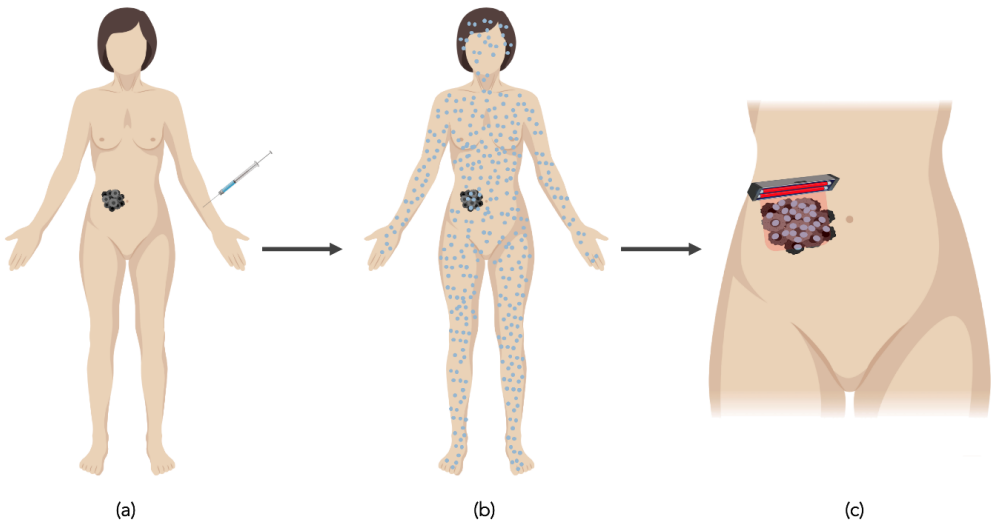

Figure 12: PDT in clinics is composed of three steps: (a) PS administration, usually intravenously; (b) distribution of the drug in all the body; (c) concentration of PS in the cancerous area and after, irradiation of the zone. PS is represented as dots.[87]

1.3.2.2. Energetic transfers involved in PDT

The mechanism of PDT corresponds to an energy transfer between the three main elements with several stages.[69,87] The first step consists of the irradiation of the PS, initially at its singlet ground state S_0 (so PS is named as $^1PS_0$): the energy is absorbed and the photosensitizer reaches an excited singlet state S_1 ($^1PS_1$). This state is very unstable and it has a short lifetime. $^1PS_1$ quickly reacts (within 10^{-9}-10^{-8} s), either by returning to its ground state (by emitting fluorescence, heat or by being subjected to a non-radiative transition) or sometimes by undergoing an intersystem crossing (ISC). Due to the ISC, the PS is able to get to a triplet excited state T_1 ($^3PS_1$) by reversing one electron spin. The triplet state T_1 is lower in energy than the singlet state S_1 and results of a spin forbidden transition: its probability to occur is very small and when it is made possible, T_1 has a longer lifetime (roughly from 10^{-4} to 10^{-2} s). Therefore, $^3PS_1$ has more time to interact with the molecules in its surroundings. Three outcomes can happen to the drug: (1) it can come back directly to its ground state S_0 by emitting phosphorescence; (2) it can interact with biological substrates such as vitamins, flavin compounds, amino acids, unsaturated lipids or nitrogenous bases (type I) or (3) it can transfer its non-radiative energy to molecular oxygen, also named $^3O_2$, to permit its own conversion in singlet oxygen $^1O_2$ (type II).[89] Types I and II are two kinds of photochemical reaction that trigger the formation of ROS, which creates an oxidative stress and leads to a fatal outcome for the cell (figure 13). [90,91] Both reactions will be better explained in the next section.

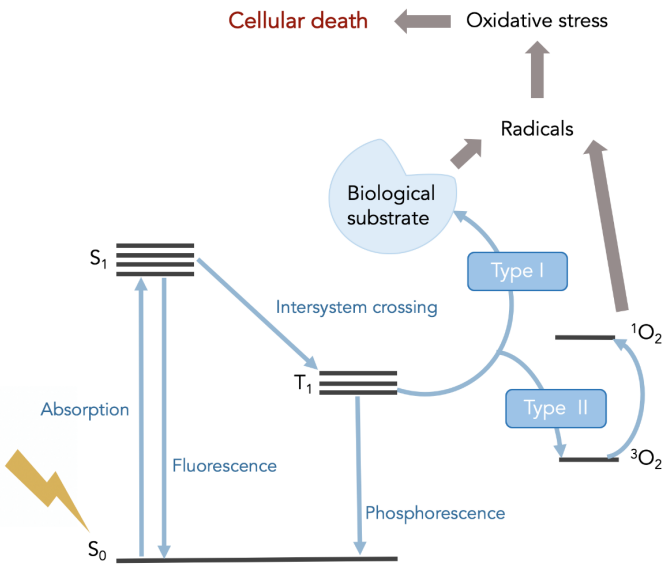

Figure 13: Modified Jablonski diagram: energy transfers between light, PS and O_2 during PDT.

1.3.2.3. Mechanisms leading to an oxidative stress

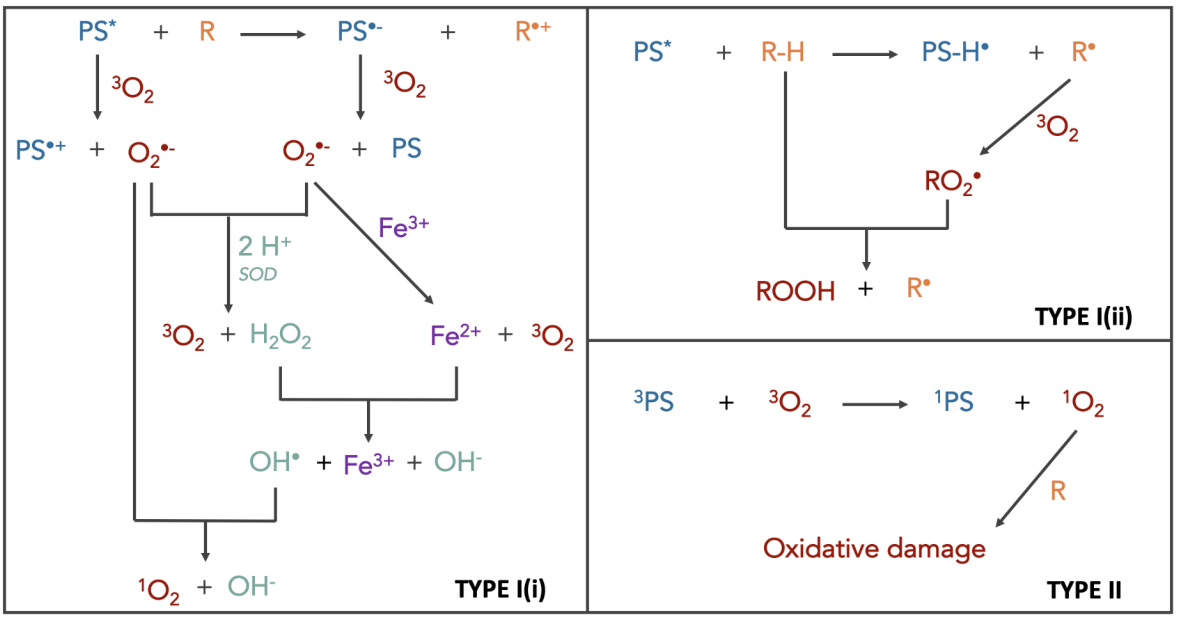

Figure 14: The three different routes during PDT reaction.[92]

Figure 14 shows the three different mechanisms of reaction when the photosensitizer is at its T_1 state.[92,93] Type I is subdivided into two reactions. On the one hand, the type I(i) corresponds to an electron transfer and it starts with the excited photosensitizer (in figure 14, named as PS^*). It reacts either with a biological substrate R (predominant path) or with $^3O_2$ (low probability to occur). In both routes, the PS^* becomes a radical, an anion $PS^{\bullet-}$ or a cation $PS^{\bullet+}$, and generates a superoxide radical anion $O2^{\bullet-}$. The superoxide will instantly react with Fe^{3+} or with two protons H^+. On one part, thanks to a superoxide dismutase (SOD), $O2^{\bullet-}$ can be disproportionated into $^3O_2$ and H_2O_2. On the other part, the Haber-Weiss reaction begins: Fe^{3+} is reduced into Fe^{2+}, which can catalyze the formation of the hydroxyl radical $OH^\bullet$ from H_2O_2. The $OH^\bullet$ is one of the most damaging radicals for cells because it can easily cross membranes and cannot be excreted from intracellular compartments. Moreover, $OH^\bullet$ has a high redox potential (E_0 = +2,3 V) that allows it to oxidize nearby molecules.[94] On the other hand, type I(ii) corresponds to a transfer of protonss. The excited PS^* reacts with a biological substrate bearing a labile proton (R-H) and produces the substrate radical $R^\bullet$, that can interact with $^3O_2$ and form other kinds of radicals. Finally, for both subtypes I(i) and I(ii), chain reactions with cytotoxic free radicals are triggered and led to oxidative damages and cell death. Alternatively, type II involves a spin-allowed transition between $^3PS^*$ and $^3O_2$. When they

interact, there is a triplet-triplet annihilation: in other words, triplet state compounds become singlet state compounds. During that process, ^{1}PS and two forms of singlet oxygen $^1O_2$ ($1\Delta g$ and $1\Sigma g$) are produced. Singlet oxygen is extremely reactive and particularly oxidizes unsaturated lipids of cellular membranes. These lipids undergo a peroxidation which provokes structure damages.[95] Like type I, the production of singlet oxygen results in the cells death. Both type I and II play a role in the death mechanisms but, it is established that type II is the main pathway during PDT in human cells. It can be explained by the very fast reaction of $^1O_2$ with its surroundings, since its lifetime is very short (< 0.04 to 3 µs in biological media) limiting then its own diffusion to the cell, where the PS is standing (about 10 nm).[93] Therefore, all PDT damages strongly depend on the PS localization.[91,92,93]

1.3.2.4. PDT elements: a deeper description

1.3.2.4.1. Oxygen

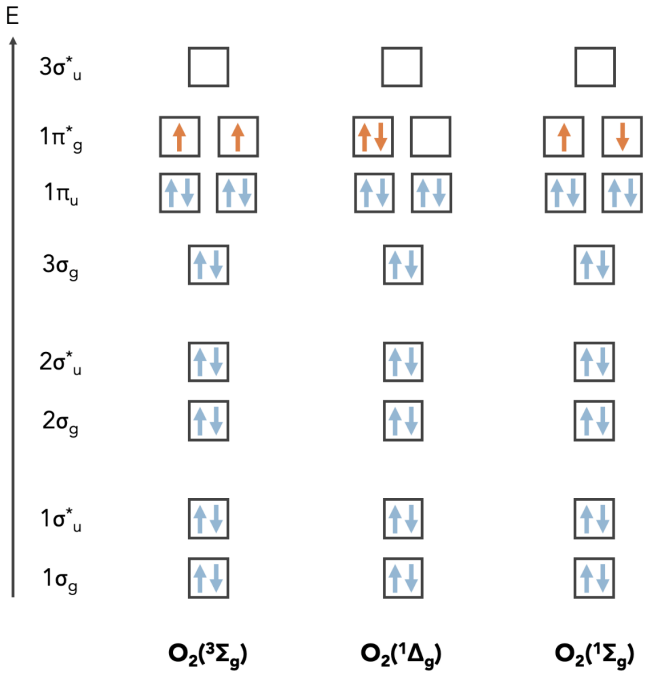

Figure 15: Electronic configurations of molecular oxygen and its first excited states.

Molecular oxygen ($^3O_2$) is a diatomic mononuclear molecule. It can be also named as $O_2(^3\Sigma_g)$. Following Pauli's and Hund's rules, its electronic configuration is $(1\sigma_g)^2\,(1\sigma^*_u)^2\,(2\sigma_g)^2\,(2\sigma^*_u)^2\,(3\sigma_g)^2\,(1\pi_{u,x})^2\,(1\pi_{u,y})^2\,(1\pi^*_{g,x})^1\,(1\pi^*_{g,y})^1$: there are two unpaired electrons with the same value of spin in the external orbital.[96] Then, the multiplicity of its ground state is triplet, unlike the

majority of molecules (figure 15). The two lowest states of $^1O_2$ correspond to either a spin pairing or a spin inversion, both in the $3\pi_u$ orbital, respectively for $O_2(^1\Delta_g)$ and $O_2(^1\Sigma_g)$. Figure 15 explicitly represents their electronic configuration. In terms of energy levels, 94.3 kJ.mol^{-1} are required to reach the first excited state ($^1\Delta_g$) from the ground state; and add 63 kJ.mol^{-1} on top of that to get the second first excited state ($^1\Sigma_g$). Then, two implications can be highlighted: $O_2(^1\Delta_g)$ can be detected at 1270 nm and $O_2(^1\Sigma_g)$ is too high in energy to be stable, so $O_2(^1\Delta_g)$ is the usual state involved in PDT reactions.[93,96,97]

1.3.2.4.2. Photosensitizer

The drug employed during PDT is a light-absorbing compound, mostly based on a tetrapyrrolic structure. It can be hematoporphyrin (Photofrin®), chlorin (Foscan®, Litx®), phtalocyanin (Photosens®) or benzoporphyrin (Visudyne®) derivatives.[98] To be efficient, the PS should have ideal properties. First of all, it must show a very low toxicity when it is injected and without light irradiation, which also implies a high stability during storage and when the PS is traveling inside the body. Its administration should be easy, painless and realized in multiple ways. PS should absorb a light in the therapeutic window (see next section), with a high extinction coefficient (around 5.10^4 to 1.10^5 M^{-1}.cm^{-1}) in order to receive enough light and have enough energy to produce singlet oxygen upon irradiation. So, PS should have a high singlet oxygen quantum yield. Moreover, PS should present a high tumor selectivity and a good clearance (natural removal of the drug), in order to reduce the possibility of skin photosensitivity. Photosensitizers are categorized in three generations.[99] The first generation gathers all the hematoporphyrin and its derivatives (HpD). Nowadays, the most widely used PS in clinics is the porfimer sodium, commercially known as photofrin®. Even its large utilization, photofrin® still has a lot of defects: its poor tumor selectivity, its low absorption wavelength (630 nm; ε=3000 M^{-1}.cm^{-1}) and to be efficient, its high required dose. Then, other PS were synthetized to overcome these issues and tune their properties (2nd and 3rd generations).[100,101] Despite a large number of PS under clinical trials, a relatively small number of drugs have received authorizations from national organizations (table 4).[102] Since there is still no PS bringing all the requirements to become an ideal drug, a lot of research is focusing on developing new molecules for PDT applications.[103,104,105,10]

Photosensitizer Trade name of drugs	Chemical structure of PS	Approval Country (Date of the first trial)	Potential recommendations
8-Methoxypsoralen (8-MOP) Methoxsalen®	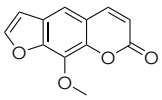	USA (1999)	Cutaneous T-cell lymphoma
9-acetoxy-2,7,12,17-tetrakis-(β-methoxyethyl) ATMPn®	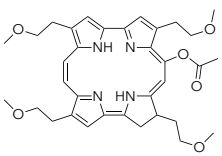	Germany (1997)	Psoriasis non-melanoma skin cancer Head and neck cancer
Aluminium phthalocyanine tetrasulfonate (AlPcS4) Photosens®	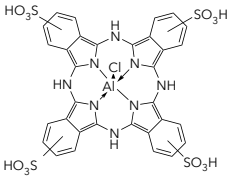	Russia (2001)	Stomach cancer Skin cancer Lip cancer Oral cavity cancer Breast cancer Age-related macular degeneration
Aminolevulinic acid (5-ALA) Alacare®, Ameluz®, Levulan®	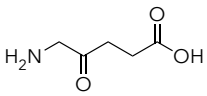	Levulan®: USA (1994), EU (2001), Sweden (2001) ; Alacare®: UK (2009), Austria (2009), Germany (2009); Ameluz®: EU (2011)	Actinic keratosis Basal cell carcinoma Esophageal dysplasia
Benzoporphyrin derivative monoacid ring A Visudyne®	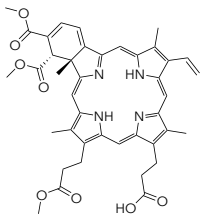	USA (1999)	Age-related macular degeneration
Chlorin e6 (Ce6-PVP) Photolon®, Phoditazin®, Radachlorin®	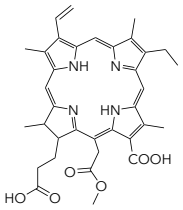	Republic of Belarus (2001), Russia (2004)	Basal cell carcinoma Squamous cell carcinoma Esophageal cancer Breast cancer Oral cancer Skin cancer
Hexaminolevulinate (HAL) Hexvix®, Cysview®	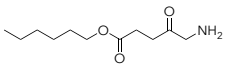	EU (2006), USA (2010)	Bladder cancer diagnosis Colon cancer diagnosis Cervical intraepithelial neoplasia
Methyl ester-aminolevulinate (MAL) Metvixia®, Metvix®	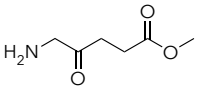	EU (2001), Sweden (2001), Australia (2003), New Zealand (2004), USA (2004), Canada (2009)	Actinic keratosis Basal cell carcinoma Bowen's disease

N-Aspartyl chlorin e6 (NPe6) or taloporphin Laserphyrin®, Litx®	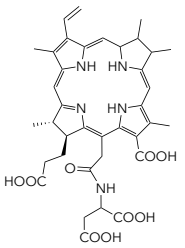	Japan (2003)	Lung cancer Glioma
Porfimer sodium Photofrin®, Photosan®, Photogem®, Photohem®	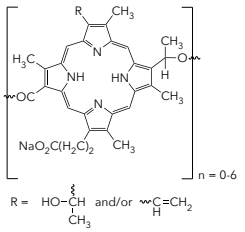	Canada (1993), USA (1995), Germany (1997), UK (1999), EU (2000)	Bladder cancer Obstructive esophageal cancer Lung cancer Actinic Keratosis Barrett's esophagus Gastric cancer Basal cell carcinoma Squamous cell carcinoma
Tetra (m-hydroxy phenyl) or mTHPC Foscan®	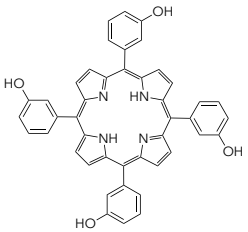	EU (2001)	Advanced head and neck cancer Squamous cell carcinoma Prostate cancer Pancreatic cancer

Table 4: Approved photosensitizers for anti-cancer treatment and diagnosis (EU = European Union; UK = United Kingdom; USA = United States of America),

1.3.2.4.1. Light

The choice of PDT light is mainly based on the employed PS; but it also depends on the tumor type, its physical availability and the cost of the PDT setting up.[107] Moreover, not all wavelength can penetrate the human skin. In fact, crossing a heterogenous milieu, the light beam can be either reflected, refracted, scattered or absorbed. The light wavelength plays an important part in the efficiency of PDT for deeper tumors: lower values affect only peripheral tumors (figure 16).[108] The interval between 600 and 1200 nm is known to be the optimal therapeutic window. However, the optimal therapeutic window for PDT ranges from 680 to 800 nm because of (1) a smaller number of interactions with natural pigments in the body (for example, hemoglobin or melanin) and (2) the light energy is adequate to obtain a high singlet oxygen quantum yield. In practice, diode lasers are widely used because they are very practical, have a reasonable cost and an easy set up. Nowadays, Light-Emitting Diodes (LEDs) are the preferential light source for treatments since they can furnish narrow spectral bandwidths and permit a better targeting of the PS.[107,109]

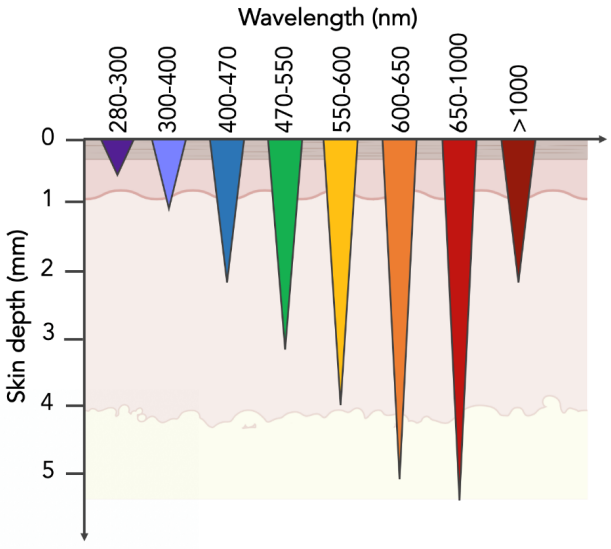

Figure 16: The light penetration in human skin depends on its wavelength.[108]

1.3.3. Impacts of PDT treatment

1.3.3.1. Importance of PS location after its administration

PDT affects cancer cells at different levels (cellular and tumoral). However, its impacts are very complex and results from many factors. One of the most important factor is the location of the photosensitizer, rather than ROS production.[107] In fact, two dyes employed as PS, crystal violet and methylene blue, were compared. Despite the fact that crystal violet produces less ROS than methylene blue, they have a similar impact on cells after PDT. This is due to the location of the PS: for crystal violet, PS is in the mitochondria, whereas it is in the cytosol and in the lysosomes for methylene blue.[110] Generally, PS is efficient when it is concentrated in organelles such as Golgi apparatus, lysosomes, endoplasmic reticulum, mitochondria and plasma membrane.[111]

1.3.3.2. Cellular damages

At the cellular level, photodamages from PDT lead to cell death *via* three main death morphotypes: necrosis, apoptosis and autophagy (figure 17).[112,113,114,115] One mechanism is preferred over the others depending on the PDT dose (light and drug quantities) received by cells and the location of the PS.[107] Firstly, apoptosis is the common mechanism for cells to die. Usually, it arises when light and drug are in small quantities. In that case, PS is commonly

located in mitochondria. After irrradiation, photodamages causes the permeabilization of the mitochondrial membrane: the cytochrome c, a key element intiator of the pro-apoptotic cascade, is released into the cytosol and the cell enter in apoptosis.[116] Secondly, necrosis takes over apoptosis when PDT doses are higher. In that case, PS is found in plasma membranes and frequently leads to an inflammatory response after intracellular material leakage and the destruction of membranes.[107,115] Lastly, autophagy can also replace apoptosis when it is impaired. In normal cell, autophagy is a cytoprotective mechanism that recycle all the damaged material. Neverthless during PDT, autophagy leads as well to cell death when doses are considerably high.[107,115]

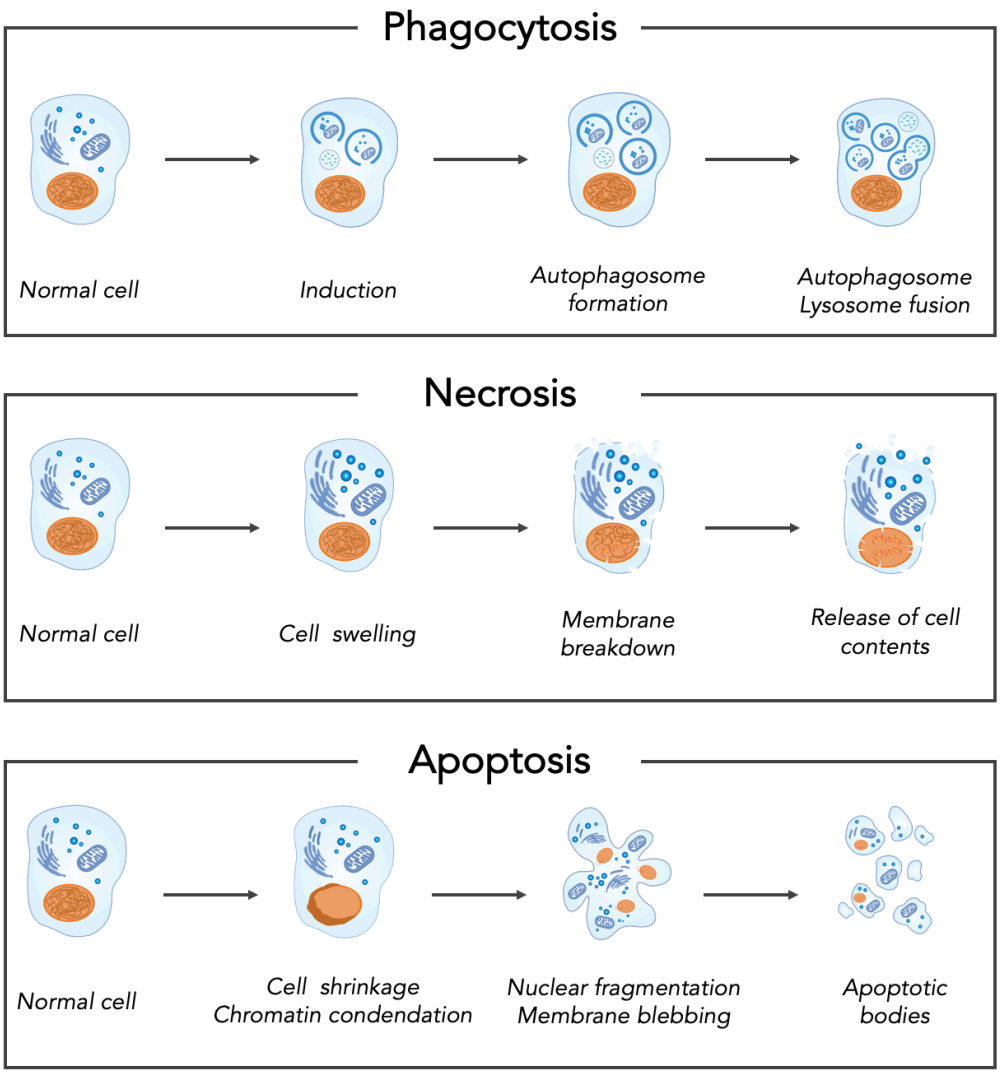

Figure 17: Cell death morphologies and their characteristics.[112]

1.3.3.3. Consequences of PDT on tumors

At the tumor level, all the former types of destruction cause fatal damages that bring destruction to the tumor. Three frequent phenomena occur when PDT is carried out: the direct death by generation of ROS, the shortage of the vascularization and the activation of the immune system. [87,107] First, the production of free radicals, especially ROS, disrupts the fine tuned redox balance of cells and thus, provokes an oxidative stress. ROS directly attack a specific tissue, called stroma. Stroma is a supportive and vascularized tissue that brings all the nutrients needed by cells and throws out all their waste. So, reaching the nutritive zone of tumor cells, PDT leads to their death by apoptosis or necrosis.[117,118] Another event that disturbed the nourishement of cancerous cells is the destruction of their circulation. Many anti-cancerous strategies are based on the production of anti-angiogenic drugs. In the case of PDT, photodamages have an impact on tumor vessels. This impact is proportional to the drug light interval (DLI): the more reduced DLI is, the more vascularization is destroyed. During this proccess, endothelial cells are mainly ruined and they release some signals that activate platelets and lead to the formation of thrombus and vasoconstriction. Blood flow is then reduced, tumors cells are deprived of their nutritive elements, and the cell destruction occurs.[107, 115, 119,120] Another consequence of PDT on cancer cells is the activation of the immune system. In the first place, an inflammatory response is triggered due to the release of several molecules, such as Heat Shock Proteins (HSPs) or damage-associated molecular paterns (DAMPS). There is also the activation of NFκB, the key factor in inducing inflammatory responses. Furthermore, the number of nucleophiles in the circulation increases. These white blood cells play a major part in phagocytosis, that allows the removal of damaged cells, and intensify the activity of T cells, also important in the immunity response. Finally, a memory immunity sets in: an adaptative immune reaction takes place and primes the organism to a relapse or an attack by similar tumor cells.[107,121,122,123]

1.3.4. PDT for treating: advantages and limitations

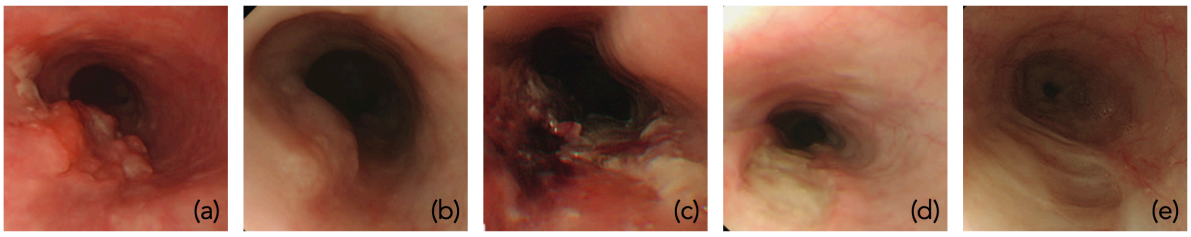

Figure 18: Use of PDT in complement of chemoradiotherapy (CRT) for treating esophageal squamous cell carcinoma. (a) before the beginning of any treatment; (b) local residue after the first treatment (CRT); (c) ischemic change after two days of PDT; (d) remained ulceration after one month of PDT; (e) complete response after 3 years of PDT.[125]

Nowadays, PDT is a technique for a wide spectrum of applications: diagnostic tool, palliative, curative or preventive cares. It can take place before or after classical treatments (surgery, radio- and chemotherapies) and be repeated, without overlapping the toxicities. As already explained, PDT drugs show no toxicity until they are irradiated and lead to different biological mechanisms for damaging or killing cancer cells. Even though it is not yet largely used as anti-cancer treatment, PDT represents also a cheaper technique, since it is an ambulatory method. The one-day treatment can also appear more pleasant for patients.[107,124] Some examples of clinical application are summarized in table 4. Figure 18 shows the evolution of an esophageal squamous cell carcinoma during a multimodal treatment.[125] On the first picture (figure 18, a), the tumor, without treatment, is clearly present. Chemoradiotherapy (CRT) is carried out but is inefficient (figure 18, b). To complete the treatment, PDT is employed and causes damages on the tumoral zone (figure 18, c and d). Three years after, there is no trace of tumor: it is a success for the PDT treatment (figure 18, e). However, there are many reasons why PDT is not yet a common therapy for cancers. The main ones are: (1) an insufficient light penetration in the body to reach deep tumors, (2) no general-purpose light devices, (3) skin photosensitivity and (4) a considerable lack of oxygen in solid tumors.[68,87,126]

Then, there is a real need to optimize the photodynamic therapy by synthesizing more efficient PSs, by building devices providing a light at an optimal wavelength or by founding a strategy to overcome hypoxia and providing a favorable oxygen level for the success of PDT.

1.4. Thesis project

To tackle the hypoxic issues in solid cancers during PDT, oxygen concentrations should be increased. The general strategy is to carry molecular oxygen in the treated area in order to maximize the PDT effect with a higher singlet oxygen production. Supramolecular chemistry can be a solution and more specifically assemblies with arene ruthenium units. In fact, our team has demonstrated the great potential of these complexes for a PDT purpose.[127,128,129] A recent work was about the synthesis of an octonuclear metalla-cube $[Ru_8(\eta^6\text{-p-cymene})_8(tpvb)_2(donq)_4]^{8+}$ (with tpvb: 1,2,3,4-tetrakis{2-(4-pyridyl)vinyl}benzene; and donq: 5,8-dioxido-1,4-naphtoquinonato) and the study of its ability to entrap and transport a photosensitizer to cancer cells. The study showed first, the non-toxic effect of PS when it is inside the hydrophobic cavity, being shielded by the assembly; and second, the release of the photosensitizer within the cell allows its toxicity to be revealed, upon irradiation with an adapted light wavelength.[130] Some other supramolecular assemblies with ruthenium or other d-metals were also studied and described in the literature for PDT purposes (e.g. singlet oxygen production or photosensitizer improvements).[131]

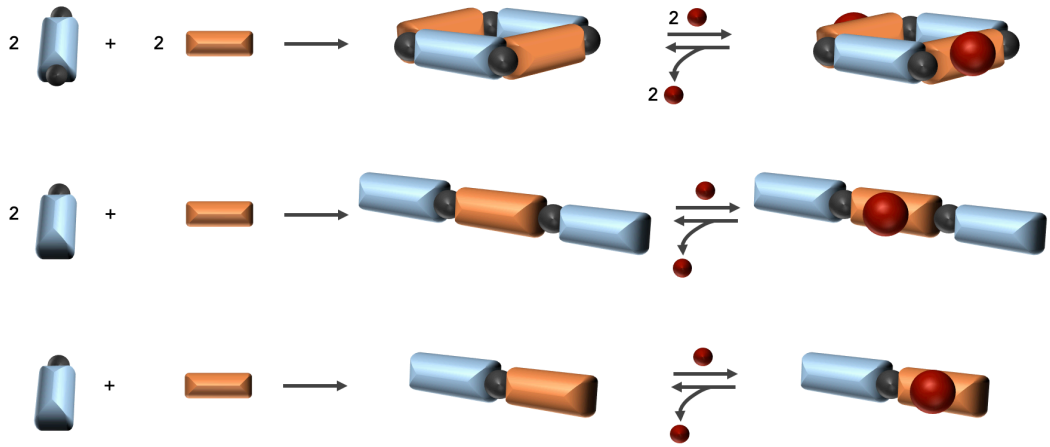

Figure 19: Schematic representation of the followed synthetic strategies in the perspective of oxygen carriers: formation of metalla-rectangles (first line), di- (second line) or mono- (third line) nuclear assemblies. Dark ball: arene ruthenium; Light rectangle: organic linker of ruthenium clip; Dark rectangle: oxygen carrier (ligand); Big dark ball: molecular oxygen.

Therefore, a new strategy consists of using arene ruthenium metalla-assemblies to transport molecules of oxygen into the cancer area (figure 19). Metalla-assemblies could be either rectangles, dinuclear or mononuclear species. They can be tuned and functionalized to

optimize their properties, such as their solubility, their stability or their ability to encapsulate a photosensitizer.

For that purpose, oxygen carriers can be added anywhere on the assembly: on the linker or attached on the ruthenium clip. The literature gives several examples of oxygen carriers but the most intensively studied is undoubtedly the acene class.[132,133] One of the characteristics of many polycyclic aromatic hydrocarbons is to trap singlet oxygen, in a reversible manner. The first observations were made by Dufraisse and Moureu in 1926: rubrene, initially red, slowly becomes colorless in contact with air at room temperature and becomes again red under heating at 120 °C (scheme 1).[134] Later, Dufraisse described this phenomenon as "the labile bonding of oxygen to carbon".[135]

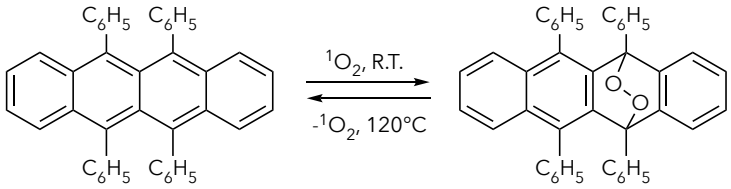

Scheme 1: Singlet oxygen reacts with rubrene, the first observation made by Dufraisse.[141]

During the 1960s, Foote and Wasserman proved the involvement of singlet oxygen in the formation of endoperoxides (EPOs) from polycyclic aromatic compounds.[136,137] The mechanism of this reaction, a [2+4] cycloaddition, is similar to a normal Diels-Alder reaction, where singlet oxygen is considered the dienophile and the aromatic molecules, the dienes (scheme 2).[138,139, 140]

Aubry and coworkers studied extensively the formation of naphthalene and anthracene EPOs and their ability to reversibly bind $^1O_2$.[141] They resume the principal effects of modifications on or around the molecule: (1) the addition of electron donating groups on the binding site of $^1O_2$ has an activating effect on its cycloaddition; (2) the reactivity increases when the number of fused rings is higher; (3) the cycloaddition kinetics depend on the polarity of the solvent (e. g. water or *N*-methylformamide slow down the reactivity of $^1O_2$).[140] Then, both electronic and steric factors are important to consider when dealing of cycloaddition of singlet oxygen.

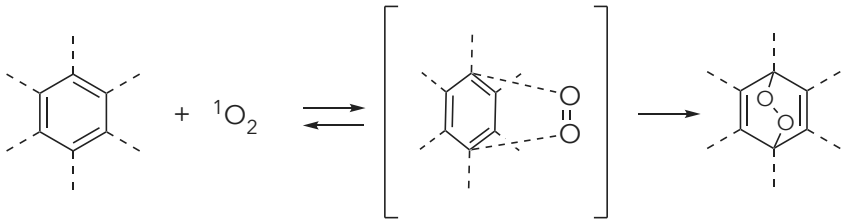

Scheme 2: General mechanism of the [2+4] cycloaddition between polycyclic aromatic hydrocarbons and singlet oxygen.[141]

This subject holds also Fudickar's and Linker's attention.[142] They studied the formation of EPOs from attractive pyridylanthracenes (scheme 3).[143] They demonstrated that the cycloaddition kinetics is controlled by the position of the nitrogen on the pyridine group and also by the employed solvent. In fact, in polar solvents, the reaction is faster with the pyridine containing nitrogen on meta position than on ortho or on para positions; and in non-polar solvents, it is the ortho position that permits a faster formation of EPOs than the nitrogen on meta and on para positions.[143]

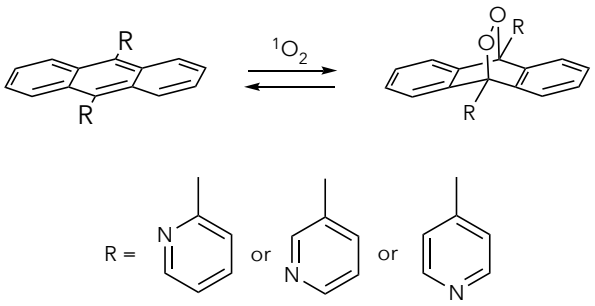

Scheme 3: Formation of EPOs from different isomers of 9,10-dipyridylanthracene.[143]

In addition, the anthracene pattern was already tested as a PDT agent on cancer cells (HeLa, breast, lung, prostate or ovarian cancer cell lines). In these examples, anthracene was attached to BODIPY or coordinated to d-block metals (cobalt, rhodium or iridium). They showed excellent results on tested cell lines and they demonstrate a great potential as new generation of PDT drugs.[144]

However, for all the species described in these examples, the need of an external photosensitizer (usually porphyrin derivatives or methylene blue) is required and its activation is only possible by irradiation. To extend the possibilities of singlet oxygen formation, another interesting pattern was developed by the team of Royal.[145,146] They studied the pyridinium-substituted couple dimethyldihydropyrene-cyclophanediene (DHP-CPD) and they found that

it can reversibly link oxygen (scheme 4). DHP is a molecular switch and it is described as a negative T-photochrom.[147,148] The rigid and planar 14 π-electrons structure (DHP) can undergo an opening of its central C-C bond under light irradiation and give a less aromatic system (CPD), with two virtually isolated 6 π-electrons benzoic core. This process is a *sine qua non* condition for the structure to capture $^1O_2$. The attractiveness of this molecule is also its useful property to be activated by a low-energy light. The team of Royal, Mitchell and Muratsugu gave some examples of DHP structures that can be coordinated with ruthenium atoms.[149] Then, with the perspective of using them as a PDT agent, DHP derivatives seem to be an appealing pattern, despite its long and laborious synthetic route (see section 2.3.1.).

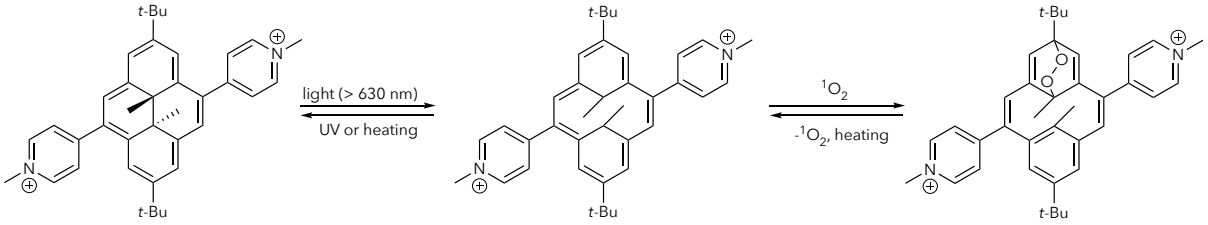

Scheme 4: Singlet oxygen reacts with CPD, the open form of DHP, to give CPD-EPO.[145]

So, this research manuscript is describes the synthesis and the characterization of derivatives containing these two last building blocks (anthracene and dimethyldihydropyrene), to be used as oxygen carriers, and grafted on ruthenium(II) assemblies (chapter 2). Some studies in solution and on cancer cells were carried out to determine their effectiveness as possible new PDT drugs (chapter 3).

2. Synthesis and characterization of new ruthenium(II) assemblies with $^1O_2$ carriers

This chapter is dedicated to the realization of all the molecules that will be studied and discussed in the next chapter, as potential new biological singlet oxygen carriers and with the perspective of a PDT application. All the reaction and characterization details are described in the experimental part of the manuscript.

2.1. Synthesis of ruthenium(II) precursors

All the dinuclear clips are prepared according to standard procedures, initially from ruthenium(III) chloride hydrate.[150,151,152,153,154] Three types of OO∩OO ligands between two ruthenium atoms were chosen in order to have rectangles of different size: $[Ru_2(\eta^6\text{-}p\text{-cymene})_2(\mu^4\text{-oxa})Cl_2]$, $[Ru_2(\eta^6\text{-}p\text{-cymene})_2(\mu^4\text{-dobq})Cl_2]$, $[Ru_2(\eta^6\text{-}p\text{-cymene})_2(\mu^4\text{-donq})Cl_2]$ (figure 20). However, it is not the size itself that is important, but the distance between two anthracene units. In fact, as already mentioned before, the formation of endoperoxides is dependent on the electronic environment. Then, changing the degree of with the π-π stacking interactions between the two anthracene units can have an impact on the [2+4] cycloaddition. The synthesis of different kinds of ruthenium(II) rectangles will permit to discuss that point.

The complex $[Ru(\eta^6\text{-}p\text{-cymene})(pta)Cl_2]$ was also synthetized (figure 20) in order to increase the solubility of the corresponding ruthenium assemblies containing at least one anthracene derivative (A_{anthr}). In fact, the presence of pta can give versatile soluble properties to the new molecules: their solubilization in water and polar organic solvents should be higher, which is convenient for a future biological application.[153]

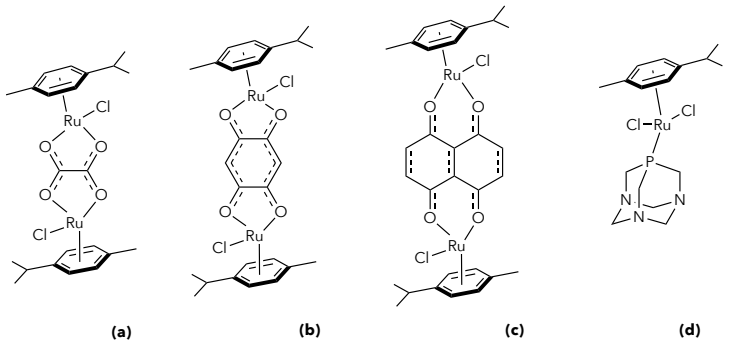

Figure 20: Ruthenium(II) precursors: (a) = $[Ru_2(\eta^6\text{-}p\text{-cymene})_2(\mu^4\text{-oxa})Cl_2]$, (b) = $[Ru_2(\eta^6\text{-}p\text{-cymene})_2(\mu^4\text{-dobq})Cl_2]$, (c) = $[Ru_2(\eta^6\text{-}p\text{-cymene})_2(\mu^4\text{-donq})Cl_2]$ and (d) = $[Ru(\eta^6\text{-}p\text{-cymene})(pta)Cl_2]$.

2.2. Synthesis and characterization of ligands with an anthracenyl core (L_{anthr})

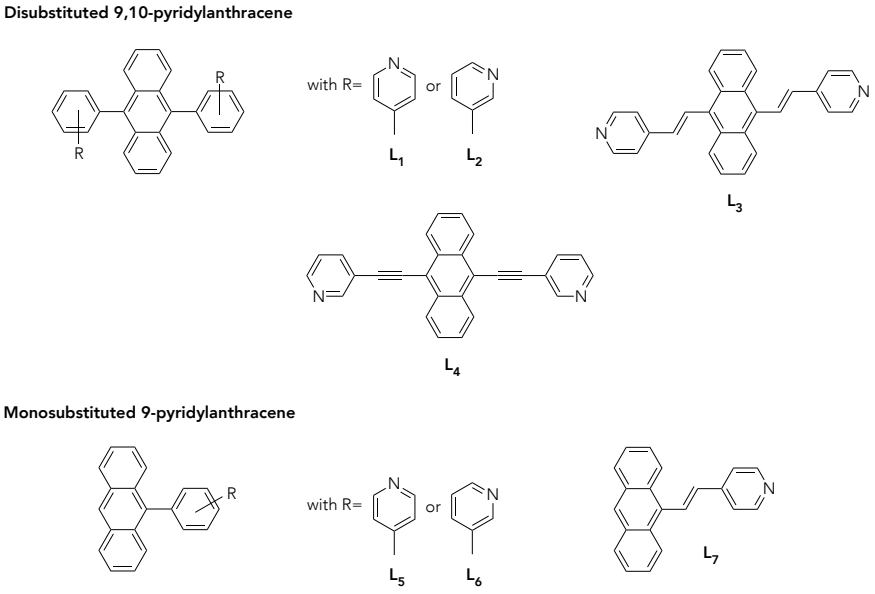

Figure 21: Structures of the different L_{anthr}.

Pyridylanthracene derivatives, described by Fudickar and Linker, were chosen for two main reasons: (1) for their coordination site with ruthenium atoms, *via* the nitrogen of the pyridyl group; and (2) for the fact that pyridine is inert towards singlet oxygen and that cannot be an impediment to the ability of anthracene to catch $^1O_2$.[152] Both mono- and di-substitutions were considered with different pyridyl isomers (meta and para). L_{anthr} were synthetized *via* different palladium-catalyzed cross-coupling reactions, starting from a bromo- or a dibromo-anthracene. All reactions were realized under an inert atmosphere in order to avoid the oxidation of the catalyst, especially when palladium(0) tetrakis(triphenylphosphine) was used,

which would have reduced the reaction yield. First, Suzuki reactions were realized to obtain **L_1**, **L_2**, **L_5** and **L_6**[143,156, 157]; then, Heck reactions for **L_3** and **L_7**[158]; and finally, a Sonogashira reaction for **L_4**[159]. As shown in figure 21, the structures of **L_1-L_7** differ from each other by a different electronic repartition around the $^1O_2$ capture unit, thanks to simple, double or triple bond(s) between the anthracene and the pyridyl units. All syntheses were previously published and were realized with minor modifications to their initial protocol (cf experimental part). They are all obtained as a powder, with different tints of yellow or white, in yields ranging from 27 to 73%, depending on the ligands.

All ligands were characterized by ^{1}H NMR, ^{13}C NMR and mass spectrometry. Since only **L_6** was never described in the literature, it was more thoroughly characterized, including 2D NMR (COSY, HSQC and HBMC) experiments (figure 22), UV-VIS measurements and elemental analysis. In ^{1}H NMR spectra (figure 23), signals for the different patterns are easy to recognize because they possess the typical shifts for pyridylanthracene derivatives. For example, the signal for the proton just next to the nitrogen atom on the pyridyl group is always deshielded in comparison to the others (superior at 8.7 ppm); the two doublets corresponding to the vinyl protons of **L_3** and **L_7** are in the similar area of the spectrum and their coupling constant $^3J_{HH}$ is 16.4 Hz; signals for the anthracene unit are almost the same for the two isomers (4- and 3-pyridyl, **L_5** and **L_6** respectively).

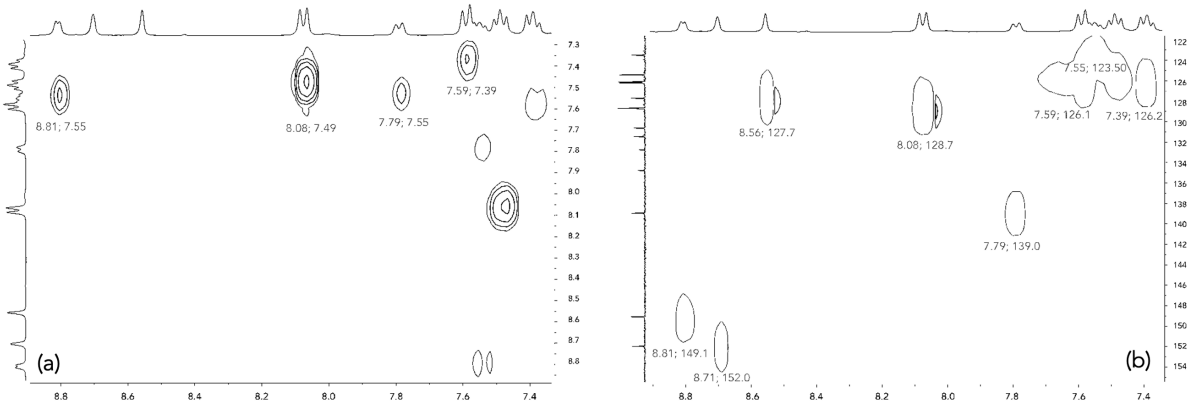

Figure 22: COSY (a) and HSQC (b) NMR spectra for **L_6** ($CDCl_3$, 23 °C).

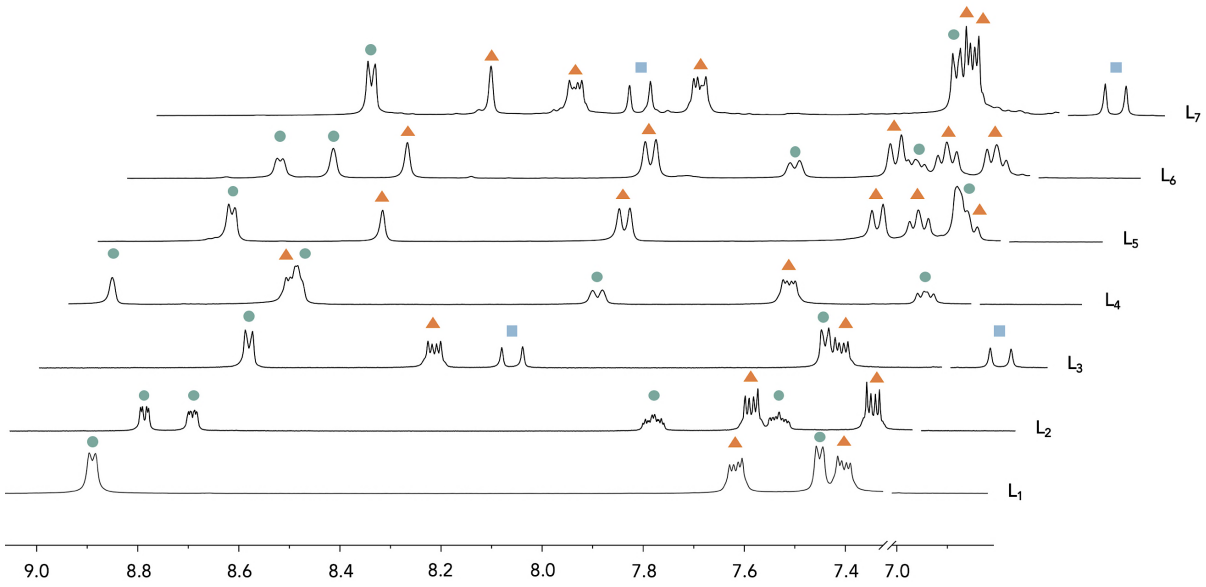

Figure 23: ^{1}H NMR spectra of **L1-L7** ($CDCl_3$, 23 °C, 400 MHz). In the aromatic region, signals are identified as pyridyl (●), anthracenyl (▲) and vinyl protons (■). The signal for $CHCl_3$ was removed for clarity.

The UV-spectra of L_{anthr} show typical absorption bands for the anthracene core, in the region between 300 and 400 nm and the pyridyl group, below 270 nm.[160] All data are summarized in table 5. Peaks for **L3** and **L4** are emphasized in comparison to the others: only two absorption bands for the derivative containing two double bonds (**L3**) and six for the molecule with two triple bonds (**L4**). In the window between 325 and 385 nm, the bands for the monopyridyl compounds **L5** and **L6** are blue shifted in comparison to their corresponding di-substituted analogues **L1** and **L2**.

L_{anthr}	Wavelength, nm (ε, x10^4 M^{-1}.cm^{-1})
L1	255 (11.3), 337 (1.5), 354 (2.7), 375 (3.8), 394 (5.7)
L2	254 (10.9), 336 (9.4), 355 (2.1), 376 (3.0), 397 (4.4)
L3	260 (11.6), 398 (5.5)
L4	275 (10.4), 299 (4.2), 314 (5.1), 438 (5.9), 464 (6.2)
L5	258 (14.1), 333(1.4), 349 (2.5), 367 (3.1), 398 (7.5)
L6	255 (11.3), 335 (0.8), 349 (1.6), 367 (2.3), 387 (2.3), 399 (2.9)
L7	259 (11.9), 350 (1.3), 370 (1.9), 398 (3.7)

Table 5: UV-VIS spectroscopic data for L_{anthr} (10^{-5} M, CH_2Cl_2).

Crystals were obtained by slow vapor diffusion of toluene into a solution of **L4** in CH_2Cl_2 and by a slow evaporation of a solution of **L6** in CH_2Cl_2/EtOAc (8/2). Both structures were also fully characterized by ^{1}H and ^{13}C NMR but their crystallographic data confirm their molecular structures (figure 24).

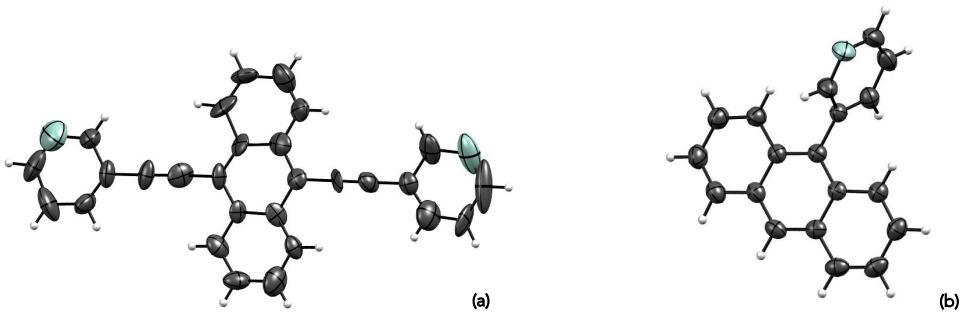

Figure 24: Ortep drawing of **L4** (a) and **L6** (b) at 50% probability level ellipsoids.

Compound **L4** crystallized in the non-centrosymmetric space group $P2_1$, a monoclinic crystalline system. In the solid state, the anthracene unit is nearly planar with the root mean square deviation of the 12 carbon atoms of the plane being 0.024 Å. The angles between the anthracene plane and the pyridyl rings are 1.6° and 2.9°, respectively. As illustrated in figure 24, the occupancy of the nitrogen atoms of pyridyl rings is poorly defined, showing the rotating flexibility around the ethynyl axes despite the conjugated aromatic system. Concerning **L6**, it crystallized in the centrosymmetric space group $P2_{1/c}$, a monoclinic crystalline system. In the crystal, the anthracene and pyridyl units are in two different planes, almost orthogonal (respectively, in blue and orange, in figure 25). This is confirmed by the value of the angle between the three carbons C_b, C_f and C_i that is 103,11°. So, there is 13,11° of deviation from a hypothetical orthogonal plane. This configuration is probably due to an optimization of the electronic density repartition within the molecule, since the nitrogen atom is in a *meta* position from the anthracene core.

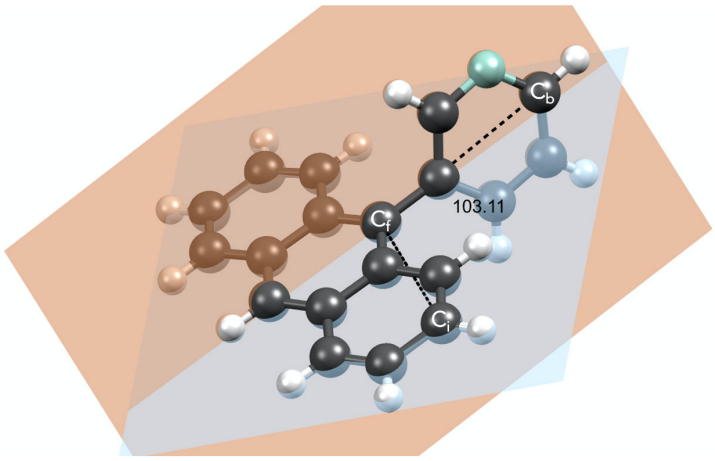

Figure 25: Crystallographic structure of **L6** with two planes: one containing the anthracene core and one corresponding to the pyridyl group. 103,11° is the value of the angle between C_b, C_f and C_i.

2.3. Synthesis and characterization of ligands with a dimethyldihydropyrenyl core (L_{dhp})

The other main ligand for building new arene ruthenium(II) assemblies is a derivative of dimethyldihydropyrene (L_{dhp}). This molecule was first extensively studied by Mitchell and then by Royal and others, mainly for its redox properties.[161,162,163] The biggest advantage of that molecule is its ability to trap singlet oxygen without the need of an external photosensitizer.

2.3.1. Synthesis of DHP precursor: 4,9-dibromo-2,7-di-*tert*-butyl-*trans*-10b,10c-dimethyl-10b,10c-dihydropyrene (DHP-Br_2)

To obtain a dibromo derivative, a multi-step synthesis is required (scheme 5). The procedure was well described in the literature, mostly by Mitchell, and then slightly modified by Royal.[164,165] The main drawback of this synthesis is its overall yield, that is only 1% after seven steps, as illustrated in scheme 5.

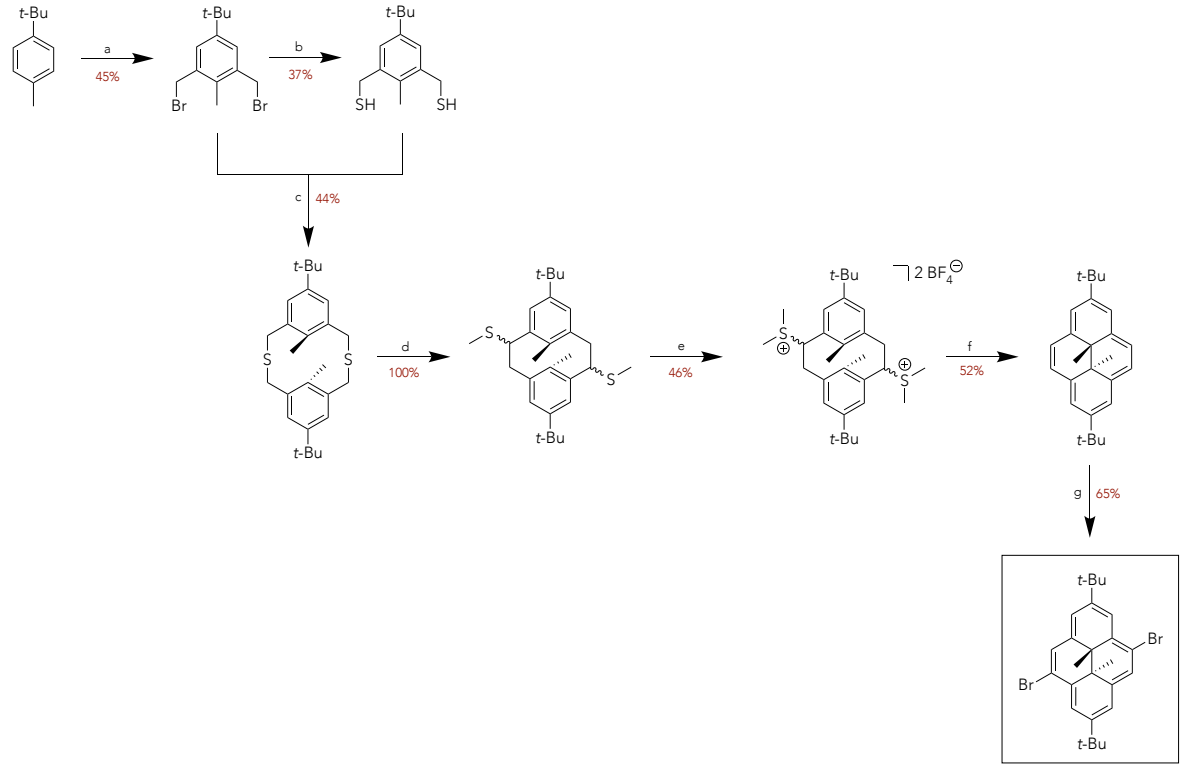

Scheme 5: Multi-step synthesis of DHP-Br_2 a) 1,3,5-trioxane, $ZnBr_2$, 33% HBr in acetic acid, acetic anhydride, 85 °C, 4 days; b) thiourea, EtOH, 80 °C, 3 h; NaOH, 100 °C, 3 h; c) KOH, $NaBH_4$, EtOH/H_2O/C_6H_6, 25 °C, 2 days; d) *n*-BuLi, dried THF, 0 °C, 1 h; MeI, 0 °C, 30 min; e) $BF_3.Et_2O$, trimethylorthoformate, dried CH_2Cl_2, -30 °C, 5 h; f) *t*-BuOK, dried THF, 85 °C, 15 h; g) NBS, DMF/CH_2Cl_2; -78 °C, 2 h.

2.3.2. Synthesis of pyridyl substituted DHP: **L8** and **L9**

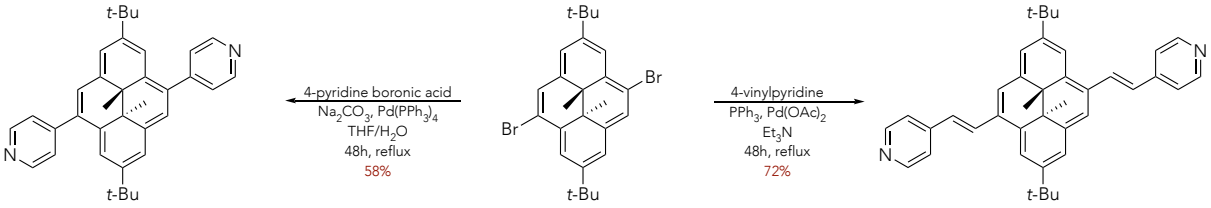

Scheme 6: Cross-coupling reactions from DHP-Br_2 to obtain **L8** (left) and **L9** (right).

As illustrated in scheme 6, DHP-Br_2 is the starting material for the synthesis of the bispyridyl derivatives **L8** and **L9**.[166] To obtain them, palladium-catalyzed cross-coupling reactions were carried out under an inert atmosphere: Suzuki and Heck reactions for **L8** and **L9** respectively (scheme 6). **L8** was isolated as a dark green powder, while **L9** as a dark red solid. Both molecules were characterized by ^1H, ^{13}C, mass spectrometry and UV-VIS measurements; elemental analysis was made only for **L9**, since it was not previously described in the literature (see experimental part). The ^1H NMR spectra for both **L8** and **L9** show typical signals for DHP: internal methyl groups, in the anisotropic cone of the pyrenyl core, as depicted by a singlet at around -3.50 ppm, *tert*-butyl groups by a singlet at around 1.70 ppm and all other signals being located in the aromatic region, superior to 7.30 ppm (figure 26).[166]

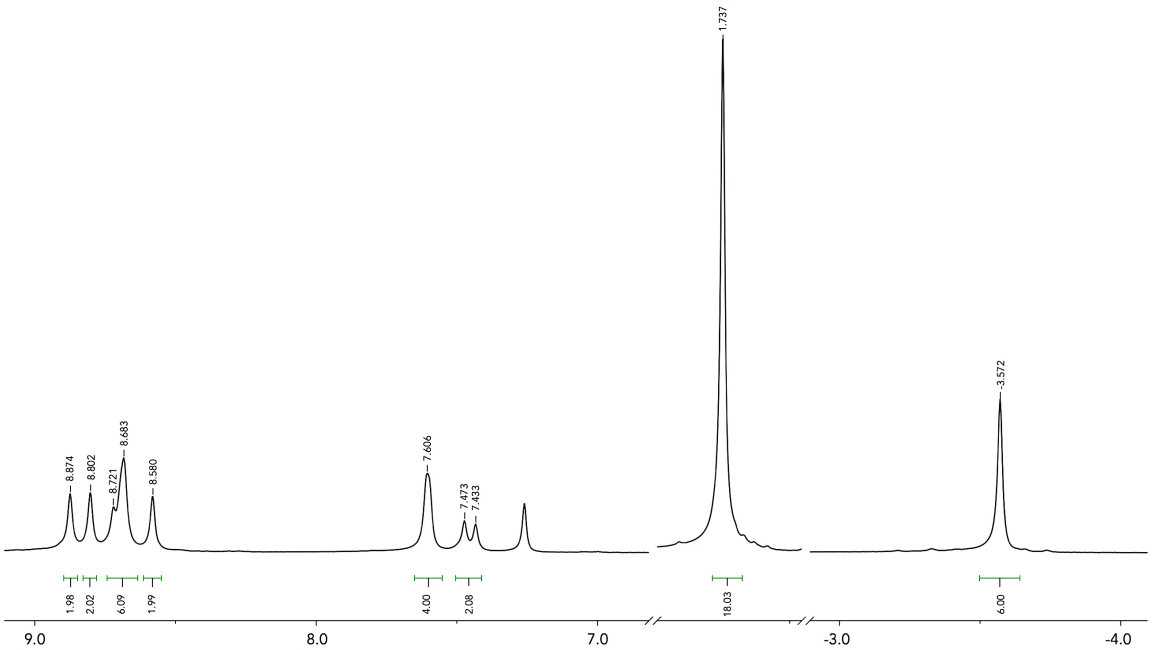

Figure 26: ^1H NMR spectrum of **L9** ($CDCl_3$, 23 °C, 400 MHz).

The UV-VIS spectrum of **L9** shows not only the typical absorption bands, attributed to π-π* transitions involving the first excited singlet states of the DHP unit, but also additional bands, in comparison to **L8** (figure 27).[147] This is probably due to the extension of the aromaticity with the double bonds between the DHP and the pyridyl moieties.

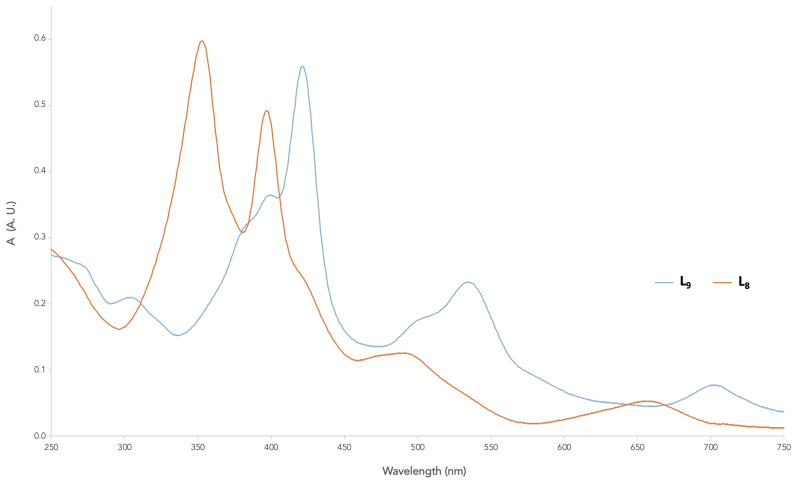

Figure 27: UV-VIS spectra of **L8** and **L9** (10^{-5} M in CH_3CN).

2.3.3. Synthesis of pyridinium substituted DHP: **L10**, **L11** and **L12**

In 2015, Royal and coworkers published their studies about trapping and releasing singlet oxygen by two DHP derivatives.[145,146] Both structures contain at least one pyridinium group. Moreover, the suggested mechanism of such molecular trap was confirmed by DFT calculations in 2017 and the study concluded with "*this type of system could be attractive oxygen carriers and singlet oxygen delivery agents*".[167] Therefore, our goal was to introduce pyridinium groups to **L8** and **L9**.

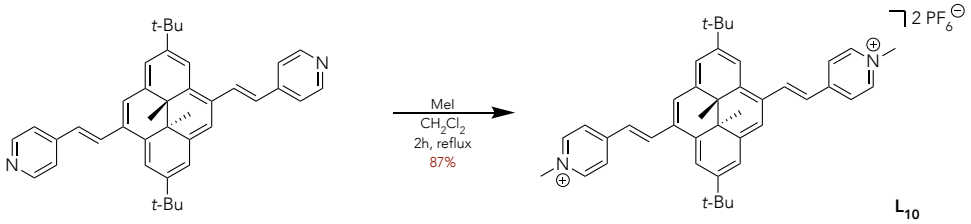

Scheme 7: Synthesis of compound **L10**.

First, to compare with the known bis-pyridinium structure of **L8**, the same procedure was carried out on **L9** to obtained 2,7-di-*tert*-butyl-4,9-di-(*N*-methyl-4-vinylpyridyl)-*trans*-10b,10c-

dimethyl-10b,10c-dihydropyrene hexafluorophosphate (**L_{10}**).[145] Iodomethane was added in excess in a solution of **L_9** in dichloromethane and was stirred for two hours at reflux (scheme 7). Then, the exchange of counter anion, from I^- to PF_6^-, was easily made by the dissolution of the iodo product in methanol followed by precipitation in a saturated aqueous solution of potassium hexafluorophosphate. **L_{10}** was obtained as a black powder, with an excellent yield (87%). It was fully characterized by NMR (^1H and ^{13}C), mass spectrometry, UV-VIS spectroscopy and elemental analysis. Typical shifts of the DHP core are observed in the ^1H NMR spectrum of **L_{10}**. It differs from **L_9** by the appearance of a singlet corresponding to the protons of the two methyl groups brought by the pyridinium units.

To introduce several pyridinium units on DHP cores, another synthetic route is to attach 4′-(4-(bromomethyl)phenyl)-2,2′:6′,2″-terpyridine to the pyridyl groups of **L_8** or **L_9** (scheme 8).[168,169] The molecules were also isolated as hexafluorophosphate salts, in moderate yields. **L_{11}** was already described in the literature, but not **L_{12}**. They are both characterized by ^1H and ^{13}C NMR and mass spectrometry (figure 28 and experimental part). The mass spectrum of **L_{12}** (electrospray ionization in a mixture acetonitrile/methanol) shows a cationic peak, corresponding to the drawn molecule in figure 29, with a *m/z* value of 597.8.

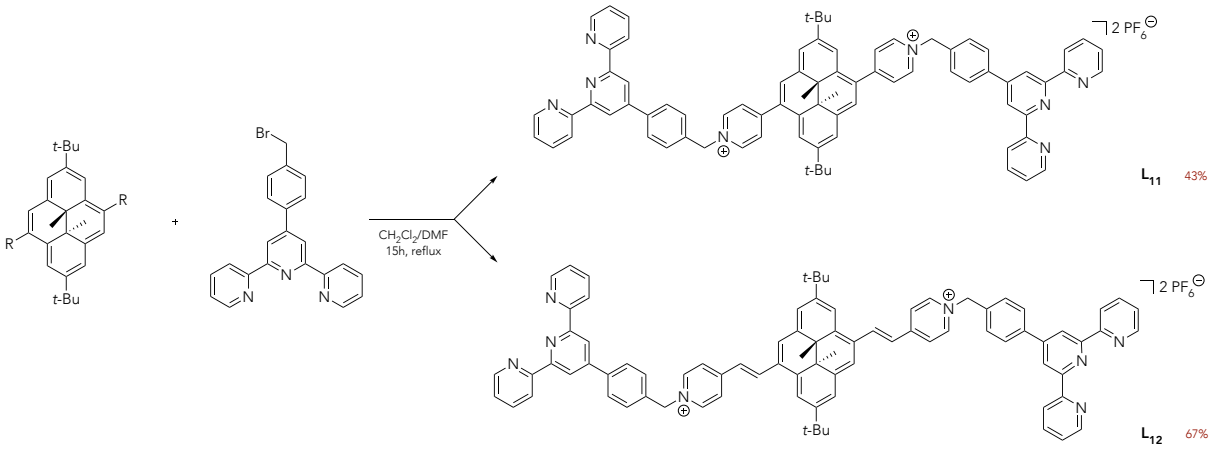

Scheme 8: Synthesis of compounds **L_{11}** and **L_{12}**.

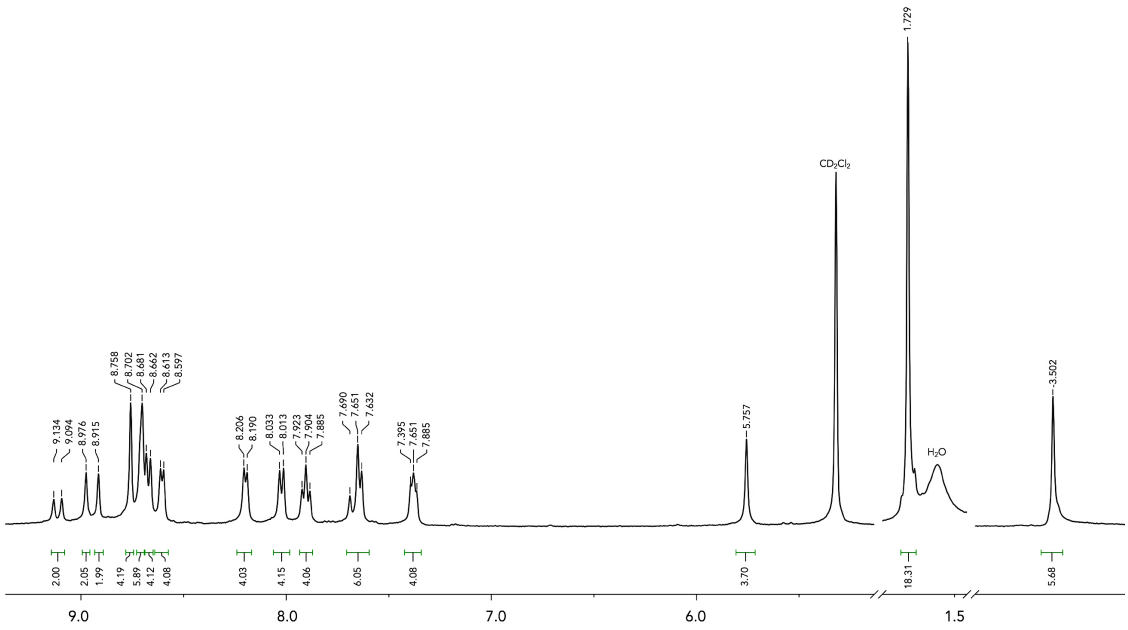

Figure 28: ^{1}H NMR spectrum of **L_{12}** (CD_2Cl_2, 23 °C, 400 MHz).

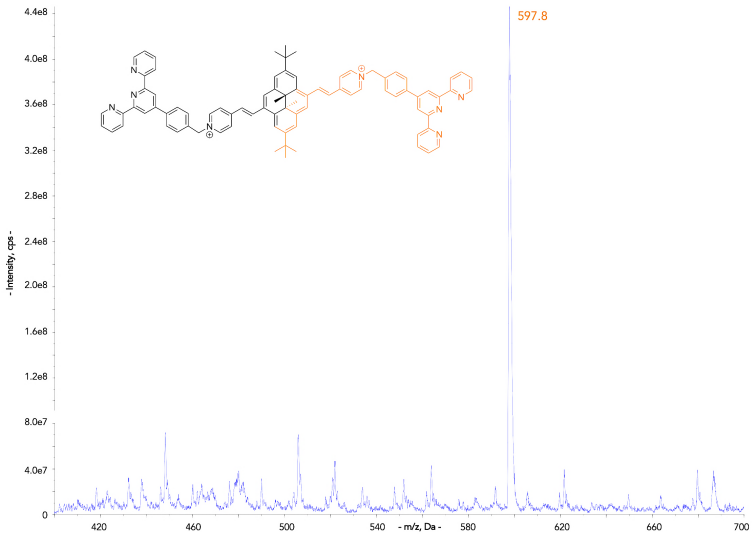

Figure 29: ESI-MS of compound **L_{12}** (CH_3CN/MeOH, positive mode).

The three **L_{DHP}** containing pyridinium derivatives have similar profiles on their UV-VIS spectra: a strong absorption in the UV region and smaller bands in the visible part (figure 30). However, the transitions associated to the absorption bands might depend more on the presence of a double bond than a terpyridyl unit. In fact, the spectrum of **L_{10}** is almost the same as **L_{12}**, only slightly blue shifted, and totally different from **L_{11}**. Regarding **L_{11}**, it undergoes an important hypsochromic shift compared to **L_{10}** and **L_{12}** and it presents two bands with a lower intensity in the region of 250-275 nm, those matches with the terpyridyl unit.

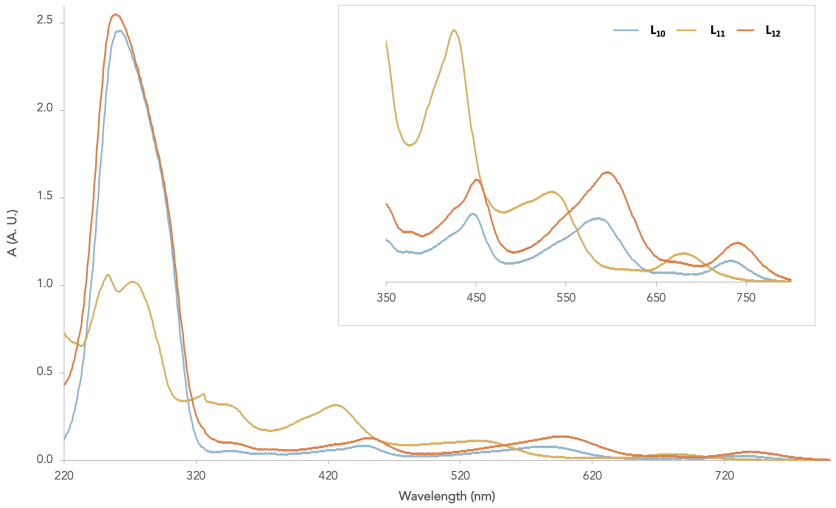

Figure 30: UV-VIS spectra of **L_{10}**, **L_{11}** and **L_{12}** (10^{-5} M in CH_3CN).

2.4. Synthesis and characterization of ruthenium(II) assemblies

The general idea is to attach the former ligands **L_1**-**L_{12}** to arene ruthenium(II) entities in order to get mono-, di- or tetra-nuclear complexes. General procedures were carried out to obtain the assemblies **A_1**-**A_{16}** (see experimental part).[150]

2.4.1. Description of tetranuclear ruthenium(II) complexes

For the synthesis of metalla-rectangles **A_1**-**A_9** (figure 31), one equivalent of ruthenium(II) precursor is first mixed with two equivalents of silver trifluoromethanesulfonate (AgOTf) to remove four chlorine atoms from the ruthenium precursor and to afford a reactive intermediate, that is not isolated. After the elimination of silver chloride by filtration, one equivalent of **L_{anthr}** is added, and the mixture stirred overnight in dichloromethane. The resulting product is concentrated and purified by precipitation in ether. Cationic *p*-cymene ruthenium(II) rectangles **A_1**-**A_9** were isolated as their trifluoromethanesulfonate salts, in variable yields (between 39% and 82%). The color is usually the same as the ruthenium(II) precursors: yellow for Ru(oxa), red for Ru(dobq) and green for Ru(donq). They were all characterized by various common spectroscopic techniques. Unfortunately, elemental analysis were consistent with theoretical calculations for only three rectangles (**A_7**, **A_8**, **A_9**), despite several purifications (precipitation in diethyl ether and in pentane) and a long drying

period, using a vacuum pump (about 10^{-3} mbar). The solubility of the assemblies depends on the nature of the dinuclear ruthenium(II) precursors: **A_3** and **A_7** are both soluble in ethanol and slightly in dichloromethane, while the others (**A_1**-**A_2**; **A_4**-**A_6** and **A_8**-**A_9**) show an opposite tendency. However, they are all soluble in acetone and in acetonitrile.

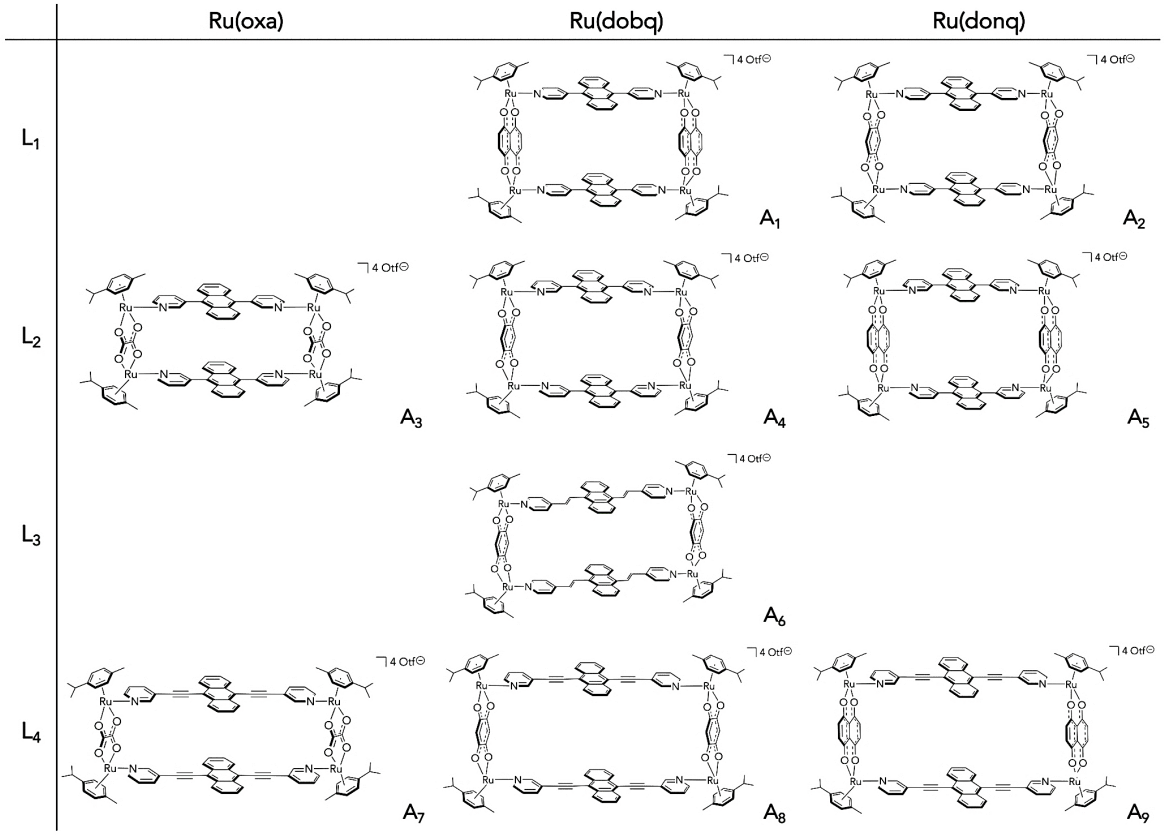

Figure 31: Structures of ruthenium(II) rectangles **A_1**-**A_9**. With Ru(x) = ruthenium precursors, with x corresponding to oxa = oxalate; dobq = 2,5-dioxido-1,4-benzoquinonato; donq = 5,8-dioxido-1,4-naphtoquinonato.

The formation of the tetranuclear ruthenium(II) complexes **A_1**-**A_9** were first confirmed by electrospray mass spectrometry (ESI-MS). These analyses were realized by the team of Pr. Schalley, at the University of Berlin (Germany). Some of the spectra show typical patterns of arene ruthenium(II) assemblies with trifluoromethanesulfonate counterions: mono- to tetra-cationic structures were observed, corresponding to the loss of the equivalent quantity of trifluoromethanesulfonate anions (table 6). Some others display more original peaks, with the loss of parts from the *p*-cymene (methyl or isopropyl) and parts of the ruthenium clip (table 6). The experimental results perfectly correlate with the calculated isotopic distributions of the different species.

	[M-4OTf$^-$]$^{4+}$	[M-3OTf$^-$]$^{3+}$	[M-2OTf$^-$]$^{2+}$	[M-OTf$^-$]$^+$	Other peaks
A_1	470.6	677.1	1090.1	2329.1	/
A_2	496.1	/	1140.2	/	/
A_3	/	/	1041.1	/	/
A_4	471.1	677.8	1091.1	/	/
A_5	/	/	/	/	[M-2donq-2methyl-3OTf$^-$]$^{3+}$: 575.9 [M-2*p*cymene-4methyl-3OTf$^-$]$^{3+}$: 603.1 [M-isopropyl-2methyl-3OTf$^-$]$^{3+}$: 689.9
A_6	/	/	/	/	[M-2methyl-4OTf$^-$]$^{4+}$: 489.0
A_7	/	/	1088.9	2323.2	[M-2**L_4**-2OTf$^-$]$^{4+}$: 708.0
A_8	/	/	1139.2	2423.0	[M-2**L_4**-2OTf$^-$]$^{4+}$: 759.3
A_9	/	/	1188.1	/	[M-2**L_4**-2OTf$^-$]$^{4+}$: 809.0

Table 6: *m/z* values from ESI-MS spectra for **A_1**-**A_9**

^{1}H NMR spectra show typical peak multiplicities and chemical shifts of the arene ruthenium units (table 7). For example, depending on the assembly, aryl protons of the *p*-cymene are present around 5.65 and 6.65 ppm; isopropyl protons at around 1.25-1.45 ppm; and methyl protons at 1.95-2.35 ppm. Figure 32 shows the ^{1}H NMR spectrum of **A_6**, displaying the common peaks and multiplicities of this kind of ruthenium(II) assemblies. The signals are well-defined, like on the spectra of **A_8** and **A_9**. Interestingly, the majority of the tetranuclear complexes (**A_1**-**A_5** and **A_7**) has broad signals in the aromatic region and additional splitting of some protons from the *p*-cymene unit. Such observation strongly suggests the formation of two isomers, *cis* and *trans*, in which the pyridyl units are pointing to the same or opposite sides of the metalla-rectangles.

The presence of *cis*-*trans* isomers can also be explained by the shorter distance between two ruthenium atoms, which forces the two anthracene units to be in close proximity and be stabilized by π-π stacking interactions. This is illustrated in figure 33, which shows the single-crystal X-rays structure of **A_7**. Crystals were obtained by slow diffusion of a mixture of diethyl ether/benzene (99/1) into an acetone solution of **A_7**. The tetracationic salt crystallized in the triclinic space group *P*-1. The asymmetric unit includes the ruthenium(II) rectangle, its four trifluoromethanesulfonate counterions and four acetone molecules. The size of **A_7** as defined by the four Ru-Ru edges is 5.4 x 17.7 x 5.4 x 17.9 Å.

		A_1	A_2	A_3	A_4	A_5	A_6	A_7	A_8	A_9
		CD_3CN	CD_3CN	CD_3CN	CD_3CN	CD_3CN	CD_3CN	$(CD_3)_2CO$	$(CD_3)_2CO$	$(CD_3)_2CO$
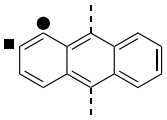	●	6.82	7.59	7.56	7.46	7.37	7.17	7.34	7.47	7.48
	■	7.27	7.59	7.56	7.63	7.37	7.90	8.16	8.05	8.01
	▲	8.46	8.92	/	/	/	8.18	/	/	/
	★	7.50	7.78	/	/	/	7.66	/	/	/
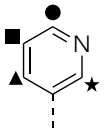	●	/	/	8.67	8.66	8.86	/	8.16	8.64	8.48
	■	/	/	7.84	7.70	8.14	/	7.65	7.70	7.62
	▲	/	/	8.06	7.93	7.85	/	8.64	8.31	8.56
	★	/	/	8.97	8.81	9.04	/	8.64	8.58	8.72
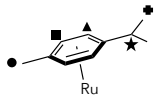	●	2.28	1.96	2.11;2.07	1.96	2.05	2.20	2.35	2.33	2.26
	■	5.81	6.30	5.67	5.82	5.81	5.73	6.05	6.11	5.86
	▲	6.01	5.83	5.67	5.82	5.81	5.95	6.20	6.34	6.09
	★	2.96	2.97	2.84	2.84	2.85	2.88	3.04	3.04	3.04
	✤	1.41	1.32	1.30	1.29	1.24	1.36	1.43	1.42	1.42
dobq		5.93	/	/	7.46	/	5.78	/	5.96	/
donq		/	7.59	/	/	7.37	/	/	/	7.44

Table 7: Chemical shifts (in ppm) of ruthenium(II) complexes **A_1-A_9**.

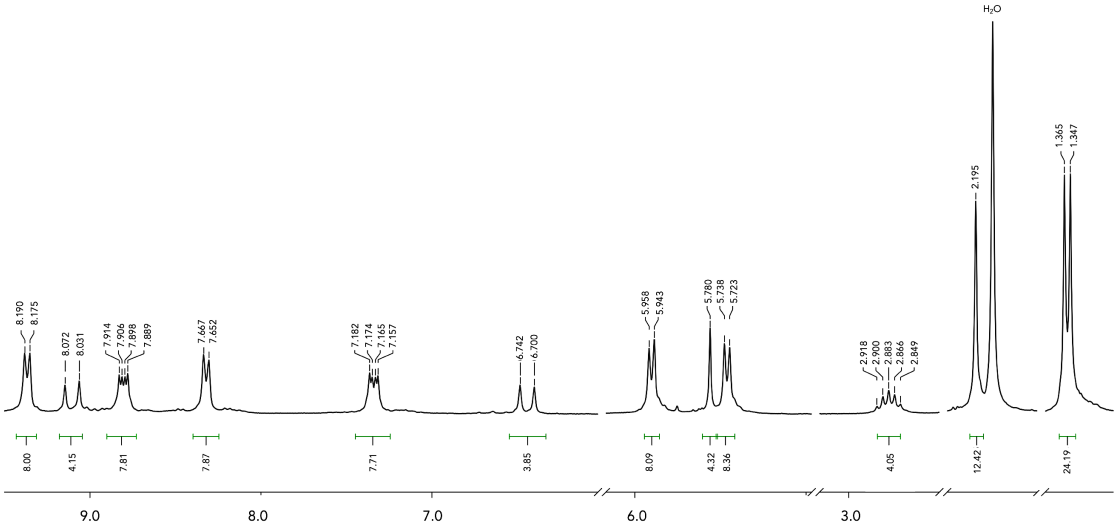

Figure 32: ^{1}H NMR spectrum of **A_6** (CD_3CN, 23 °C, 400 MHz).

As mentioned before, π-π stacking interactions play an important role in the formation of these ruthenium(II) complexes. On figure 33, both anthracene units are positioned in a "parallel fashion" and are separated by a distance of about 3.8 Å, which is smaller than the distance between two ruthenium atoms (5.4 Å). The existence of π-π interactions and its maximization can explain this spatial arrangement. This optimization can also be a reason why the pyridyl groups are not in the same plane as the anthracene units. In fact, two of them are observed at an angle of approximately 7°, while the two others are rotated by 34° from the idealized plane of the anthracene units.

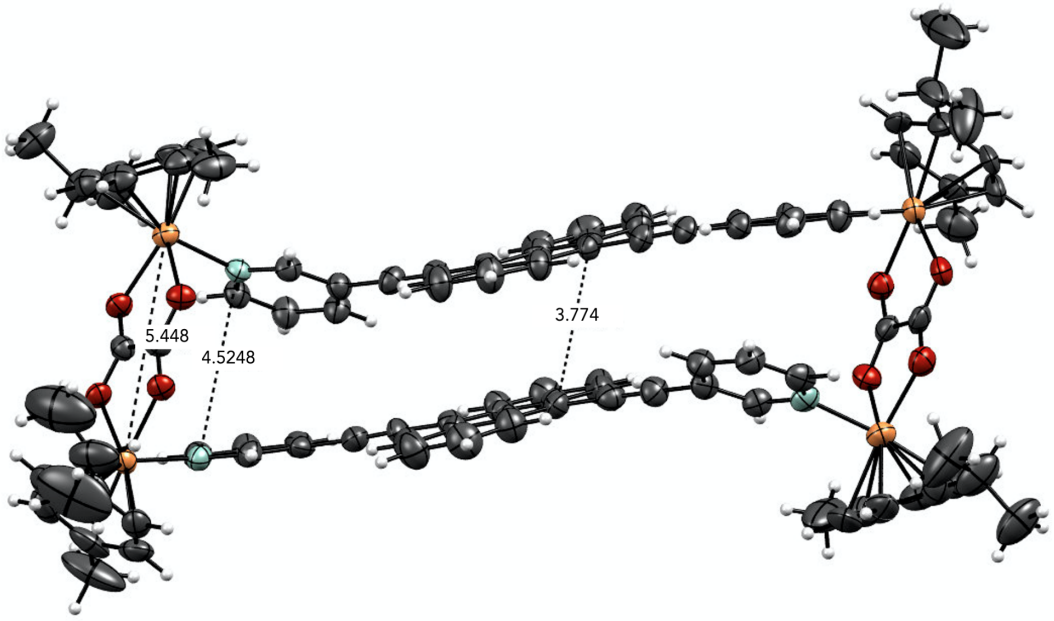

Figure 33: Ortep drawing of **A₇**·4 acetone at 50% probability level ellipsoids. Trifluoromethanesulfonate and acetone molecules are omitted for clarity.

The tetracationic ruthenium(II) complexes **A₁**-**A₉** were also characterized by UV-VIS spectroscopy. All measurements, in the range of 250 and 700 nm, were made at room temperature in a mixture of dichloromethane/acetonitrile (95/5), in order to dilute the metalla-rectangles and to compare them in similar conditions (table 8). The intense high energy band centered at 270-330 nm is assigned to ligand π-π* transition and intra-ligand charge transfer (ILCT). They also display a broad low-energy band, which corresponds to metal-to-ligand charge transfer (MLCT). Anthracene units let their prints in the UV-VIS spectra in the region around 300 and 550 nm. However, the absorption bands are usually broader than the respective **L$_{anthr}$** alone.[170]

A_{anthr}	Wavelength, nm (ε, x10^4 M^{-1}.cm^{-1})
A_1	306 (7.76); 361 (4.27); 379 (5.55); 399 (9.33); 482 (5.52), 513 (5.99)
A_2	340 (1.98); 358 (3.05); 375 (4.22); 398 (0.70)
A_3	340 (2.50); 360 (3.93); 378 (5.61); 399 (7.63); 468 (0.8)
A_4	304 (7.19); 362 (5.36); 382 (6.87); 400 (9.90)
A_5	324 (2.69); 341 (3.24); 359 (5.16); 377 (7.57); 396 (8.73)
A_6	309 (12.0); 397 (8.97); 458 (9.16); 513 (6.32)
A_7	271 (16.7); 310 (10.3); 459 (9.80); 486 (6.26)
A_8	274 (13.2); 447 (11.7); 476 (11.3)
A_9	271 (16.6); 310 (12.7); 445; (10.9); 473 (9.19)

Table 8: UV-VIS data for A_{anthr} (10^{-5}M, CH_2Cl_2/CH_3CN = 95/5).

2.4.2. Description of mono- and di-nuclear ruthenium(II) complexes

2.4.2.1. Ruthenium(II) assemblies containing L_{anthr}

In order to have an idea of the impact of the number of ruthenium atoms composing the assembly and the π-π stacking interaction between the anthracene units on the ability of A_{anthr} to capture singlet oxygen, mono- and dinuclear ruthenium(II) complexes A_{10}-A_{15} were synthetized. They were all prepared from [Ru(η^6-*p*-cymene)(pta)Cl_2], since the use of the chloro derivative [{Ru(η^6-*p*-cymene)(μ^2-Cl)Cl}$_2$] reduced the solubility and generated purification issues (schemes 9 and 10).

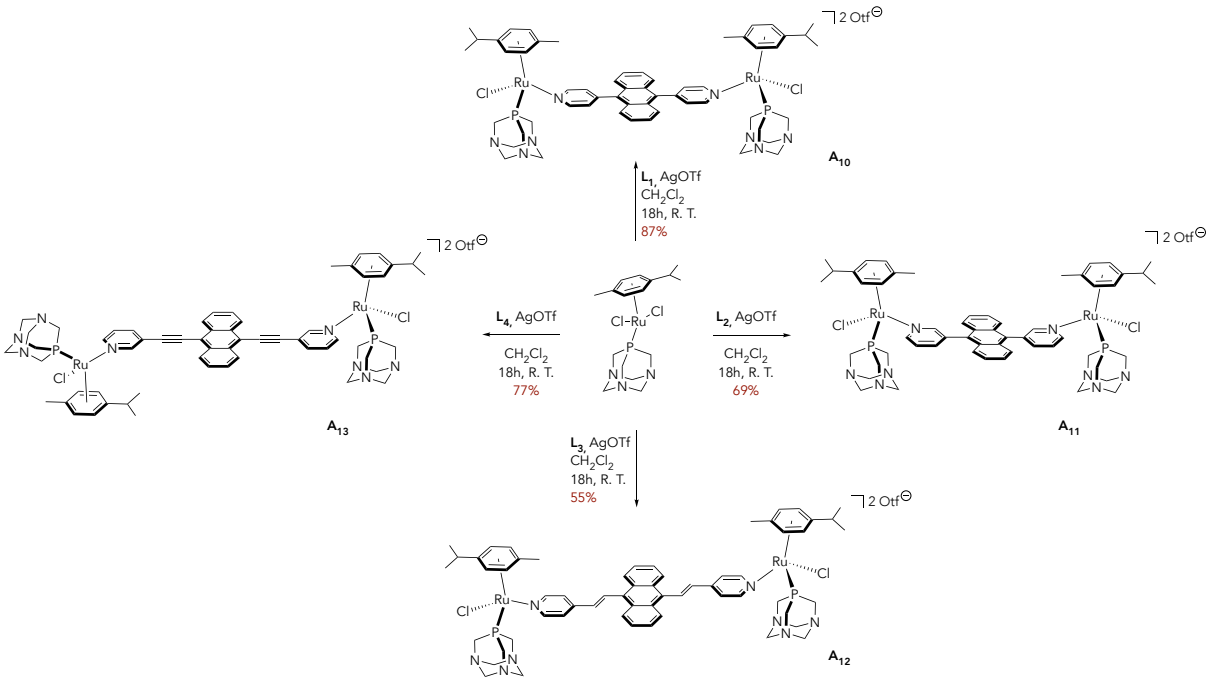

Scheme 9: Synthesis of dinuclear ruthenium(II) assemblies A_{10}-A_{13}.

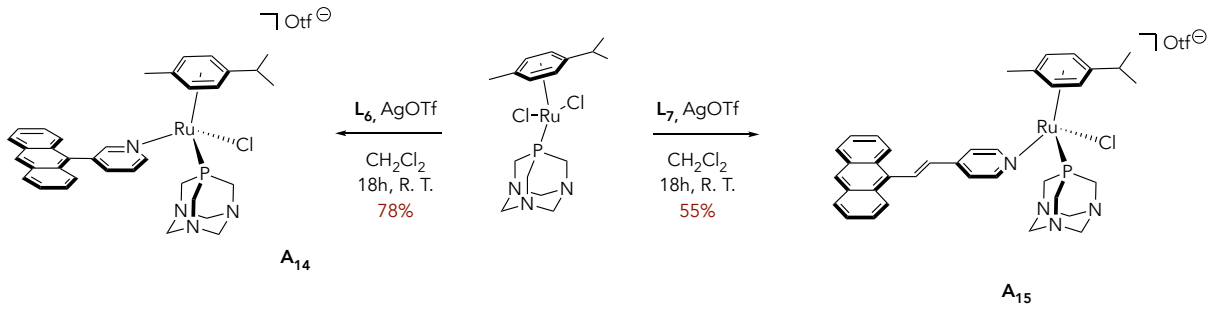

Scheme 10: Synthesis of mononuclear ruthenium(II) assemblies **A_{14}-A_{15}**.

As for the tetranuclear structures, AgOTf was employed to obtain a reactive intermediate before the addition of **L_{anthr}**. The purification of the trifluoromethanesulfonate salts was made by precipitation in cold diethyl ether and/or pentane. They were isolated as yellow or orange solids, in various yields (from 45 to 87%).

The ^{1}H NMR spectra of **A_{10}-A_{15}** show similar chemical shifts to those observed for the ligands (figure 34). The main difference is the appearance of two multiplets for the -CH_2 groups of the pta ligand (at around 4.20 ppm and 4.55 ppm respectively).

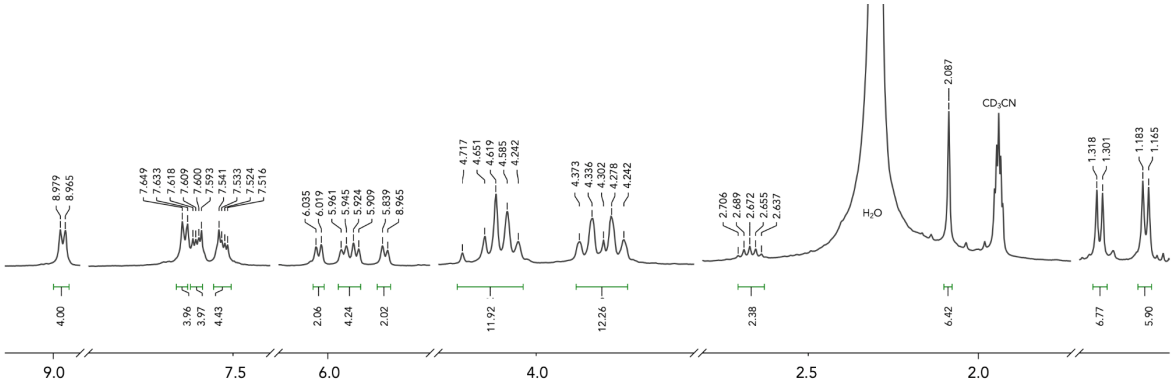

Figure 34: ^{1}H NMR spectrum of **A_{10}** (CD_3CN, 23 °C, 400 MHz).

Diffusion ordered spectroscopy (DOSY) experiments were carried out for all the **A_{anthr}** derivatives.[171] This experiment can prove the formation of ruthenium assemblies since it provides an idea of their size, with the calculation of their hydrodynamic radius *via* the determination of the diffusion coefficients and the use of the Stokes-Einstein equation. Then, diffusion coefficients also strongly depend on physical parameters, such as the temperature and the solvent viscosity. Table 9 gives the diffusion coefficients for **A_1-A_{15}**. Different solvents were used (acetonitrile and acetone) and they can have an impact on the diffusion.

Nevertheless, their viscosity are very close: 3.2 x10^{-4} Pa.s and 3.7 x10^{-4} Pa.s, respectively for acetone and acetonitrile, and therefore do not really influence the values in table 9.[172] The calculated values correspond to the ones usually found for ruthenium(II) assemblies and there is almost no difference between mono-, di- or tetra-nuclear entities (figure 35).[173]

A_{anthr}	D ($m^2.s^{-1}$)	Log D	NMR Solvent
A_1	6.76 x 10^{-10}	-9.17	CD_3CN
A_2	8.96 x 10^{-10}	-9.05	CD_3CN
A_3	9.41 x 10^{-10}	-9.03	CD_3CN
A_4	6.39 x 10^{-10}	-9.19	CD_3CN
A_5	9.67 x 10^{-10}	-9.01	CD_3CN
A_6	6.09 x 10^{-10}	-9.22	CD_3CN
A_7	6.67 x 10^{-10}	-9.18	$(CD_3)_2CO$
A_8	6.04 x 10^{-10}	-9.22	$(CD_3)_2CO$
A_9	6.80 x 10^{-10}	-9.17	$(CD_3)_2CO$
A_{10}	5.85 x 10^{-10}	-9.23	CD_3CN
A_{11}	5.49 x 10^{-10}	-9.26	CD_3CN
A_{12}	6.09 x 10^{-10}	-9.22	CD_3CN
A_{13}	6.57 x 10^{-10}	-9.18	CD_3CN
A_{14}	6.57 x 10^{-10}	-9.18	CD_3CN
A_{15}	6.86 x 10^{-10}	-9.16	CD_3CN

Table 9: Diffusion coefficients (D) and their corresponding log D for **A_1-A_{15}**.

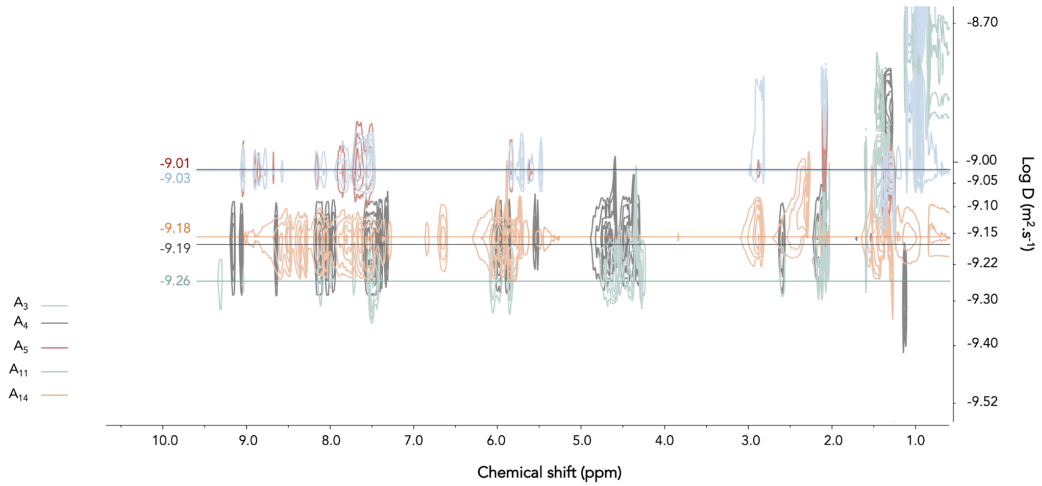

Figure 35: DOSY NMR superimposed spectra of **A_3**, **A_4**, **A_5**, **A_{11}** and **A_{14}** (CD_3CN, 23 °C, 400 MHz).

The formation of **A_{10}-A_{15}** was also confirmed by ESI-MS experiments and the appearance of common peaks for arene ruthenium(II) complexes, with the loss of one or several OTf^- ions (table 10). For **A_{12}**, the mass spectrum displays a peak with a *m/z* value of 619.1 corresponding to the additional loss of the entity {Ru(*p*-cymene)(pta)Cl} and one Cl^-.

	$[M\text{-}2OTf^-]^{2+}$	$[M\text{-}OTf^-]^+$	$[M\text{-}\{Ru(p\text{-cymene})(pta)Cl\}\text{-}2OTf^-]^+$	$[M\text{-}\{Ru(p\text{-cymene})(pta)Cl\}\text{-}Cl^-\text{-}2OTf^-]^+$
A_{10}	/	1337.2	760.2	/
A_{11}	594.6	1337.2	760.2	/
A_{12}	/	/	808.2	619.1
A_{13}	618.1	1385.2	/	/
A_{14}	/	683.2	/	/
A_{15}	/	709.3	/	/

Table 10: *m/z* values from ESI-MS spectra for **A_{10}-A_{15}**.

2.4.2.2. Ruthenium(II) assemblies containing L_{DHP}

With the perspective of introducing arene ruthenium(II) units and exploiting its potential as cytotoxic agent, several reactions were carried out with **L_8**, **L_9**, **L_{11}** and **L_{12}**. Unfortunately, only one reaction was successful as illustrated in scheme 11. The failure of the other reactions, especially with **L_{11}** and **L_{12}**, might come from the possible steric hindrance with the particular geometry of the ruthenium complexes, constrained by the presence of the *p*-cymene with the terpyridyl units.

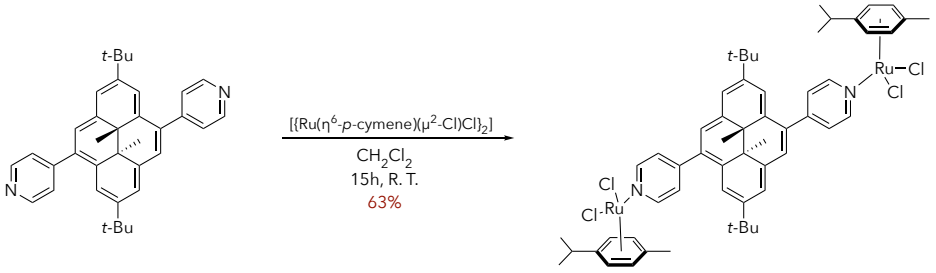

Scheme 11: Synthesis of $[\{Ru(\eta^6\text{-}p\text{-cymene})Cl\}_2(\mu^2\text{-}L_8)Cl_2]$ (**A_{16}**).

A_{16} was obtained by mixing **L_8** and $[\{Ru(\eta^6\text{-}p\text{-cymene})(\mu^2\text{-}Cl)Cl\}_2]$ in dichloromethane overnight. The resulting solution was poured into cold diethyl ether and the product was obtained as a brownish powder, in a moderate yield (63%). It was characterized by all the common analytical techniques. In the ^1H NMR spectrum, all chemical shifts correspond perfectly to the precursors of **A_{16}** (**L_8** and the ruthenium complex). First, in the upper aromatic region, two doublets associated to the protons of the pyridine and three singlets to the pyrenyl core are observed. The lower aromatic region displays the multiplets for the aryl protons of the *p*-cymene. In the shielded part of the ^1H NMR spectrum, all signals for the

protons of the *tert*-butyl, -CH_3 and -CH_2 are observed. Finally, the two internal methyl groups of the DHP core are observed at -3.71 ppm (figure 36).

A solution of **A_{16}** was prepared in acetonitrile and analyzed by UV-VIS spectroscopy. In comparison with the corresponding ligand **L_8**, this ruthenium(II) complex has a quite similar absorption spectrum (figure 37). However, three differences are noticeable: (1) a less intense band centered at 350 nm, (2) a bathochromic shift and a more intense band at 410 nm and (3) the appearance of a weak low-energy band at around 600 nm. These observations can be explained by the addition of the arene ruthenium(II) unit to the ligand **L_8** and the presence of new transitions. In fact, the introduction of an electron withdrawing metal center changes the energy of the LUMO and has a direct consequence on the absorption spectra, especially with the appearance of bands corresponding to metal-to-ligand charge transfers (MLCT).[165]

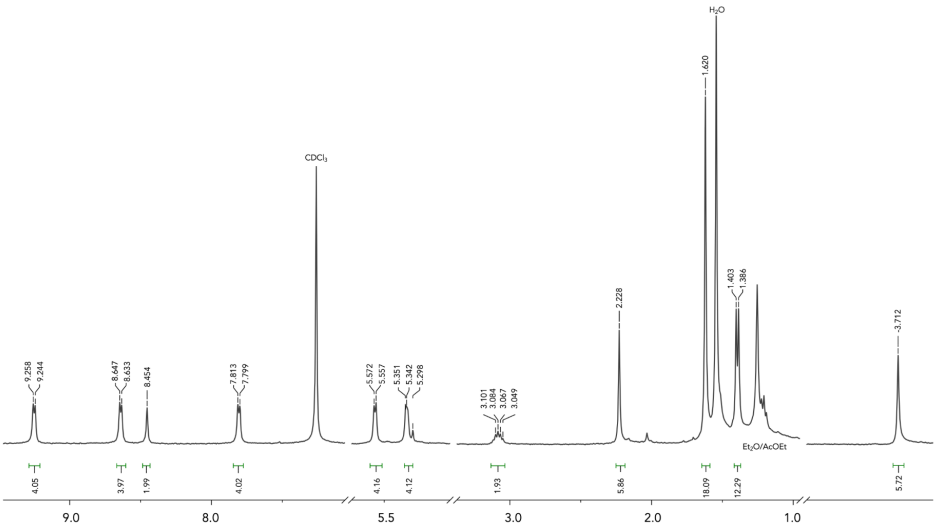

Figure 36: ^{1}H NMR spectrum of **A_{16}** ($CDCl_3$, 23 °C, 400 MHz).

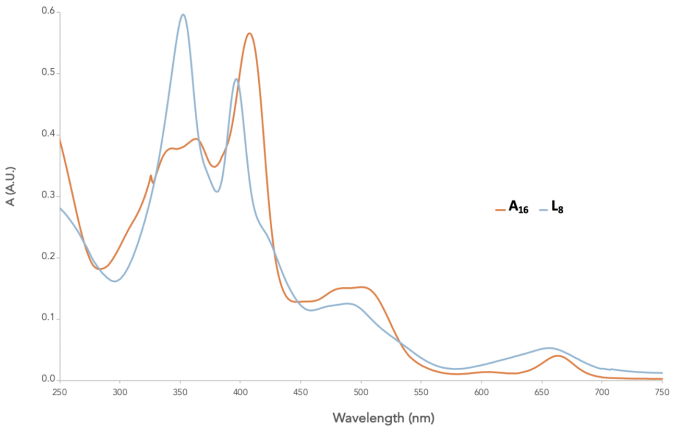

Figure 37: UV-VIS spectra of **L_8** (10^{-5} M in CH_3CN) and **A_{16}** (10^{-5} M in CH_2Cl_2).

3. Photooxygenation of Lanthr and Aanthr: behaviors in solution and in vitro studies

The first part of the studies focusses on the comparisons between the photooxygenation of L_{anthr} and A_{anthr}. The main question is to determine if the formation of metal-based assemblies and the presence of arene ruthenium unit(s) enhance the reactivity towards $^1O_2$ in solution or, quite the contrary, decrease the endoperoxide formation. A second part consists to test L_{DHP} and determine their ability to trap $^1O_2$. Finally, the last part is about the biological studies on prostatic cancer cells, with the anthracene derivatives.

3.1. Photooxygenation of L_{anthr} and A_{anthr} in solution

In this section, the ability of the species with one or several anthracene units, ligands or arene ruthenium(II) assemblies, to capture $^1O_2$ is determined by several techniques: UV-VIS measurements, ^{1}H NMR spectroscopy and mass spectrometry. The solutions were strictly prepared just before the experiments, with solvents previously made "oxygen free" by several cycles of freeze-pumping, followed by the addition of anthracene derivative (L_{anthr} or A_{anthr}) and an external photosensitizer, such as tetraphenylporphyrin (TPP). For each experiment, a first analysis was carried out to obtain a result without oxygen in order to compare the following results with O_2. Then, a closed vial was filled with oxygen gas for 30 seconds and it was placed inside of a photoreactor, equipped with white light lamps (400-800 nm).

For the photooxygenation, several photosensitizers were commonly employed because of their attractive characteristics: they have a higher triplet energy than singlet

oxygen (> 94.2 kJ.mol^{-1}), a long triplet lifetime, a high absorption coefficient and a high quantum yield of the triplet state. Among them, TPP was arbitrarily chosen. The ratio TPP/anthracene was 1/5.[143]

3.1.1. Results for anthracenyl ligands L_{anthr}

Since the ability of L_{anthr} to trap and release singlet oxygen was already described in the literature, several series of tests were realized for two main reasons: (1) to physically tune the experiment conditions (UV-VIS spectrometer, wavelength, irradiation time, etc.); and (2) to have an idea of how the anthracene unit is behaving during/after the photooxygenation of L_{anthr}.[142,143]

Unlike L_4, ^{1}H NMR spectra of all L_{anthr} display signal shifts after 15 hours of irradiation. Generally, the signals for the pyridyl protons are deshielded, whereas the signals for the anthracenyl protons are shielded. These observations are encountered for both mono- and di-substituted L_{anthr} (figure 38 and 39). The most impacted signals by the [2+4] cycloaddition correspond to the protons around the site where singlet oxygen is added. It is the case for the proton which is directly linked to the same carbon as the singlet oxygen on monosubstituted anthracene derivatives (L_5, L_6 and L_7). This signal is usually displaced by around 2 ppm (figure 39). All these observations can be explained by the fact that the addition of the singlet oxygen increases the electron density on the anthracenyl core, which is translated in ^{1}H NMR spectra into an upfield shift of its signals; while the electronic impoverishment of the pyridyl core is expressed by the downfielded signals.

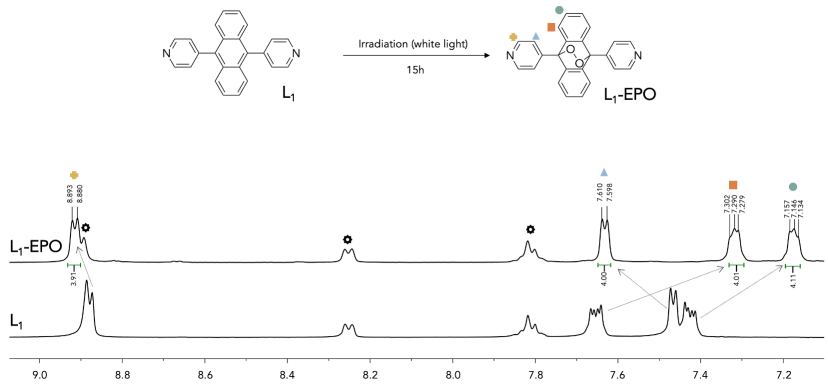

Figure 38: ^{1}H NMR spectra of L_1 with TPP (✪), before and after irradiation (CD_2Cl_2, 23 °C, 400 MHz). The signal shifts show the formation of L_1-EPO.

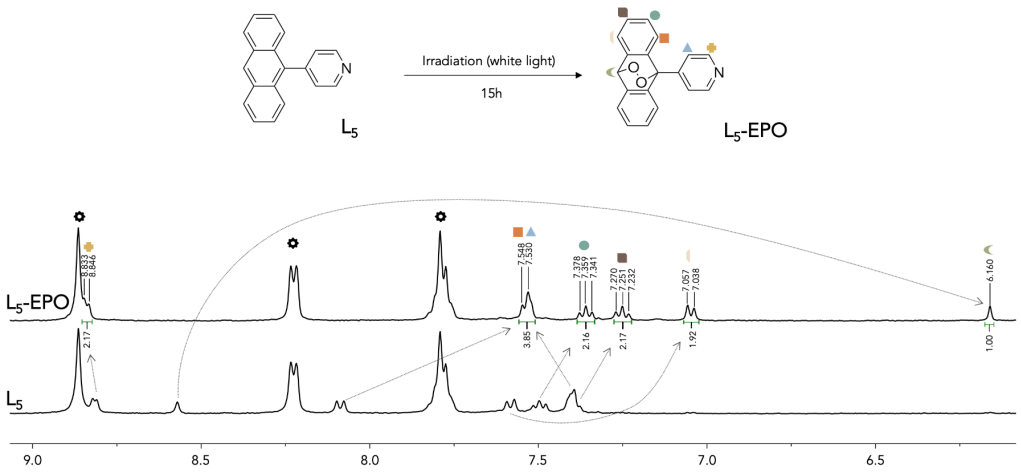

Figure 39: ^{1}H NMR spectra of **L_5** with TPP (✪), before and after irradiation (CD_2Cl_2, 23 °C, 400 MHz). The signal shifts show the formation of **L_5-EPO**.

Another hint for the formation of the endoperoxide forms of **L_{anthr}** (**L_{anthr}-EPO**) can be seen on UV-VIS measurements. In fact, when the [2+4] cycloaddition takes place, the aromaticity and the electronic density change, which also affects the electronic transitions and by extension, the UV-VIS profile. Then, the addition of $^1O_2$ on **L_{anthr}** can be monitored by the extinction of the absorption band corresponding to the anthracenyl core (around 300 and 400 nm). Figure 40 shows the UV-VIS spectra of **L_{anthr}** dichloromethane solutions during the first hour of irradiation. Three profiles can be seen. First, ligands containing one or several pyridyl group(s) (**L_1**, **L_2**, **L_5**, **L_6**): four or five bands in the spectral window are nicely distinguishable; while the second profile, corresponding to the derivatives with one or two (pyridin-4-yl)vinyl unit(s) (**L_3** and **L_7**), presents a less well-drawn bands in the same spectral window. For both groups, the overnight irradiation with a white lamp provokes a progressive extinction of the absorption bands, which strongly suggests the formation of the corresponding endoperoxides **L_{anthr}-EPO**. Finally, the last type is composed by only **L_4**. Despite a two-day irradiation, no change on UV-VIS spectrum and ^{1}H NMR was noticeable. In 2012, Fudickar and Linker published a study about a set of alkynyl acenes and their unusual behavior to undergo a slow cycloaddition of singlet oxygen.[174] They observed the same behavior as **L_4** towards singlet oxygen. This phenomenon will be described in more details later (section 3.1.3.).

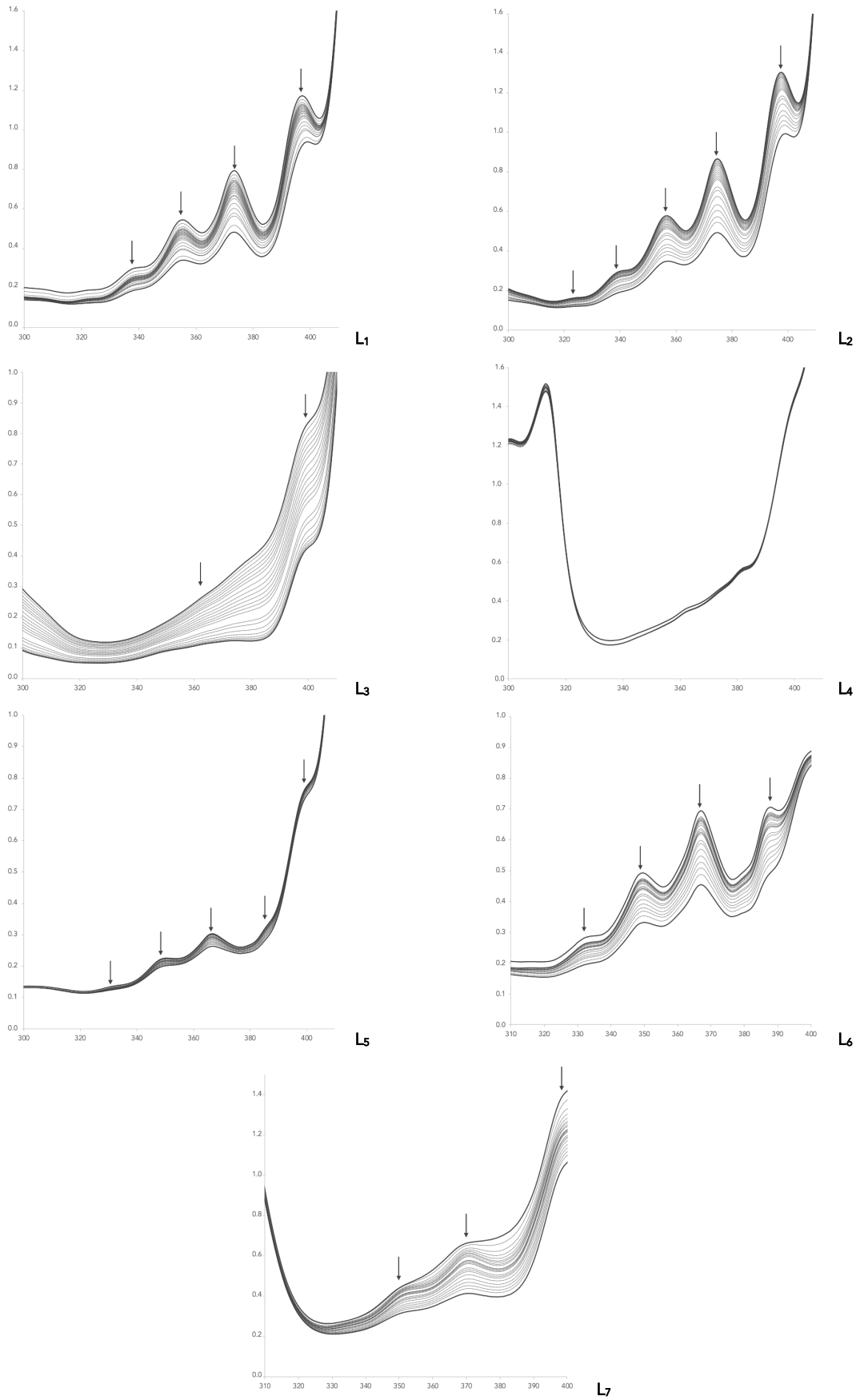

Figure 40: UV-VIS spectra of **L_1-L_7** (5.0 x 10^{-5} M in CH_2Cl_2) during irradiation (white light; t = 0 to 60 min).

^{1}H NMR and UV-VIS analysis do not completely prove the existence of **L_{anthr}-EPO**. In order to confirm their formation, mass spectra were realized by the team of Pr. Schaley in Berlin. Two batches of solutions were analyzed. The first batch was the irradiated **L_{anthr}** solutions in dichloromethane (5.0 x 10^{-5} M) without photosensitizer and the second batch correspond to the same solution but with the addition of TPP (10^{-5}M in dichloromethane). The results undoubtedly confirm the formation of **L_{anthr}-EPO**, and only when a photosensitizer is added to the solution (figure 41). As expected, no peak corresponding to $[M\text{-}EPO+H]^+$ was found for **L_4** (table 11).

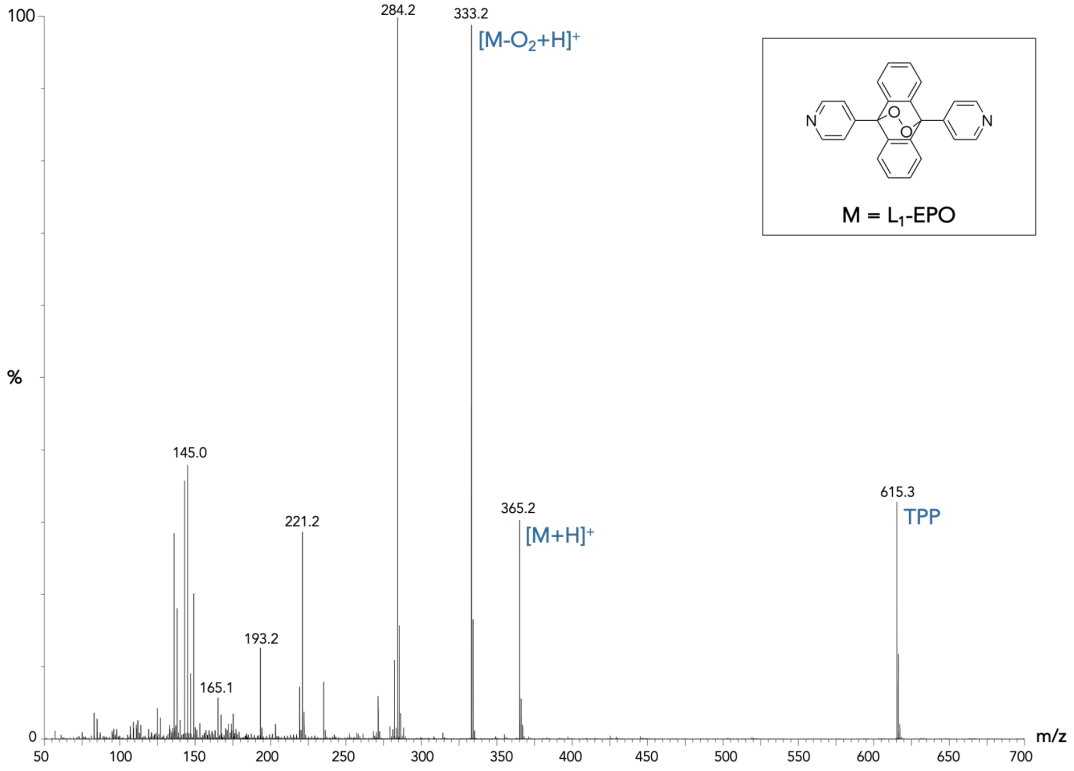

Figure 41 : TOF ESI-MS of compound **L_1-EPO** (CH_2Cl_2, positive mode).

	$[M+H]^+$	$[M\text{-}O_2+H]^+$
L_1-EPO	365.2	333.2
L_2-EPO	365.1	333.1
L_3-EPO	417.1	385.1
L_4-EPO	/	381.1
L_5-EPO	288.2	256.2
L_6-EPO	288.1	256.1
L_7-EPO	314.2	284.2

Table 11 m/z values from TOF ESI-MS spectra for **L_{anthr}-EPO.**

3.1.2. Results for anthracenyl ruthenium(II) assemblies A_{anthr}

Once the characteristics and the behaviors of L_{anthr} were determined, our attention was focused on the corresponding A_{anthr}. These experiments are similar to the previous ones in order to compare the formation of A_{anthr}-EPO with the corresponding L_{anthr}-EPO.

First, contrary to the spectra obtained after the photooxygenation of L_{anthr}, the conversion into A_{anthr}-EPO is not clear, since the appearance of new signals in ^{1}H NMR spectra was really shy. The best quality spectrum that was recorded is displayed in figure 42 and it corresponds to the monitoring of A_6 photooxygenation. The first line shows the ruthenium(II) assembly in CD_2Cl_2, while the second depicts the signals of A_6 when TPP is added to the first solution. Interestingly, the signals for the ligand L_3 are slightly upshifted. It suggests that TPP may be in interaction with A_6 or be encapsulated into the cavity of A_6, since our team already observed this phenomenon with the encapsulation of a porphyrin in an octanuclear metalla-cube.[170c]The third spectrum was recorded after 15 hours of irradiation and it shows new signals. Unfortunately, there was no improvement of the spectrum even after one week of irradiation. Nevertheless, the appearance of new signals can be a sign for the formation of A_6-EPO. This description in ^{1}H NMR spectrum can also be valid for the other A_{anthr}. However, other analysis should be done to clearly prove the formation of A_{anthr}-EPO after irradiation.

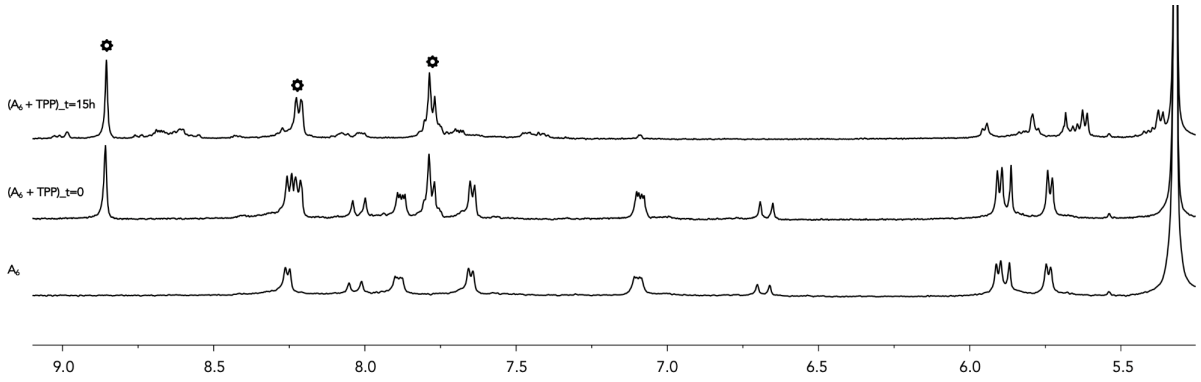

Figure 42: ^{1}H NMR spectra of A_6 with TPP (✿), before and after irradiation (CD_2Cl_2), 23 °C, 400 MHz). New signals are present after 15 h of irradiation (white light).

Then, photooxygenations of A_{anthr} solutions in a mixture of dichloromethane/acetonitrile (95/5) were monitored by UV-VIS spectroscopy. For tetranuclear ruthenium(II) rectangles A_1-A_9, a tendency appears at first sight (figure 43). Firstly, when L_{anthr} are attached to Ru(oxa), the

complexes seem more sensitive to the irradiation. **A_3** is prey to a higher decrease of its absorption bands than **A_4** and **A_5**; and **A_7** was the only derivative from **L_4** to be impacted by white light irradiation. Surprisingly, during the first five minutes of irradiation of **A_7**, two isobestic points were observed, followed by an important decrease of the whole absorption profile (figures 43 and 44). Usually, the presence of an isobestic point reveals an equilibrium of two species in solution, which gives hope of the formation of **A_7-EPO**. Secondly, the introduction of Ru(dobq) has a more negative impact than the introduction of Ru(donq). This observation comes from the comparison of the spectra of ruthenium(II) complexes derivating from **L_1** and **L_2** (so **A_1**, **A_2**, **A_3** and **A_4**), since the ones from **L_4** do not give a real change of the general behavior. Finally, for the major part of the di- and mono-nuclear ruthenium(II) assemblies **A_{10}-A_{15}** (figure 45), the presence of Ru(pta) does not prevent the irradiation. Only **A_{12}**, derivating from **L_3**, appears to be unreactive towards the photooxygenation. Here again, the decrease of the absorption bands is a good omen for the cycloaddition of $^1O_2$ on **A_{anthr}**, but it must be confirmed by additionnal analysis.

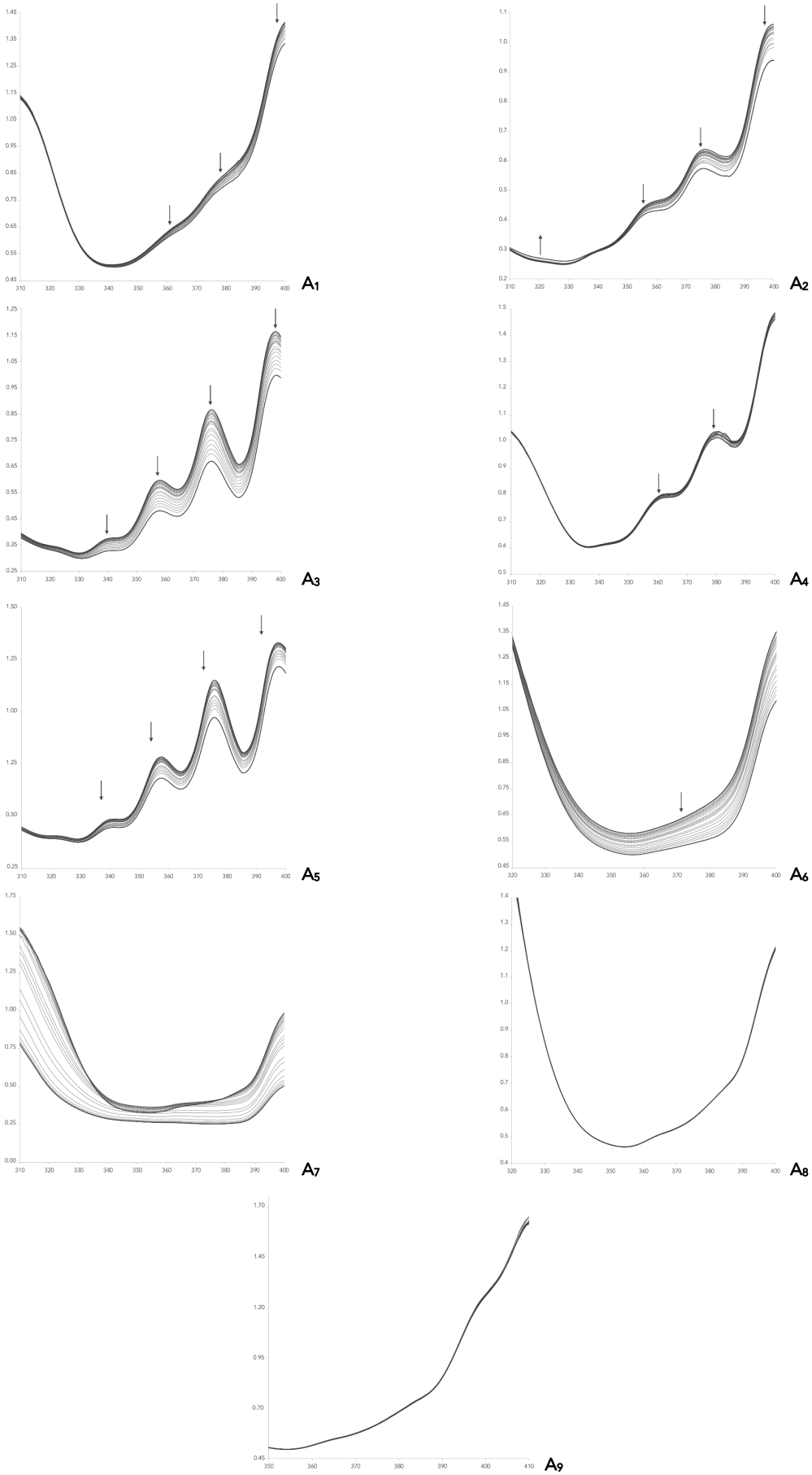

Figure 43: UV-VIS spectra of **A_1-A_9** (5.0×10^{-5} M in CH_3CN/CH_2Cl_2) during irradiation (white light; t = 0 to 60 min; with TPP).

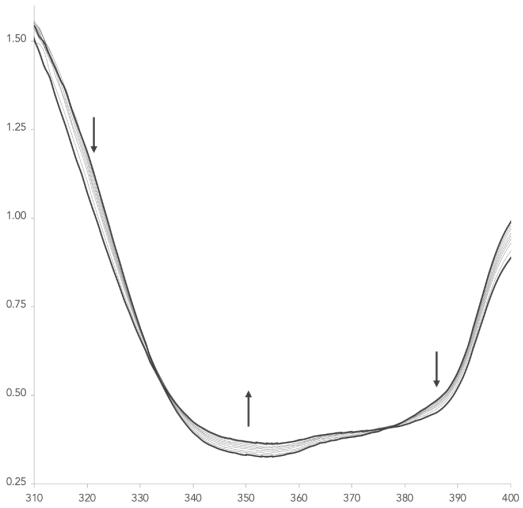

Figure 44: UV-VIS spectra of **A7** (5.0 x 10^{-5} M in CH_3CN/CH_2Cl_2) during irradiation (white light; t = 0 to 5 min).

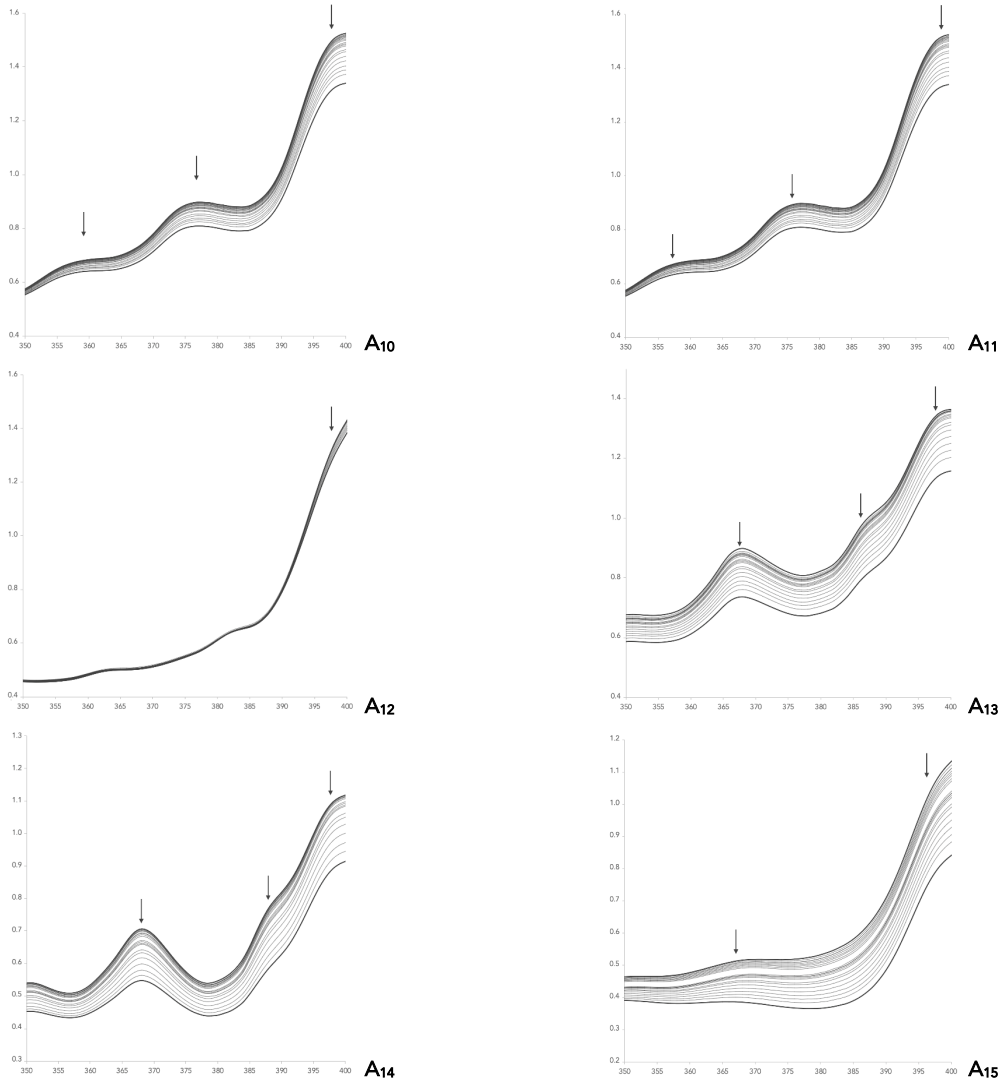

Figure 45: UV-VIS spectra of **A10-A15** (5.0 x 10^{-5} M in CH_3CN/CH_2Cl_2) during irradiation (white light; t = 0 to 60 min; with TPP).

Therefore, mass spectra were obtained from the team of Pr. Schaley in Berlin. As for **L_{anthr}**, two batches of solutions were analyzed (with and without a photosensitizer). The results are not as clear as those obtained for **L_{anthr}** (table 12). In fact, they are sometimes inconclusive because of an easy fragmentation of **A_{10}-A_{15}**, since a peak corresponding to Ru(pta) (with a *m/z* value of 428.1) is always present. In addition, some fragments can also overlap with a peak corresponding to the half ruthenium(II) assemblies, which lead to a small change of the isotopic pattern. However, some patterns matching with the loss of some OTf^- ions and/or the loss of one molecule of O_2 are typically found for the big majority of **A_{anthr}**. Figure 46 focuses on the fragmentation of **A_6**, with and without the use of TPP. The formation of **A_6-EPO** was clearly proven. Nevertheless, the solution of this ruthenium(II) rectangle, without TPP, displays two peaks, in a very low proportion, that can be also assigned to the formation of **A_6-EPO**. Then, another experiment was carried out to have more information about the ability of **A_6** to be oxygenated without a photosensitizer.

A_{anthr}	Founded peaks	*m/z* values
A_1-EPO	$[M\text{-}4OTf\text{-}O_2]^{4+}$	478.6
	$[M\text{-}3OTf\text{-}O_2]^{3+}$	688.1
	$[M\text{-}2OTf\text{-}O_2]^{2+}$	1106.6
A_2-EPO	$[M\text{-}4OTf\text{-}O_2\text{-arene-}3CH_3\text{-}3isopropyl]^{4+}$	431.9
A_3-EPO	$[M\text{-}4OTf\text{-}O_2]^{4+}$	474.1
	$[M\text{-}3OTf\text{-}O_2]^{3+}$	663.3
A_4-EPO	$[M\text{-}4OTf]^{4+}$	487.1
	$[M\text{-}3OTf\text{-}O_2]^{3+}$	688.1
	$[M\text{-}2OTf\text{-}O_2]^{2+}$	1106.6
	$[M\text{-}2OTf]^{2+}$	1123.1
A_5-EPO	$[M\text{-}3OTf\text{-}O_2\text{-}3arene\text{-}CH_3]^{4+}$	583.1
A_6-EPO	$[M\text{-}4OTf\text{-}O_2]^{4+}$	504.6
	$[M\text{-}4OTf]^{4+}$	513.2
	$[M\text{-}2OTf]^{2+}$	1174.1
A_7-EPO	$[M\text{-}4OTf\text{-}O_2]^{4+}$	489.8
A_{10}-EPO	$[M+2H]^{2+}$	760.2
A_{11}-EPO	$[M+2H]^{2+}$	760.2
A_{15}-EPO	$[M\text{-}OTf]^{+}$	741.2

Table 12: *m/z* values from TOF ESI-MS spectra for some **A_{anthr}-EPO**

A mass experiment was performed with a solution of **A_6** in acetonitrile (1 µM), by Daniel Stares from the team of Pr. Schaley. Two measurements were realized: one after keeping the solution in the dark and one after letting the solution stand under irradiation (with natural light), without any sensitizer, for only 30 minutes. Interestingly, the fragmentation gave the same peaks as observed for **A_6-EPO** (figures 46 and 47), confirming with no ambiguity that **A_6** can act as a photosensitizer.

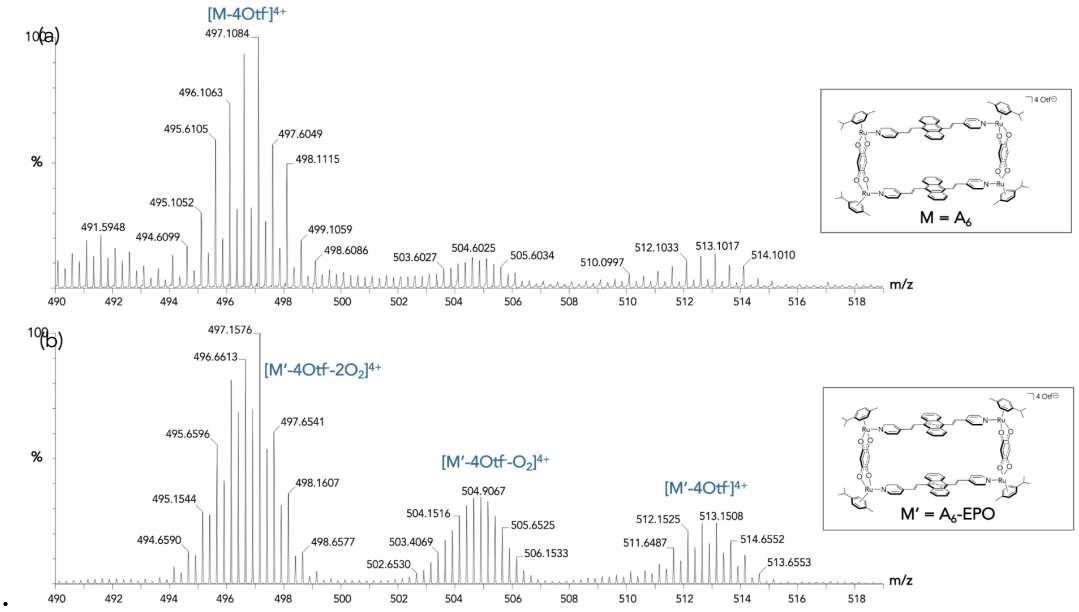

Figure 46: TOF ESI-MS of compound **A_6** and **A_6-EPO** (CH_2Cl_2, positive mode); experiments with (b) and without (a) TPP.

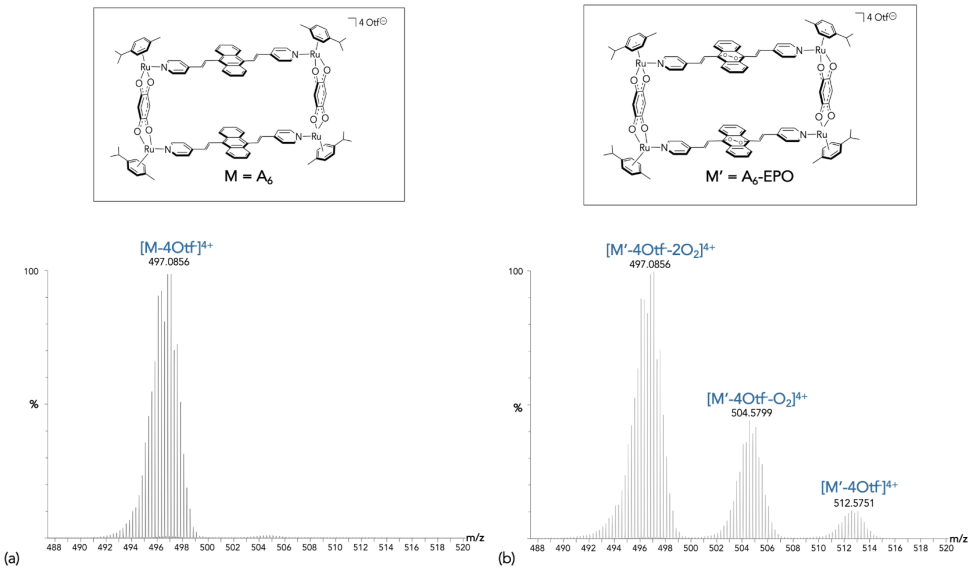

Figure 47: TOF ESI-MS of compound **A_6** (CH_3CN, positive mode), (a) after 30 min in the dark and (b) after 30 min of irradiation.

3.1.3. Kinetics of the photooxygenations of L_{anthr} and A_{anthr}.

Now, it is interesting to approach the kinetics of the former photooxygenations. In fact, it was proven for some of A_{anthr} that they are able to undergo a [2+4] cycloaddition with $^1O_2$ and they should be compared to "known" species as well as to the corresponding L_{anthr}. These comparisons will help to determine if the presence of the arene ruthenium(II) unit is an advantage, or not, for the photooxygenation.

To carry out kinetic studies, some kinetic statements should be made.[175] The reaction of the photooxygenation is described by equation (1). "Anthr" is a general term for the molecule, both L_{anthr} or A_{anthr}, that reacts with $^1O_2$, to afford "Anthr-EPO"

$$\text{Anthr} + {}^1O_2 \rightarrow \text{Anthr-EPO} \qquad (1)$$

$$v = \frac{d[\text{anthr}-\text{EPO}]}{dt} = -\frac{d[\text{anthr}]}{dt} = k \cdot [\text{anthr}] \cdot [{}^1O_2] \qquad (2)$$

The rate of this reaction is proportional to the concentration of the two reactants, Anthr and $^1O_2$, as explained in equation (2). So, the photooxygenation of L_{anthr} and A_{anthr} correspond to a second order reaction but it can be simplified. In fact, the concentration of $^1O_2$ can be assumed to be constant since it is in excess compared to "Anthr". The reaction becomes then a pseudo-first order reaction. The equation (2) can be simplified by equation (3), and gives by the following equation (4).

$$v = k \cdot [\text{anthr}] \cdot [{}^1O_2] = k' \cdot [\text{anthr}] \qquad \text{where } k = k'[{}^1O_2] \qquad (3)$$

$$v = -\frac{d[\text{anthr}]}{dt} = k' \cdot [\text{anthr}]$$

$$\Leftrightarrow \quad -\frac{d[\text{anthr}]}{[\text{anthr}]} = k' \cdot dt$$

$$\Leftrightarrow \quad -\int_{[\text{anthr}]_0}^{[\text{anthr}]} \frac{d[\text{anthr}]}{[\text{anthr}]} = k' \cdot \int_0^t dt$$

$$\Leftrightarrow \quad \ln\left(\frac{[\text{anthr}]_0}{[\text{anthr}]}\right) = k' \cdot t$$

$$\Leftrightarrow \quad \ln\left(\frac{[anthr]}{[anthr]_0}\right) = -k' \cdot t \tag{4}$$

So, if the natural logarithm of the concentration of **L_{anthr}** or **A_{anthr}** on its initial concentration is plotted against the time, the slope will give a value of the rate coefficient. The higher this value is, faster is the reaction and the more efficient is the photooxygenation. Therefore, the graphs were drawn for the first 50 minutes of the reaction for all anthracenyl derivatives, with TPP (figure 48). For an easier comparison and for determining the impact of the presence of ruthenium(II), the same data were used in different fashions (figure 49). Here, diphenylanthracene (DPA) was always taken for reference, since it is already well described in the literature.[176]

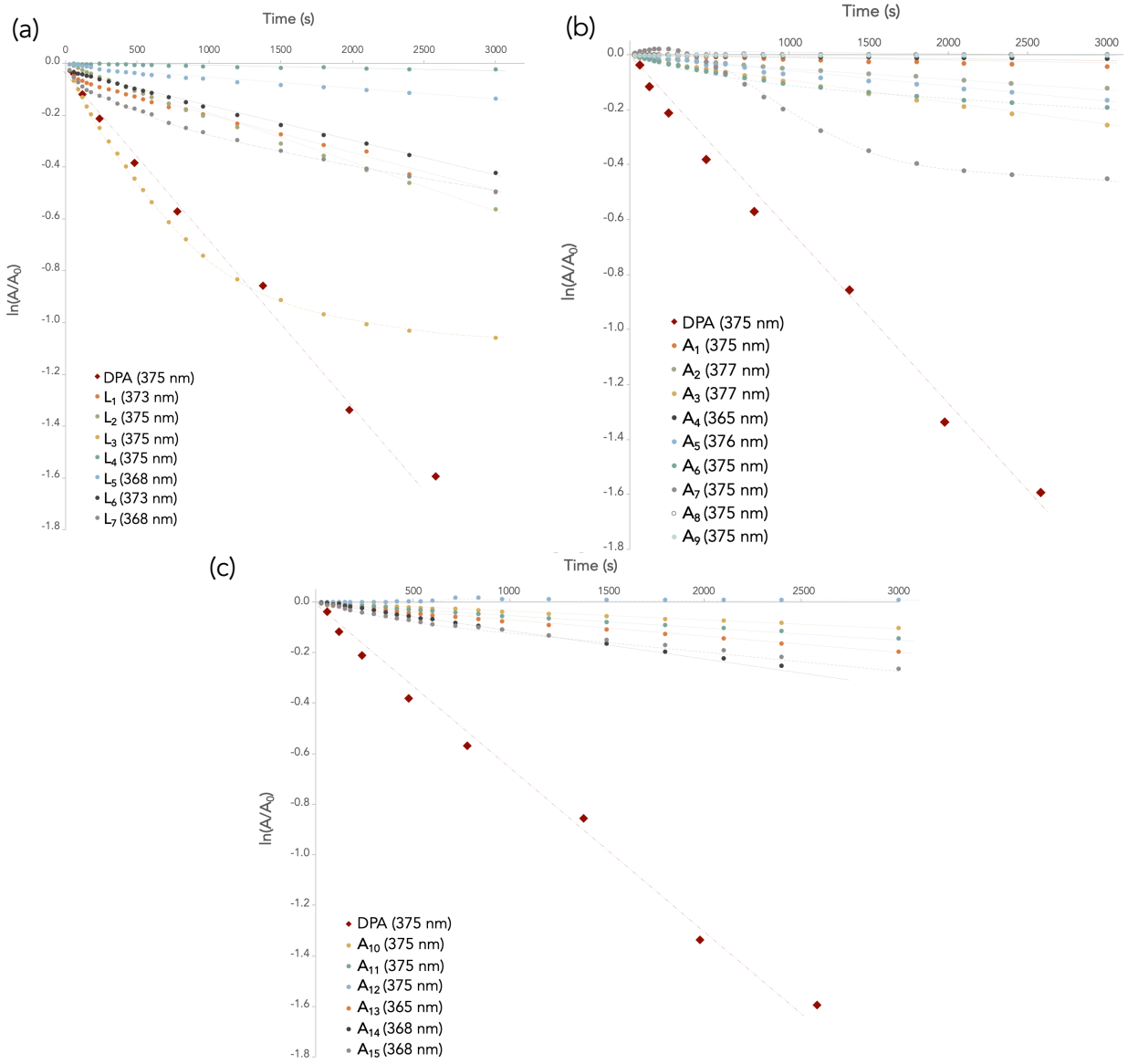

Figure 48: Semi logarithmic plots of the photooxygenation of: (a) **L_1-L_7** (10^{-5} M in CH_2Cl_2); (b) **A_1-A_9** (10^{-5} M in CH_2Cl_2/CH_3CN) and (c) **A_{10}-A_{15}** (10^{-5} M in CH_2Cl_2/CH_3CN).

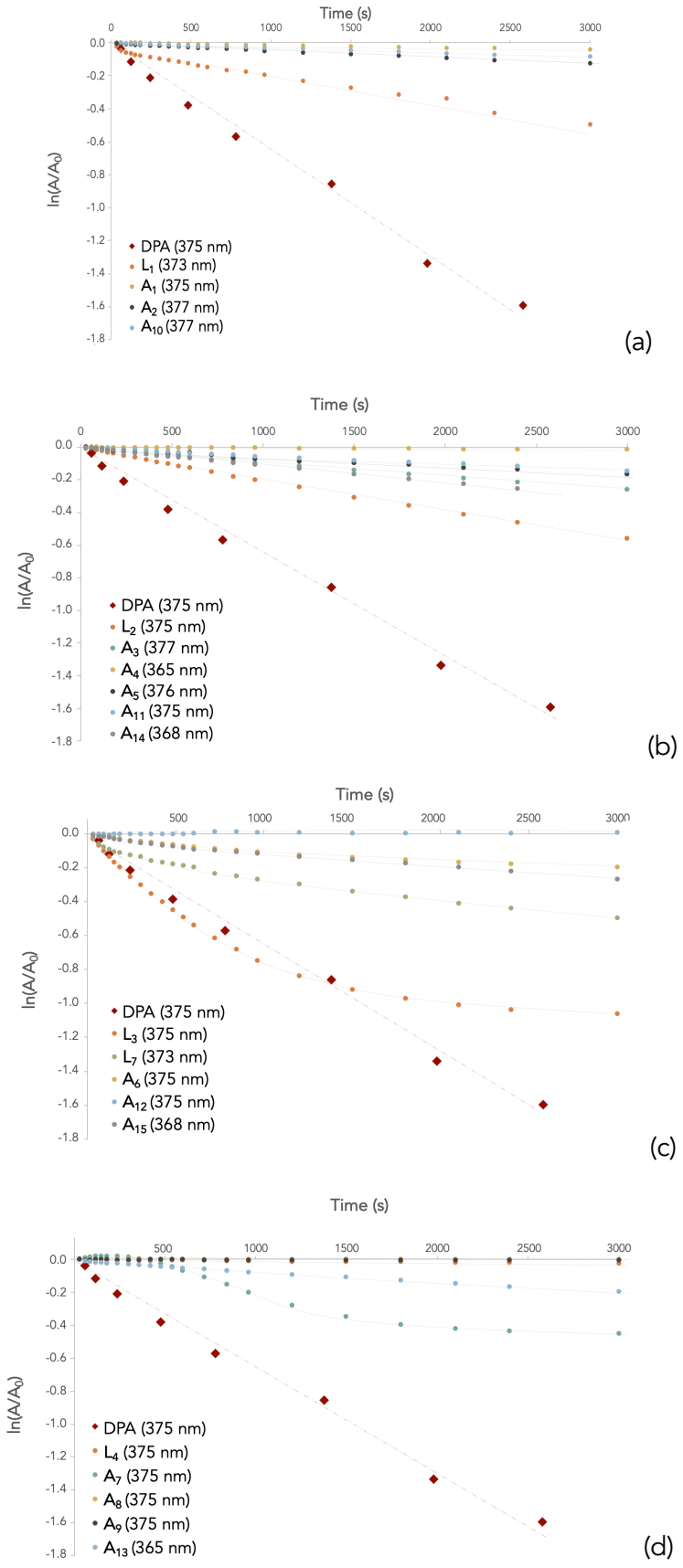

Figure 49: Semi logarithmic plots of the photooxygenation of: (a) **L_1** derivatives, (b) **L_2** derivatives, (c) **L_3** derivatives and (d) **L_4** derivatives.

As shown on figures 48 and 49, not all the curves are linear. This is the case for a majority of molecules derivating from L_3 or L_7 and also for those derived from L_4. Then, their kinetics are different from the postulated simplification and in other words, they did not have a pseudo-first order reaction. For L_{anthr} and A_{anthr} that present a linear curve, the kinetics data are summarized in table 13.

	k' (s^{-1})	k ($x10^6$ $M^{-1}.s^{-1}$)
DPA	6.14×10^{-4}	4.20
L_1	1.50×10^{-4}	1.02
L_2	1.91×10^{-4}	1.31
L_4	8.20×10^{-6}	0.06
L_5	4.47×10^{-5}	0.31
L_6	1.35×10^{-4}	0.92
A_1	1.53×10^{-5}	0.10
A_2	4.07×10^{-5}	0.28
A_3	8.52×10^{-4}	0.58
A_4	5.15×10^{-6}	0.04
A_5	5.65×10^{-5}	0.39
A_{10}	3.37×10^{-5}	0.23
A_{11}	4.78×10^{-5}	0.33
A_{13}	6.37×10^{-5}	0.44
A_{14}	1.08×10^{-4}	0.74
A_{15}	4.78×10^{-5}	0.58

Table 13: Determination for L_{anthr} and A_{anthr} of k' and their corresponding absolute second order rate constant (k) values, based on literature data for DPA.[176]

The absolute second order rate constant values can be determined by using the data in the literature for DPA, which is 4.20 $x10^6$ $M^{-1}.s^{-1}$.[176] The results found for L_1 and L_2 are consistent with the ones obtained by Fudickar and Linker.[174] Nevertheless, to correctly use these results, a particular caution must be made: the chemical deactivation is assumed to be done by L_{anthr} and A_{anthr} and the physical deactivation only by the solvent. Then, from the collected kinetic data and from a general point of view, it appears that all the anthracenyl derivatives are less efficient than DPA, with at least a factor of 3.2. Then, the introduction of ruthenium(II) complexes does not improve the photooxygenation, except for the molecules derived from L_4.

To summarize from these kinetic experiments, some statements can be made:

- There is not a logical sequence for the whole group of studied molecules when

introducing ruthenium(II) precursors;

- The different precursors bring different behaviors of photooxygenation;
- However, for L_1 and L_2 and their derivatives, the difference of isomerization of the pyridyl group almost does not affect the impact of the addition of arene ruthenium units. The efficiency of these species can be summarized by: Ru(oxa) > Ru(donq) > Ru(dobq);
- L_2 is the most powerful derivative, while the corresponding Ru(dobq) A_4 is the least efficient;
- The disubstituted ligand of L_4 is more effective than the corresponding monosubstituted ligand and ruthenium(II) assemblies;
- L_3, L_4 and L_7 have their own kinetics but do not fit with other approximations (order 0,1 or 2);
- Nonetheless, L_3 and L_7 seems to be more reactive than the other L_{anthr}.

Concerning L_4 and its derivatives, this study shows that they have a different behavior than the other species. It is not surprising since the initial ligand L_4 has an uncommon reactivity towards singlet oxygen. From Fudickar and Linker's observations and comparison with different substituted anthracene, alkynyl derivatives react slower with singlet oxygen and in an opposite tendency, are transformed faster in the parent anthracene. To explain this fact, they suggested a change in the mechanistic pathway during the addition of $^1O_2$ on ethynyl anthracene derivatives, and consequently, a change of the kinetics and the feasibility of the reaction.[173] In fact, they explained this hypothesis by combining their observations and the results of their theoretical calculations. In general, a reaction depends on the difference of energy between the HOMO and the LUMO. So, each substituent able to lift the HOMO energy will enhance the reactivity of the anthracene core. However, despite their different abilities to capture $^1O_2$, the aryl and the alkynyl substituents have similar HOMO energies. Then, the idea of a change in the singlet oxygen addition mechanism was mentioned (scheme 12). Usually, a stepwise process is commonly involved. The creation of a zwitterionic intermediate is possible thanks to the stabilization of a positive charge combined with the rotation of the substituent (in the study, the aryl core directly attached to the anthracene). The energy demand is lower for that kind of mechanism, so it is the preferred pathway. However,

when a triple bond is present, the stabilization of the corresponding propargyl anion is not efficient enough and the mechanism is converted into a concerted process, which is energetically unfavorable and then, the reaction is slower.[174]

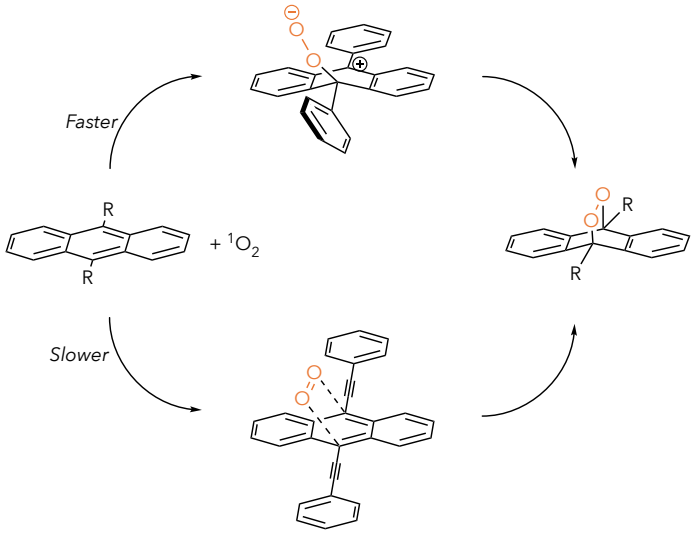

Scheme 12: Proposed mechanisms for the reactivity of different substituted anthracene.[174]

This explanation may fit also with the pyridinyl substituents and can explain why **L_4** is the only one to not undergo a cycloaddition with singlet oxygen. This explanation can be also transposed to all ruthenium(II) assemblies **A_1-A_{15}**. In fact, the presence of ruthenium orders a stiffness of the whole structure, especially when concerning rectangles. The geometrical constraints are important in those kinds of structures and the stabilization of a zwitterionic cation is consequently more difficult. In addition, the smaller reactivity of **A_1-A_{15}** can also be ascribed to the decrease of the electron density on the anthracenyl core after the coordination of the ruthenium atoms to the pyridyl units. The same phenomenon was also recently observed by Stang, in collaboration with Fudickar and Linker, on organoplatinum(II) metallacycles.[131a]

To conclude on the studies of anthracene derivatives, the introduction of arene ruthenium(II) units clearly decreases the ability of the whole structure to capture singlet oxygen, whatever the number of metal atoms or the isomer pattern of the pyridine core, but it is not totally impossible. With the perspective of clinical applications, the low kinetics can become a severe barrier for its use.

3.2. Studies about the trapping of $^1O_2$ by L_{DHP} in solution

3.2.1. General behavior of DHP under irradiation

When a DHP core is irradiated with light, its central C-C bond opens and it provokes several common consequences (scheme 13)[177]:

- A loss of the aromaticity: the planar structure with 14 delocalized π-electrons (DHP) becomes two virtually isolated 6 π-electrons benzoic core in a twisted arrangement (CPD);
- A change of symmetry: the two internal methyl groups, initially pointing in opposite direction on each side of the DHP core, are now in the same plane;
- On UV-VIS spectrum, a progressive disappearance of the absorption bands corresponding to the π-π* transitions and in the meantime, the emergence of a new band in the UV region;
- In ^{1}H NMR spectrum, a global shifting of the aromatic protons and of the two internal methyl;
- The possible appearance of isobestic points on UV-VIS spectra can support the idea of a clean one-step isomerization DHP-CPD process.

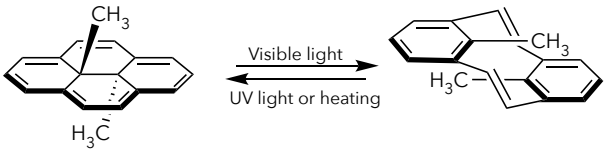

Scheme 13: Isomerization of the DHP core.[177]

With the introduction of pyridyl substituents on DHP core, the electronic and steric environments are different. Then, the initial opening of the central C-C bond and the photooxygenation of the DHP derivatives should be impacted and deserve to be studied. The first section will be dedicated to a surprising and unexpected result with **L_8**, then several experiments on **L_9** and its pyridinium version **L_{10}** were carried out and finally tests were realized on the terpyridinyl DHP derivates **L_{11}** and **L_{12}**.

3.2.2. Studies of the ligand **L_8**

To have a "control-solution", a solution of **L_8** was prepared in acetonitrile (10^{-5} M) and was irradiated with a green light (λ= 510-530 nm). This light was chosen because it corresponds to one of the absorption bands. After 15 hours of irradiation, a diminution of the bands in the visible region was noticed on the UV-VIS spectrum, at the expense of an increase in the UV region (figure 50). After 24 hours, the evolution of the absorption profile stops, suggesting that the transformation is finished. These observations are typical of the opening of the central C-C bond of **L_8**, as explained in the former section.

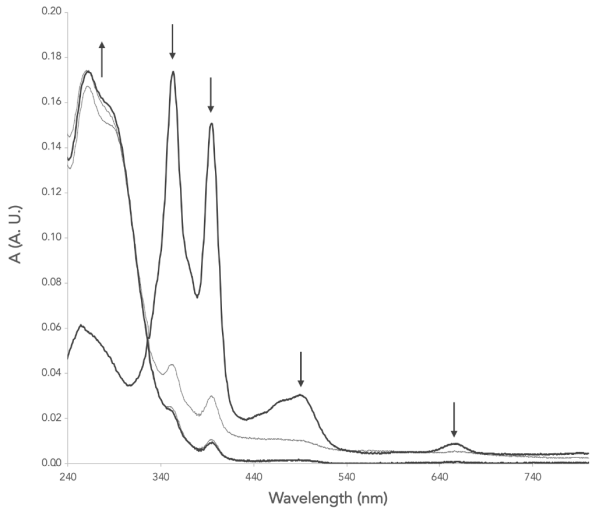

Figure 50: UV-VIS spectra of **L_8** (10^{-5} M in CH_3CN) during irradiation (green light; t = 0 to 39 h).

However, a ^{1}H NMR spectroscopy study of a $CDCl_3$ solution of **L_8** (10^{-3} M) revealed that not only the C-C bond was opened, but also a loss of symmetry has happened as indicated by the presence of new signals (figures 51 and 52). In ^{1}H NMR spectrum post-irradiation (after 15 hours), all the signals of **L_8** were impacted and shifted: (1) each doublet of the pyridyl protons is split into two upfielded doublets (at about 8.65 and 7.43 ppm), (2) the protons for the DHP core are located in a lower part of the aromatic region (around 7.21-6.30 ppm) and are also split into two signals each, (3) the split into two singlet for the protons of *tert*-butyl (at 1.22 and 1.05 ppm) and the internal methyl groups (at 2.10 and 0.03 ppm). The absence of signals corresponding to the initial molecule demonstrates also the total conversion of **L_8** into another form. In 2015, Royal and his team observed similar shifts for the protonated

version of **L_8**, while singled oxygen was trapped.[145] So, the idea of a possible photooxygenation was established and was further confirmed by mass spectrometry. For both solutions (10^{-3} M and 10^{-5} M), a peak with a value *m/z* of 531.9 was found and it corresponds to [**L_8-EPO**+H]$^+$.

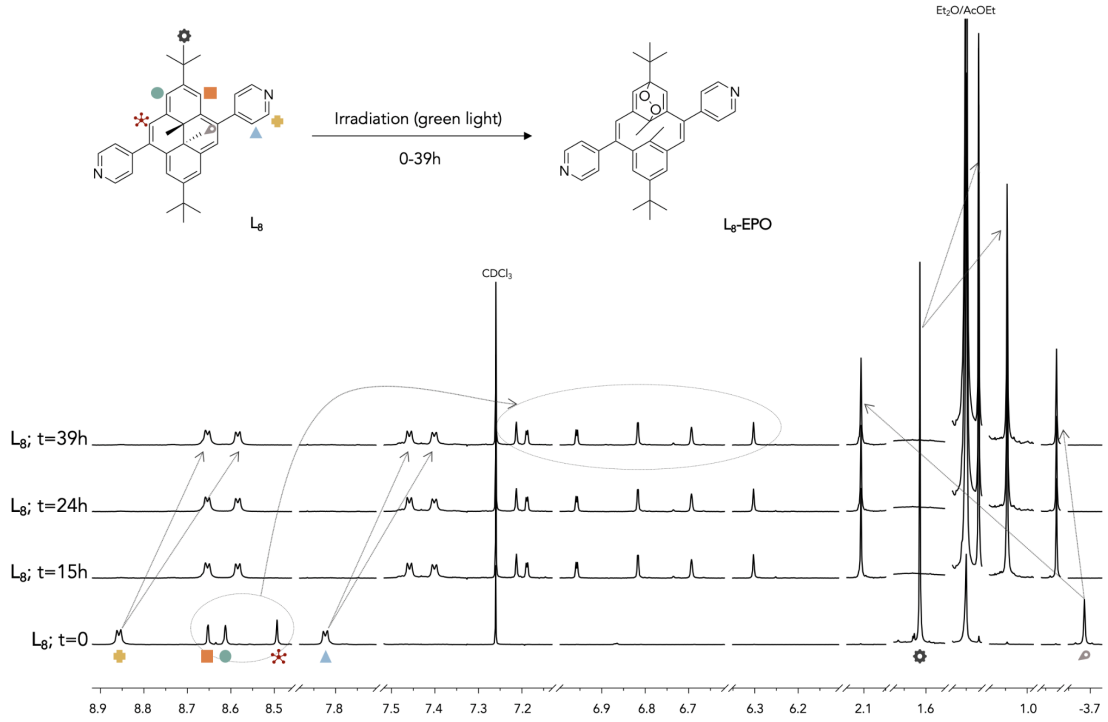

Figure 51: ^{1}H NMR spectra of **L_8**, before and after irradiation ($CDCl_3$, 23 °C, 600 MHz). New signals are present after 15 h of irradiation (green light).

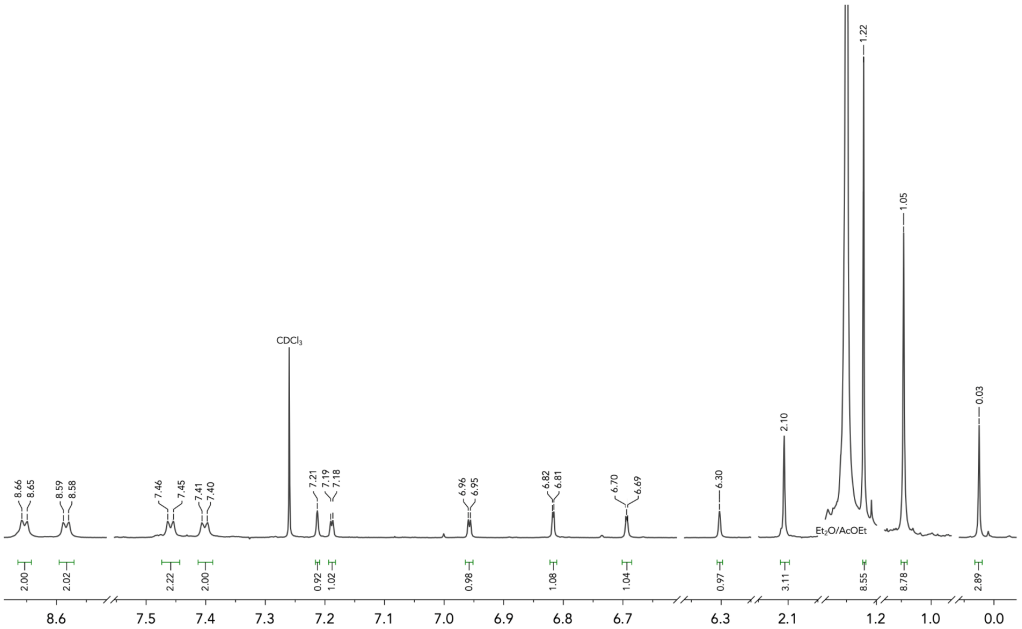

Figure 52: ^{1}H NMR spectrum of **L_8-EPO** ($CDCl_3$, 23 °C, 600 MHz).

Supported by theoretical calculations, Royal and Boggio-Pasqua have proposed a mechanism that can explain the ability of the protonated version of **L8** to capture $^1O_2$.[145,167] Figure 53 describes the steps during its photooxygenation. Upon the irradiation, DHP can reach its first excited state, from where, two routes are possible: (1) its conversion into CPD form or (2) reaching its triplet state by ISC. From the second option, DHP can quench oxygen, resulting in the production of singlet oxygen and the return of DHP in its ground state. The $^1O_2$ produced can in turn react with CPD to give the oxygenated form CPD-EPO.

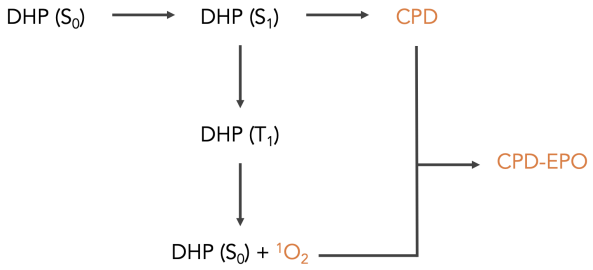

Figure 53: Mechanism of the photooxygenation proposed by Boggio-Pasqua and Royal.[145,167]

In the case of **L8**, without the quaternization of the pyridyl units, this mechanism might be also the one that rules the cycloaddition of singlet oxygen, but most probably with the second excited state S_2. However, the formation of **L8-EPO** was only observed when the irradiation was made with light at a specific wavelength (λ= 510-530 nm). Then, this interval should be the one, specific to **L8**, that permits to pass through the different energetic states and allows the addition of singlet oxygen. Now, **L8** can undoubtedly be considered as an $^1O_2$ trap.

3.2.3. Studies of the ligands L9 and L10

It is known that the ability of a DHP core to capture $^1O_2$ is intimately dependent to the electronic environment around the addition place. The new compounds **L9** and **L10** were synthetized and studied, to firstly, explore the potential of an extended π-system and secondly, to keep track of Royal's work in order to compare the results.

Initially, **L9** was dissolved in acetonitrile under an inert atmosphere in a glovebox. The solution was irradiated with a Xe-Hg lamp with a 469 nm cut-off filter and UV-VIS

measurements were realized during the 24 hours of the irradiation. The resulting decrease of absorption bands in the visible region is only the consequence of the opening of the central C-C bond of **L₉**, since there is no oxygen dissolved in solution (figure 54).

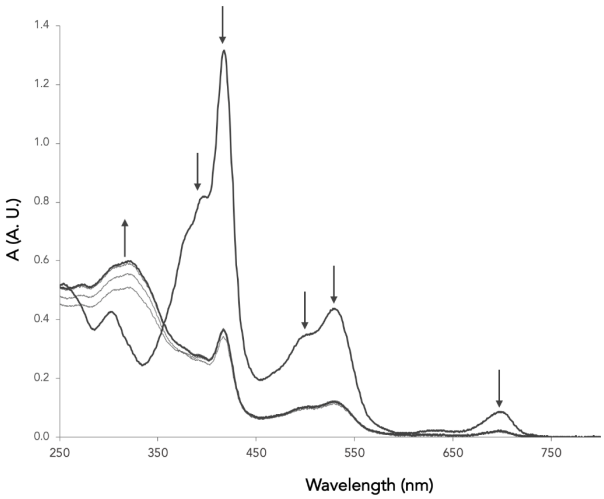

Figure 54: UV-VIS spectra of **L₉** (10^{-5} M in CH_3CN) during irradiation (469 nm; t = 0 to 24 h).

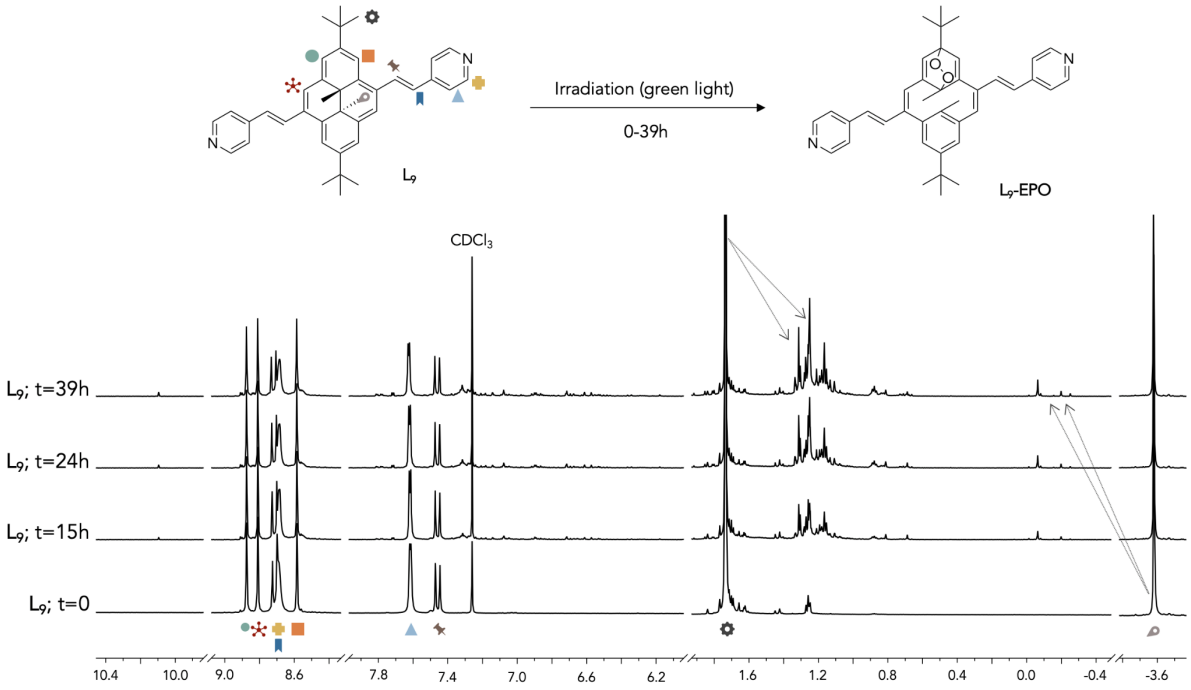

Figure 55: ^1H NMR spectra of **L₉**, before and after irradiation ($CDCl_3$, 23 °C, 600 MHz). New signals are present after 15 h of irradiation (green light).

A similar experiment was performed at a different wavelength (510-530 nm) and with O_2. The result on the UV-VIS spectrum was similar. The irradiation of the $CDCl_3$ solution of **L₉**

was also monitored by ^{1}H NMR spectroscopy (figure 55). New small signals appear from the first measurement after the beginning of the irradiation (15 hours). The sets of new peaks follow the same trend as molecules able to undergo a cycloaddition with $^1O_2$.[145,146] Moreover, the mass spectrum shows the formation of **L_9-EPO**, with a *m/z* peak at 583.9. However, the ^{1}H NMR spectra also show that the conversion of **L_9** into **L_9-EPO**, or even just into the open form of **L_9**, was not complete since the major peaks correspond to the initial molecule.

Later on, the quaternization of nitrogen atoms of the pyridyl group was considered. To obtain **$L_9H_2^{2+}$**, few microliters of methanesulfonic acid (MSA) were added in excess to a solution of **L_9** in acetonitrile. Surprisingly, the red solution turned into a dark green solution from the first drop of MSA. On figure 56, the change of color was observed by a severe bathochromic shift of all the absorption bands, combined with a hyperchromic effect. So, the electronic transitions corresponding to bands on the UV-VIS spectrum have also changed and will have a possible positive impact on the aptitude to produce **$L_9H_2^{2+}$-EPO.** A solution of **$L_9H_2^{2+}$** was irradiated firstly at 715 nm for 18 hours and then, at 555 nm for three additional hours. All the expected trends were visible on the UV-VIS spectra (figure 57), showing here again, the ability of **$L_9H_2^{2+}$** to undergo an opening of its central C-C bond and maybe also the capture of singlet oxygen.

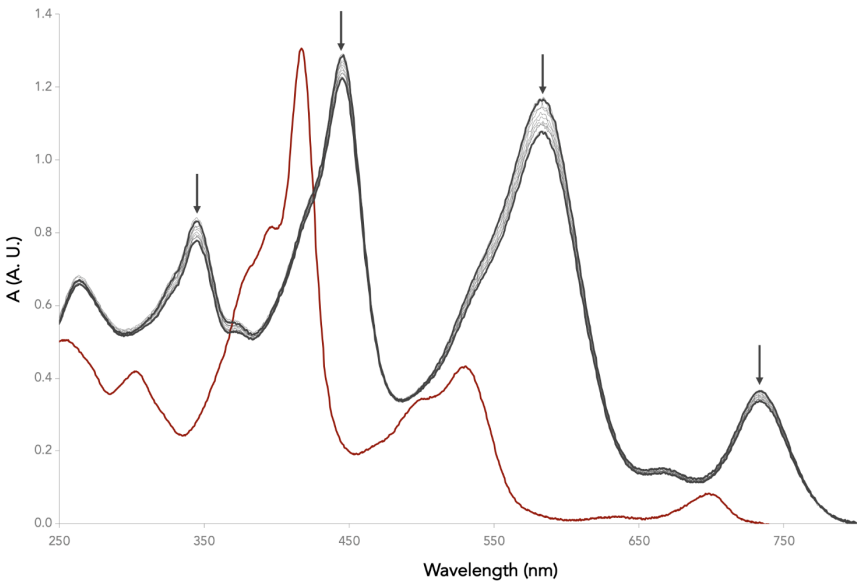

Figure 56: UV-VIS spectra after each addition of 0.25 equivalent of MSA in a solution of **L_9** (10^{-5} M in CH_3CN).

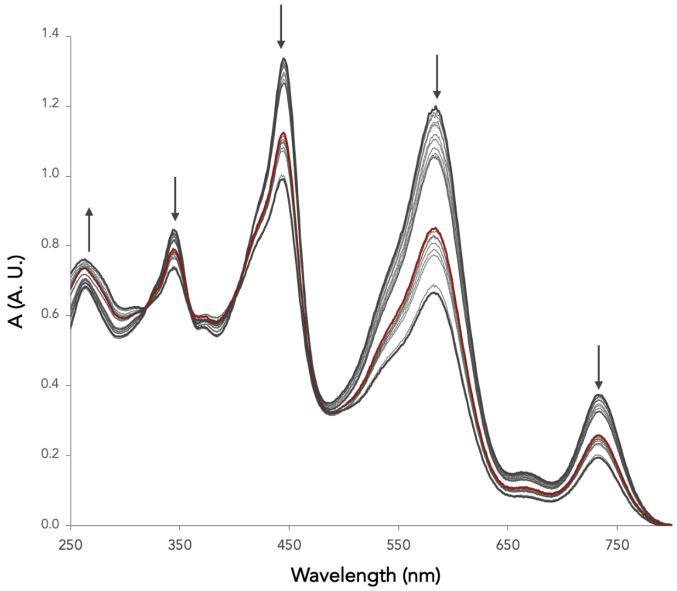

Figure 57: UV-VIS spectra of $\mathbf{L_9H_2^{2+}}$ (10^{-5} M in CH_3CN) during irradiation (715 nm, t = 0 to 18 h; and then 555 nm, t = 0 to 3 h).

To confirm this eventual characteristic of $\mathbf{L_9H_2^{2+}}$, ^{1}H NMR spectra were recorded before and after the irradiation with a Xe-Hg lamp with a 469 nm cut-off filter (figure 58). After irradiation, the spectrum displays new signals, with no remaining traces of the initial $\mathbf{L_9H_2^{2+}}$, suggesting a total conversion into $\mathbf{L_9H_2^{2+}}$**-EPO**. The splitting and the shift of the signals for the internal methyl groups and for the *tert*-butyl units are reliable clues for this hypothesis.

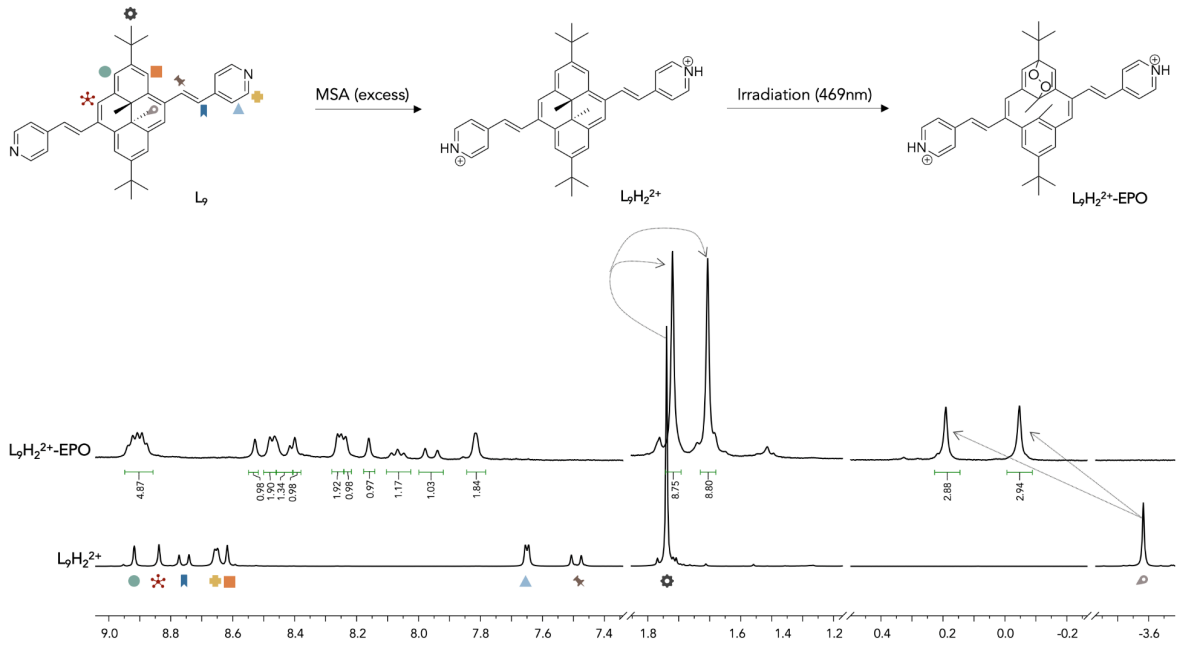

Figure 58: ^{1}H NMR spectra of $\mathbf{L_9H_2^{2+}}$, before and after the irradiation at 715 nm (CD_2Cl_2, 23 °C, 600 MHz).

After the promising results obtained with $\mathbf{L_9H_2^{2+}}$, the photooxygenation of $\mathbf{L_{10}}$ was expected to be as efficient as the protonated form of $\mathbf{L_9}$. The irradiation of an acetonitrile solution of 10^{-5} M was made with an amber light, at 580-600 nm, for more than four days and then with a green light, at 510-530 nm for 39 additional more. As usual, the UV-VIS spectra on figure 59 show the opening of the central C-C bond and eventually the fixing of $^1O_2$ on the DHP core of $\mathbf{L_{10}}$. Concerning the ^{1}H NMR monitoring, the results are not as exciting as expected at first sight (figure 60). The appearance and the splitting of new signals are undoubtedly linked to the capture of singlet oxygen. In fact, the formation of $\mathbf{L_{10}}$-EPO was also confirmed by mass spectrometry, displaying a peak for [($\mathbf{L_{10}}$-EPO/2)-2PF_6^-]$^{2+}$ with a *m/z* value at 307.5. However, the conversion rate is obviously insufficient. Nevertheless, this experiment reveal an interesting characteristic of $\mathbf{L_{10}}$. With the wavelength change (from 580-600 to 510-530 nm), new signals attributed to $\mathbf{L_{10}}$-EPO disappeared progressively and resulted in the signals for the initial $\mathbf{L_{10}}$. So, the application of a green light, a lower energy light than UV, allows the system to reverse and probably release $^1O_2$. Unfortunately, no more experiments were done to prove this statement. To conclude, vinyl-DHP derivatives are really interesting molecules, since the modifications on the nitrogen atom from the pyridyl core change their reactivity towards singlet oxygen. It deserves to be extensively studied in the future.

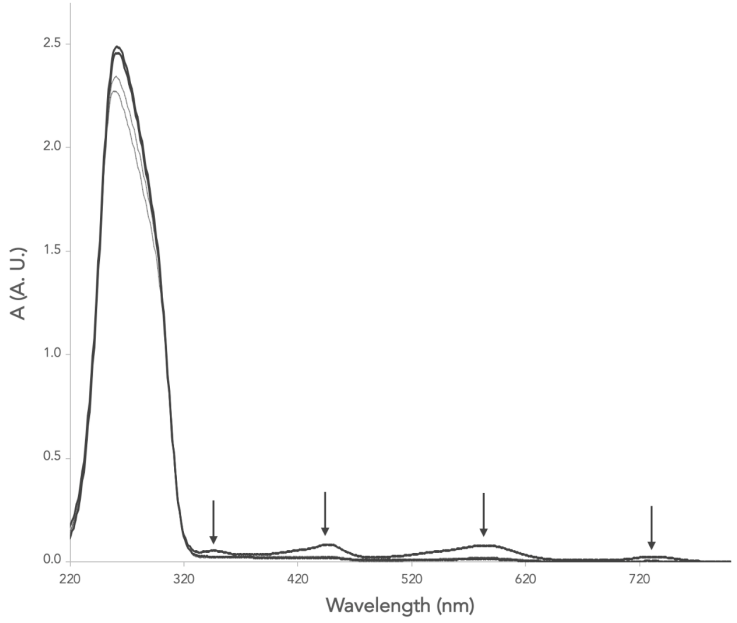

Figure 59: UV-VIS spectra of $\mathbf{L_{10}}$ (10^{-5} M in CH_3CN) during irradiation (amber light; t = 0 to 39 h).

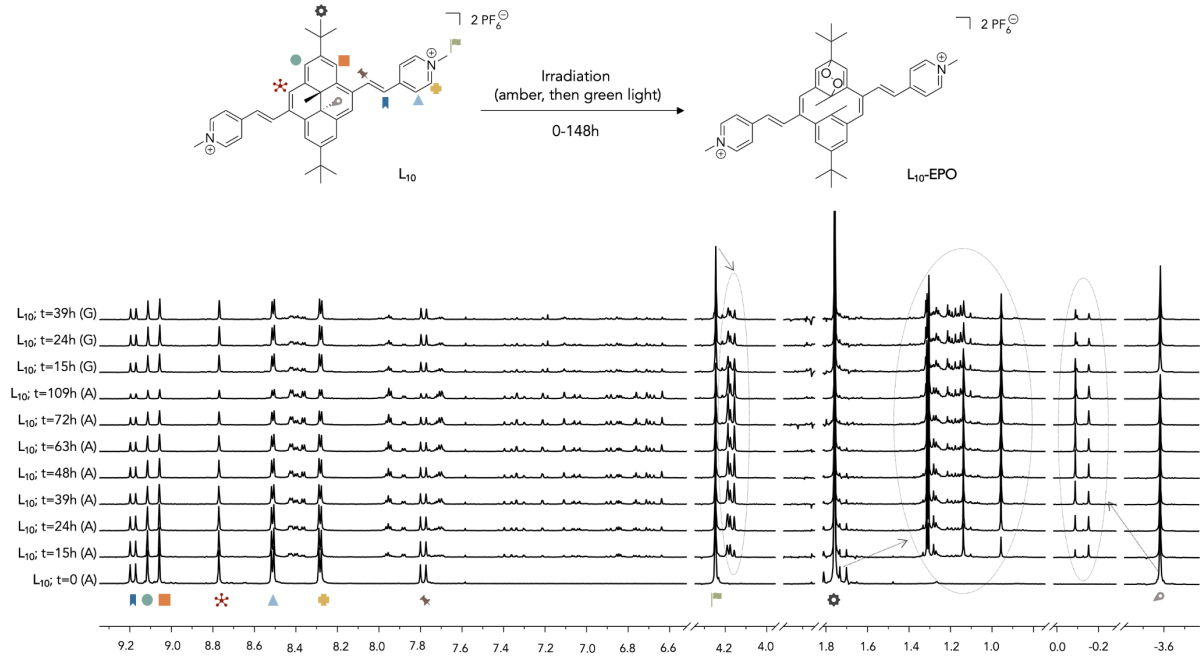

Figure 60: ^{1}H NMR spectra of **L_{10}**, before and after irradiation (CD_3CN, 23 °C, 600 MHz). New signals are present after 15 h of irradiation (amber light). The successive green-light irradiation seems to convert back **L_{10}-EPO** into **L_{10}**.

3.2.4. Studies of the ligands L_{11} and L_{12}

Terpyridyl derivatives of DHP **L_{11}** and **L_{12}** were also tested. The irradiation is efficient only when the employed wavelength corresponds to absorption bands: two types of light were chosen for **L_{11}** and **L_{12}** according to their own UV-VIS spectra. For **L_{11}**, green light (510-530 nm) was used, whereas the amber light (580-600 nm) was employed for **L_{12}**. Solutions of **L_{11}** and **L_{12}** in acetonitrile (10^{-5} M) were then irradiated for 39 hours. They were monitored by UV-VIS spectroscopy (figure 61). As usually observed, the decrease of the absorption bands suggests the opening of the central C-C bond.

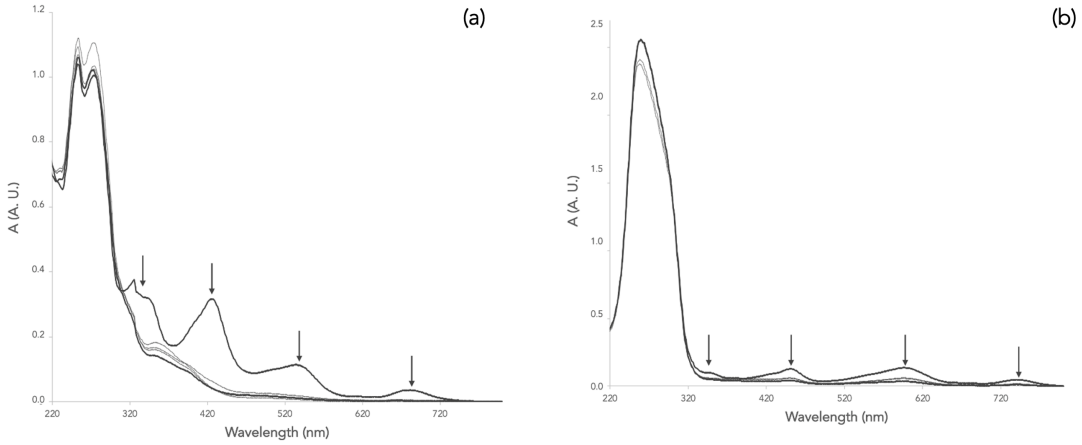

Figure 61: UV-VIS spectra of **L_{11}** (a) and **L_{12}** (b) during irradiation (10^{-5} M in CH_3CN; t = 0 to 39 h).

Here again, ^{1}H NMR spectroscopy was used to monitor the irradiation of **L_{11}** and **L_{12}**. The solutions were prepared in CD_3CN at 10^{-3} M and were irradiated for 39 hours. On one hand, only the color of **L_{11}** changed after 15 hours. In ^{1}H NMR spectrum (figure 62), all peaks are shifted and the ones that can considered as indicators for the photooxygenation of the structure are present. In fact, the internal methyl groups are at -0.04 and -0.06 ppm, and *tert*-butyl groups are at 1.03-1.00 and 1.23-1.21 ppm. In addition, all the peaks seem to be split in two sets, due to the loss of symmetry. The formation of **L_{11}-EPO** was also proven by mass spectrometry: a *m/z* peak 585.1 was observed, corresponding to $[(\mathbf{L_{11}\text{-EPO}}/2)\text{-}2PF_6^-]^{2+}$. So, **$L_{11}$** can react with $^1O_2$ but **L_{11}-EPO** is not stable at room temperature. After one night of non-irradiation, the color of the solution in the NMR tube changed. ^{1}H NMR spectra were then recorded to follow the back reaction and in two days, **L_{11}** was totally recovered and without any traces of **L_{11}-EPO**. This characteristic could be an important drawback for its use, depending on the conditions of its application.

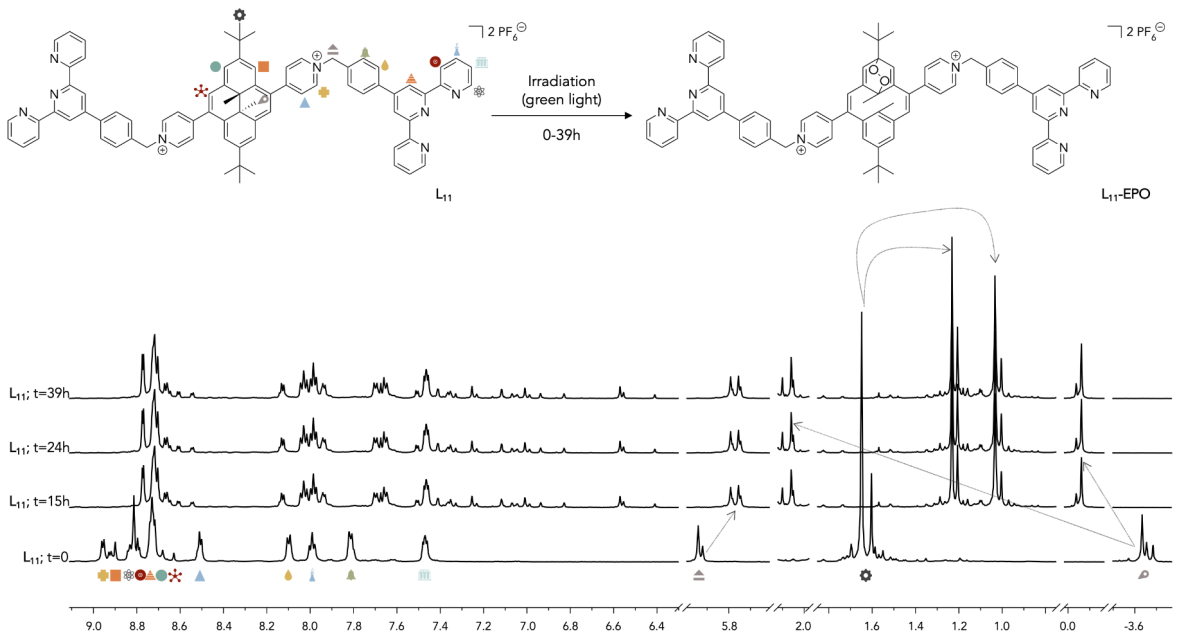

Figure 62: ^{1}H NMR spectra of **L_{11}**, before and after irradiation (CD_3CN, 23 °C, 600 MHz). New signals are present after 15 h of irradiation (green light).

On the other hand, the results are less enthusiastic for **L_{12}**. There is not a real conversion of **L_{12}** into **L_{12}-EPO**. Only small signals appear in the expected regions of the ^{1}H NMR spectrum (figure 63). Even the mass spectrum does not display a proof of its formation. Then, the quaternization of the nitrogen atoms plays a central role in the ability and in the efficiency of

the vinyl-pyridine derivatives of DHP to undergo its transformation into CPD and CPD-EPO forms.

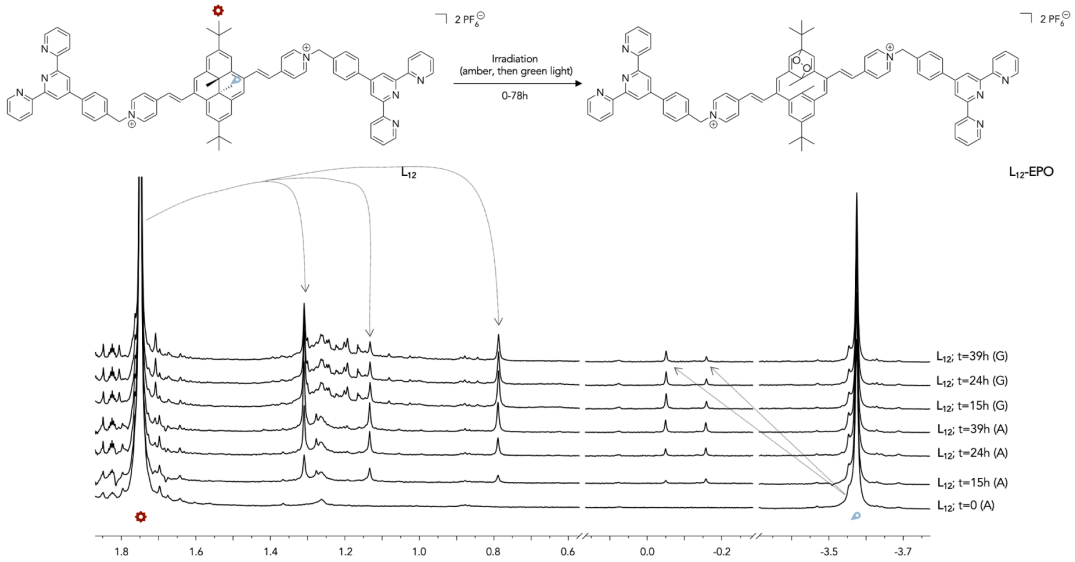

Figure 63: ^{1}H NMR spectra of **L_{12}**, before and after irradiation (CD_3CN, 23 °C, 600 MHz). New signals are present after 15 h of irradiation (amber light, succeeded by a green light).

To sum up, only some **L_{DHP}** derivatives are good candidates to be considered as oxygen carriers. Only the photooxygenation of **L_8**, **$L_9H_2^{2+}$** and **L_{11}** seems to be adequate for the purpose of PDT. In fact, the formation of their endoperoxide forms were confirmed but the light irradiation was not the best in terms of biological context (too high in energy to cross the different layers of the skin). Efforts are still needed on the tuning of the light and the substitution on the DHP core to obtain appealing structures for PDT.

3.3. Biological studies on cancer cells with anthracene derivatives

The photocytoxiciy of **L_{anthr}** and **A_{anthr}** were also determined by performing MTT assays (MTT = 3-(4,5-dimethylthiazol-2-yl)-2,5-diphenyltetrazoliumbromide). All experiments were carried out by my colleague, Manuel Ángel Gallardo Villagrán, in the laboratory of Pr. Bertrand Liagre at the University of Limoges (France). DU145 prostatic cancer cells were plated in 96-well plates (7000 cells/100 µL per well). They were incubated in the dark and the temperature was maintained at 37 °C. After 24 hours of incubation, 100 µL medium with different concentrations of **L_{anthr}** or **A_{anthr}** (10, 100, 250, 500, 750 and 1000 nM), sometimes

mixed with TPP (1/5 of concentrations of the anthracenyl derivatives), were added and maintained with the cells for 24 additional hours. Then, after the change of medium, cells were irradiated at 630 nm (40 mW/cm^2) for 30 minutes. Cell survival was tested by MTT assay 24 hours after irradiation, using 10 µL of MTT per well. After four hours, the medium was removed and 200 µL of DMSO were added.

Dark and phototoxicity were tested, with and without TPP for both. The results are presented in figure 64. In addition, from MTT assays results, IC50 were calculated and the phototoxic index (PI) was estimated (table 14). PI is the ratio of the IC_{50} in the dark to the IC_{50} upon light irradiation: the higher is PI, the higher is the phototoxicity; in other words, the irradiation was efficient and has a real impact on cell viability. From these studies, some observations can be made:

- Generally, the addition of TPP does not have an impact on the toxicity provoked by the compounds;
- For the majority of the compounds, there is not an important phototoxicity observed, since PI is close to 1. However, some exceptions can be made;
- A_5: a phototoxicity is observed at 500 nM (TPP and irradiation), with a percentage of surviving cells at 50%, while about 100% are noticed under other conditions;
- A_8 and A_{10}: there is a clearer difference between the dark and light conditions. A phototoxicity was then observed.
- A_7: The use of TPP has only a real impact on the toxicity;

L_1-L_4: they showed a relative toxicity, with similar values of cell viability.

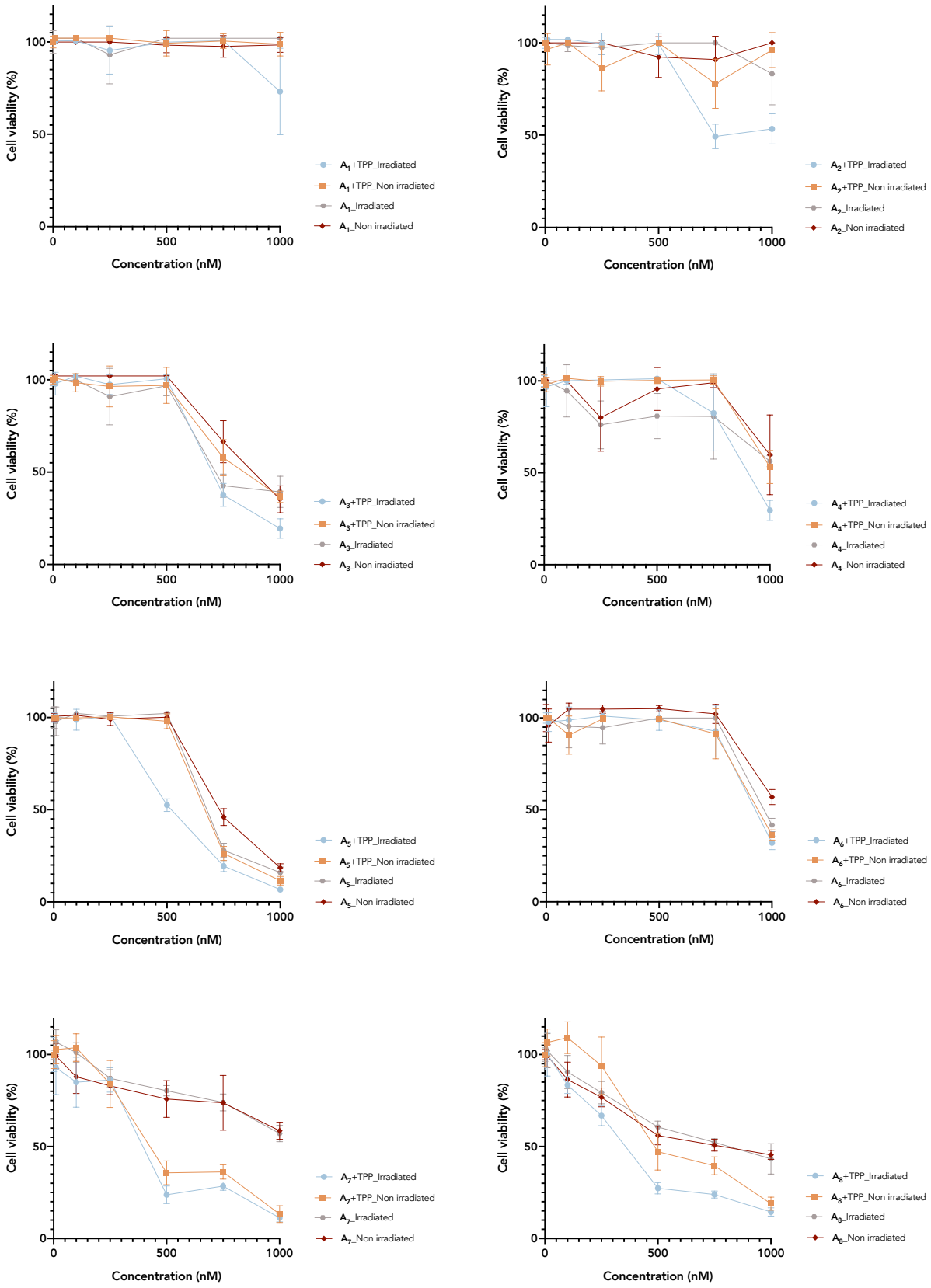

Figure 64 (Part A)*:* MTT assays and determination of dark and phototoxicity of **L_{anthr}** and **$A_{anthr.}$**

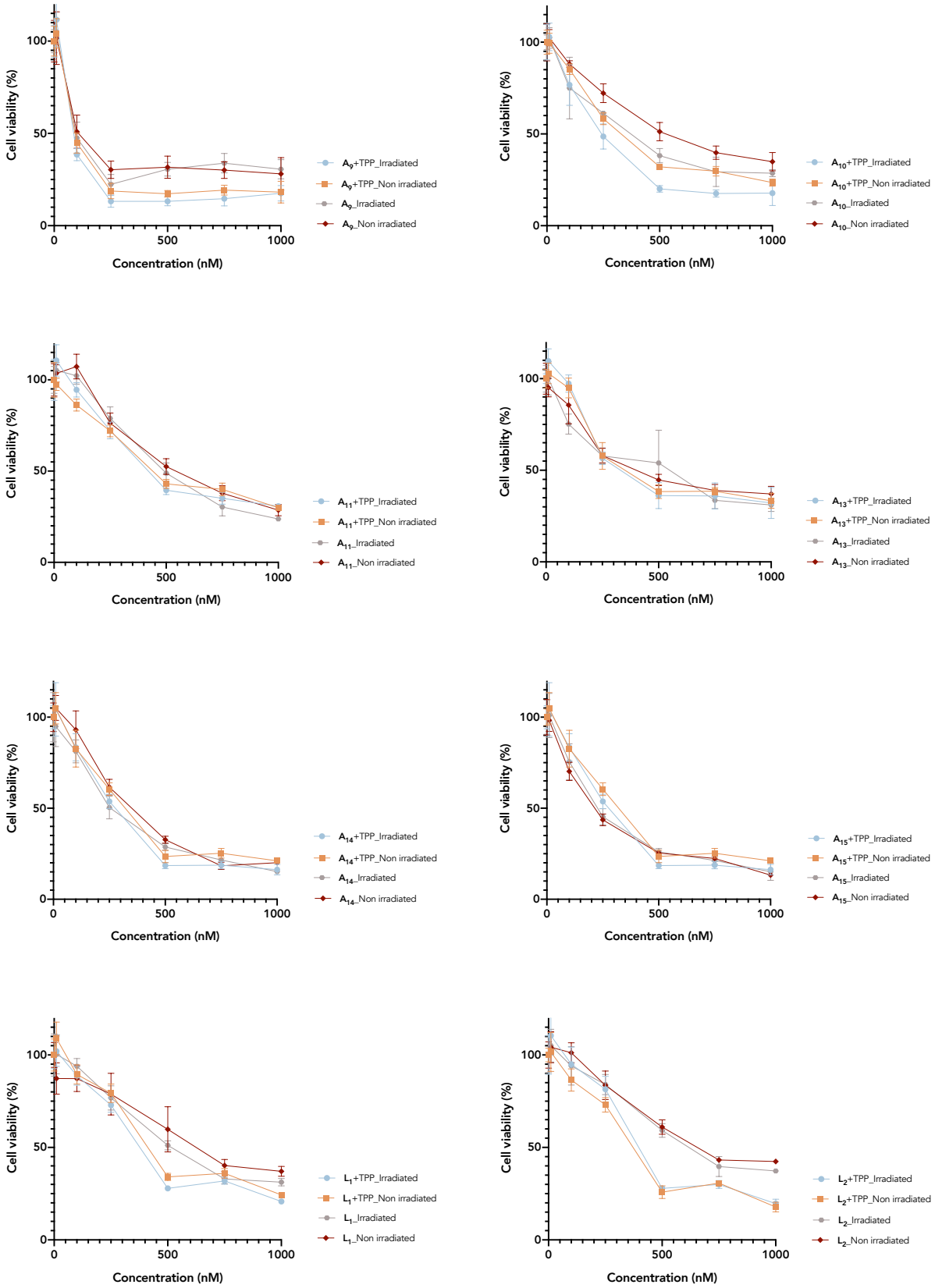

Figure 65 (Part B)*:* MTT assays and determination of dark and phototoxicity of **L_{anthr}** and **$A_{anthr.}$**

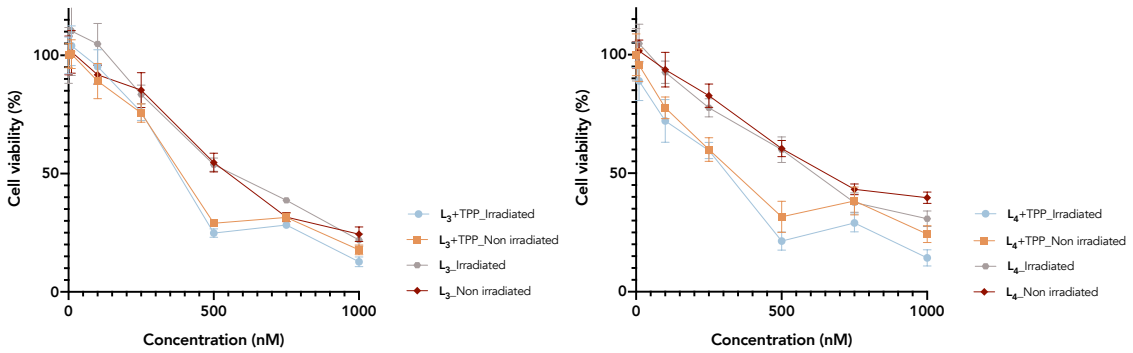

Figure 66 (Part C)*:* MTT assays and determination of dark and phototoxicity of **L_{anthr}** and **$A_{anthr.}$**

	Product alone		Product with TPP		Phototoxic index	
	non irradiated	*irradiated*	*non irradiated*	*irradiated*	*without TPP*	*with TPP*
TPP	-	-	1993 ± 333	853.5 ± 84	-	2.3
L_1	630.4 ± 96	525.9 ± 38	450.4 ± 48	387.2 ± 37	1.2	1.2
L_2	705.9 ± 61	643.5 ± 56	370.5 ± 40	420.0 ± 47	1.1	0.9
L_3	544.0 ± 33	563.3 ± 56	396.2 ± 36	382.5 ±33	1.0	1.0
L_4	681.9 ± 44	586.3 ± 41	336.3 ± 43	254.7 ± 44	1.2	1.3
A_1	n.d.	n.d.	n.d.	n.d.	n.d.	n.d.
A_2	n.d.	n.d.	n.d.	929.9 ± 99	n.d.	n.d.
A_3	878.7 ± 29	800.9 ± 65	851.2 ± 43	722.0 ± 25	1.1	1.2
A_4	1028.0 ± 145	n.d.	n.d.	902.3 ± 33	n.d.	n.d.
A_5	750.4 ± 16	690.8 ± 22	679.5 ± 16	521.9 ± 13	1,1	1.3
A_6	n.d.	n.d.	946.5 ± 25	936.8 ± 24	n.d.	1.0
A_7	2106.0 ± 1769	1325.0 ± 261	466.4 ± 47	402.5 ± 54	1.6	1.2
A_8	766.3 ± 96	784.2 ± 97	557.3 ± 58	330.2 ± 31	1.0	1.7
A_9	152.5 ± 46	138.5 ± 49	97.6 ± 21	83.4 ± 21	1.1	1.2
A_{10}	547.3 ± 37	345.4 ± 50	336.7 ± 23	233.5 ± 28	1.6	1.4
A_{11}	556.0 ± 45	504.0 ± 31	480.8 ± 30	468.5 ± 48	1.1	1.0
A_{13}	452.0 ± 56	414.5 ± 77	431.3 ± 57	411.2 ± 65	1.1	1.0
A_{14}	343.0 ± 28	266.2 ± 25	305.3 ± 35	263.5 ± 30	1.3	1.2
A_{15}	207.7 ± 15	231.5 ± 27	305.3 ± 35	263.5 ± 30	0.9	1.2

Table 14: IC_{50} (in nM) and phototoxic index values of TPP, **L_1-L_4** and **A_1-A_{15}**. Values calculated with the data of MTT assays on DU145 prostatic cancer cells. "n.d", for values non determined; "-", for conditions non tested. Data obtained with the software GraphPad.

To conclude, the results of MTT assays are not showing a real phototoxicity of the tested anthracenyl derivatives **L_{anthr}** and **A_{anthr}** on DU145 prostatic cancer cells. These results were expected since their studies in solution did not show an efficient photooxygenation. However, a remark must be made: the wavelength used for these biological tests was not the same as the one employed for the studies in solution. Then, a lack of energy is conceivable and the transfer of energy may be not possible to provoke the toxicity on cancerous cells.

4. Conclusions and perspectives

The work presented in this thesis was realized in the context of a biological application, photodynamic therapy. The lack of oxygen in most cancers is one of the main reason why the efficiency of treatments is limited. Therefore, our attention has focused on the design and the study of new molecules, and among them new arene ruthenium(II) complexes that can transport oxygen into cancer cells. To reach our goal, dinuclear ruthenium(II) clips were attached to oxygen carrier(s), such as derivatives of anthracene (anthr) or dimethyldihydropyrene (DHP). Seven $\mathbf{L_{anthr}}$ ligands, five $\mathbf{L_{DHP}}$ ligands and 16 ruthenium(II) complexes, divided in to fifteen $\mathbf{A_{anthr}}$ and one $\mathbf{A_{DHP}}$ derivatives, were synthesized and fully characterized by common analytic methods (chapter II). To determine their ability to capture singlet oxygen, most compounds were irradiated in solution and monitored by UV-VIS and ^{1}H NMR spectroscopic methods and mass spectrometry (chapter III). Both ligands and ruthenium(II) assemblies with anthracene core were also evaluated *in vitro* on DU145 prostatic cancer cells to determine their cytotoxicity and phototoxicity (chapter III).

The coordination of ruthenium atoms to $\mathbf{L_{anthr}}$ generally prevents the molecules to perform a [2+4] cycloaddition with singlet oxygen. It was also noticed that isomerization of the pyridine has a limited impact on the efficiency of the photooxygenation. After optimization of the experiments with the already known anthracenyl derivatives $\mathbf{L_1}$-$\mathbf{L_5}$, all experiments showed that the photooxygenation of the majority of $\mathbf{A_{anthr}}$ assemblies can occur (confirmed by ^{1}H NMR and mass analyses) but with a low conversion. However, some ruthenium(II) complexes emerged unscathed. Three ruthenium(II) rectangles, composed by a vinyl-pyridinyl anthracene derivative ($\mathbf{A_6}$) as well as $\mathbf{A_7}$ and $\mathbf{A_8}$, composed by an ethynyl-pyridyl anthracene derivative and one dinuclear ruthenium(II) assembly ($\mathbf{A_{10}}$), display interesting features and deserve further attention in the future. In fact, some observations allow us to conclude that these compounds: (1) have different kinetics than the other structures; (2) mass

analysis confirmed the formation of **A_6-EPO** after irradiation of **A_6** with normal light and without photosensitizer; (3) **A_8** and **A_{10}** seem to be the only ruthenium(II) assemblies tested on cancer cells that provoke a small degree of phototoxicity, since the percentage of viable cells are noticeably reduced compared with the one under dark conditions; (4) The use of TPP is not necessary to obtain a toxicity on cancer cells with **A_7**.

Furthermore, it seems promising to consider the synthesis of other assemblies that involve arene ruthenium(II) and anthracenyl derivatives but not directly linked together (figure 65). An ideal strategy can be to introduce an alkyl chain in order to isolate the singlet oxygen probe from the metal. Therefore, the coordination to ruthenium atoms will have a smaller impact on: (1) the electronic density around the reactive center of the anthracenyl core; and (2) the stiffness of the structure, which can be a reason for the low reactivity of **A_{anthr}**. Introducing a relative flexibility in the molecule can enhance the photooxygenation and the phototoxicity. Some examples of structures bearing a remote anthracenyl core have showed a certain ability to produce singlet oxygen and ROS (figure 66).[178]

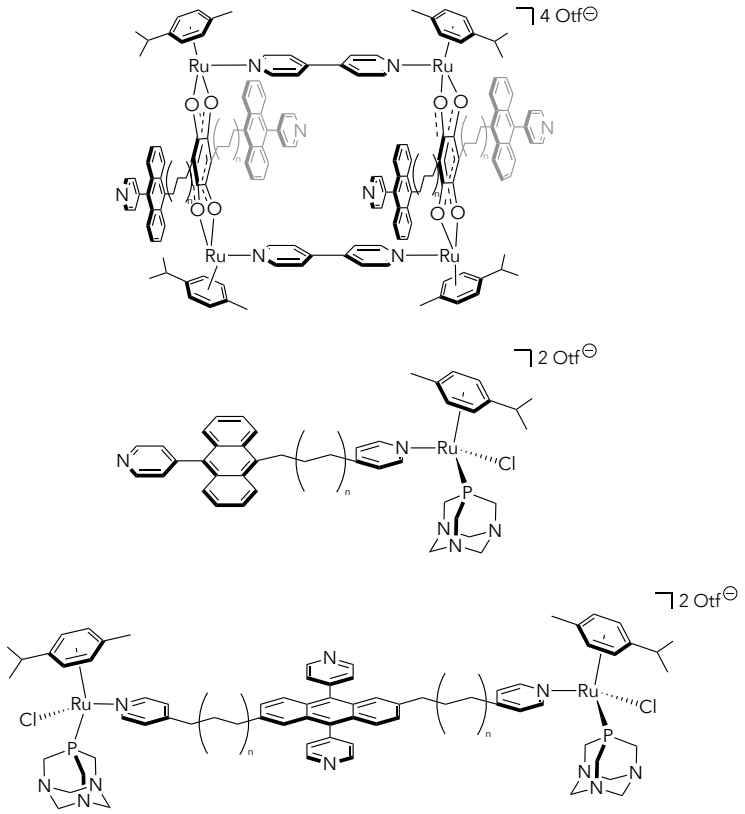

Figure 65: Possible structures with arene ruthenium(II) to consider in future projects (n≥0).

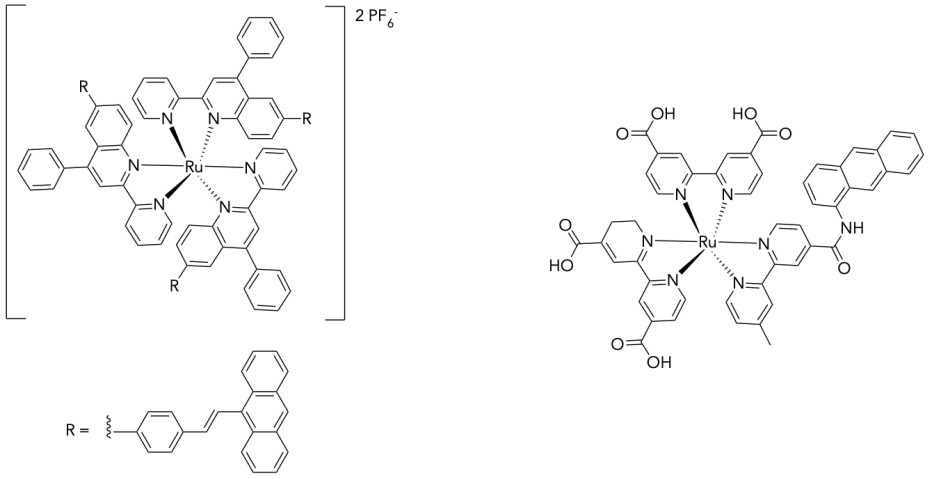

Figure 66: Structures from the literature that can generate singlet oxygen.[179]

The tuning of the irradiation may be also a key to obtain a better response of phototoxicity on cancer cells, since the wavelength applied was low in energy, and can decrease the efficiency of the tested molecules.

Concerning the derivatives of DHP, only the ligands were studied to determine their ability to produce **L_{DHP}-EPO**. Our observations led to the conclusions that the addition of a new unit on the nitrogen, to provoke its quaternization, changes the ability of the DHP core to act as a photosensitizer. In fact, when there is a double bond between the DHP unit and the pyridinyl group, **$L_9H_2^{2+}$** and **L_{11}**, the transformation into **$L_9H_2^{2+}$-EPO** and **L_{11}-EPO** was easier, unlike **L_{10}** that remains unreactive. Surprisingly, the structure without a pyridinium core **L_8** underwent a cycloaddition with $^1O_2$ and various analyses demonstrated the formation of **L_8-EPO**. A reverse reaction was also observed when **L_8-EPO** was irradiated with a green light (510-530 nm). So, from this study, the ionization of the structure of DHP is not always required to obtain the capture and the release of singlet oxygen.

In the future, tests should be performed with **L_{DHP}** linked to arene ruthenium(II) units. The addition of terpyridine units was tested in order to introduce the quaternization of the nitrogen atoms and to get three coordination sites. However, the results were disappointing: possibly because of the arene ruthenium geometry, that is not compatible with the terpyridine units. Furthermore, to gain coordination flexibility, the same strategy could be employed by replacing the terpyridinyl unit by a bipyridine. A general structure is depicted in figure 67.

Finally, after the synthesis and the characterization of these new arene ruthenium(II) complexes $\mathbf{A_{DHP}}$, biological tests should be perfomed in order to determine the ability of DHP to generate phototoxicity in cancer cells.

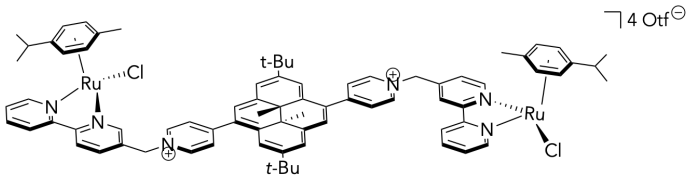

Figure67: A strategy to coordinate arene ruthenium to $\mathbf{L_{DHP}}$.

For our lab, this work was a first step of the study of arene ruthenium(II) complexes used as oxygen carriers with the perspective of PDT applications. Even though the introduction of ruthenium atoms can constitue a barrier to the efficiency of the trapping of $^1O_2$, next studies should take into account the results of this work and slowly steer towards the synthesis of structures that can transport both the PS and $^1O_2$ into hypoxic cancerous areas.

5. Experimental part

General remarks

All commercially available chemicals and solvents were purchased from Sigma-Aldrich, Brunschwig, TCI Europe and/or Fisher Scientific. Chemicals were used as received, without further purification. All solvents were dried before use on silica, molecular sieve or by distillation. All reactions were performed under an inert N_2 atmosphere (unless specified otherwise). Thin layer chromatography (TLC) plates were purchased from Merck and the products were visualized with UV light (254 or 365 nm). Purifications by column chromatography were realized on silica gel 60 Å (32-63 Mesh) and technical solvents were used for elution. Removal of solvents was performed on a rotary evaporator at 40 °C and under reduced pressure. Final products were dried under high vacuum (around 10^{-3} mbar) at room temperature.

NMR spectra were recorded on a Bruker Avance II 400 Spectrometer or on a Bruker Avance Neo Ascend 600 MHz (Karlsruhe, Germany), using deuterated solvents as internal standard. The chemical shifts are referenced to deuterated solvent residual peaks [$CDCl_3$: δ = 7.26 ppm; CD_2Cl_2: δ = 5.32 ppm; CD_3OD δ =3.31 ppm; $(CD_3)_2CO$: δ = 2.05 ppm; and $(CD_3)CN$: δ = 1.94 ppm]. ^1H signals are assigned as s for singlet, d for doublet, t for triplet, sept for septet and m for multiplet. UV−Visible absorption spectra were recorded with a PerkinElmer Lambda 25 spectrophotometer (Waltham, Massachusetts, USA) using quartz cells having an optical path length of 1 cm. IR spectra were recorded with a Thermoscientific Nicolet iS5 spectrometer (Waltham, Massachusetts, USA). Signals were defined as s for strong, m for medium and w for weak. Electrospray ionization mass spectrometry (ESI-MS) spectra were obtained in a positive mode with a LCQ Finnigan mass spectrometer (San Jose, California, USA) at the University of Fribourg (Switzerland) under the supervision of Dr. Freddy Nydegger

and Dr. Albert Ruggi. ESI-MS spectra were also recorded with a 4000 QTrap mass spectrometer at the University of Neuchâtel, under the supervision of Dr. Armelle Vallat-Michel. Ruthenium(II) assemblies were studied by mass spectroscopy at the University of Berlin (Germany), under the supervision of Pr. Christoph Schalley. ESI-MS were recorded on a Synapt G2-S HDMS (Waters Co., Milford, Massachusetts, USA). Typical tunings were: capillary voltage of 2.5-3 kV; source temperature of 80-100 °C, sampling cone voltage of 10-20 V, source offset of 10-20 V; desolvation gas temperature 180 °C. Microanalyzes were carried out by the Mikroelementaranalytisches Laboratorium, ETH Zürich (Zürich, Switzerland). Irradiation studies were performed using a Luzchem LZC-ORG photometer (Montreal, QC, Canada) equipped with the corresponding lamp (cool white lamp, Hg, 8 W, Sylvania® F8T5/CW), Green LED (LZC-LGR, centered at 510-530 nm, 8W) or Amber LED (LZC-LAM, centered at 580-600 nm, 8W).

Precursors molecules were prepared according to published methods: 4,9-dibromo-2,7-di-*tert*-butyl-*trans*-10b,10c-dimethyl-10b,10c-dihydropyrene[164], 4′-(4-(bromomethyl) phenyl)-2,2′:6′,2″-terpyridine[165], $[Ru_2(\eta^6\text{-}p\text{-cymene})_2(\mu^4\text{-oxa})Cl_2]$[150], $[Ru_2(\eta^6\text{-}p\text{-cymene})_2(\mu^4\text{-dobq})Cl_2]$[151], $[Ru_2(\eta^6\text{-}p\text{-cymene})_2(\mu^4\text{-donq})Cl_2]$[152], $[Ru(\eta^6\text{-}p\text{-cymene})(pta)Cl_2]$[153] and $[\{(\eta^6\text{-}p\text{-cymene})Ru(\mu^2\text{-Cl})Cl\}_2]$[154].

Synthesis and characterization

General procedure for 9,10-bis(pyridyl)anthracene (**L_1** and **L_2**) [143,156,157]

9,10-Dibromoanthracene (1.00 g, 2.98 mmol), 4-pyridylboronic acid (914 mg, 7.44 mmol, for **L_1**) or 3-pyridylboronic acid (914 mg, 7.44 mmol, for **L_2**), potassium carbonate (4.11 g, 20 mmol) and tetrakis(triphenylphosphine) palladium(0) (344 mg, 0.29 mmol) were dissolved in DMF (80 mL) and H_2O (10 mL). Three cycles of freeze pumping were realized. After stirring 12 h at 105 °C, the solvents were removed under vacuum. The residue was dissolved in $CHCl_3$ and then extracted with the same solvent. The organic layer was twice washed with H_2O. Hydrochloric acid (1 M) was slowly added until the aqueous pH reached 1: the phase got a yellow color, and the organic phase was discarded. Then, potassium hydroxide (1 M) was

slowly added until the aqueous pH reached 8. The product was isolated by another extraction using $CHCl_3$. The evaporation of the solvent, after drying the organic phase over dried $MgSO_4$, gave the desired product. When needed, a column chromatography (silica gel; EtOAc) was realized for further purification.

9,10-bis(4-pyridyl)anthracene (L_1) pale-yellow solid (633 mg; 64%). ^{1}H-NMR ($CDCl_3$, 400 MHz). δ 8.89 (dd, *J* = 4.4 Hz and *J* = 1.6 Hz , 4H, H_a), 7.62 (dd, *J* = 6.8 Hz and *J* = 3.2 Hz, 4H, H_f), 7.45 (dd, *J* = 4.4 Hz and *J* = 1.6 Hz , 4H, H_b), 7.40 (dd, *J* = 6.8 Hz and *J* = 3.2 Hz, 4H, H_d).^{13}C{^{1}H}-NMR ($CDCl_3$, 100 MHz). δ 150.3 (4C, C_a), 147.5 (2C, C_c), 134.9 (2C, C_d), 129.2 (4C, C_e), 126.6 (4C, C_f), 126.5 (4C, C_b), 126.1 (4C, C_g).

9,10-bis(3-pyridyl)anthracene (L_2) pale-yellow solid (742 mg; 75%). ^{1}H-NMR ($CDCl_3$, 400 MHz). δ 8.84 (dd, *J* = 4.8 Hz and *J* = 1.6 Hz, 2H, H_b), 8.75 (dd, *J* = 4.8 Hz and *J* = 2.4 Hz, 2H, H_a), 7.84 (m, 2H, H_d), 7.64 (dd, *J* = 6.8 Hz and *J* = 3.6 Hz, 4H, H_h), 7.59 (m, 2H, H_c), 7.40 (dd, *J* = 8.0 Hz and *J* = 3.2 Hz, 4H, H_i). ^{13}C{^{1}H}-NMR ($CDCl_3$, 100 MHz). δ 152.0 (1C, C_a), 151.9 (1C, C_a), 149.3 (2C, C_b), 139.0 (1C, C_d), 138.9 (1C, C_d), 134.8 (2C, C_e), 133.9 (2C, C_f), 130.3 (2C, C_g), 126,6 (4C, C_h), 126.0 (4C, C_i), 123.6 (1C, C_c), 123.6 (1C, C_c).

Procedure for 9,10-bis((pyridin-4-yl)vinyl)anthracene (L_3) [158]

9,10-Dibromoanthracene (1.00 g, 2.98 mmol), 4-vinylpyridine (625 mg, 5.94 mmol), palladium(II)acetate (67 mg, 0.30 mmol), triphenylphosphine (156 mg, 0.60 mmol) and triethylamine (600 mg, 5.93 mmol) were dissolved in dried DMF (20 mL). Nitrogen was bubbled through the solution in a Schlenk flask for 20 min. After stirring 24 h at 115 °C, the solution was poured into H_2O. The product was extracted several times with CH_2Cl_2 and the combined organic phases were washed with brine, dried over $MgSO_4$ and concentrated by rotary evaporator. The crude product was purified by column chromatography (silica gel; hexane/EtOAc = 4/1). The pure product was obtained as a yellow solid (229 mg; 27%). ^{1}H-NMR ($CDCl_3$, 400 MHz). δ 8.70 (m, 4H, H_a), 8.33 (dd, *J* = 6.8 Hz and *J* = 3.2 Hz, 4H, H_h), 8.17 (d, *J* = 16.4 Hz, 2H, H_e), 7.56 (m, 4H, H_b), 7.52 (dd, *J* = 6.8 Hz and *J* = 3.2 Hz, 2H, H_i), 6.91 (d, *J* = 16.4 Hz, 2H, H_j). ^{13}C{^{1}H}-NMR ($CDCl_3$, 100 MHz). δ 150.6 (4C, C_a), 144.5 (2C, C_c), 135.4 (2C, C_d), 132.3 (2C, C_f), 130.2 (2C, C_e), 129.6 (4C, C_g), 126.3 (4C, C_h), 126.0 (4C, C_i), 121.2 (4C, C_b).

Procedure for 9,10-bis(3,3'-ethynylpyridyl)anthracene (**L_4**) [159]

In a Schlenk flask, a mixture of 9,10-dibromoanthracene (400 mg, 1.19 mmol) and 3-ethynylpyridine (270 mg, 2.62 mmol) was dissolved in a solution of toluene/Et_3N (1/1, 25 mL) and kept under a nitrogen atmosphere for 20 min. Then, a mixture of palladium(II)acetate (5 mg, 0.024 mmol), copper(I)iodide (6 mg, 0.030 mmol) and triphenylphosphine (17 mg, 0.065 mmol) was added with the other reactants. The reaction mixture was stirred at reflux for 24 h. Then, the solvent was removed under vacuum. The residue was dissolved in H_2O and stirred for 2 h at room temperature, to eliminate the triethylammonium salt. The solid was filtered off and dried under vacuum. Recrystallization was done in toluene and the product was obtained as orange needles, which were dried under vacuum (285 mg, 63%).^{1}H-NMR ($CDCl_3$, 400 MHz): δ 9.02 (s, 2H, H_a), 8.66 (m, 6H, H_b and H_j), 8.06 (d, *J* = 7.6 Hz, 2H, H_d), 7.69 (m, 4H, H_k), 7.42 (m, 2H, H_c). $^{13}C\{^1H\}$-NMR ($CDCl_3$, 100 MHz): δ 152.4 (2C,C_a), 149.2 (2C, C_b), 138.6 (2C, C_d), 132.3 (4C, C_i), 127.4 (4C, C_k), 127.3 (4C, C_j), 123.4 (2C, C_c), 120.7 (2C, C_e), 118.4 (2C, C_h), 99.12 (2C, C_f), 89.77 (2C, C_g). IR (cm^{-1}): 3078 (w; C-H aromatic), 2200 (w; C≡C), 1557 (m; C=C aromatic), 1477 (m; C=C aromatic), 799 (s, C-H aromatic), 763 (s, C-H aromatic), 697 (s, C-H aromatic). ESI-MS (+): m/z = 381.2 $[M+H]^+$. UV−vis [1.0 x 10^{-5} M, CH_2Cl_2; λ_{max}, nm (ε, $M^{-1}.m^{-1}$)]: 275 (1.4 × 10^5), 299 (4.2 × 10^4), 314 (5.1 × 10^4), 438 (5.9 × 10^4), 464 (6.2 × 10^4). Anal. calc. for $C_{28}H_{16}N_2$ (380.46): C 88.38, H 4.25, N 7.37; Found: C 88.26, H 4.14, N 7.26.

General procedure for 9-(pyridyl)anthracene (**L_5** and **L_6**) [143,156]

9-Bromoanthracene (1.00 g, 3.89 mmol), 4-pyridylboronic acid (526 mg, 4.28 mmol, for **L_5**) or 3-pyridylboronic acid (526 mg, 4.28 mmol, for **L_6**), potassium carbonate (5.39 g, 39 mmol) and tetrakis(triphenylphosphine) palladium(0) (451 mg, 0.39 mmol) were dissolved in THF (40 mL) and H_2O (20 mL). Three cycles of freeze pumping were realized. After stirring 48 h at 110 °C, the solvents were removed under vacuum. The residue was extracted with EtOAc several times. The organic layer was twice washed with brine and dried over $MgSO_4$. Then, the solvent was removed by rotary evaporation. The crude product was recrystallized from hot acetone to yield a pure white powder.

9-(4-pyridyl)anthracene (L_5) (436 mg, 44%). ^{1}H-NMR ($CDCl_3$, 400 MHz). δ 8.85 (d, *J* = 5.2 Hz,

2H, H_a), 8.55 (s, 1H, H_k), 8.06 (d, *J* = 8.4 Hz, 2H, H_f), 7.57 (d, *J* = 8.8 Hz, 2H, H_i), 7.49 (t, *J* = 7.4 Hz, 2H, H_g), 7.39 (m, 4H, H_b + H_h). $^{13}C\{^1H\}$-NMR ($CDCl_3$, 100 MHz). δ 150.1 (2C, C_a), 147.6 (1C, C_c), 137.7 (1C, C_d), 131.4 (2C, C_e), 129.6 (2C, C_j), 128.7 (2C, C_f), 127.7 (1C, C_k), 126.6 (2C, C_b), 126.2 (2C, C_i), 126.0 (2C, C_g), 125.5 (2C, C_h).

9-(3-pyridyl)anthracene (L_6) (626 mg, 63%). ^{1}H-NMR ($CDCl_3$, 400 MHz). δ 8.81 (d, *J* = 4.8 Hz, 1H, H_b), 8.71 (s, 1H, H_a), 8.56 (s, 1H, H_m), 8.08 (d, *J* = 4.2 Hz, 2H, H_h), 7.79 (dd, *J* = 7.6 Hz, 1H, H_d), 7.59 (d, *J* = 4.4 Hz, 2H, H_k), 7.55 (t, *J* = 6.8 Hz, 1H, H_c), 7.49 (t, *J* = 7.4 Hz, 2H, H_i), 7.39 (m, 2H, H_j). $^{13}C\{^1H\}$-NMR ($CDCl_3$, 100 MHz). δ 150.1 (2C, C_a), 147.6 (1C, C_c), 137.7 (1C, C_d), 131.4 (2C, C_e), 129.6 (2C, C_j), 128.7 (2C, C_f), 127.7 (1C, C_k), 126.6 (2C, C_b), 126.2 (2C, C_i), 126.0 (2C, C_g), 125.5 (2C, C_h). IR (cm^{-1}): 3050 (w; C-H aromatic), 1403 and 1027 (m; C=C aromatic), 741 (s, C-H aromatic). ESI-MS (+): m/z = 256.1 $[M+H]^+$. UV–vis [1.0×10^{-5} M, CH_2Cl_2; λ_{max}, nm (ε, $M^{-1}.m^{-1}$)]: 253 (1.1×10^5), 333 (0.8×10^4), 349 (1.6×10^4), 367 (2.3×10^4), 387 (2.3×10^4), 399 (2.9×10^4). Anal. calc. for $C_{19}H_{13}N$ (255.33): C 89.38, H 5.13, N 5.49; Found: C 89.21, H 5.15, N 5.34.

Procedure for 9-((pyridin-4-yl)vinyl)anthracene (**L_7**) [158]

9-Bromoanthracene (500 mg, 1.94 mmol), 4-vinylpyridine (322 mg, 3.06 mmol), palladium(II)acetate (46 mg, 0.19 mmol), triphenylphosphine (102 mg, 0.39 mmol) were dissolved in a mixture of dried DMF (10 mL) and Et_3N (0,5 mL). Nitrogen was bubbled into the solution for 20 min. After stirring 24 h at 115 °C, H_2O (10 mL) was added. The product was extracted several times with CH_2Cl_2 and the combined organic phases were washed with brine, dried over $MgSO_4$ and concentrated by rotary evaporator. The crude product was purified by column chromatography (silica gel; hexane/EtOAc = 4/1 to 1/1). The pure product was obtained as a yellow solid (398 mg; 73%). ^{1}H-NMR ($CDCl_3$, 400 MHz). δ 8.68 (d, *J* = 6 Hz, 2H, H_a), 8.45 (s, 1H, H_m), 8.28 (s, 2H, H_h), 8.15 (d, *J* = 16.4 Hz, 1H, H_e), 8.06 (m, 2H, H_k), 7.53 (d, *J* = 6 Hz, 2H, H_b), 7.50 (dd, *J* = 6.4 Hz and *J* = 3.4 Hz, 4H, H_i and H_j), 6.92 (d, *J* = 16.4 Hz, 1H, H_c). $^{13}C\{^1H\}$-NMR ($CDCl_3$, 100 MHz). δ 150.6 (2C, C_a), 144.5 (2C, C_c), 135.1 (1C, C_d), 131.6 (2C, C_g), 131.4 (2C, C_l), 130.0 (1C, C_e), 129.8 (1C, C_f), 129.0 (2C, C_k), 127.4 (1C, C_m), 126.1 (2C, C_i), 125.7 (2C, C_j), 125.5 (2C, C_h), 121.1 (2C, C_b).

Procedure for 2,7-di-*tert*-butyl-4,9-di-(4-pyridyl)-*trans*-10b,10c-dimethyl-10b,10c-dihydropyrene (**L8**) [166]

4,9-Dibromo-2,7-di-*tert*-butyl-*trans*-10b,10c-dimethyl-10b,10c-dihydropyrene [161,162] (250 mg, 0.50 mmol) and 4-pyridinylboronic acid (141 mg, 1.15 mmol) were dissolved in fresh distilled THF (20 mL) in a Schlenk tube. Three cycles of freeze pumping were realized. A degassed (with nitrogen) aqueous solution (5 mL) with sodium carbonate (265 mg, 2.50 mmol) and tetrakis(triphenylphosphine) palladium(0) (58 mg, 0.05 mmol) was then added into the Schlenk tube. The resulting mixture was heated to reflux and was stirred for 48 h. After cooling the mixture to room temperature, the solution was concentrated under reduced pressure. The product was extracted with CH_2Cl_2. The organic phase was washed with H_2O and dried over anhydrous $MgSO_4$. The solvent was evaporated under reduced pressure. The crude solid product was purified by a column chromatography (silica gel; from cyclohex./EtOAc = 1/0 to cyclohex./EtOAc = 1/1). The pure product was isolated as a dark green solid (177 mg, 71%).^{1}H-NMR (CD_3OD, 400 MHz). δ 8.63 (s, 2H, H_f), 8.53 (s, 2H, H_g), 8.40 (s, 2H, H_j), 7.62 (d, *J* = 8 Hz, 4H, H_n), 7.04 (d, *J* = 8 Hz, 4H, H_m), 1,60 (s, 18H, H_c), -3.71 (s, 6H, H_a) . $^{13}C\{^1H\}$-NMR (CD_3OD, 100 MHz). δ 157.8 (2C, C_k), 146.7 (2C, C_l), 138.1 (2C, C_b), 136.3 (2C, C_h), 135.2 (2C, C_i), 134.7 (2C, C_e), 132.9 (4C, C_n), 126.2 (4C, C_j), 122.0 (2C, C_f), 121.0 (2C, C_g), 116.1 (4C, C_m), 36.9 (1C, C_d), 32.2 (6C, C_c), 31.5 (1C, C_d), 15.3 (2C, C_a).

Procedure for 2,7-di-*tert*-butyl-4,9-di-(4-vinylpyridyl)-*trans*-10b,10c-dimethyl-10b,10c-dihydropyrene (**L9**)

In a Schlenk tube, 4,9-dibromo-2,7-di-*tert*-butyl-*trans*-10b,10c-dimethyl-10b,10c-dihydropyrene [164,165] (200 mg, 0.4 mmol), 4-vinylpyridine (168 mg, 1.6 mmol), palladium(II)acetate (9 mg, 0.04 mmol) and triphenylphosphine (11 mg, 0.04 mmol) were dissolved in dried Et_3N (10 mL). Nitrogen was bubbled through the Schlenk during 20 min. The resulting mixture was heated to reflux and was stirred for 48 h. After cooling the mixture to room temperature, the solution was filtrated through a celite pad. HCl (1 M, 10 mL) was carefully added to the solution and the product was extracted with CH_2Cl_2. The organic layer was washed several times with H_2O and dried over anhydrous $MgSO_4$. The solvent was then concentrated under reduced pressure and then the product was precipitated in Et_2O. The

pure product was isolated as a dark red solid (128 mg, 58%).^{1}H-NMR ($CDCl_3$, 400 MHz). δ 8.88 (s, 2H, H_g), 8.80 (s, 2H, H_j), 8.70 (m, 6H, H_m and H_p), 8.58 (s, 2H, H_f), 7.60 (m, 4H, H_o), 7.45 (d, J = 16 Hz, 2H, H_l), 1.74 (s, 18H, H_c), -3.57 (s, 6H, H_a) . $^{13}C\{^{1}H\}$-NMR ($CDCl_3$, 100 MHz). δ 150.5 (4C, C_p), 147.2 (2C, C_d), 145.6 (2C, C_n), 138.2 (2C, C_i), 135.3 (2C, C_h), 130.7 (2C, C_m), 128.3 (2C, C_k), 127.4 (2C, C_l), 122.6 (2C, C_f), 121.2 (4C, C_o), 121.1 (2C, C_j), 117.5 (2C, C_g), 36.5 (2C, C_e), 32.0 (2C, C_c), 31.4 (2C, C_b), 16.0 (2C, C_a).). IR (cm^{-1}): 3041 (w; C-H aromatic), 2957 (m; C-H aromatic), 2865 (w; C-H aromatic), 1615 (w; C=C aromatic), 1592 (m; C=C aromatic), 122 (m; C=C aromatic), 961 (m, C-H aromatic), 795 (m, C-H aromatic). ESI-MS (+): m/z = 551.8 $[M+H]^+$. UV−vis [1.0 x 10^{-5} M, CH_3CN; λ_{max}, nm (ε, $M^{-1}.m^{-1}$)]: 277 (1.8 × 10^5), 379 (3.0 × 10^4), 396 (3.5 × 10^4), 420 (5.1 × 10^4), 497 (1.7 × 10^4), 535 (2.1 × 10^4), 700 (4.6× 10^3). Anal. calc. for $C_{19}H_{13}N$ (255.33): C 87.23, H 7.69, N 5.09; Found: C 87.12, H 7.54, N 5.12.

Procedure for 2,7-di-*tert*-butyl-4,9-di-(*N*-methyl-4-vinylpyridyl)-*trans*-10b,10c-dimethyl-10b,10c-dihydropyrene hexafluorophosphate (**L_{10}**) [145]

2,7-Di-*tert*-butyl-4,9-di-(4-vinylpyridyl)-*trans*-10b,10c-dimethyl-10b,10c-dihydropyrene (**L_9**, 50 mg, 0.09 mmol) was dissolved in CH_2Cl_2 (25 mL). Nitrogen was bubbled in the solution for 20 min. Iodomethane (1 mL, excess) was added. The solution was refluxed for 2h. After cooling down to room temperature, the black precipitate was filtrated, washed with cold CH_2Cl_2 and then dissolved in CH_3OH (40 mL). The product was precipitated into a saturated aqueous solution of potassium hexafluorophosphate. Then, it was washed with cold CH_3OH and dried under vacuum. The product was isolated as a black solid (68 mg, 87%). ^{1}H-NMR (CD_3CN, 400 MHz). δ 9.18 (d, *J* = 16 Hz, 2H, H_l), 9.11 (s, 2H, H_f), 9.05 (s, 2H, H_g), 8.77 (s, 2H, H_j), 8.51 (d, *J* = 6.4 Hz, 4H, H_p), 8.28 (d, *J* = 6.8 Hz, 4H, H_o), 7.78 (d, *J* = 15.6 Hz, 2H, H_m), 4.25 (s, 6H, H_q), 1.76 (s, 18H, H_c), -3.56 (s, 6H, H_a). $^{13}C\{^{1}H\}$-NMR (CD_3CN, 100 MHz). δ 154.6 (2C, C_n), 150.2 (2C, C_d), 145.5 (4C, C_p), 140.0 (2C, C_k), 138.8 (2C, C_l), 137.9 (2C, C_b), 128.8 (2C, C_i), 125.0 (4C, C_o), 124.8 (2C, C_m), 124.6 (2C, C_j), 122.4 (4C, C_f), 119.7 (2C, C_g), 48.2 (2C, C_q), 37.2 (2C, C_e), 31.9 (6C, C_c), 16.7 (2C, C_a). IR (cm^{-1}): 2952 (m; C-H aromatic), 2864 (m; C-H aromatic), 1641 (m; C=C aromatic), 1587 (m; C=C aromatic), 1189 (m; C=C aromatic), 842 (s, C-H aromatic). ESI-MS (+): m/z = 290.3 $[M\text{-}2PF_6^-]^{2+}$; 275.3 $[M\text{-}2PF_6^-\text{-}CH_3]^{2+}$. UV−vis [$1.10^{-5}$ M, CH_3CN; λ_{max}, nm (ε, $M^{-1}.m^{-1}$)]: 264 (2.5 × 10^5), 348 (5.4 × 10^3), 447 (8.6 × 10^3), 588 (8.8× 10^3), 735 (2.7× 10^3) . Anal.

calc. for $C_{19}H_{13}N$ (255.33): C 57.93, H 5.56, N 3.22; Found: C 58.18, H 5.83, N 3.24.

General procedure for 2,7-di-*tert*-butyl-4,9-di-(*N*-(4′-(4-methylphenyl)-2,2′:6′,2′′-terpyridin-yl)pyridin-4-yl)-*trans*-10b,10c-dimethyl-10b,10c-dihydropyrene hexafluorophosphate (**L_{11}**) and 2,7-di-*tert*-butyl-4,9-di-(*N*-(4′-(4-methylphenyl)-2,2′:6′,2′′-terpyridin-yl)4-vinylpyridyl)-*trans*-10b,10c-dimethyl-10b,10c-dihydropyrene hexafluorophosphate (**L_{12}**) [168]

2,7-Di-*tert*-butyl-4,9-di-(4-pyridyl)-*trans*-10b,10c-dimethyl-10b,10c-dihydropyrene (**L_8**, 50 mg, 0.1 mmol) or 2,7-di-*tert*-butyl-4,9-di-(4-vinylpyridyl)-*trans*-10b,10c-dimethyl-10b,10c-dihydropyrene (**L_9**, 50 mg, 0.1 mmol) was dissolved in 50 mL of degassed CH_3CN and 4′-(4-(bromomethyl)phenyl)-2,2′:6′,2′′-terpyridine [169] (161 mg, 0. 4 mmol) was dissolved in CH_2Cl_2 (10 mL). The second solution was slowly added to the first solution, under a constant stirring. The mixture was stirred for 15 h at reflux. After cooling down to room temperature, the solution was concentrated under reduced pressure. The product was precipitated with Et_2O. The precipitated was then dissolved in CH_3OH and poured into a saturated aqueous solution of potassium hexafluorophosphate. The final precipitate was filtered, washed several times with H_2O and dried under vacuum.

2,7-di-*tert*-butyl-4,9-di-(*N*-(4′-(4-methylphenyl)-2,2′:6′,2′′-terpyridin-yl)pyridin-4-yl)-*trans*-10b, 10c-dimethyl-10b,10c-dihydropyrene hexafluorophosphate (L_{11}) Red powder (107 mg, 75%). ^{1}H-NMR (CD_3CN, 400 MHz). δ 8.93 (m, 4H, H_f and H_n), 8.70 (m, 162H, H_g, H_j, H_u and H_x), 8.51 (s, 4H, H_m), 8.07 (s, 4H, H_r), 7.97 (s, 4H, H_y), 7.80 (s, 4H, H_q), 7.45 (s, 4H, H_y), 5.94 (m, 4H, H_o), 1.62 (m, 18H, H_c), -3.65 (m, 6H, H_a). ^{13}C{^{1}H}-NMR (CD_3CN, 100 MHz). δ 159.0 (2C, C_k), 156.3 (4C, C_v), 155.5 (4C, C_w), 150.1 (1C, C_{aa}), 149.8 (1C, C_{aa}), 149.3 (2C, C_{aa}), 149.0 (2C, C_t), 148.0 (2C, C_l), 143.9 (2C, C_n), 143.8 (2C, C_n), 139.9 (1C, C_s), 139.8 (1C, C_s), 137.9 (2C, C_b), 137.3 (4C, C_y), 134.1 (2C, C_e), 134.0 (2C, C_i), 133.8 (2C, C_h), 130.3 (4C, C_q), 130.2 (4C, C_m), 129.8 (1C, C_j), 129.6 (1C, C_j), 129.1 (2C, C_p), 128.2 (4C, C_r), 125.7 (1C, C_g), 125.0 (1C, C_g), 124.5 (2C, C_z), 124.4 (2C, C_z), 123.8 (1C, C_f), 122.9 (1C, C_f), 121.1 (2C, C_x), 120.4 (2C, C_x), 118.6 (2C, C_u), 118.5 (2C, C_u), 63.4 (1C, C_o), 63.2 (1C, C_o), 36.2 (1C, C_d), 35.9 (1C, C_d), 30.8 (3C, C_c), 30.7 (3C, C_c), 14.4 (2C, C_a).

2,7-di-*tert*-butyl-4,9-di-(*N*-(4′-(4-methylphenyl)-2,2′:6′,2′′-terpyridin-yl) 4-vinylpyridyl)- *trans*-10b,10c-dimethyl-10b,10c-dihydropyrene hexafluorophosphate (L_{12}) Green powder (99 mg, 67%).^{1}H-NMR (CD_2Cl_2, 400 MHz). δ 9.11 (d, *J* = 16 Hz, 2H, H_l), 8.98 (s, 2H, H_f), 8.92 (s, 2H, H_g), 8.76 (s, 4H, H_w), 8.70 (m, 4H, H_j and H_q), 8.67 (d, *J* = 8 Hz, 4H, H_z), 8.61 (d, *J* = 6.4 Hz, 4H, H_r), 8.20 (d, *J* = 6.4 Hz, 4H, H_s), 8.02 (d, *J* = 8 Hz, 4H, H_p), 7.90 (t, *J* = 7.6 Hz, 4H, H_{aa}), 7.65 (m, 4H, H_m and H_o), 7.38 (m, 4H, H_{ab}), 5.76 (s, 4H, H_q), 1.73 (m, 18H, H_c), -3.50 (s, 6H, H_a). ^{13}C{^{1}H}-NMR (CD_2Cl_2, 100 MHz). δ 156.7 (2C, C_k), 156.2 (4C, C_x), 155.1 (4C, C_y), 150.3 (2C, C_v), 149.6 (4C, C_{ac}), 149.2 (2C, C_n), 143.6 (4C, C_s), 140.1 (1C, C_u), 140.0 (1C, C_u), 139.5 (2C, C_l), 138.1 (2C, C_b), 137.4 (4C, C_{aa}), 134.8 (2C, C_e), 134.4 (2C, C_i), 133.8 (2C, C_h), 130.2 (4C, C_o), 129.2 (6C, C_p and C_r), 124.9 (4C, C_t), 124.7 (2C, C_{ab}), 124.5 (2C, C_{ab}), 123.2 (2C, C_m), 121.9 (4C, C_z), 121.6 (2C, C_g), 119.2 (2C, C_j), 119.1 (6C, C_f and C_w), 64.2 (2C, C_q), 36.9 (2C, C_d), 31.8 (3C, C_c), 29.5 (3C, C_c), 16.7 (2C, C_a). IR (cm^{-1}): 3660 (w; C-H aromatic), 2968 (m; C-H aromatic), 2865 (w; C-H aromatic), 1635 (m; C=C aromatic), 1582 (s; C=C aromatic), 1155 (m; C=C aromatic), 845 (s, C-H aromatic). ESI-MS (+): m/z = 597.8 $[M\text{-}2PF_6^-]^{2+}$. UV−vis [1.10^{-5} M, CH_3CN; λ_{max}, nm (ε, $M^{-1}.m^{-1}$)]: 262 (2.5×10^5), 352 (1.1×10^4), 454 (1.3×10^4), 597 (1.4×10^4), 743 (4.9×10^3). Anal. calc. for $C_{19}H_{13}N$ (255.33): C 67.92, H 5.02, N 7.54; Found: C 68.03, H 5.18, N 7.35.

General procedure for the synthesis of ruthenium rectangles with anthracene derivatives (A_1 – A_9)

A mixture of metalla-clip (oxa [150], dobq [151], or donq [152], 0.27 mmol) and silver trifluoromethanesulfonate (139 mg, 0.54 mmol) was dissolved in CH_2Cl_2 and stirred for 3 h at room temperature. The mixture was filtrated in order to eliminate silver chloride. The resulting solution was added to a CH_2Cl_2 solution containing the anthracene ligand (**L_1-L_4**, 0.27 mmol). Then, the mixture was refluxed overnight and consequently concentrated under vacuum. The concentrated solution was slowly poured into cold Et_2O to induce precipitation. After filtration, the metalla-rectangles were dried under vacuum.

$[Ru_4(\eta^6\text{-}p\text{-cymene})_4(\mu^4\text{-dobq})_2(\mu^2\text{-}L_1)_2][CF_3SO_3]_4$ (A_1): Red solid (374 mg, 56%). ^{1}H-NMR (CD_3CN, 400 MHz): δ 8.46 (d, *J* = 5.6 Hz, 8H, H_h), 7.50 (m, 8H, H_i), 7.27 (dd, *J* = 6.8 Hz and *J* = 3.2 Hz, 8H, H_m), 6.82 (m, 8H, H_n), 6.01 (d, *J* = 6 Hz, 8H, H_d), 5.93 (s, 4H, H_p), 5.81 (d, *J* = 6.4 Hz, 8H, H_e), 2.96 (sept, *J* = 6.8 Hz, 84H, H_b), 2.28 (s, 12H, H_g), 1.41 (d, *J* = 8.8 Hz, 24H, H_a). ^{13}C{^{1}H}-

NMR (CD_3CN, 100 MHz): δ 184.55 (8C, C_o), 184.6 (8C, C_o), 153.1 (8C, C_h), 133.1 (12C, C_k and C_l), 128.9 (8C, C_i), 128.3 (4C, C_j), 126.3 (8C, C_n), 125.5 (8C, C_m), 103.6 (4C, C_c), 101.8 (4C, C_p), 98.8 (4C, C_f), 83.6 (8C, C_d), 82.2 (8C, C_e), 31.3 (4C, C_b), 21.53 (8C, C_a), 17.4 (4C, C_g). IR (cm^{-1}): 3071 (w; C–H aromatic), 2969 (w; C–H aromatic), 1610 (w; C=C aromatic), 1518 (s; C=C aromatic), 1374 (s; C=C aromatic), 1255 (s; C=C aromatic), 1153 (m; C=C aromatic), 1028 (s; C=C aromatic), 635 (s; C–H aromatic). ESI–MS (+); m/z = 470.6 $[M\text{-}4OTf^-]^{4+}$, 677.1 $[M\text{-}3OTf^-]^{3+}$, 1090.1 $[M\text{-}2OTf^-]^{2+}$, 2329.1 $[M\text{-}OTf^-]^+$. UV−vis [1.0 × 10^{-5} M, CH_3CN; λ_{max}, nm (ε, $M^{-1}.m^{-1}$)]: 306 (4.6 × 10^4), 361 (2.5 × 10^4), 379 (2.5 × 10^4), 396 (5.5 × 10^4), 482 (3.3 × 10^4), 513 (3.3 × 10^4). Anal. calc. for $C_{104}H_{90}F_{12}N_4O_{20}Ru_4S_4$ (2476.50): C 50.44, H 3.67, N 2.26; Found: C 45.08, H 3.58, N 1.92.

$[Ru_4(\eta^6\text{-}p\text{-cymene})_4(\mu^4\text{-donq})_2(\mu^2\text{-}L_1)_2][CF_3SO_3]_4$ (A_2): Green solid (341 mg, 49%). ^{1}H-NMR (CD_3CN, 400 MHz): δ 8.92 (m, 8H, H_h), 7.78 (m, 8H, H_i), 7.59 (m, 24H, H_m, H_n and H_p), 6.30 (m, 8H, H_e), 5.83 (m, 8H, H_d), 2.97 (sept, *J* = 6.5 Hz, 4H, H_b), 1.96 (s, 12H, H_g), 1.32 (m, 24H, H_a). $^{13}C\{^1H\}$-NMR (CD_3CN, 100 MHz): δ 156.2 (4C, C_h), 156.1 (4C, C_h), 152.5 (4C, C_i), 139.9 (8C, C_p), 130.7 (4C, C_q), 129.8 (4C, C_k), 129.6 (8C, C_j), 127.7 (8C, C_n), 127.3 (8C, C_l), 126.9 (8C, C_m), 123.7 (8C, C_o), 120.5 (4C, C_c), 111.0 (4C, C_f), 88.6 (8C, C_d), 86.4 (8C, C_e), 31.9 (4C, C_b), 22.6 (4C, C_a), 22.4 (4C, C_a), 18.5 (4C, C_g). IR (cm^{-1}): 3073 (w; C–H aromatic), 2973 (w; C–H aromatic), 1612 (w; C=C aromatic), 1256 (s; C=C aromatic), 1167 (m; C=C aromatic), 1029 (s; C=C aromatic), 636 (s; C–H aromatic). ESI–MS (+); m/z = 496.1 $[M\text{-}4OTf^-]^{4+}$, 1140.2 $[M\text{-}2OTf^-]^{2+}$. UV−vis [1.0 × 10^{-5} M, CH_3CN; λ_{max}, nm (ε, $M^{-1}.m^{-1}$)]: 340 (1.2 × 10^4), 358 (1.8 × 10^4), 379 (2.5 × 10^4), 398 (4.2 × 10^4). Anal. calc. for $C_{112}H_{96}F_{12}N_4O_{20}Ru_4S_4$ (2578.64): C 52.16, H 3.76, N 2.17; Found: C 49.90, H 4.22, N 2.71.

$[Ru_4(\eta^6\text{-}p\text{-cymene})_4(\mu^4\text{-oxa})_2(\mu^2\text{-}L_2)_2][CF_3SO_3]_4$ (A_3): Yellow solid (270 mg, 42%). ^{1}H-NMR (CD_3CN, 400 MHz): δ 8.97 (m, 4H, H_h),8.67 (m, 4H, H_i), 8.06 (m, 4H, H_k), 7.84 (m, 4H, H_j), 7.56 (m, 16H, H_o and H_p), 5.67 (m, 16H, H_d and H_e), 2.84 (m, 4H, H_b), 2.11 (s, 6H, H_g), 2.07 (s, 6H, H_g), 1.30 (m, 24H, H_a). $^{13}C\{^1H\}$-NMR (CD_3CN, 100 MHz): δ 155.3 (4C, C_h), 153.7 (4C, C_i), 142.9 (2C, C_k), 142.7 (2C, C_k), 137.5 (4C, C_l), 130.8 (4C, C_m), 129.2 (4C, C_j), 127.7 (4C, C_o), 127.6 (4C, C_o), 127.0 (4C, C_p), 126.8 (4C, C_p), 123.7 (4C, C_n), 120.5 (4C, C_n), 102.7 (2C, C_c), 102.3 (2C, C_c), 98.2 (4C, C_f), 87.1 (2C, C_d), 87.0 (2C, C_d), 84.5 (2C, C_d), 83.4 (4C, C_e), 81.6 (4C, C_e), 76.9 (2C,

C_d), 31.8 (2C, C_b), 31.7 (2C, C_b), 22.6 (4C, C_a), 22.4 (2C, C_a), (2C, C_d), 22.3 (2C, C_a), 18.5 (2C, C_g), 18.0 (2C, C_g). IR (cm^{-1}): 3068 (w; C–H aromatic), 2974 (w; C–H aromatic), 1672 (m; C=C aromatic), 1627 (s; C=C aromatic), 1274 (s; C=C aromatic), 1254 (s; C=C aromatic), 1157 (m; C=C aromatic), 1028 (s; C=C aromatic), 636 (s; C–H aromatic). ESI–MS (+); m/z = 1041.1 [M-2OTf$^-$]$^{2+}$. UV−vis [1.0 × 10^{-5} M, CH_3CN; λ_{max}, nm (ε, $M^{-1}.m^{-1}$)]: 341 (1.5 × 10^4), 356 (2.3 × 10^4), 377 (3.4 × 10^4), 399 (4.6 × 10^4). Anal. calc. for $C_{98}H_{88}F_{12}N_4O_{20}Ru_4S_4$ (2378.4): C 48.48, H 3.74, N 2.36; Found: C 47.80, H 4.08, N 3.31.

[Ru$_4$(η^6-*p*-cymene)$_4$(μ^4-dobq)$_2$(μ^2-L$_2$)$_2$][CF$_3$SO$_3$]$_4$ (A$_4$): Red solid (361 mg, 54%). ^{1}H-NMR (CD_3CN, 400 MHz): δ 8.81 (d, *J* = 4.8 Hz, 4H, H_i), 8.66 (s, 4H, H_h), 7.93 (d, *J* = 8 Hz, 4H, H_k), 7.70 (d, *J* = 6.6 Hz, 4H, H_j), 7.63 (m, 8H, H_o), 7.46 (m, 12H, H_p and H_r), 5.82 (m, 16H, H_d and H_e), 2.84 (sept, *J* = 7 Hz, 4H, H_b), 1.96 (s, 12H, H_g), 1.29 (m, 24H, H_a). ^{13}C{^{1}H}-NMR ($(CD_3)_2CO$, 100 MHz): δ 185.3 (8C, C_q), 151.6 (2C, C_h), 151.2 (2C, C_h), 148.6 (2C, C_i), 147.6 (2C, C_i), 140.8 (8C, C_p), 136.6 (4C, C_m), 133.8 (8C, C_n), 127.7 (2C, C_k), 127.6 (2C, C_k), 127.2 (2C, C_j), 126.9 (2C, C_j),126.4 (4C, C_l), 120.8 (8C, C_o), 111.1 (4C, C_c), 105.8 (4C, C_f), 105.0 (4C, C_m), 84.4 (8C, C_d), 83.3 (8C, C_e), 32.2 (4C, C_b), 22.7 (8C, C_a), 18.5 (4C, C_g). IR (cm^{-1}): 3072 (w; C–H aromatic), 2968 (w; C–H aromatic), 1631 (w; C=C aromatic), 1518 (s; C=C aromatic), 1374 (s; C=C aromatic), 1255 (s; C=C aromatic), 1156 (m; C=C aromatic), 1027 (s; C=C aromatic), 635 (s; C–H aromatic). ESI–MS (+); m/z = 471.1 [M-4OTf$^-$]$^{4+}$, 677.8 [M-3OTf$^-$]$^{3+}$, 1091.1 [M-2OTf$^-$]$^{2+}$. UV−vis [1.0 × 10^{-5} M, CH_3CN; λ_{max}, nm (ε, $M^{-1}.m^{-1}$)]: 303 (4.3 × 10^4), 362 (3.2 × 10^4), 381 (4.2 × 10^4), 402 (5.9 × 10^4). Anal. calc. for $C_{104}H_{90}F_{12}N_4O_{20}Ru_4S_4$ (2476.50): C 50.44, H 3.67, N 2.26; Found: C 40.15, H 3.63, N 2.28.

[Ru$_4$(η^6-*p*-cymene)$_4$(μ^4-donq)$_2$(μ^2-L$_2$)$_2$][CF$_3$SO$_3$]$_4$ (A$_5$): Green solid (271 mg, 39%). ^{1}H-NMR (CD_3CN, 400 MHz): δ 9.04 (m, 4H, H_h), 8.86 (m, 4H, H_i), 8.14 (m, 4H, H_k),7.85 (m, 4H, H_j), 7.37 (m, 24H, H_o, H_p and H_r), 5.81 (m, 16H, H_d and H_e), 2.85 (sept, *J* = 6.8 Hz, 4H, H_b), 2.05 (m, 12H, H_g), 1.24 (m, 24H, H_a). ^{13}C{^{1}H}-NMR (CD_3CN, 100 MHz): δ 156.8 (2C, C_i), 155.9 (2C, C_h), 155.3 (2C, C_i), 151.1 (2C, C_h), 143.3 (2C, C_k) 142.9 (2C, C_k), 137.2 (8C, C_r), 135.8 (4C, C_m), 133.3 (2C, C_s), 133.0 (2C, C_s), 130.9 (4C, C_p), 129.3 (4C, C_p), 127.7 (4C, C_n), 127.5 (4C, C_n), 127.0 (2C, C_j), 126.8 (2C, C_j), 123.7 (8C, C_o), 120.5 (4C, C_l), 110.9 (4C, C_c), 106.6 (4C, C_{OTf}), 102.3 (4C, C_f), 87.0 (4C, C_d), 86.0 (4C, C_d), 84.6 (2C, C_e), 84.5 (4C, C_e), 84.4 (2C, C_e), 31.7 (4C, C_b), 22.4 (4C,

C_a), 22.3 (4C, C_a), 18.5 (4C, C_g). IR (cm^{-1}): 3070 (w; C–H aromatic), 2975 (w; C–H aromatic), 1611 (w; C=C aromatic), 1274 (s; C=C aromatic), 1258 (s; C=C aromatic), 1156 (m; C=C aromatic), 1030 (s; C=C aromatic), 637 (s; C–H aromatic). ESI–MS (+); m/z = 575.9 [M-2donq-$2CH_3$-$3OTf^-$]$^{3+}$, 603.1 [M-2*p*cymene-$4CH_3$-$3OTf^-$]$^{3+}$, 689.9 [M-isopropyl-$2CH_3$-$3OTf^-$]$^{3+}$. UV−vis [1.0×10^{-5} M, CH_3CN; λ_{max}, nm (ε, $M^{-1}.m^{-1}$)]: 341 (1.9×10^4), 359 (3.1×10^4), 377 (4.5×10^4), 398 (5.3×10^4). Anal. calc. for $C_{112}H_{96}F_{12}N_4O_{20}Ru_4S_4$ (2578.64): C 52.16, H 3.76, N 2.17; Found: C 51.91, H 4.01, N 2.96.

$[Ru_4(\eta^6$-*p*-cymene$)_4(\mu^4$-dobq$)_2(\mu^2$-$L_3)_2][CF_3SO_3]_4$ (A_6): Red solid (502 mg, 72%). ^{1}H-NMR (CD_3CN, 400 MHz): δ 8.18 (d, *J* = 6 Hz, 8H, H_h), 8.05 (d, *J* = 16.4 Hz, 4H, H_l), 7.90 (dd, *J* = 6.8 Hz and *J* = 3.6 Hz,8, H_o), 7.66 (d, *J* = 6 Hz, 8H, H_i), 7.17 (dd, *J* = 6.8 Hz and *J* = 3.2 Hz, 8H, H_p), 6.72 (dd, *J* = 16.4 Hz, 4H, H_k), 5.95 (d, *J* = 6 Hz, 8H, H_d), 5.78 (s, 4H, H_r), 5.73 (d, *J* = 6 Hz, 8H, H_e), 2.88 (sept, *J* = 6.8 Hz, 4H, H_b), 2.20 (s, 12H, H_g), 1.36 (d, *J* = 6.8 Hz, 24H, H_a). $^{13}C\{^1H\}$-NMR (CD_3CN, 100 MHz): δ 185.0 (8C, C_q), 153.8 (8C, C_h), 148.5 (4C, C_j), 134.6 (4C, C_l), 133.8 (4C, C_k), 132.1 (4C, C_m), 129.5 (8C, C_n), 126.8 (8C, C_o), 124.1 (8C, C_i), 104.6 (4C, C_c), 102.4 (4C, C_r), 98.8 (4C, C_f), 84.6 (8C, C_d), 82.7 (8C, C_e), 32.16 (4C, C_b), 22.5 (8C, C_a), 18.4 (4C, C_g). IR (cm^{-1}): 3072 (w; C–H aromatic), 2974 (w; C–H aromatic), 1610 (w; C=C aromatic), 1521 (s; C=C aromatic), 13745 (s; C=C aromatic), 1257 (s; C=C aromatic), 1158 (m; C=C aromatic), 1028 (s; C=C aromatic), 636 (s; C–H aromatic). ESI–MS (+); m/z = 489.0 [M-4OTf$^-$-$2CH_3$]$^{4+}$. UV−vis [1.0×10^{-5} M, CH_3CN; λ_{max}, nm (ε, $M^{-1}.m^{-1}$)]: 399 (5.3×10^4), 458 (5.5×10^4), 513 (3.8×10^4). Anal. calc. for $C_{112}H_{98}F_{12}N_4O_{20}Ru_4S_4$ (2580.66): C 52.12, H 3.84, N 2.17; Found: C 50.75, H 3.91, N 2.03.

$[Ru_4(\eta^6$-*p*-cymene$)_4(\mu^4$-oxa$)_2(\mu^2$-$L_4)_2][CF_3SO_3]_4$ (A_7): Yellow solid (494 mg, 74%). ^{1}H-NMR ($(CD_3)_2CO$, 400 MHz): δ 8.64 (m, 8H, H_h and H_k), 8.16 (m, 12H, H_i and H_q), 7.65 (t, *J* = 6.6 Hz, 4H, H_j), 7.34 (m, 8H, H_r), 6.20 (dd, *J* = 11.6 Hz and *J* = 6.0 Hz, 8H, H_d), 6.05 (m, 8H, H_e), 3.04 (sept, *J* = 6.6 Hz, 4H, H_b), 2.35 (s, 12H, H_g), 1.45 (d, *J* = 6.8 Hz, 12H, H_a), 1.43 (d, *J* = 6.8 Hz, 12H, H_a). $^{13}C\{^1H\}$-NMR ($(CD_3)_2CO$, 100 MHz): δ 172.1 (2C, C_s), 172.0 (2C, C_s), 154.7 (4C, C_H), 152.5 (4C, C_l), 143.8 (4C, C_k), 137.2 (4C, C_p), 131.4 (4C, C_p), 128.2 (8C, C_r), 127.7 (4C, C_j), 127.2 (8C, C_q), 123.78 (4C, C_l), 120.9 (4C, C_o), 117.9 (4C, C_{OTf}), 103.4 (4C, C_c), 99.0 (4C, C_f), 97.4 (4C, C_m), 92.9 (4C, C_n), 83.3 (2C, C_d), 83.2 (2C, C_d), 83.1 (4C, C_d), 82.9 (2C, C_e), 82.8 (2C,

C_s), 82.3 (4C, C_e), 32.0 (4C, C_b), 22.7 (4C, C_a), 22.4 (4C, C_a), 18.2 (4C, C_g). IR (cm^{-1}): 3079 (w; C–H aromatic), 2211 (w; C≡C), 1625 (s; C=O), 1482 (m; C=C aromatic), 765 (m; C–H aromatic), 636 (s; C–H aromatic). ESI–MS (+); m/z = 708.0 [M-2**L4**-2OTf$^-$]$^{2+}$, 1088.9 [M-2OTf$^-$]$^{2+}$, 2323.2 [M-OTf$^-$]$^+$. UV−vis [1.0 x 10^{-5} M, EtOH; λ_{max}, nm (ε, $M^{-1}\cdot cm^{-1}$)]: 271 (3.1 × 10^5), 312 (7.5 × 10^4), 437 (7.6 × 10^4), 459 (7.8 × 10^4), 742 (7.3 × 10^3). Anal. calc. for $C_{104}H_{88}F_{12}N_4O_{20}Ru_4S_4$ (2474.48): C 50.48, H 3.59, N 2.27; Found: C 50.56, H 3.68, N 2.22.

[Ru4(η6-*p*-cymene)4(μ4-dobq)2(μ2-L4)2][CF3SO3]4 (A8): Red solid (472 mg, 68%). ^{1}H-NMR ($(CD_3)_2CO$, 400 MHz): δ 8.64 (d, *J* = 7.6 Hz, 4H, H_i), 8.58 (s, 4H, H_h), 8.31 (d, *J* = 6.0 Hz, 4H, H_k),8.05 (dd, *J* = 6.8 Hz and *J* = 3.2 Hz, 8H, H_q), 7.70 (t, *J* = 6.8 Hz, 4H, H_j), 7.47 (m, 8H, H_r), 6.34 (d, *J* = 6.0 Hz, 8H, H_d), 6.11 (d, *J* = 6.0 Hz, 8H, H_e), 5.96 (s, 4H, H_t), 3.04 (sept, *J* = 6.6 Hz, 4H, H_b), 2.33 (s, 12H, H_g), 1.42 (d, *J* = 6.8 Hz, 24H, H_a). ^{13}C{^{1}H}-NMR ($(CD_3)_2CO$, 100 MHz): δ 184.4 (8C, C_s), 155.3 (4C, C_h), 153.2 (4C, C_i), 142.8 (4C, C_k), 131.3 (8C, C_p), 128.3 (8C, C_r), 127.3 (4C, C_j), 127.1 (8C, C_q), 124.0 (1C, C_o), 123.3 (1C, C_o), 120.8 (4C, C_l), 117.7 (2C, C_o), 104.8 (4C, C_c), 102.4 (4C, C_t), 100.1 (4C, C_{OTf}), 97.0 (4C, C_f), 92.1 (4C, C_m), 90.6 (4C, C_n), 84.6 (8C, C_d), 82.6 (8C, C_e), 32.1 (4C, C_b), 22.5 (8C, C_a), 18.24 (4C, C_g). IR (cm^{-1}): 3075 (w; C–H aromatic), 2198 (w; C≡C), 1574 (m; C=C aromatic), 817 (m; C–H aromatic), 764 (m; C–H aromatic) and 693 (s; C–H aromatic). ESI-MS (+); m/z = 759.3 [M-2**L4**-2OTf$^-$]$^{2+}$, 1139.2 [M-2OTf$^-$]$^{2+}$, 2423.0 [M-OTf$^-$]$^+$. UV−vis [1.0 x 10^{-5} M, CH_2Cl_2; λmax, nm (ε, $M^{-1}\cdot cm^{-1}$)]: 274 (1.2 × 10^5), 314 (8.3 × 10^4), 457 (8.2 × 10^4), 722 (8.2 × 10^3). Anal. calc. for $C_{112}H_{92}F_{12}N_4O_{20}Ru_4S_4$ (2572.46): C 52.24, H 3.61, N 2.18; Found: C 52.45, H 3.81, N 2.22.

[Ru4(η6-*p*-cymene)4(μ4-donq)2(μ2-L4)2][CF3SO3]4 (A9): Green solid (570 mg, 82%). ^{1}H-NMR ($(CD_3)_2CO$, 400 MHz): δ 8.72 (s, 4H, H_h), 8.55 (d, *J* =6.8 Hz, 4H, H_k), 8.48 (d, *J* = 5.6 Hz, 4H, H_i), 8.01 (dd, *J* = 6.4 Hz and *J* = 2.8 Hz, 8H, H_q), 7.62 (t, *J* = 6.8 Hz, 4H, H_j), 7.48 (dd, *J* = 6.8 Hz and *J* = 3.2 Hz, 8H, H_r), 7.44 (s, 8H, H_t), 6.09 (d, *J* = 6.0 Hz, 8H, H_d), 5.86 (d, *J* = 6.0 Hz, 8H, H_e), 3.04 (sept, *J* = 6.8 Hz, 4H, H_b), 2.26 (s, 12H, H_g), 1.42 (d, *J* = 6.8 Hz, 24H, H_a). ^{13}C{^{1}H}-NMR ($(CD_3)_2CO$, 100 MHz): δ 154.9 (4C, C_h), 152.7 (4C, C_i), 142.4 (4C, C_k), 138.6 (8C, C_t), 133.0 (4C, C_u), 131.8 (8C, C_p), 128.3 (8C, C_r), 127.0 (8C, C_q), 126.8 (4C, C_j), 122.9 (4C, C_l), 117.7 (4C, C_o), 112.4 (8C, C_s), 109.3 (4C, C_{OTf}), 104.4 (4C, C_c), 100.9 (4C, C_f), 97.2 (4C, C_m), 91.7 (4C, C_n), 85.5 (8C, C_d), 83.72 (8C, C_e), 31.62 (4C, C_b), 22.48 (8C, C_a), 17.43 (4C, C_g). IR (cm^{-1}): 2971 (w; C–H

aromatic), 2204 (w; C≡C), 1531 (m; C=C aromatic), 967 (m; C–H aromatic), 852 (m; C–H aromatic), 763 (m; C–H aromatic), 635 (s, sharp; C–H aromatic). ESI–MS (+); m/z = 809.0 [M-2**L$_4$**-2 OTf$^-$]$^{2+}$, 1188.1 [M-2 OTf$^-$]$^{2+}$. UV−vis [1.0 x 10^{-5} M, CH_2Cl_2; λ_{max}, nm (ε, M^{-1}·cm^{-1})]: 271 (1.8 × 10^5), 310 (9.0 × 10^4), 445 (9.1 × 10^4), 476 (6.7 × 10^4), 694 (1.9 × 10^4). Anal. calc. for $C_{120}H_{96}F_{12}N_4O_{20}Ru_4S_4$ (2674.72): C 53.88, H 3.63, N 2.08; Found: C 53.69, H 3.59, N 2.15.

General procedure for the synthesis of dinuclear ruthenium(II) complexes with anthracene derivatives (**A$_{10}$ – A$_{13}$**)

A mixture of [Ru(η^6-*p*-cymene)(pta)Cl$_2$] [153] (100 mg, 0.22 mmol) and silver trifluoromethanesulfonate (55 mg, 0.22 mmol) was dissolved in CH_2Cl_2 (10 mL) and stirred for 3 h at room temperature. The mixture was filtrated in order to eliminate silver chloride. The resulting solution was added to a CH_2Cl_2 solution containing the anthracene ligand (**L$_1$-L$_4$**, 0.11 mmol). Then, the mixture was refluxed overnight and consequently concentrated under vacuum. The concentrated solution was slowly poured into cold Et_2O and/or pentane to induce precipitation. After filtration, the dinuclear assemblies were dried under vacuum.

[{Ru(η^6-*p*-cymene)(pta)Cl}$_2$(μ^2-L$_1$)][CF$_3$SO$_3$]$_2$ (A$_{10}$): Yellow solid (142 mg, 87%). ^{1}H-NMR (CD_3CN, 400 MHz): δ 8.97 (m, 4H, H$_j$), 7.64 (m, 4H, H$_k$), 7.60 (m, 4H, H$_o$), 7.52 (m, 4H, H$_p$), 5.93 (m, 8H, H$_d$ and H$_e$), 4.60 (m, 12H, H$_i$), 4.31 (m, 12H, H$_h$), 2.67 (sept, *J* = 6.8 Hz, 2H, H$_b$), 2.09 (s, 6H, H$_g$), 1.31 (d, *J* = 6.8 Hz, 6H, H$_a$), 1.17 (d, *J* = 7.2 Hz, 6H, H$_a$). ^{13}C{^{1}H}-NMR (CD_3CN, 100 MHz): δ 157.5 (4C, C$_j$), 134.5 (2C, C$_m$), 129.8 (4C, C$_i$), 129.7 (2C, C$_l$), 127.8 (4C, C$_o$), 126.9 (4C, C$_p$),123.7 (4C, C$_n$), 111.0 (2C, C$_c$), 101.4 (2C, C$_f$), 91.5 (2C, C$_d$), 89.7 (2C, C$_d$), 89.5 (2C, C$_e$), 85.6 (2C, C$_e$), 73.3 (3C, C$_i$), 73.2 (3C, C$_i$), 52.1 (3C, C$_h$), 52.0 (3C, C$_h$), 31.9 (2C, C$_b$), 22.5 (2C, C$_a$), 22.4 (2C, C$_a$), 18.6 (2C, C$_g$). IR (cm^{-1}): 3070 (w; C–H aromatic), 2938 (w; C–H aromatic), 1609 (m; C=C aromatic), 1255 (s; C=C aromatic), 1155 (m; C=C aromatic), 1028 (s; C=C aromatic), 637 (s; C–H aromatic). ESI–MS (+); m/z = 760.2 [M-{Ru(*p*-cymene)(pta)Cl}-2OTf$^-$]$^+$, 1337.2 [M-OTf$^-$]$^+$. UV−vis [1.0 x 10^{-5} M, CH_3CN; λ_{max}, nm (ε, M^{-1}.m^{-1})]: 359 (1.3 × 10^4), 377 (1.8 × 10^4), 399 (3.0 × 10^4), 439 (2.2 × 10^4). Anal. calc. for $C_{58}H_{68}N_8F_6P_2O_6Ru_2S_2Cl_2$ (1485.84): C 46.88, H 4.62, N 7.54; Found: C 44.07, H 4.66, N 7.17.

[{Ru(η^6-*p*-cymene)(pta)Cl}$_2$(μ^2-L$_2$)][CF$_3$SO$_3$]$_2$ (A$_{11}$): Yellow solid (113 mg, 69%). ^{1}H-NMR (CD_3CN,

400 MHz): δ 8.91 (m, 4H, H_j and H_k), 8.17 (d, *J* = 8 Hz, 2H, H_m), 7.86 (m, 2H, H_h), 7.58 (m, 8H, H_o and H_p), 5.89 (m, 8H, H_d and H_e), 4.59 (m, 12H, H_i), 4.24 (m, 12H, H_h), 2.58 (sept, *J* = 6.4 Hz, 2H, H_b), 2.01 (m, 6H, H_g), 1.15 (m, 12H, H_a). $^{13}C\{^1H\}$-NMR (CD_3CN, 100 MHz): δ 157.8 (1C, C_j), 157.0 (1C, C_j), 150.0 (2C, C_k), 143.2 (2C, C_m), 137.7 (2C, C_o), 133.1 (2C, C_p), 130.9 (2C, C_p), 129.8 (1C, C_l), 129.6 (1C, C_l), 127.7 (1C, C_q), 127.6 (1C, C_q), 127.5 (1C, C_q), 127.4 (1C, C_q), 127.2 (1C, C_r), 127.0 (1C, C_r), 126.9 (1C, C_r), 124.8 (1C, C_r), 123.7 (1C, C_n), 120.7 (1C, C_n), 113.0 (2C, C_c), 101.3 (2C, C_f), 91.2 (1C, C_d), 89.6 (1C, C_d), 89.5 (1C, C_d), 89.4 (1C, C_d), 89.3 (1C, C_e), 89.2 (1C, C_e), 85.7 (1C, C_e), 85.6 (1C, C_e), 73.3 (3C, C_i), 73.2 (3C, C_i), 52.2 (3C, C_h), 52.0 (3C, C_h), 31.9 (1C, C_b), 31.7 (1C, C_b), 22.4 (1C, C_a), 22.3 (1C, C_a), 22.2 (1C, C_a), 22.1 (1C, C_a), 18.6 (1C, C_g), (1C, C_g). IR (cm^{-1}): 3071 (w; C–H aromatic), 2936 (w; C–H aromatic), 1608 (m; C=C aromatic), 1257 (s; C=C aromatic), 1155 (m; C=C aromatic), 1028 (s; C=C aromatic), 636 (s; C–H aromatic). ESI–MS (+); m/z = 594.6 $[M\text{-}2OTf^-]^{2+}$, 760.2 [M-{Ru(*p*-cymene)(pta)Cl}-$2OTf^-]^+$, 1337.2 $[M\text{-}OTf^-]^+$. UV−vis [1.0 x 10^{-5} M, CH_3CN; λ_{max}, nm (ε, $M^{-1}.m^{-1}$)]: 357 (1.4 × 10^4), 376 (1.9 × 10^4), 399 (3.0 × 10^4), 441 (1.1 × 10^4). Anal. calc. for $C_{58}H_{68}N_8F_6P_2O_6Ru_2S_2Cl_2$ (1485.84): C 46.88, H 4.62, N 7.54; Found: C 44.88, H 4.49, N 7.16.

[{Ru(η⁶-*p*-cymene)(pta)Cl}₂(μ²-L₃)][CF₃SO₃]₂ (A₁₂): Dark yellow solid (93 mg, 55%). ^{1}H-NMR (CD_3CN, 400 MHz): δ 8.68 (m, 4H, H_j), 8.47 (d, *J* = 16.4 Hz, 1H, H_n), 8.39 (m, 4H, H_q), 8.31 (d, *J* = 16.4 Hz, 1H, H_n), 7.74 (m, 4H, H_k), 7.58 (m, 4H, H_r), 7.06 (d, *J* = 16.8 Hz, 1H, H_m), 6.97 (d, *J* = 16.4 Hz, 1H, H_m), 5.83 (m, 8H, H_d and H_e), 4.56 (m, 12H, H_i), 4.22 (m, 12H, H_h), 2.60 (sept, *J* = 7 Hz, 2H, H_b), 2.00 (s, 6H, H_g), 1.20 (m, 12H, H_a). IR (cm^{-1}): 3065 (w; C–H aromatic), 2940 (w; C–H aromatic), 1607 (m; C=C aromatic), 1257 (s; C=C aromatic), 1155 (m; C=C aromatic), 1029 (s; C=C aromatic), 637 (s; C–H aromatic). ESI–MS (+); m/z = 619.1 [M-{Ru(*p*-cymene)(pta)$_2$Cl$_2$}-$2OTf^-]^+$, 808.2 [M-{Ru(*p*-cymene)(pta)Cl}-$2OTf^-]^+$. UV−vis [1.0 x 10^{-5} M, CH_3CN; λ_{max}, nm (ε, $M^{-1}.m^{-1}$)]: 442 (5.1 × 10^4), 384 (1.3 × 10^4), 470 (3.6 × 10^4). Anal. calc. for $C_{62}H_{72}N_8F_6P_2O_6Ru_2S_2Cl_2$ (1537.92): C 48.42, H 4.73, N 7.29; Found: C 47.24, H 4.39, N 6.62.

[{Ru(η⁶-*p*-cymene)(pta)Cl}₂(μ²-L₄)][CF₃SO₃]₂ (A₁₃): Orange solid (130 mg, 77%). ^{1}H-NMR (CD_3CN, 400 MHz): δ 8.92 (d, *J* = 5.6 Hz, 2H, H_j), 8.73 (s, 1H, H_k), 8.17 (d, *J* = 8.4 Hz, 2H, H_l), 7.61 (d, *J* = 6 Hz, 2H, H_m), 7.58 (s, 1H, H_k), 7.52 (m, 8H, H_s and H_t), 5.78 (m, 8H, H_d and H_e), 4.56 (m, 12H, H_i), 4.28 (m, 12H, H_h), 2.65 (sept, *J* = 7.1 Hz, 2H, H_b), 2.06 (s, 6H, H_g), 1.30 (d, *J*

= 6.8 Hz, 6H, H_a), 1.16 (d, *J* = 7.2 Hz, 6H, H_a). $^{13}C\{^1H\}$-NMR (CD_3CN, 100 MHz): δ 157.1 (2C, C_j), 151.6 (1C, C_k), 150.6 (1C, C_k), 144.9 (2C, C_m), 132.1 (2C, C_r), 132.0 (2C, C_r), 129.9 (1C, C_t), 129.8 (1C, C_t), 129.6 (1C, C_t), 129.5 (1C, C_t), 129.4 (1C, C_l), 128.5 (1C, C_l), 127.7 (1C, C_n), 127.3 (1C, C_n), 127.1 (1C, C_s), 126.6 (1C, C_s), 126.5 (1C, C_s), 126.3 (1C, C_s), 126.0 (1C, C_q), 110.8 (2C, C_c), 101.1 (1C, C_f), 100.8 (1C, C_f), 96.8 (2C, C_p), 95.8 (2C, C_o), 91.2 (2C, C_d), 89.5 (2C, C_d), 89.2 (2C, C_e), 88.7 (2C, C_e), 73.1 (3C, C_i), 73.0 (3C, C_i), 52.8 (1C, C_h), 52.6 (1C, C_h), 52.1 (2C, C_h), 52.0 (2C, C_h), 31.8 (1C, C_b), 31.7 (1C, C_b), 22.4 (1C, C_a), 22.3 (1C, C_a), 22.2 (1C, C_a), 22.0 (1C, C_a), 18.5 (2C, C_g). IR (cm^{-1}): 3057 (w; C–H aromatic), 2940 (w; C–H aromatic), 2385 (w; C≡C), 1609 (m; C=C aromatic), 1259 (s; C=C aromatic), 1156 (m; C=C aromatic), 1029 (s; C=C aromatic), 367 (s; C–H aromatic). ESI–MS (+); m/z = 618.1 $[M\text{-}2OTf^-]^{2+}$, 808.2 [M-{Ru(*p*-cymene)(pta)Cl}-$2OTf^-]^+$, 1385.2 $[M\text{-}OTf^-]^+$. UV−vis [1.0×10^{-5} M, CH_3CN; λ_{max}, nm (ε, $M^{-1}.m^{-1}$)]: 371 (1.7×10^4), 385 (1.9×10^4), 396 (2.6×10^4), 444 (8.3×10^3). Anal. calc. for $C_{62}H_{68}N_8F_6P_2O_6Ru_2S_2Cl_2$ (1533.88): C 48.54, H 4.48, N 7.31; Found: C 48.18, H 5.01, N 6.82.

General procedure for the synthesis of mononuclear ruthenium(II) complexes with anthracene derivatives (**A_{14}** – **A_{15}**)

A mixture of [Ru(η^6-*p*-cymene)(pta)Cl_2] [153] (50 mg, 0.11 mmol) and silver trifluoromethanesulfonate (28 mg, 0.11 mmol) was dissolved in CH_2Cl_2 (5 mL) an stirred for 3 h at room temperature. The mixture was filtrated in order to eliminate silver chloride. The resulting solution was added to a CH_2Cl_2 solution containing the anthracene ligand (**L_6** or **L_7**, 0.11 mmol). Then, the mixture was refluxed overnight and consequently concentrated under vacuum. The concentrated solution was slowly poured into cold pentane to induce precipitation. After filtration, the mononuclear assemblies were dried under vacuum.

[{Ru(η^6-*p*-cymene)(pta)Cl}(μ^2-L_6)][CF_3SO_3] (A_{14}): yellow solid (71 mg, 78%). ^{1}H-NMR (CD_3CN, 400 MHz): δ 8.91 (d, *J* = 6 Hz, 1H, H_k), 8.74 (m, 2H, H_j and H_v), 8.19 (t, *J* = 7 Hz, 2H, H_q), 8.12 (d, *J* = 8 Hz, 1H, H_m), 7.78 (t, *J* = 6.4 Hz, 1H, H_l), 7.51 (m, 6H, H_k, H_r and H_s), 5.73 (m, 4H, H_d and H_e), 4.54 (m, 6H, H_i), 4.20 (m, 6H, H_h), 2.54 (sept, *J* = 7 Hz, 1H, H_b), 1.96 (s, 3H, H_g), 1.17 (d, *J* = 6.6 Hz, 3H, H_a), 1.09 (d, *J* = 6.8 Hz, 3H, H_a). $^{13}C\{^1H\}$-NMR (CD_3CN, 100 MHz): δ 157.1 (1C, C_j), 155.5 (1C, C_k), 142.2 (1C, C_m), 137.1 (1C, C_n), 131.3 (1C, C_o), 130.2 (4C, C_u and C_p), 128.8 (1C, C_v), 128.7 (1C, C_q), 128.6 (1C, C_q), 126.7 (2C, C_r), 126.2 (2C, C_s), 125.6 (1C, C_l),

125.2 (2C, C_t), 111.5 (1C, C_c), 100.3 (1C, C_f), 90.0 (1C, C_s), 88.3 (1C, C_s), 84.9 (2C, C_t), 72.3 (2C, C_i), 72.2 (1C, C_i), 51.2 (2C, C_h), 51.1 (1C, C_h), 30.7 (1C, C_b), 21.4 (1C, C_a), 21.2 (1C, C_a), 17.6 (1C, C_g). IR (cm^{-1}): 3057 (w; C–H aromatic), 2940 (w; C–H aromatic), 1444 (w; C=C aromatic), 1257 (s; C=C aromatic), 1156 (m; C=C aromatic), 1029 (s; C=C aromatic), 659 (s; C–H aromatic). ESI–MS (+); m/z = 683.2 $[M\text{-}OTf^-]^+$. UV−vis [1.0 x 10^{-5} M, CH_3CN; λ_{max}, nm (ε, $M^{-1}.m^{-1}$)]: 370 (1.4 × 10^4), 388 (1.5 × 10^4), 398 (2.2 × 10^4). Anal. calc. for $C_{36}H_{39}N_4F_3PO_3RuSCl$ (832.04): C 51.96, H 4.73, N 6.74; Found: C 48.35, H 4.78, N 6.85.

[{Ru(η⁶-*p*-cymene)(pta)Cl}(μ²-L₇)][CF₃SO₃] (A₁₅): yellow solid (42 mg, 45%). ^{1}H-NMR (CD_3CN, 400 MHz): δ 8.68 (d, *J* = 6.4 Hz, 2H, H_j), 8.59 (s, 1H, H_v), 8.48 (d, *J* = 16.4 Hz, 1H, H_m), 8.34 (m, 2H, H_q), 8.12 (m, 2H, H_t), 7.78 (d, *J* = 6.2 Hz, 2H, H_k), 7.56 (m, 4H, H_r and H_s), 7.09 (d, *J* = 16.8 Hz, 1H, H_n), 5.87 (m, 4H, H_d and H_e), 4.58 (m, 6H, H_i), 4.19 (m, 6H, H_h), 2.60 (sept, *J* = 6.8 Hz, 1H, H_b), 2.00 (s, 3H, H_g), 1.27 (m, 3H, H_a), 1.13 (d, *J* = 7.2 Hz, 3H, H_a). $^{13}C\{^1H\}$-NMR (CD_3CN, 100 MHz): δ 157.1 (2C, C_j), 147.4 (1C, C_l), 134.7 (1C, C_m), 133.9 (1C, C_n), 132.4 (1C, C_g), 131.7 (1C, C_l), 130.2 (1C, C_o), 129.9 (2C, C_t), 128.9 (1C, C_v), 127.3 (2C, C_r), 126.6 (2C, C_s), 126.3 (2C, C_q), 124.3 (2C, C_k), 116.4 (1C, C_c), 109.9 (1C, C_f), 91.5 (1C, C_d), 89.1 (2C, C_e), 85.8 (1C, C_d), 73.1 (3C, C_i), 51.5 (3C, C_h), 31.9 (1C, C_b), 22.5 (1C, C_a), 22.2 (1C, C_a), 18.6 (1C, C_g). IR (cm^{-1}): 3064 (w; C–H aromatic), 2942 (w; C–H aromatic), 1609 (m; C=C aromatic), 1253 (s; C=C aromatic), 1156 (m; C=C aromatic), 1027 (s; C=C aromatic), 637 (s; C–H aromatic). ESI–MS (+); m/z = 709.3 $[M\text{-}OTf^-]^+$. UV−vis [1.0 x 10^{-5} M, CH_3CN; λ_{max}, nm (ε, $M^{-1}.m^{-1}$)]: 371 (1.0 × 10^4), 396 (2.0 × 10^4), 342 (3.5 × 10^4). Anal. calc. for $C_{38}H_{41}N_4F_3PO_3RuSCl$ (858.08): C 53.19, H 4.83, N 6.53; Found: C 41.85, H 3.96, N 5.74.

Procedure for [{Ru(η⁶-*p*-cymene)Cl}₂(μ²-**L₈**)Cl₂] (**A₁₆**)

A mixture of [{Ru(η⁶-*p*-cymene)(μ²-Cl)Cl}₂] [154] (122 mg, 0.20 mmol) and 2,7-di-*tert*-butyl-4,9-di-(4-pyridyl)-*trans*-10b,10c-dimethyl-10b,10c-dihydropyrene (**L₈**, 100 mg, 0.20 mmol) were dissolved in CH_2Cl_2 (20 mL) and was stirred overnight at room temperature. The mixture was consequently concentrated under vacuum. The concentrated solution was slowly poured into cold Et_2O to induce precipitation. After filtration, the dinuclear assembly was dried under vacuum. The product was obtained as a brownish solid (140 mg, 63%). ^{1}H-NMR ($CDCl_3$, 400 MHz): δ 9,24 (d, *J* = 6 Hz, 4H, H_n), 8.65 (s, 2H, H_f), 8.63 (s, 2H, H_g), 8.46 (s, 2H, H_j), 7.81 (d, *J* =

5.6 Hz, 4H, H_m), 5.57 (d, *J* = 6 Hz, 4H, H_r), 5.34 (m, 4H, H_s), 3.08 (sept, *J* = 6.8 Hz, 2H, H_p), 2.23 (s, 6H, H_u), 1.62 (s, 18H, H_c), 1.39 (d, *J* = 6.8 Hz, 12H, H_o), -3.72 (s, 6H, H_a). $^{13}C\{^1H\}$-NMR ($CDCl_3$), 100 MHz): δ 154.6 (4C, C_n), 152.1 (2C, C_k), 148.4 (2C, C_e), 134.6 (2C, C_b), 133.3 (2C, C_h), 126.6 (4C, C_m), 125.6 (2C, C_l), 124.8 (2C, C_j), 123.2 (2C, C_g), 120.8 (2C, C_i), 120.1 (2C, C_f), 110.2 (2C, C_q), 97.6 (2C, C_t), 83.4 (4C, C_r), 82.4 (4C, C_s), 31.9 (6C, C_c), 30.9 (1C, C_p), 30.4 (2C, C_d), 29.9 (1C, C_p), 22.6 (4C, C_o), 18.5 (2C, C_u), 15.1 (2C, C_a). IR (cm^{-1}): 3038 (w; C–H aromatic), 2959 (m; C–H aromatic), 2866 (w; C–H aromatic), 1608 (m; C=C aromatic), 1467 (m; C=C aromatic), 1057 (m; C=C aromatic), 584 (s; C–H aromatic). ESI–MS (+); m/z = 520.2 $[M\text{-}2OTf^-]^+$. UV−vis [1.0 x 10^{-5} M, CH_2Cl_2; λ_{max}, nm (ε, $M^{-1}\cdot cm^{-1}$)]: 341 (3.7 × 10^4), 366 (3.9 × 10^4), 410 (5.6 × 10^4), 493 (1.5 × 10^4), 602 (1.3 × 10^3), 665 (3.9 x 10^3). Anal. calc. for $C_{56}H_{66}N_2Ru_2Cl_4$ (1111.18): C 60.53, H 6.00, N 2.52; Found: C 50.67, H 5.84, N 2.24.

X-ray Crystallographic data

Crystals were mounted on a Stoe Image Plate Diffraction system equipped with a Φ circle goniometer, using Mo Kα graphite monochromated radiation (λ = 0.71073 Å) with Φ range 0–200°. The structures were solved by direct methods using the program *SHELXS–97* [180], while the refinement and all further calculations were carried out using *SHELXL–97*. The H-atoms were included in calculated positions and treated as riding atoms using *SHELXL–97* default parameters. The non-H atoms were refined anisotropically using weighted full-matrix least-square on F^2. Figures were drawn with *ORTEP-32* [181]. The structural data deposited at The Cambridge Crystallographic Data Center: CCDC-1853676 (**L_4**), CCDC-1853677 (**A_7** · 4 acetone). This can be obtained free of charge at www.ccdc.cam.ac.uk/conts/retrieving.html (or from the Cambridge Crystallographic Data Center, 12, Union Road, Cambridge CB2 1EZ, UK; fax: (internat.) +44-1223/336-033; E-mail: deposit@ccdc.cam.ac.uk).

	L_4	L_6	A_7 · 4 acetone
Chemical formula	$C_{28}H_{16}N_2$	$C_{19}H_{13}N$	$C_{116}H_{112}F_{12}N_4O_{24}Ru_4S_4$
Formula weight	380.43	255.33	2706.61
Crystal system	monoclinic	monoclinic	triclinic
Space group	$P\,2_1$	$P\,2_{1/C}$	P -1
Crystal size (mm^3)	0.23 × 0.13 × 0.12	0.20 x 0.18 x 0.17	0.25 × 0.18 × 0.14
Crystal color and shape	colorless rod	Colorless block	yellow plate
a (Å)	5.0015(6)	9.2682(11)	16.0557(11)
b (Å)	16.944(2)	13.8896(17)	20.7694(15)
c (Å)	11.5374(15)	11.0542(12)	21.3136(14)
α (°)	90	90	115.639(5)
β (°)	92.433(10)	113.744(8)	98.267(5)
γ (°)	90	90	101.194(6)
Cell volume ($Å^3$)	976.9(2)	1302.57	6073.6(8)
T (K)	293(2)	293(2)	203(2)
Z	2	4	2
Scan range (°)	$1.77 < \vartheta < 29.30$	$2.40 < \vartheta < 26.21$	$1.48 < \vartheta < 29.33$
ρ_{calcd} ($g.cm^{-3}$)	1.293	1.302	1.480
μ (mm^{-1})	0.076	0.076	0.644
Unique reflections	5272	2611	32944
Reflections used [$I > 2\sigma(I)$]	1378	1959	9666
R_{int}	0.1715	0.0244	0.2498
final R indices [$I > 2\sigma(I)$][a]	0.0799, wR_2 0.1714	0.0608, wR_2 0.1040	0.0911, wR_2 0.2228
R indices (all data)[b]	0.2499, wR_2 0.2388	0.0396, wR_2 0.0912	0.2609, wR_2 0.2939
GOF[c]	0.805	1.074	0.836
max, min $\Delta\rho/e$ ($Å^{-3}$)	0.268, -0.196	1.138, -0.124	1.627, -1.213

[a] $R_1 = \Sigma||F_o| - |F_c||/\Sigma|F_o|$. [b] $wR_2 = \{\Sigma[w(F_o^2 - F_c^2)^2]/\Sigma[w(F_o^2)^2]\}^{1/2}$. [c] GOF = $\{\Sigma[w(F_o^2 - F_c^2)^2]/(n - p)\}^{1/2}$, where n is the number of reflections and p is the total number of parameters refined.

Procedure for the photooxygenation of ligands L_{anthr} (L_1-L_7) and assemblies A_{anthr} (A_1-A_{15}) with anthracene derivatives. [143]

Stock solutions of L_{anthr} (L_1-L_7; 10^{-3} M; 2 mL) and TPP (1.10^{-4} M; 2 mL) were prepared in CH_2Cl_2 while stock solutions of A_{anthr} (A_1-A_{15}; 10^{-3} M; 2 mL) were prepared in CH_3CN, both solvents were firstly degassed with three cycles of freeze-pumping. The different samples were prepared by mixing TPP (250 µL) and L_{anthr} or A_{anthr} (500 µL). Each sample has a final concentration in CH_2Cl_2 of TPP of 1.10^{-5} M and L_{anthr} or A_{anthr} of 5.10^{-5} M.

Photooxygenation was realized on each sample by first, bubbling O_2 in a closed vial for 30 seconds and then, by irradiating with white lamp in a photoreactor. In order to follow the kinetics of the photooxygenation, measurements were realized at 0, 30, 60, 90, 120, 150, 180, 240, 300, 360, 420, 480, 540, 600, 720, 840, 960, 1200, 1500, 1800, 2100, 2400, 3000

seconds. ^{1}H NMR were also realized to follow the formation of endoperoxides (at 0 h and 15 h of irradiation).

Procedure for the photooxygenation of ligands L_{DHP} (L_8-L_{12}).

Solutions of L_{DHP} (L_8-L_{12}; 2.5 or 1.0 x 10^{-5} M; 5 mL) were prepared in CH_3CN. For L_8 and L_9, few drops of $CDCl_3$ were added to help the dissolution of the compound. Several cycles of freeze-pumping were realized to remove the diluted oxygen. In some case, preparation of solutions was made in a glovebox to avoid any contamination with oxygen. The irradiations were made either with a Xe-Hg lamp (500 W, unless otherwise specified) and using appropriate cut-off filter (490, 555 and 715 nm) or with the special LEDs (green and amber, see above). Oxygen gas was not bubbled into the solution: the atmospheric air was enough for the experiment. Measurements were realized at different time points. ^{1}H NMR of the L_{DHP} solutions (1.0 x 10^{-5} M, 500 µL) were also realized to follow the formation of endoperoxides (usually at 0,15, 24, 39 h of irradiation). 0.25 equivalent of MSA was used for each addition in an acetonitrile solution (2.5 x 10^{-5} M), until an excess (3 equivalents).

Biological tests for ligands and assemblies with anthracene derivatives

All manipulations were carried out under an inert atmosphere and strict sterilization conditions. DU145 prostatic cancer cells were provided by the American Type Culture Collection (LGC Standards,Middlesex, UK). 3-(4,5-dimethylthiazol-2-yl)-2,5-diphenyltetrazoliumbromide (MTT) and L-glutamine were purchased from Sigma-Aldrich Steinheim, Germany. Dimethyl sulfoxide (DMSO) were purchased from Acros Organics New Jersey, USA. RPMI-1640, fetal bovine serum (FBS) and penicillin/streptomycin were purchased from Gibco BRL Cergy-Pontoise, France. The organometallic complexes and organic compounds were dissolved at 1 mM in DMSO as the stock solution and then diluted in complete medium to the required concentration immediately preceding to use. DMSO concentrations used were always < 0.1 %. Cell irradiation was carried out using a red light source of 630 nm, 75 J/cm^2, CureLight®, PhotoCure ASA. Absorbanse after MTT assay was

measured by Dynex Triad Multi Mode Microplate Reader, Dynex Technologies.

Cell culture

DU145 cells were grown in a 75 cm^2 culture flasks in RPMI complete medium containing 10 % of FBS, 5 % of L-glutamine and 5 % of penicillin/streptomycin. The culture medium was renewed every 2 days. Cells were subcultured by dispersal with trypsin-EDTA and replated at 7.5 x 10^4 cells/ml in fresh medium.

Photodynamic therapy

DU145 prostatic cancer cells were plated in 96-well plates (7000 cells/100 µl per well) and incubated in the dark in complete medium for 24 h, maintained at 37 °C in humidified atmosphere with 5 % CO_2. Then, 100 µl of medium with different concentrations of ruthenium complexes (10, 100, 250, 500, 750 and 1000 nM) and TPP (1/5 of concentrations of the complex) were added, maintained 24 h at 37 °C in humidified atmosphere with 5% CO_2. After 24 h, the medium was removed and replaced by medium without phenol red containing 10 % FBS, 5 % of L-glutamine and 5 % of penicillin/streptomycin. Cells were irradiated at 40 mW/cm^2 for 30 minutes. Cell survival was tested by MTT assay 24 h after, using 10 µL of MTT per well. After 4 h, the medium was removed and added 200 µL of DMSO.

6. References

1. Fior, R. Cancer – when Cells Break the Rules and Hijack Their Own Planet. In *Molecular and Cell Biology of Cancer;* Fior, R.; Zilhão, R., Eds.; Springer Nature Switzerland AG: Cham, Switzerland, 2019, pp. 1-20.
2. WHO I Home. https://www.who.int (accessed in October 2019)
3. WHO I Cancer, Key facts. https://www.who.int/news-room/fact-sheets/detail/cancer (accessed in October 2019)
4. International Agency for Research on Cancer I Cancer Fact Sheet. https://gco.iarc.fr/today/data/factsheets/cancers/39-All-cancers-fact-sheet.pdf (accessed in October 2019)
5. International Agency for Research on Cancer I Cancer Today. https://gco.iarc.fr/today/online-analysis-map?v=2018&mode=population&mode_population=continents&population=900&npopulations=900&key=asr&sex=0&cancer=39&type=0&statistic=5&prevalence=0&population_group=0&ages_group%5B%5D=0&ages_group%5B%5D=17&nb_items=5&gro (accessed in October 2019)
6. Forman, D; Ferlay, J. - The global and regional burden of cancer. In *World Cancer Report 2014*; Stewart, B. W.; Wild, C. P., eds. The international Agency for Research on Cancer: Lyon, France, 2014, pp. 16-53.
7. Sutcliffe, S. B. - National cancer control plans. In *World Cancer Report 2014*; Stewart, B. W.; Wild, C. P., eds. The international Agency for Research on Cancer: Lyon, France, 2014, pp. 529-535.
8. Miller, M. E. – Introduction. In *Cancer;* Campbell, A. M., Eds.; Momentum Press: New York, USA, 2018, pp. xiii-xxii.
9. Cooper, G. M.; Hausman, R. E. – Cancer. In *The Cell, A Molecular Approach;* Cooper, G. M.; Hausman, R. E., Eds.; The American Society for Microbiology: Washington, USA, 2007, 4th edition, pp. 719-765.
10. Vogelstein, B.; Papadopoulos, N.; Velculescu, V. E.; Zhou, S.; Diaz Jr., L. A.; Kinzler, K. W. Cancer Genome Landscapes. *Science*, 2013, *339*, 1546-1558.
11. American Society of Clinical Oncology I Cancer terms. https://www.cancer.net/navigating-cancer-care/cancer-basics/cancer-terms (accessed October 2019)
12. Luo, W.; Wang, Y. – Hypoxia Mediates Tumor Malignancy and Therapy Resistance. In *Hypoxia and Cancer Metastasis;* Gilkes, D. M., Eds.; Springer Nature Switzerland: Cham, Switzerland, 2019, pp. 1-18.

13. Höckel, M.; Vaupel, P. Tumor Hypoxia : Definitions and Current Clinical, Biologic, and Molecular Aspects. *J. Natl. Cancer Inst.*, **2001**, *93*, 266-276.
14. Muz, B.; de la Puente, P.; Azab, F.; Azab, A. K. The role of hypoxia in cancer progression, angiogenesis, metastasis, and resistance to therapy. *Hypoxia*, **2015**, 3, 83-92.
15. Al Tameemi, W.; Dale, T. P.; Al-Jumaily, R. M. K.; Forsyth, N. R. Hypoxia-Modifies Cancer Cell Metabolism. *Front. Cell Dev. Biol.*, **2019**, *7*, 1-15.
16. Mckeown, S. R. Defining normoxia, physoxia and hypoxia in tumours-implications for treatment response. *Br. J. Radiol.*, **2014**, *87*,1-12.
17. Gray, L. H.; Conger, A. D.; Ebert, M.; Hornsey, S.; Scott, O. C. Concentration of oxygen dissolved in tissues at the time of irradiation as a factor in radiotherapy. *Br. J. Radiol.* **1953**, *26*, 638-648.
18. Thomlinson, R. H.; Gray, L. H. The histological structure of some human lung cancers and the possible implications for radiotherapy. *Br. J. Radiol.* **1955**, *9*, 539-549.
19. Tatum, J. L.; Kelloff, G. J.; Gillies, R. J; Arbeit, J. M.; Brown, J. M.; Chao, K. S.; Chapman, J. D.; Eckelman, W. C.; Fyles, A. W.; Giaccia, A. J.; Hill, R. P.; Koch, C. J.; Krishna, M. C.; Krohn, K. A.; Lewis, J. S.; Mason, R. P.; Melillo, G.; Padhani, A. R.; Powis, G.; Rajendran, J. G.; Reba, R.; Robinson, S. P.; Semenza, G. L.; Swartz, H. M.; Vaupel, P.; Yang, D. Hypoxia: Importance in tumor biology, noninvasive measurement by imaging, and value of its measurement in the management of cancer therapy. *Int. J. Radiat. Biol.*, **2006**, *82*, 699-757.
20. Vaupel, P.; Schlenger, K.; Knoop, C.; Höckel, M. Oxygenation of human tumors: evaluation of tissue oxygen distribution in breast cancers by computerized O2 tension measurements. *Cancer Res.* **1991**, *51*, 3316-3322.
21. Vaupel, P.; Höckel, M.; Mayer, A. Dectection and characterization of tumor hypoxia using pO2 histograpy. *Antioxid.Redox Signaling*, **2007**, *9*, 1221-1235.
22. Le, Q. T.; Kovacs, M. S.; Dorie, M. J.; Koong, A.; Terris, D. J.; Pinto, H. A.; Goffinet, D. R.; Nowels, K.; Bloch, O.; Brown, J. M. Comparison of the comet assay and the oxygen microelectrode for measuring tumor oxygenation in head-and-neck cancer patients. Int. J. Radiat. Oncol., Biol., Phys., **2003**, *56*, 375-383.
23. Le, Q. T.; Chen, E.; Salim, A.; Cao, H.; Kong, C. S.; Whyte, R.; Donington, J.; Cannon, W.; Wakelee, H.; Tibshirani, R.; Mitchell, J. D.; Richardson, D.; O'Byrne, K. J.; Koong, A. C.; Giaccia, A. J. An evaluation of tumor oxygenation and gene expression in patients with early stage non-small cell lung cancers. *Clin. Cancer Res.*, **2006**, *12*, 1507-1514.
24. Koong, A. C.; Mehta, V. K.; Le, Q. T., Fisher, G. A.; Terris, D. J.; Brown, J. M.; Bastidas, A. J.; Vierra, M. Pancreatic tumors show high levels of hypoxia. *Int. J. Radiat. Oncol., Biol., Phys.*, **2000**, *48*, 919-922.
25. Movsas, B.; Chapman, J. D.; Hanlon, A. L.; Horwitz, E. M.; Pinover, W. H.; Greenberg, R. E.; Stobbe, C.; Hanks, G. E. Hypoxia in human prostate carcinoma: an Eppendorf PO_2 study. *Am. J. Clin. Oncol.*, **2001**, 24, 458-61.
26. Vaupel, P.; Kelleher, D. K – Blood Flow and Oxygenation Status of Gastrointestinal Tumors. In

Oxygen transport to tissue XXXIII; Wolf, M.; Bucher, H. U.; Rudin, M., Van Huggels, S.; Wolf, U.; Bruley, D. F.; Harison, D. K., Eds.; Springer: New York, USA, 2012, pp. 133-138.

27. Collingridge, D. R.; Young, W. K.; Vojnovic, B.; Wardman, P.; Lynch, E. M.; Hill, S. A.; Chaplin D. J. Measurement of Tumor Oxygenation: A Comparison between Polarographic Needle Electrodes and a Time-Resolved Luminescence-Based Optical Sensor. *Radiat. Res.*, **1997**, *147*, 329-334.
28. Dhani, N.; Fyles, A.; Hedley, D.; Milosevic, M. The clinical significance of hypoxia in human cancers. *Semin. Nucl. Med.*, **2015**, *45*, 110-121.
29. Graham, K.; Unger, E. Overcoming tumor hypoxia as a barrier to radiotherapy, chemotherapy and immunotherapy in cancer treatment. *Int. J. Nanomed.*, **2018**, *13*, 6049-6058.
30. Russell, J.; Carlin, S.; Burke, S. A.; Wen, B.; Yang K. M.; Ling, C. C. Immunohistochemical Detection of Changes in Tumor Hypoxia. *Int. J. Radiat. Oncol. Biol. Phys.*, **2009**, *73*, 1177-1186.
31. Ziemer, L.S.; Evans, S. M.; Kachur, A. V.; Shuman, A. L.; Cardi, C. A.; Jenkins, W. T.; Karp, J. S.; Alavi, A.; Dolbier, W. R.; Koch, C. J. Noninvasive imaging of tumor hypoxia in rats using the 2-nitroimidazole 18F-EF5. *Eur. J. Nucl. Med. Mol. Imaging*, **2003**, *30*, 259-266.
32. Piert, M.; Machulla, H. J.; Picchio, M.; Reischl, G.; Ziegler, S.; Kumar, P.; Wester, H. J.; Beck, R.; McEwan, A. J.; Wiebe, L. I.; Schwaiger, M. Hypoxia-specific tumor imaging with 18F-fluoroazomycin arabinoside. *J. Nucl. Med.*, **2005**, *46*, 106-113.
33. Van Loon, J.; Janssen, M. H. M.; Öller, M.; Aerts, H. J. W. L.; Dubois, L.; Hochstenbag, M.; Dingemans, A.-M. C.; Lalisang, R.; Brans, B.; Windhorst, B.; Van Dongen, G. A.; Kolb, H.; Zhang, J.; De Ruysscher, D.; Lambin, P. PET imaging of hypoxia using [18F]HX4: a phase I trial. *Eur. J. Nucl. Med. Mol. Imaging*. **2010**, *37*, 1663-1668.
34. O'Connor, J. P. B.; Robinson, S. P.; Waterton, J. C. Imaging tumour hypoxia with oxygen-enhancerd MRI and BOLD MRI. *Br. J. Radiol.*, **2018**, *92*, 20180642.
35. Minassian, L. M.; Cotechini, T.; Huitema, E.; Graham, C. H. – Hypoxia-Induced Resistance to Chemotherapy in Cancer. In *Hypoxia and Cancer Metastasis;* Gilkes, D. M., Eds.; Springer Nature Switzerland: Cham, Switzerland, 2019, pp. 123-139.
36. Semenza, G. L.; Wang, G. L. A Nuclear Factor Induced by Hypoxia via De Novo Protein Synthesis Binds to the Human Erythropoietin Gene Enhancer at a Site Required for Transcriptional Activation. *Mol. Cell Biol.*, **1992**, *12*, 5447-5454.
37. Weidemann, A.; Johnson, R. S. Biology of HIF-1α. *Cell Death Differ.*, **2008**, *15*, 621-627.
38. Brahimi-Horn, M. C.; Pouysségur, J. Oxygen, a source of life and stress. *FEBS Lett.*, **2007**, *581*, 3582-3591.
39. Rohwer, N.; Cramer, T. Hypoxia-mediated drug resistance: Novel insight on the functional interaction of HIFs and cell death pathways. *Drug Resist. Updates*, **2011**, *14*, 191-201
40. Shito, L. – Hypoxia-Dependent Angiogenesis and Lymphangiogenesis in Cancer. In *Hypoxia and Cancer Metastasis;* Gilkes, D. M., Eds.; Springer Nature Switzerland: Cham, Switzerland, 2019, pp. 71-85.

41. Forster, J. C.; Hariss-Phillips, W. M.; Douglass, M. J.-J.; Bezak, E. A review of the development of tumor vasculature and its effects on the tumor microenvironment. *Hypoxia*, **2017**, *5*, 21-32.
42. Sever, R.; Brugge, J. S. Signal Transduction in Cancer. *Cold Spring Harbor Perspectives in Medicine*, **2015**, *5*, 1-20.
43. Hay, E. D. An overview of epithelio-mesenchymal transformation. *Acta Anat.*, **1995**, *154*, 8-20.
44. Kalluri, R.; Weinberg, R. A. The basics of epithelial-senchymal transition. J. *Clin. Inverst.*, **2009**, *119*, 1420-1428.
45. Lash, G. E.; Fitzpatrick, T. E.; Graham, C. H. Effect of Hypoxia on Cellular Adhesion to Vitronectin and Fibronectin. *Biochem. Biophys. Res. Commun.*, **2001**, *287*, 622-629.
46. Hasan, N. M.; Adams, G. E.; Joiner, M. C.; Marshall, J. F.; Hart, I. R. Hypoxia facilitates tumour cell detachment by reducing expression of surface adhesion molecules and adhesion to extracellular matrices without loss of cell viability. *Br. J. Cancer*, **1998**, *77*, 1799-1805.
47. Kokura, S.; Yoshida, N.; Imamoto, E.; Ueda, M.; Ishikawa, T.; Uchiyama, K.; Kuchide, M.; Naito, Y.; Okanoue, T.; Yoshikawa, T. Anoxia/reoxygenation down-regulates the expression of E-cadherin in human colon cancer cell lines. *Cancer Lett.*, **2004**, *211*, 79-87.
48. Warburg, O. The Metabolism of Carcinoma Cells. *J. Cancer Res.*, **1925**, *9*, 148-163.
49. Warburg, O.; Posener, K.; Negelein, E. Ueber den stoffwechsel der tumoren. *Biochem. Z.*, **1924**, *152*, 319-344.
50. Warburg, O. On the origin of cancer cells. *Science,* **1956**;*123,* 309–314.
51. Siekevitz, P. Powerhouse of the cell. *Sci. Am.*, **1957**, *197*, 131-144.
52. Vander Heiden, M. G.; Cantley, L. C.; Thompson, C. B. Understanding the Warburg Effect: The Metabolic Requirements of Cell Proliferation. *Science*, **2009**, *324*, 1029-1033.
53. Pavlova, N. N.; Thompson, C. B. The Emerging Hallmarks of Cancer Metabolism. *Cell Metab.*, **2016**, *23*, 27-47.
54. DeBerardinis, R. J.; Lum, J. J.; Hatzivassiliou, G.; Thompson, C. B. The Biology of Cancer: Matabolic Reprogramming Fuels Cell Growth and Proliferation. *Cell Metab.* **2008**, *7*, 11-20.
55. Lehninger, A. L.; Nelson, D. L.; Cox, M. M. Oxidative Phosphorylation. In *Principles of Biochemistry;* Freeman, W. H., Eds.; Macmillan Higher Education: Houndmills, England, 6th Ed., 2013, 731-798.
56. Lehninger, A. L.; Nelson, D. L.; Cox, M. M. *Principles of Biochemistry;* Freeman, W. H., Eds.; Macmillan Higher Education: Houndmills, England, 7th Ed, 2017, 1328 p.
57. Webb, B. A.; Chimenti, M.; Jacobson, M. P.; Barber, D. L. Dysregulated pH: a perfect storm for cancer progression. *Nat. Rev. Cancer*, **2011**, *11*, 671-677.
58. Gallagher, F. A.; Kettunen, M. I.; Day, S. E.; Hu, D. E.; Ardenkjær-Larsen, J. H.; Jensen, P. R., Karlsson, M.; Golma, K.; Lerche, M. H.; Brindle, K. M. Magnetic resonance imaging of pH in vivo using hyperpolarized 13 C-labelled bicarbonate. *Nature*, **2008**, *453*, 940-943.
59. Stüwe, L.; Müller, M.; Fabian, A.; Waning, J.; Mally, S.; Noël, J.; Schwab, A.; Stock, C. pH dependence of melanoma cell migration: protons extruded by NHE1 dominate protons of the bulk

solution. *J. Physiol.,* **2007**, *585*, 351-360.

60. Wang, H.; Jiang, H.; Van De Gucht, M.; De Ridder, M. Hypoxic Radioresistance: Can ROS Be the Key to Overcome It? *Cancers,* **2019**, *11*, 112-134.
61. Wouters, A.; Pauwels, B.; Lardon, F.; Vermorken, J. B. Review: Implications of In Vitro Research on the Effect of Radiotherapy and Chemotherapy Under Hypoxic Conditions. *Oncologist,* **2007**, *12*, 690-712.
62. Minassian, L. M.; Cotechini, T.; Huitema, E.; Graham, C. H. – Hypoxia-Induced Resistance to Chemotherapy in Cancer. In *Hypoxia and Cancer Metastasis;* Gilkes, D. M., Eds.; Springer Nature Switzerland: Cham, Switzerland, 2019, pp. 123-139.
63. Teicher, B. A. Hypoxia and drug resistance. *Cancer Metastasis Rev.*, **1994**, *13*,139-168.
64. Assaraf, Y. G.; Brozovic, A.; Gonçalves, A. C.; Jurkovicova, D.; Linē, A.; Machuqueiro, M.; Saponara, S.; Sarmento-Ribeiro, A. B.; Xavier, C. P. R.; Vasconcelos, M. H. The multi-factorial nature of clinical multidrug resistance in cancer. *Drug Resist Updat.*, **2019**, *46*:100645.
65. Miller, M. E. – Treatment and Therapy. In *Cancer;* Campbell, A. M., Eds.; Momentum Press: New York, USA, 2018, pp. 33-46.
66. Melford, J. A guide to Cancer. Origins and Revelations*;* Melford, J., Eds.; CRC Press: Boca Raton, USA, 2017, 207 pp.
67. Universitäts Bibliothek Leipzig (UBL) I Ebers Papyrus. www.ub.uni-leipzig.de:9000/54d8b146f3e91b134c000038/apps/55327c81569c2c2d3d000ed3/en.html (accessed in December 2019)
68. Dolmans, D.E.J.G.J.; Fukumura, D.; Jain, R.K. Photodynamic therapy for cancer. *Nat. Rev. Cancer* **2003**, *3*, 380–387.
69. Grzybowski, A.; Sak, J.; Pawlikowski, J. A brief report on the history of phototherapy. *Clin. Dermatol.*, **2016**, *34*, 532-537.
70. Ackroyd, R.; Kelty, C.; Brown, N.; Reed, M. The History of Photodetection anf Photodynamic Therapy. *Photochem. Photobiol.*, **2001**, *74*, 656-669.
71. Raab, O. Uber die wirkung fluoreszierender stoffe auf infusorien. *Zeitung Biol.* **1900**, *39*, 524–526.
72. Prime, J. *Des Accidents Toxiques Produit par l'Eosinate de Sodium.* Jouve et Boyer: Paris, France, 1900, 76 pp.
73. Møller, K. I.; Kongshoj, B.; Phillipsen, P. A.; Thomsen, V. O.; Wulf, H. C. How Finsen's light cured lupus vulgaris. *Photodermatol. Photoimmunol. Photomed.*, **2005**, *21*, 118-124.
74. Von Tappeiner, H.; Jesionek, A. A. Therapeutische versuche mit fluoreszierenden stoffen. *Muench Med. Wochenschr,* **1903**, *47,* 2042-2044.
75. Von Tappeiner, H. A.; Jodlbauer, A. Die Sensibilisierende Wirkung Fluorescierender Substanzen: Gesammelte Untersuchungen u□ber die Photodynamische Erscheinung. F.C.W. Vogel.: Leipzig, Germany, 1907.

76. Meyer-Betz, F. Untersuchungen uber die biologische photodynamische wirkung des hematoporphyrins und anderer derivative des blut und galenafarbstoffs. *Dtsch. Arch. Klin.* **1913**, 112, 476–503.
77. Wikipedia I Niels Ryberg Finsen. en.wikipedia.org/wiki/Niels_Ryberg_Finsen (accessed in December 2019).
78. Wikipedia I Hermann von Tappeiner. en.wikipedia.org/wiki/Hermann_von_Tappeiner (accessed in December 2019).
79. Rassmussan-Taxdal, D. S.; Ward, G. E.; Figge, F. H. Fluorescence of human lymphatic and cancer tissues following high doses of intravenous hematoporphyrin. *Cancer,* **1955**, *8*, 78–81.
80. (a) Lipson, R. L.; Baldes, E. J. The photodynamic properties of a particular hematoporphyrin derivative. *Arch. Dermatol.*, **1960**, *82*, 508–516. (b) Lipson, R. L.; Baldes, E. J.; Olsen, A. M. The use of an derivative of hematoporphyrin in tumor detection. *J. Natl Cancer Inst.*, **1961**, *26*, 1–11. (c) Lipson, R. L.; Baldes, E. J.; Olsen, A. M. Hematoporphyrin derivative: a new aid for endoscopic detection of malignant disease. *J. Thorac. Cardiovasc. Surg.*, **1961**, *42*, 623–629.
81. Schwartz, S. K.; Abolon, K.; Vermund, H. Some relationships of porphyrins, X-rays and tumors. *Univ. Minn. Med. Bull.*, ***1955***, 27, 7–8.
82. Diamond, I.; Granelli, S. G.; McDonagh, A. F.; Nielsen, S.; Wilson, C. B.; Jaenicke, R. Photodynamic therapy of malignant tumours. *Lancet*, **1972**, *2*, 1175–1177.
83. (a) Dougherty, T. J.; Grindey, G. B.; Fiel, R.; Weishaupt, K. R.; Boyle, D. G. Photoradiation therapy. II. Cure of animal tumors with hematoporphyrin and light. *J. Natl. Cancer Inst.,* **1975**, *55*, 115–121. (b) Dougherty, T. J.; Kaufman, J. E.; Goldfarb, A.; Weishaupt, K. R.; Boyle, D.; Mittleman, A. Photoradiation therapy for the treatment of malignant tumors. *Cancer Res.*, **1978**, *38*, 2628-2635.
84. (a) Kelly, J. F.; Snell, M. E.; Berenbaum, M. C. Photodynamic destruction of human bladder carcinoma. *Br. J. Cancer*, **1975**, *31*, 237–244. (b) Kelly, J. F.; Snell, M. E. Hematoporphyrin derivative: a possible aid in the diagnosis and therapy of carcinoma of the bladder. *J. Urol.*, **1976**, *115*, 150–151.
85. Erickson, L.; Nguyen, V. H.; Niamba, S. Assessment of photodynamic therapy using porfimer sodium for esophageal, bladder and lung cancers. Agence d'e□valuation des technologies et des modes d'intervention en sante□ (AETMIS) : Montréal, Canada, 2004, 51 pp.
86. Juarranz, A.; Jaén, P.; Sanz-Rodríguez, F.; Cuevas, J.; González, S. Photodynamic therapy of cancer. Basic principles and applications. *Clin. Trans. Oncol.*, **2008**, *10*, 148-154.
87. Agostinis, P.; Berg, K.; Cengel, K.A.; Foster, T.H.; Girotti, A.W.; Gollnick, S.O.; Hahn, S.M.; Hamblin, M.R.; Juzeniene, A.; Kessel, D.; et al. Photodynamic therapy of cancer: An update. *CA Cancer J. Clin.*, **2011**, *61*, 250–281.
88. Matsumura, Y.; Maeda, H. A new concept for macromolecular therapeutics in cancer chemotherapy: mechanism of tumoritropic accumulation of proteins and the antitumor agent smancs. *Cancer Res.*, **1986**, *46*, 6387-6392.

89. Foote, C. S. Definition of type I and type II photosensitized oxidation. *Photochem. Photobiol.*, **1991**, *54*, 659.
90. Debele, T.A.; Peng, S.; Tsai, H.C. Drug carrier for photodynamic cancer therapy. *Int. J. Mol. Sci.* **2015**, *16*, 22094–22136.
91. Juzeniene, A.; Nielsen, K. P.; Moan, J. Biophysical aspects of photodynamic therapy. *J. Environ. Pathol. Toxicol. Oncol.*, **2006**, *25*, 7-28.
92. Josefsen, L. B.; Boyle, R. W. Photodynamic Therapy and the development of metal-based photosensitizers. *Metal-based drugs*, **2008**, *4*, 250-281.
93. Ogilby, P. R. Singlet oxygen: there is indeed something new under the sun.
94. Krumova, K.; Cosa, G. Overview of Reactive Oxygen Species. In *Singlet Oxygen: Applications in Biosciences and Nanosciences*; Nonell, S., Flors, C., Eds.; The Royal Society of Chemistry: Cambridge, UK, 2016; Volume 2, pp. 3–21.
95. Girotti, A. W. Photosensitized oxidation of membrane lipids: reaction pathways, cytotoxic effects, and cytoprotective mechanisms. *J. Photochem. Photobiol. B.*, **2001**, *63*, 103-113.
96. Schweitzer, C.; Schmidt, R. Physical Mechanisms of Generation and Deactivation of Singlet Oxygen. *Chem. Rev.*, **2003**, *103*, 1685-1757.
97. Boix-Garriga, E.; Rodríguez-Amigo, B.; Planas, O.; Nonell, S. Properties of Singlet Oxygen. In *Singlet Oxygen: Applications in Biosciences and Nanosciences*; Nonell, S., Flors, C., Eds.; The Royal Society of Chemistry: Cambridge, UK, 2016; Volume 2, pp. 23–46.
98. Baskaran, R.; Lee, J.; Yang, S.-G. Clinical development of photodynamic agents and therapeutic applications. *Biomater. Res.*, **2018**, *2018*, 22-25.
99. Allison, R. R.; Sibata, C. H. Oncologic photodynamic therapy photosensitizers: A clinical review. *Photodiagn. Photodyn. Ther.*, **2010**, *7*, 61-75.
100. O'Connor, A. E.; Gallagher, W. M.; Byrne, A. T. Porphyrin and nonporphyrin photosensitizers in oncology: preclinical and clinical advances in photodynamic therapy. *Photochem. Photobiol.*, **2009**, *85*, 1053-1074.
101. Ormond, A. B.; Freeman, H. S. Dye Sensitizers for Photodynamic Therapy. *Materials*, **2013**, *6*, 817-840.
102. (a) Abdel-Kader, M. H. The journey of PDT throughout History: PDT from Pharos to Present. In *Photodynamic Medicine: From Bench to Clinic*; Kostron, H.; Hasan, T., Eds.; The Royal Society of Chemistry: Cambridge, UK, 2016; pp. 1-21. (b) Rodríguez-Amigo, B.; Planas, O.; Bresolí-Obach, R.; Torra, J.; Ruiz-González, R.; Nonell, S. Photosensitizers for Photodynamic Therapy: State of the Art and Perspectives. In *Photodynamic Medicine: From Bench to Clinic*; Kostron, H.; Hasan, T., Eds.; The Royal Society of Chemistry: Cambridge, UK, 2016; pp. 1-21.
103. Heinemann, F.; Karges, J.; Gasser, G. Critical overview of the use of Ru(II) polypyridyl complexes as photosensitizers in one-photon and two-photon photodynamic therapy. *Acc. Chem. Res.*, **2017**, *50*, 2727–2736.
104. Zhang, J.; Jiang, C.; Figueiró Longo, J. P.; Bentes Azevedo, R.; Zhang, H.; Muehlmann, L. A. An

updated overview on the development of new photosensitizers for anticancer photodynamic therapy. *Acta Pharm. Sin. B.*, **2018**, *8*, 137-146.

105. Abrahamse, H.; Hamblin, M. R. New photosensitizers for photodynamic therapy. *Biochem. J.*, **2016**, *473*, 347-364.
106. Lan, M.; Zhao, S.; Liu, W.; Lee, C. S.; Zhang, W.; Wang, P. Photosensitizers for Photodynamic Therapy. *Adv. Healthcare Mater.,* **2019**, 8, 1900132.
107. van Straten, D.; Mashayekhi, V.; de Bruijn, H. S.; Oliveira, S.; Robinson, D. J. Oncologic Photodynamic Therapy: Basic Principles, Current Clinical Status and Future Directions. *Cancers,* **2017**, *9,* 19-72.
108. Ruggiero, E.; Alonso-de Castro, S.; Habtemariam, A.; Salassa, L. Upconverting nanoparticles for the near infrared photoactivation of transition metal complexes: new opportunities and challenges in medicinal inorganic photochemistry. *Dalton Trans.*, **2016**, *45*, 13012-13020.
109. Brancaleon, L.; Moseley, H. Laser and Non-Laser Light Sources for Photodynamic Therapy. *Lasers Med. Sci.*, **2002**, *17*, 173-186.
110. Oliveira, C. S.; Turchiello, R. Kowaltowski, A. J.; Indig, G. L.; Baptista, M. S.; Major determinants of photoinduced celle death: Subcellular licalization versus photosensitization efficiency. *Free Radic. Biol. Med.*, **2011**, *51*, 824-833.
111. Castano, A. P.; Demimova, T. N.; Hamblin, M. R. Mechanisms in photodynamic therapy: part one- photosensitizers, photochemistry and cellular localization. *Photodiagn. Photodyn. Ther.*, **2004**, *1*, 279-293.
112. Novusbio I Apoptosis, Necroptosis & Autophagy. images.novusbio.com/design/ apoptosis_poster.pdf (accessed in December 2019)
113. Castano, A. P.; Demimova, T. N.; Hamblin, M. R. Mechanisms in photodynamic therapy: part two- Cellular signaling, cell metabolism and modes of cell death. *Photodiagn. Photodyn. Ther.*, **2004**, *1*, 279-293.
114. Mroz, P.; Yaroslavsky, A.; Kharkwal, G. B.; Hamblin, M. R. Cell Death Pathways in Photodynamic Therapy of Cancer. *Cancers*, **2011**, *3*, 2516-2539.
115. Bacellar, I. O. L.; Tsubone, T. M.; Pavanim, C.; Baptista, M. S. Photodynamic Efiiciency: From molecular Photochemistry to Cell Death. *Int. J. Mol. Sci.,* **2015**, *16*, 20523-20559.
116. Oleinick, N. L.; Morris, R. L.; Belichenko, I. The role of apoptosis in response to photodynamic therapy: What, where, why, and how. *Photochem. Photobiol. Sci*, **2002**, *1*, 1-21.
117. Celli, J. P. Stromal interactions as regulators of tumor growth and therapeutic response: A potential target for photodynamic therapy? *Isr. J. Chem.,* **2012**, *52,* 757-766.
118. Peng, Q.; Nesland, J. M. Effects of photodynamic therapy on tumor stroma.*Ultrastruc. Pathol.*, **2004**, *28*, 333-40.
119. Yadav, L.; Puri, N.; Rastogi, V.; Satpute, P.; Sharma, V. Tumour Angiogenesis and Angiogenic Inhibitors: A Review. *J. Clin. Diagn. Res.*, **2015**, *9*, 1-5.
120. Maas, A. L.; Carter, S. L.; Wileyto, E. P.; Miller, J.; Yuan, M.; Yu, G.; Durham, A. C.; Busch, T. M.

Tumor vascular microenvironment determines responsiveness to photodynamic therapy. *Cancer Rev.*, **2012**, *72*, 2079-2088.

121. Korbelik, M.; Sun, J. Photodynamic therapy-generated vaccine for cancer therapy. *Cancer Immunol. Immunother.*, **2006**, *55*, 900-909.
122. Garg, A. D.; Nowis, D.; Golab, J.; Agostinis, P. Photodynamic therapy: illumitating the road from cell death towards anti-tumour immunity. *Apoptosis*, **2010**, *15*, 1050-1071.
123. Castano, A. P.; Mroz, P.; Hamblin, M. R. Photodynamic therapy and anti-tumor immunity. *Nat. Rev. Cancer*, **2006**, *6*, 535-545.
124. Wilson, B. C.; Patterson, M. S. The physics, biophysics and technology of photodynamic therapy. *Phys. Med. Biol.*, **2008**, *53*, 61-109.
125. Yano, T.; Muto, M.; Minashi, K.; Iwasaki, J.; Kojima, T.;Fuse, N.; Doi, T.; Kaneko, K.; Ohtsu, A. Photodynamic therapy as salvage treatment for local failure after chemoradiotherapy in patients with esophageal squamous cell carcinoma: a phase II study. *Int. J. Cancer.*, **2012**, *131*, 1228-1234.
126. Hu, J.; Tang, Y.; Elmenoufy, A. H.; Xu, H.; Cheng, Z.; Yang, X. Nanocomposite-Based Photodynamic Therapy Strategies for Deep Tumor Treatment. *Small,* **2015**, *11*, 5860-5887.
127. Schmitt, F.; Govindaswamy, P.; Suss-Fink, G.; Ang, W.H.; Dyson, P.J.; Juillerat-Jeanneret, L.; Therrien, B. Ruthenium porphyrin compounds for photodynamic therapy of cancer. *J. Med. Chem.*, **2008**, *51*, 1811-1816.
128. Schmitt, F.; Govindaswamy, P.; Zava, O.; Su□ss-Fink, G.; Juillerat-Jeanneret, L.; Therrien, B. Combined arene ruthenium porphyrins as chemotherapeutics and photosensitizers for cancer therapy. *J. Biol. Inorg. Chem.*, **2009**, *14*, 101–109.
129. Pernot, M.; Bastogne, T.; Barry, N.P.E.; Therrien, B.; Koellensperger, G.; Hann, S.; Reshetov, V.; Barberi-Heyob, M. Systems biology approach for invivo photodynamic therapy optimization of ruthenium-porphyrin compounds. *J. Photochem. Photobiol. B.*, **2012**, *117*, 80–89
130. Freudenreich, J.; Barry, N.P.E.; Süss-Fink, G.; Therrien, B. Permanent encapsulation or host–guest behavior of aromatic molecules in hexanuclear arene ruthenium prisms. *Eur. J. Inorg. Chem.*, **2010**, *2010*, 2400–2405.
131. (a) He, Y.-Q.; Fudickar, W.; Tang, J.-H.; Wang, H.; Li, X.; Han, J.; Wang, Z.; Liu, M.; Zhong, Y.-W.; Linker, T.; Stang, P. J. Capture and Release of Singlet Oxygen in Coordination-Driven Self-Assembled Organoplatinum(II) Metallacyles. *J. Am. Chem. Soc.,* **2020** (b) Qin, Y.; Chen, L.-J.; Dong, F.; Yin, G.-Q.; Li, X.; Tian, Y.; Yang, H.-B. Light-Controlled Generation of Singlet Oxygen within a Discrete Dual-Stage Metallacyle for Cancer Therapy. *J. Am. Chem. Soc.*, **2019**, *141*, 8943-8950. (c) Sun, W.; Zeng, X.; Wu, S. Photoresponsive ruthenium-containing polymers: potential polymeric metallodrugs for anticancer phototherapy. *Dalton Trans.*, **2018**, *47*, 283-286. (d) Rohrabaugh, Jr., T. N.; Collins, K. A.; Xue, C.; White, J. K.; Kodanko, J. J.; Turro, C. New Ru(II) complex for dual photochemotherapy: release of cathepsin K inhibitor and $^1O_2$ production. *Dalton Trans.*, **2018**, *47*, 11851-11858. (e) Sun, W.; Wen, Y; Thiramanas, R.; Chen, M.; Han, J.;

Gong, N.; Wagner, M.; Jiang, S.; Meijer, M. S.; Bonnet, S.; Butt, H.-J.; Mailänder, V.; Liang, X.-J.; Wu, S. Red-Light Controlled Release of Drug-Ru Complex Conjugates from Metallopolymer Micelles for Phototherapy in Hypoxic Tumor Environments. *Adv. Funct. Matter.*, **2018**, *28*, 1804227. (f) Frei, A.; Rubbiani, R.; Tubafard, S.; Blacque, O.; Anstaett, P.; Felgenträger, A.; Maisch, T.; Spiccia, L.; Gasser, G. Synthesis, Characterization, and Biological Evaluation of New Ru(II) Polypyridyl Photosensitizers for Photodynamic Therapy. *J. Med. Chem.*, **2014**, *57*, 7280-7292. (g) Davia, K.; King, D.; Hong, Y.; Swavey, S. A porphyrin− ruthenium photosensitizer as a potential photodynamic therapy agent. Inorg. Chem. Commun. 2008, 11, 584−586. (h) Gianferrara, T.; Bergamo, A.; Bratsos, I.; Milani, B.; Spagnul, C.; Sava, G.; Alessio, E. Ruthenium−porphyrin conjugates with cytotoxic and phototoxic antitumor activity. *J. Med. Chem.*, **2010**, *53*, 4678−4690. (i) Pernot, M.; Bastogne, T.; Barry, N. P. E.; Therrien, B.; Koellensperger, G.; Hann, S.; Reshetov, V.; Barberi-Heyob, M. Systems biology approach for in vivo photodynamic therapy optimization of ruthenium−porphyrin compounds. J. Photochem. Photobiol., B. **2012**, *117*, 80−89.

132. (a) Matsumoto, M.; Yamada, M.; Watanabe, N. Reversible 1,4-cycloaddition of a singlet oxygen to *N*-substituted 2-pyridones: 1,4- endoperoxide as a versatile chemical sourcer of singlet oxygen. *Chem.Commun.*, **2005**, *2005*, 483–485. (b) Wiegand, C.; Herdtweck, E.; Bach, T. Enantioselectivity in visible light-induced, singlet oxygen [2+4] cycloaddition reactions (type II photooxygenations) of 2-pyridones. *Chem. Commun.*, **2012**, *48*, 10195–10197. (c) Benz, S.; Nötzli, S.; Siegel, J. S.; Eberli, D.; Jessen, H. J. Controlled Oxygen Release from Pyridone Endoperoxides Promotes Cell Survival under Anoxic Conditions. *J. Med. Chem.*, **2013**, *56*, 10171–10182. (d) Turan, I. S.; Yildiz, D.; Turksoy, A.; Gunaydin, G.; Akkaya, E. U. A Bifunctional Photosensitizer for Enhanced Fractional Photodynamic Therapy: Singlet Oxygen Generation in the Presence and Absence of Light. *Angew. Chem. Int. Ed.*, **2016**, *55*, 2875-2878. (e) Xiao, W. Y.; Wang, P.; Ou, C. J.; Huang, X. Y.; Tang, Y. Y.; Wu, M. Y.; Si, W. L.; Shao, J. J.; Huang, W.; Dong, X. C. 2-Pyridone-Functionalized Aza-BODIPY Photosensitizer for Imaging-Guided Sustainable Phototherapy. *Biomaterials*, **2018**, *183*, 1-9.

133. (a) [1] Naphthalene endoperoxides as generators of singlet oxygen in biological media. Pierlot, C.; Aubry, J.-M.; Briviba, K.; Sies, H.; Mascio, P. D. *Methods Enzymol.*, **2000**, *319*, 3–20. (b) Klaper, M.; Linker, T. New Singlet Oxygen Donors Based on Naphthalenes: Synthesis, Physical Chemical Data, and Improved Stability. *Chem. - Eur. J.*, **2015**, *21*, 8569- 8577. (c) Fudickar, W.; Linker, T. Release of Singlet Oxygen from Aromatic Endoperoxides by Chemial Triggers. *Angew. Chem. Int. Ed.*, **2018**, *57*, 12971-12975. (d) Fudickar, W.; Linker, T. Release of Singlet Oxygen from Organic Peroxides under Mild Conditions. *ChemPhoChem.*, **2018**, *2*, 548-558. (e) Liu, K.; Lalancette, R. A.; Jäkle, F. Tuning the Structure and Electronic Properties of B-N Fused Dipyridylanthracene and Implications on the Self-Sensitized Reactivity with Singlet Oxygen. *J. Am. Chem. Soc.*, **2019**, *141*, 7453-7462. (f) Martins, S.; Farinha, J. P. S.; Baleizão, C.; Berberan-San-

tos, M. N. Controlled release of singlet oxygen using diphenylanthracene functionalized polymer nanoparticules. *Chem. Commun.*, **2014**, *50*, 3317-3320.

134. Moureu, C.; Dufraisse, C.; Dean, P. M. Un peroxyde organique dissociable : le peroxyde de rubrène. *Comptes Rendus Acad. Sci.*, **1926**, *182*, 1584-1587.
135. Dufraisse, C.; Velluz, L. L'union labile de l'oxygène au carbone. Influences des méthoxyles et de leurs positions sur l'état de labilité de l'oxygène dans les photooxydes mésodiphénylanthracéniques : un peroxide spontanlment dissociable à froid. *Bull. Soc. Chim. Fr.*, **1942**, 171-184.
136. Foote, C. S.; Wexler, S. Olefin oxidations with excited singlet oxygen. *J. Am. Chem. Soc.*, **1964**, *86*, 3879-3880.
137. Wasserman, H. H.; Scheffer, J. R. Singlet oxygen reactions from photoperoxides. *J. Am. Chem. Soc.*, **1967**, *89*, 3073-3075.
138. Arbuzov, Y. A.; The Diels-Alder reaction with molecular oxygen dienophile. *Russ. Chem. Rev.*, **1965**, *34*, 558.
139. Clennan, E. L. Synthethic and mechanistic aspects of 1,3-diene photooxidation. *Tetrahedron*, **1991**, *47*, 1343-1382.
140. Reddy, A. R.; Bendikov, M. Diels–Alder reaction of acenes with singlet and triplet oxygen – theoretical study of two-state reactivity. *Chem. Commun.*, **2006**, 1179-1181.
141. Aubry, J.-M.; Pierlot, C.; Rigaudy, J.; Schmidt, R. Reversible binding of oxygen to aromatic compounds. *Acc. Chem. Res.*, **2003**, *36*, 668-675.
142. Klaper, M.; Linker, T. Evidence for an oxygen anthracene sandwich complex. *Angew. Chem. Int. Ed.*, **2013**, *52*, 11896–11899.
143. Fudickar, W.; Linker, T. Synthesis of Pyridylanthracenes and Their Reversible Reaction with Singlet Oxygen to Endoperoxides. *J. Org. Chem.*, **2017**, *82*, 17, 9258-9262.
144. (a) Zhu, J.; Zou, J.; Zhang, J.; Sun, Y.; Dong, X.; Zhang, Q. Anthracene functionalized BODIPY derivative with singlet oxygen storage ability for photothermal and continuous photodynamic synergistic therapy. *J. Mater. Chem. B.*, **2019**, *7*, 3303-3309. (b) Callaghan, S.; Filatov, M. A.; Savoie, H.; Boyle, R. W., Senge, M. O. *In vitro* cytotoxicity of a library of BODIPY-anthracene and -pyrene dyads for application in photodynamic therapy. *Photochem. Photobiol. Sci.*, **2019**, *18*, 495-504. (c) Su, W.; Dong, S.; Chen, X.; Xiao, J.-A.; Peng, B.; Li, P. Novel half-sandwich rhodium(III) and iridium(III) photosensitizers for dual chemo- and photodynamic therapy. *Photodiagn. Photodyn. Ther.*, **2019**, *26*, 448-454. (d) Das, D.; Banaspati, A.; Das, N.; Bora, B.; Raza, M. K.; Goswami, T. K. Visible light-induced cytotoxicity studies on Co(II) complexes having an anthracene-based curcuminoid ligand. *Dalton Trans.*, **2019**, 12933-12942.
145. Cobo, S.; Lafolet, F.; Saint-Aman, E.; Philouze, C.; Bucher, C.; Silvi, S.; Credi, A.; Royal, G. Reactivity of a pyridinium-substituted dimethyldihydropyrene switch under aerobic *conditions*: Self-sensitized photo-oxygenation and thermal release of singlet oxygen. *Chem. Comm.*, **2015**, *51*, 13886–13889.
146. Bakkar, A.; Cobo, S.; Lafolet, F.; Saint-Aman, E.; Royal, G. A new surface-bond molecular switch

based on the photochromic dimethyldihydropyrene with light-driven release of singlet oxygen properties. *J. Mater. Chem. C.*, **2015**, *3*, 12014-12017.

147. Roldan, D.; Cobo, S. ; Lafolet, F. ; Vilà, N.; Bochot, C. ; Bucher, C. ; Saint-Aman, E. ; Boggio-Pasqua, M. ; Garavelli, M. ; Royal, G. A Multi-Addressable Switch Based on the Dimethyldihydropyrene Photochrome with Re-markable Proton-Triggered Photo-opening Efficiency. *Chem. Eur. J.*, **2015**, *21*, 455-467.
148. Blattmann, H.-R.; Meuche, D.; Heilbronner, E.; Molyneux, R. J.; Boekelheide, V. Photoisomerization of trans-15,16-Dimethyldihydropyrene. *J. Am. Chem. Soc.*, **1965**, *87*, 130–131.
149. (a) Mitchell, R. H.; Brkic, Z.; Sauro, V. A.; Berg, D. J. A Photochromic, Electrochromic, Thermochromic Ru Complexed Benzannulene: an Organometallic Example of the Dimethyldihydropyrene-Metacyclophanediene Valence Isomerization J. Am. Chem. Soc., **2003**, 125, 25, 7581-7585 (b) Muratsugu, S.; Kume, S.; Nishihara, H. Redox-Assisted Ring Closing Reaction of the Photogenerated Cyclophanediene Form of Bis(ferrocenyl)dimethyldihydropyrene with Interferrocene Electronic Communication Switching *J. Am. Chem. Soc.*, **2008**, *130*, 7204–7205 (c) Jacquet, M.; Lafolet, F.; Cobo, S.; Loisseau, F. ; Bakkar, A. ; Boggio-Pasqua, M ; Saint-Aman, E. ; Royal, G. Efficient Photoswitch System Combining a Dimethyldihydropyrene Pyridinium Core and Ruthenium(II) Bis-Terpyridine Entities. *Inorg. Chem.*, **2017**, *56*, 4357-4368.
150. Yan, H.; Süss-Fink, G.; Neels, A.; Stoeckli-Evans, H. Mono-, di- and tetra-nuclear p-cymene ruthenium complexes containing oxalato ligands. *J. Chem. Soc. Dalton Trans.* **1997**, *1997*, 4345–4350.
151. Therrien, B.; Süss-Fink, G.; Govindaswamy, P.; Renfrew, A.K.; Dyson, P.J. The "complex-in-a-complex" cations $[(acac)_2M\subset Ru_6(p\text{-}iPrC_6H_4Me)_6(tpt)_{2(}dhbq)_3]^{6+}$: A trojan horse for cancer cells. *Angew. Chem. Int. Ed. Engl.* **2008**, *47*, 3773–3776.
152. Barry, N.P.E.; Therrien, B. Host–Guest Chemistry in the Hexanuclear (Arene)ruthenium Metalla-Prismatic Cage $[Ru_6(p\text{-cymene})_6(tpt)_2(dhnq)_3]^{6+}$. *Eur. J. Inorg. Chem.* **2009**, *2009*, 4695–4700.
153. Allardyce, C. S.; Dyson, P. J.; Ellis, D. J.; Heath, S. L. $[Ru(\eta^6\text{-}p\text{-cymene})Cl_2(pta)]$ (pta = 1,3,5-triaza-7-phosphatricyclo- [3.3.1.1]decane): a water soluble compound that exhibits pH dependent DNA binding providing selectivity for diseased cells. *Chem. Commun.* **2001**, 1396-1397.
154. Bennett, M. A.; Huang, T.- N.; Matheson, T. W.; Smith, A. K. (η^6-Hexamethylbenzene)Ruthenium Complexes. *Inorg. Chem.*, **1982**, *21*, 74-78.
155. Linker, T.; Fröhlich, L. Regio- and Diastereoselective Photooxygenation of Chiral 2,5-Cyclohexadiene-1-carboxylic Acids. *Angew. Chem. Int. Ed. Engl.*, **1994**, *33*, 1971-1972.
156. Ramsay, W. J.; Szczypiński, F. T.; Weissman, H.; Ronson, T. K.; Smulders, M. M. J.; Rybtchinski, B.; Nitschke, J. R. Designed Enclosure Enables Guest Binding Within the 4200 $Å^3$ Cavity of a Self-Assembled Cube. *Angew. Chem., Int. Ed.* **2015**, *54*, 5636-5640.
157. Chien, W.-L.; Yang, C.-M.; Chen, T.-L.; Li, S.-T.; Hong, J.-L. Enhanced emission of a pyridine-based luminogen by hydrogen-bonding to organic and polymeric phenols. *RSC Adv.* **2013**, *3*, 6930-6938.

158. Shih, K.-Y; Lin, Y.-C.; Hsiao, T.-S-; Deng, S.-L.; Kuo, S.-W.; Hong, J.-L. Amorphous and crystalline blends from polytyrosine and pyridine-functionalized anthracene: hydrogen-bond interactions, conformations, intramolecular charge transfer and aggregation-induced emission. *Polym. Chem.* **2014**, *5*, 5765-5774.

159. Ciesielski, A.; Piot, L.; Samorì, P.; Jouaiti, A.; Hosseini, M.W. Molecular tectonics at the solid/liquid interface: Controlling of 1D coordination networks on graphite surfaces. *Adv. Mater.* **2009**, *21*, 1131–1136.

160. Zhang, P.; Xia, B.; Sun, Y.; Yang, B.; Tian, W.; Wang, Y.; Zhang, G. Electronic structures and optical properties of two anthracene derivatives. Chin. Sci. Bull., **2006**, 51, 2444-2450.

161. (a) Mitchell, R. H.; Boekelheide, V. Syntheses of [2.2]metacyclophane-1,9-diene and *trans*-15,16-dihydropyrene. *J. Am. Chem. Soc.*, **1970**, *92*, 3510-3512. (b) Mitchell, R. H.; Boekelheide, V. Transformation of sulfide linkages to carbon-carbon double bond. Syntheses of *cis*- and *trans*-15,16-dimethyldihydropyrene and trans-15,16-dihydropyrene. *J. Am. Chem. Soc.,* **1974**, *96,* 1547-1557. (c) Mitchell, R. H.; Ward, T. R.; Wang, Y.; Dibble, P. W. Pi-Switches: Synthesis of Three-Way Molecular Switches Based on the Dimethyldihydropyrene−Metacyclophanediene Valence Isomerization. *J. Am. Chem. Soc.,* **1999**, *121*, 2601-2602. (d) Marsella, M. J.; Wang, Z.-Q.; Mitchell, R. H. Backbone Photochromic Polymers Containing the Dimethyldihydropyrene Moiety: Toward Optoelectronic Switches. *Org. Lett.,* **2000**, *2*, 2979-2982. (e) Sheepwash, M. A. L.; Mitchell, R. H.; Bohne, C. Mechanistic Insights into the Photochromism of *trans*-10b,10c-Dimethyl-10b,10c-dihydropyrene Derivatives. *J. Am. Chem. Soc.*, **2002**, *124,* 4693-4700.

162. Bakkar, A.; Cobo, S.; Lafolet, F.; Roldan, D.; Saint-Aman, E.; Royal, G. A redox- and photo-responsive quadri-state switch based on dimethyldihydropyrene-appended cobalt complexes. *J. Mater. Chem. C*, **2016**,*4*, 1139-1143.

163. (a) Muratsugu, S.; Nishihara, H. π-Conjugation modification of photochromic and redox-active dimethyldihydropyrene by phenyl- and ethynyl-terpyridines and Ru(bis-terpyridine) complexes. *New J. Chem.*, **2014**,*38*, 6114-6124. (b) Muratsugu, S.; Kishida, M.-A.; Sakamoto, R.; Nishihara, H. Comparative Study of Photochromic Ferrocene-Conjugated Dimethyldihydropyrene Derivatives. *Chem. Eur. J.*, **2013**, *19*, 17314-17327. (c) Muratsugu, S.; Kume, S.; Nishihara, H. Redox-Assisted Ring Closing Reaction of the Photogenerated Cyclophanediene Form of Bis(ferrocenyl)dimethyldihydropyrene with Interferrocene Electronic Communication Switching. *J. Am. Chem. Soc.*, **2008**, *130*, 7204-7205.

164. Mitchell, R. H.; Ward, T. R.; Chen, Y.; Wang, Y.; Weerawarnam S. A.; Dibble, P. W.; Marsella, M. J.; Almutairi, A.; Wang, Z.-Q. *J. Am. Chem. Soc.*, **2003**, *125*, 2974-2988.

165. Vilà, N.; Royal, G.; Loiseau, F.; Deronzier, A. Photochromic and Redox Properties of Bisterpyridine Ruthenium Complexes Based on Dimethyldihydropyrene Units as Bridging Ligands. *Inorg. Chem.*, **2011**, *50*, 10581-10591.

166. Roldan, D.; Kaliginedi, V.; Cobo, S.; Kolivoska, V.; Bucher, C.; Hong, W.; Royal, G.; Wandlowski,

T. Charge Transport in Photoswitchable Dimethyldihydropyrene Type Single Molecule Junctions. *J. Am. Chem. Soc.*, **2013**, *135*, 5974-5977.

167. Boggio-Pasqua, M.; López Vidal, M.; Garavelli, M. Theoritical mechanistic study of self-sensitized photo-oxygenation and singlet thermal release in a dimethyldihydropyrene derivative. *J. Photochem. Photobiol. A.: Chem.*, **2017**, *333*, 156-164.
168. Bakkar, A.; Cobo, S.; Lafolet, F.; Roldan, D.; Jacquet, M.; Bucher, C.; Royal, G.; Saint-Aman, E. Dimethyldihydropyrene–cyclophanediene photochromic couple functionalized with terpyridyl metal complexes as multi-addressable redox- and photo-switches. *Dalton Trans.*, **2016**, *45*, 13700-13708.
169. Tang, B.; Yu, F.; Li, P.; Tong, L.; Duan, X.; Xie, T.; Wang, X. A Near-Infrared Neutral pH Fluorescent Probe for Monitoring Minor pH Changes: Imaging in Living HepG2 and HL-7702 Cells. *J. Am. Chem. Soc.* **2009**, *131*, 3016-3023.
170. (a) Sun, W.; Zhu, H.; Barron, P. M. Binuclear Cyclometalated Platinum(II) 4,6-Diphenyl-2,2′-bipyridine Complexes: Interesting Photoluminescent and Optical Limiting Materials. *Chem. Mater.*, **2006**, *18*, 2602-2610. (b) Mathew, I.; Li, Y.; Li, Z.; Sun, W. Dinuclear platinum(ii) 4,6-diphenyl-2,2,Ä≤-bipyridine complexes tethered by a rigid bridging ligand: synthesis and photophysics in solution and in LB film. *Dalton Trans.*, **2010**, *39*, 11201-11209. (c) Barry, N. P. E.; Zava, O.; Dyson, P. J.; Therrien, B. Excellent Correlation between Drug Release and Portal Size in Metalla-Cage Drug-Delivery Systems. *Chem. Eur. J.*, **2011**, *17*, 9669-9677. (d) Vogler, A.; Kunkely, H. Ligand-to-ligand and intraligand charge transfer and their relation to charge transfer interactions in organic zwitterions. *Chem. Rev.*, **2007**, *251*, 577-583.
171. (a) Morris, K. F.; Johnson, C. S. Diffusion-ordered two-dimensional nuclear magnetic resonance spectroscopy. *J. Am. Chem. Soc.*, **1992**, *114*, 3139- 3141. (b) Johnson, C. S., Jr. Diffusion ordered nuclear magnetic resonance spectroscopy: principles and applications. *Prog. Nucl. Magn. Reson. Spectrosc.,* **1999**, *34*, 203-256.
172. Sigma aldrich I Physical properties of solvents. https://www.sigmaaldrich.com/content/dam/sigma-aldrich/docs/Aldrich/General_Information/labbasics_pg144.pdf (accessed in February 2020)
173. (a) Freudenreich, J.; Dalvit, C.; Süss-Fink, G.; Therrien, B. Encapsulation of photosensitizers in hexa- and octanuclear organometallic cages: synthesis and characterization of carceplex and host,àíguest systems in solution. *Organometallics*, **2013**, *32*, 3018-3033. (b) Schmitt, F.; Freudenreich, J.; Barry, N. P. E.; Juillerat-Jeanneret, L.; Süss-Fink, G.; Therrien, B. Organometallic cages as vehicles for intracellular release of photosensitizers. *J. Am. Chem. Soc.*, **2012**, *134*, 754-757. (c) Barry, N.; Furrer, J.; Therrien, B. In- and Out-of-Cavity Interactions by Modulating the Size of Ruthenium Metallarectangles. Helvetica Chimica Acta, 2010, 93, 1313-1328. (d) Barry, N. P. E.; Furrer, J.; Freudenreich, J.; Süss-Fink, G.; Therrien, B. Designing the host-guest properties of tetranuclear arene ruthenium metalla-rectangles to accommodate a pyrene molecule. *Eur. J. Inorg. Chem.*, **2010**, *5*, 725-728. (e) Tidmarsh, I. S.; Taylor, B. F.; Hardie, M. J.;

Russo, L.; Clegg, W.; Ward, M. D. Further investigations into tetrahedral M4L6 cage complexes containing guest anions: new structures and NMR spectroscopic studies. *New J. Chem.*, **2009**, *33*, 366-375. (f) Furrer, M. A.; Schmitt, F.; Wiederkehr, M.; Juillerat-Jeanneret, L.; Therrien, B. Cellular delivery of pyrenyl-arene ruthenium complexes by a water-soluble arene ruthenium metalla-cage. *Dalton Trans.*, **2012**, *41*, 7201-7211.

174. Fudickar, W.; Linker, T. Why Triple Bonds Protect Acenes from Oxidation and Decomposition. *J. Am. Chem. Soc.* **2012**, *134*, 15071-15082.
175. Perrin, C. L. Linear or Nonlinear Least-Squares Analysis of Kinetic Data? *J. Chem. Educ.*, **2017**, *94*, 669-672.
176. Wilkinson, F. Rate Constants for the Decay and Reactions of the Lowest Electronically Excited Singlet State of Molecular Oxygen in Solution. An Expanded and Revised Compilation. *J. of Physical and Chemical Reference Data*, **1995**, *24*, 663-1021.
177. Bohne, C.; Mitchell, R. H. Characterization of the photochromism of dihydropyrenes with photophysical techniques. *J. Photochem. Photobiol., C*, **2011**, *12*, 126-137.
178. (a) Maubert, B.; McClenaghan, N. D.; Indelli, M. T. ; Campagna, S. Absorption Spectra and Photophysical Properties of a Series of Polypyridine Ligands Containing Aggended Pyrenyl and Anthryl Chromophores and of Their Ruthenium(II) and Osmium(II) complexes. *J. Phys. Chem. A*, **2003**,*107*, 447-455 (b) Yin, H.-J.; Liu, Y.-G.; Wang, K.-W. A highly sensitive and selective visible-light excitable luminescence probe for singlet oxygen based on a dinuclear ruthenium complex. *Dalton Trans.,* **2017**, *46*, 3325-3331
179. (a) Pefkianakis, E. K.; Christodouleas, D.; Giokas, D. L.; Papadopoulos, K.; Vougioukalakis, G. C. A Family of Ru^{II} Photosensitizers with High Singlet Oxygen Quantum Yield: Synthesis, Characterization, and Evaluation. *Eur. J. Inorg. Chem.,* **2013**, *26*, 4628-4635 (b) Abreu, F. D.; Diógenes, I. C. N.; de França Lopes, L. G. ; Silva Sousa, E. H. ; Moreira de Carvalho, I. M. Ruthenium(II) Bipyridine Complexes with Pendant Anthracenyl and Naphthyl Moieties: a Strategy for a ROS Generator with DNA binding Selectivity. *Inorg. Chim. Acta*, **2016**, *439*, 92-99.
180. Sheldrick, G. M. A short history of SHELX. *Acta Crystallogr A.,* **2008**, *64*, 112-122.
181. Farrugia, L. J. ORTEP-3 for Windows - a version of ORTEP-III with a Graphical User Interface (GUI). *J. Appl. Cryst.*, **1997**, *30*, 565, 10.1107/S0021889897003117.

7. List of publications and conference contributions

Publications

- Gaschard, M.; Nehzat, F.; Cheminel, T.; Therrien, B. Arene Ruthenium Metalla-Assemblies with Anthracene Moieties for PDT Applications. *Inorganics* 2018, *6*, 97.
- Duskova, K. ; Lamarche, J. ; Amor, S. ; Caron, C. ; Queyriaux, N. ; Gaschard, M. ; Penouilh, M.-J. ; De Robillard, G. ; Delmas, D. ; Devillers , C. H. ; Granzhan, A. ; Teulade-Fichou M.-P. ; Chavarot-Kerlidou, M. ; Therrien, B. ; Britton, S.; Monchaud, D. Identification of Three-Way DNA Junction Ligands through Screening of Chemical Libraries and Validation by Complementary in Vitro Assays. *J. Med. Chem.* 2019, *62*, 4456-4466

Conference contributions

- SCS Fall Meeting 2018, EPFL, Lausanne (Switzerland) - Poster
- 28th International Conference on OrganoMetallic Chemistry (ICOMC) 2018, Florence (Italy) – Poster
- SCS Spring meeting 2018, University of Neuchâtel (Switzerland)
- SCS Fall Meeting 2017, University of Bern (Switzerland) - Poster
- ICREA Conference on Functional Nanocontainers 2017, Tarragona (Spain) – Poster and flash presentation
- SCS Fall Meeting 2016, University of Zurich (Switzerland) - Poster